UNIVERSITÉ DE GENÈVE
Dèpartement de Physique
de la Matière Condensée

FACULTÉ DES SCIENCES
Professeur D. van der Marel

Pressure Tuning of Low-energy Collective Excitations in Metals

THÈSE

présenté à la Faculté des Sciences de l'Université de Genève
pour obtenir le grade de docteur ès Sciences, mention physique

par

Riccardo Tediosi
de
Pavia (Italie)

Thèse n° XXXX

GENÈVE
Atelier de reproduction de la Section de Physique
2008

UNIVERSITÉ DE GENÈVE

FACULTÉ DES SCIENCES

This is to certify that the thesis prepared by / Ceci certifie que la thèse rédigée par

RICCARDO TEDIOSI

entitled / intitulée

PRESSURE TUNING OF LOW-ENERGY COLLECTIVE EXCITATIONS IN METALS

complies with the University of Geneva regulations and that it meets the accepted standards of the Graduate School with respect to quality, and, in the case of a doctoral thesis, originality, / satisfait aux règlements de l'Université de Genève et qu'elle respecte les normes acceptées par la Faculté des études supérieures quant à la qualité et, dans le cas d'une thèse de doctorat, l'originalité,

for the degree of / pour le diplôme de

DOCTEUR ÈS PHYSIQUE

Signed by the final examining committee:
Signé par les membres du comité examinateur de la soutenance de thèse :

____________________, Directeur de thèse (Université de Genève)
D. van der Marel

____________________, Professeur (The Johns Hopkins University)
Norman Peter Armitage

____________________, Professeur (Université de Cologne)
Jhon A. Mydosh

____________________, Maître d'Enseignement et de Recherche (Université de Genève)
Alexey Kuzmenko

Approved by the Head of Department: / Approuvé par le Directeur du Département:

Genève, le 30 Mai 2008

____
Le Doyen, Jean-Marc TRISCONE

Thèse - XXXX -

To Ana for her infinite patience during these last years
and to Giuseppe and Pierangela, my parents, for their constant support
and love.

Contents

Chapter 1

Introduction

1.1 The challenge of IR spectroscopy under pressure

“Knowledge creates needs”. The implications of this concept can be found in our everyday experience, in economics, in sociology and in many more fields. Even if this thesis work won’t be a philosophical dissertation on this subject, it certainly represents a practical example of the cited concept in the field of solid state physics.

Even if many physical systems and materials have been already extensively studied in the past, this does not mean that all of them have been totally dissected unveiling their intimate nature. A discovery in fact comes always from the combination and the reciprocal confirmation between experimental data and theories. These two aspects have been always strongly dependent on the technological level characterizing a certain historical period. The main consequence of this, is the fact that each discovery is at the same time a scientific achievement, expanding the known limits of human knowledge, and a new starting point which would allow to go deeper in the understanding of a certain matter. Every new discovery thus creates automatically new needs, both theoretical and experimental, and constitutes the basis for progress. Since this thesis work has been entirely done in Geneva, I cannot avoid to cite the Large Hadron Collider (LHC) in CERN as probably the best possible example of the technological progress being made in order to give experimental evidence to preexisting theories.

Somehow in today’s scientific research an important prerequisite necessary for the discovery of new frontiers is *power* or better *additional power*. This generic reference to power is physically represented by an increased instruments’ resolution, an increased calculation power, reduced dimensions of the instruments, faster transmissions, higher energies etc. But more powerful techniques can also be developed just by adding and combining well established preexistent techniques in order to allow the observation of a physical phenomenon from different points of view while simultaneously varying the environmental conditions around the sample.

Optical spectroscopy in this respect is nowadays considered as a well established technique and its combination with cryogenic technology is extensively used to determine the electrodynamic properties of solids close to their zero-temperature ground state. The challenging task that will be described in this thesis work, consists in the opportunity to combine optical spectroscopy and cryogeny with high pressure techniques. The possibilities eventually accessible using such an apparatus would be numerous; hydrostatic pressure in fact is able to change the interatomic distances and consequently act directly as a tuning parameter on the electronic band structure of the materials and on the consequent interactions between charge carriers in the system. It is worth saying that in this regard, pressure is much more effective than chemical doping, which is often used instead of hydrostatic pressure, this because pressure preserves the atomic order present in the system without introducing disturbing and uncontrolled unknown parameters.

The most challenging experimental aspect that needs to be faced is the fact that pressure techniques and infrared optical spectroscopy have drastically different prerequisites in terms of sample size: the former technique would require small samples in order to apply a large pressure using a limited amount of force while the latter requires large samples both for detection purposes and to avoid limitations in terms of diffraction.

The introduction of a pressure cell with a diamond based optical aperture in a standard spectrometer and cryostat, change drastically the geometry of the setup and imposes important constraints in terms of mechanical stability of the system especially at cryogenic temperatures. The first part of this work will be dedicated to the description of the main technical aspects that need to be considered and changed in order to integrate a self-clamped pressure cell in a standard Bruker 66 spectrometer. This analysis is done by constantly comparing and motivating the proposed solutions with standard spectroscopic techniques. In particular a new cryostat design which improves the cited mechanical stability will be presented and discussed.

A large section will then describe the essential steps required for the preparation of the pressure cell prior to the experiment. In this part the reader will have a detailed overview on the large number of precautions that are needed while manipulating a pressure cell and large emphasis will be given to those details which, though apparently unimportant, will constitute key points for the successful conclusion of the connected optical experiment.

From the optical point of view the presence of a pressure cell and its diamond optical access, drastically changes the standard setup mainly influencing the referencing technique that is commonly used for the extraction of the absolute value of the optical reflectivity $R(\omega)$. In fact in standard ambient pressure experiments the reflectivity is calculated by measuring the reflected signal at the air-sample interface, then repeating the measurement on a thin gold layer evaporated directly on the sample surface and finally by taking the ratio of these two quantities. In the presence of a pressure cell, this procedure is no longer possible because gold evaporation cannot be used. A complete redefinition of the data analysis procedure is then needed in order to reconstruct the reflectivity curves; the details of this new method will be discussed in Chapter 4. The knowledge of $R(\omega)$ is in fact crucial because, by applying Kramers-Kronig relations [1], it allows the calculation of all the relevant quantities which describe the electrodynamics of the sample like, for example, the complex conductivity $\hat{\sigma}(\omega) = \sigma_1(\omega) + i\sigma_2(\omega)$.

1.2 The electrodynamics of Bismuth at high pressures

In the galaxy of possible materials that could be measured using the described experimental setup we have chosen pure single crystal semimetal bismuth. This material has its main peculiarity in the extremely low carrier density due to a tiny overlap between an electron conducting band and an hole band situated at a different point in the Brillouin zone. It has been demonstrated [2, 3, 4] how the application of hydrostatic pressure is strongly affecting the relative position of these bands leading to a further reduction of carrier density. This effect can drive the system into a state where the Fermi surface is ultimately reduced to a single point and interactions could strongly dominate the physical properties of this material.

A comprehensive study of the optical properties of bismuth at ambient pressure will be presented in Chapter 5. These optical experiments, done using experimental apparatus which are the state-of-the-art of the available technology, allowed to observe for the first time clear signatures of a purely electronic electron-plasmon coupling processes [5]. These effects are the consequence of the low carrier concentration which ultimately allows the energy scale for plasmonic effects to approach the energy region where transport phenomena start to be relevant.

Since these plasmonic effects could be strongly density dependent, we measured single crystal bismuth as a function of both temperature and pressure using infrared reflectivity combined with the experimental setup described in the first chapters. The spanned pressure range covers the region immediately preceding the critical pressure $P_c = 25$ kbar which characterizes a possible semimetal to semiconductor (SMSC) transition. We discovered that the plasmonic interaction gets remarkably enhanced as a function of pressure and the scattering processes seems to follow a non-metallic behavior in close connection with the simultaneous enhancement of the electron-plasmon interaction. As will be explained, this observation suggests a scenario in which strong interactions play a significative role for the explanation of the SMSC transition in single crystal bismuth. These findings suggest that in low carrier density materials, electron-electron, electron-plasmon and electron-phonon coupling must be considered on an equal footing in attempts to understand the dynamics of quasiparticles.

1.3 Charge density modulation in 3D $RE_5Ir_4Si_{10}$ compounds

One class of structures that has usually a strong pressure dependence is represented by low-dymensional materials. In particular it is well known that charge-density-wave (CDW) instabilities are much more effective in 1D systems with respect to the three dimensional case. Since the density modulation is strongly dependent from the interatomic distances, pressure can strongly influence this peculiar collective mode. We measured and analyzed by mean of IR and visible optical spectroscopy, the temperature dependent dynamics of CDW in two members of the $RE_5Ir_4Si_{10}$ family (RE being a rare heart atom) namely the lutetium and erbium based compounds. As it will result clear from the data presented in Chapter 7, the samples showed an extremely small signal change at the CDW transition and our experimental activity was then limited only to the ambient pressure case.

From the experimental point of view the possibility to measure the evolution of the

CDW transition as a function of pressure would have been extremely interesting since the CDW and superconductivity ground states appear to be strongly competing at low temperatures.

Indeed the two samples, although mainly 3D in character, revealed interesting physics typical of strongly-coupled CDW systems already at ambient pressure. The determination of the energy gap opened at the CDW transition temperature in fact, allowed to verify according to the predictions made by McMillan [6], that the physics of these compounds is dominated by a strong electron-phonon coupling. A strong vibrational contribution to the thermodynamical properties of these compounds has been previously suggested by the anomalous behavior observed at the charge-density-wave transition temperature by mean of thermal conductivity and thermoelectric power measurements [7, 8, 9].

The analysis of the frequency dependent scattering rate across the transition temperature based on the Eliashberg formalism of electron-phonon coupling, allowed to verify the appearance of a low-frequency Einstein mode which identify the lattice mode involved in the formation of the CDW ground state. The calculated electron-phonon coupling constant showed, at least qualitatively, a substantial increase at the transition temperature. Moreover the presence of a strong electron-phonon coupling together with the quasi-total absence of fluctuations in the temperature region preceding the transition, suggested a scenario where both short-coherence length and strong interchain coupling play an important role in the determination of a ground state where CDW and superconductivity are both simultaneously present [10].

Résumé en français

Le challenge de la spectroscopie IR sous pression

“Le savoir crée le besoin”. Les implications de ce concept peuvent être trouvées dans notre expérience quotidienne, en économie, en sociologie et dans bien d’autres domaines. Même si ce travail de thèse n’a pas pour but d’être une dissertation philosophique sur ce sujet, il représente certainement un exemple concret de ce concept dans le domaine de la physique de l’état solide.

Bien qu’un grand nombre de systèmes physiques et de matériaux aient déjà été intensivement étudié dans le passé, tous n’ont pas été disséqués jusqu’à révéler leur nature profonde. Une découverte est toujours la combinaison et la confirmation réciproque entre expériences et théories. Ces deux aspects ont toujours été très dépendants du niveau technologique caractéristique d’une certaine époque. La conséquence principale de ceci, est le fait que chaque découverte est à la fois un achèvement scientifique, repoussant les limites du savoir humain, et un nouveau point de départ pour aller plus loin dans la compréhension de la matière condensée. Chaque nouvelle découverte crée automatiquement de nouveaux besoins, à la fois sur les plans expérimentaux et théoriques, et constitue une base pour les progrès à venir. Ce travail de thèse ayant été entièrement réalisé à Genève, je ne peut éviter de citer le “Large Hadron Collider” (LHC) du CERN comme un des meilleurs exemples possibles d’avancée technologique motivée par la recherche de preuves expérimentales pour étayer des théories pré-existantes.

Cependant dans la recherche scientifique actuelle un pré-requis important et nécessaire pour la découverte de nouvelles frontières est le *pouvoir* ou plutôt le *pouvoir additionnel*. Le pouvoir correspond physiquement à l’augmentation de la résolution instrumentale, à l’augmentation de la puissance de calcul, à la réduction de la taille des instruments, à des transmissions plus rapides, des énergies plus élevées, etc. Des techniques plus puissantes peuvent aussi être développées juste en ajoutant ou en combinant des techniques pré-existantes bien établies dans le but d’observer des phénomènes physiques avec des points de vues différents en changeant l’environnement autour d’un échantillon.

De ce point de vue, la spectroscopie optique est actuellement considérée comme une technique bien établie et est largement utilisée en combinaison avec la technologie cryogénique pour déterminer les propriétés électroniques de solides proches de leur état fondamental à température nulle. Le challenge relevé par cette thèse, a consisté à combiner la spectroscopie optique, la cryogénie et les hautes pressions. Les possibilités finalement accessibles grâce à cette combinaison sont nombreuses ; une pression hydrostatique est en effet capable de changer les distances inter-atomiques et par conséquent d'agir directement en tant que paramètre d'ajustement sur la structure des bandes électroniques et sur les interactions entre les porteurs de charges et le système. Dans ce sens, la pression est bien plus efficace que le dopage chimique, souvent utilisé à la place de la pression hydrostatique, parce que la pression préserve l'ordre atomique présent dans le système sans introduire de perturbations non contrôlées et non déterminées.

Le défit expérimental le plus important relevé est dû au fait que les techniques de pression et la spectroscopie optique dans l'infrarouge nécessitent des tailles dramatiquement différentes d'échantillons : la première technique nécessite des échantillons petits afin d'appliquer de hautes pressions en utilisant une force limitée tandis que la deuxième technique nécessite de grands échantillons à la fois pour la détection et pour éviter les effets de diffraction.

L'introduction d'une cellule de pression avec un ouverture optique en diamant dans un cryostat et un spectromètre standard change dramatiquement la géométrie du système et impose d'importantes contraintes en termes de stabilités mécaniques en particulier à basses températures. La première partie de ce travail est dédié à la description des points essentiels à prendre en compte pour intégrer une cellule de pression dans un spectromètre Bruker 66 standard. L'analyse est faite en comparant et motivant continuellement les solutions proposées avec les techniques standards de spectroscopie. En particulier, le dessin d'un nouveau cryostat renforçant la stabilité mécanique est présenté et discuté.

Une long chapitre. Dans cette partie le lecteur trouvera un survol d'un grand nombre de précautions indispensables pour la manipulation de la cellule de pression. L'accent est mis sur des détails, a priori insignifiants, qui constituent les points clés pour le succès d'une telle expérience.

Du point de vue de l'optique la présence de la cellule de pression avec son accès optique en diamant change dramatiquement la configuration standard, en particulier la technique de "référence" communément utilisée pour la détermination de la valeur absolue de la réflexion $R(\omega)$. En effet, pour les expériences standards à pression ambiante, la valeur absolue de la réflexion est déterminée comme le ratio du signal réfléchit à l'interface air-échantillon par celui de l'interface air-couche d'or évaporée "in-situ" sur l'échantillon. Avec la cellule de pression une telle procédure n'est plus applicable car l'évaporation d'or n'est pas possible. Une redéfinition complète de la procédure d'analyse des données est donc nécessaire. Les détails de cette nouvelle méthode sont discutés dans le chapitre 4. La connaissance de $R(\omega)$ est cruciale car en utilisant les relations de Kramers-Kronig [1] elle permet de calculer des quantités qui décrivent l'électrodynamique de l'échantillon comme, par exemple, la conductivité optique complexe sigma $\hat{\sigma}(\omega) = \sigma_1(\omega) + i\sigma_2(\omega)$.

L'électrodynamique du bismuth à haute pression

Dans la galaxie des matériaux mesurables avec le dispositif expérimental décrit précédemment nous avons choisit un monocristal de bismuth. La particularité essentielle de ce matériau est sa densité extrêmement faible de porteurs due à une petite superposition d'une bande de conduction d'électrons avec une bande de trous situées en des points différents de la zone de Brillouin. Il a été démontré [2, 3, 4] que l'application d'une pression hydrostatique affecte fortement la position relative de ces deux bandes menant à une réduction supplémentaire de la densité de porteurs. Cet effet peut amener le système dans un état où la surface de Fermi est finalement réduite à un point unique où les interactions pourraient fortement dominer les propriétés physiques du matériau.

Une étude complète des propriétés optiques du bismuth à pression ambiante est présentée dans le chapitre 5. Ces expériences optiques, faites avec des appareils qui sont l'état-de-l'art de la technologie disponible, ont permis d'observer pour la première fois les signatures d'un processus purement électronique de couplage électron-plasmon [5]. Ces effets sont la conséquence de la faible concentration de porteurs qui finalement permet, à l'échelle d'énergie des effets plasmoniques, d'approcher la région d'énergie où les phénomènes de transport deviennent importants.

Comme ces effets plasmoniques pourraient dépendre fortement de la densité, nous avons mesuré des monocristaux de bismuth en fonction de la température et de la pression en utilisant la réflexion infrarouge combinée avec le dispositif expérimental décrit dans les premiers chapitres. La gamme de pressions explorée couvre la région précédent la pression critique $P_c = 25$ kbar qui correspond à une possible transition d'un état semi-métallique vers un état semi-conducteur (SMSC). Nous avons découvert que l'interaction plasmonique est particulièrement renforcée avec la pression et que le processus de diffusion semble suivre un comportement non-métallique en relation étroite avec le renforcement simultané de l'interaction électron-plasmon. Cette observation suggère un scénario dans lequel de fortes interactions jouent un rôle important pour expliquer la transition SMSC dans les monocristaux de bismuth. Ces découvertes suggèrent que pour les matériaux à faible densité de porteurs, les couplages électron-électron, électron-plasmon et électron-phonon doivent être considérés sur un pied d'égalité afin de comprendre la dynamiques des quasi-particules.

Modulation d'onde de densité de charges dans les composés 3D $\mathbf{RE_5Ir_4Si_{10}}$

Un type de structure ayant habituellement une forte dépendance en fonction de la pression sont les matériaux à basses dimensions. En particulier il est bien connu que les instabilités d'onde de densité de charges (ODC) sont bien plus marquées dans les systèmes à une dimension que dans les systèmes à trois dimensions. Comme les modulations de densité sont fortement dépendantes des distances inter-atomiques, la pression peut influencer ce mode collectif particulier. Nous avons mesuré et analysé à l'aide de spectroscopie optique dans le visible et l'infra-rouge la dépendance en température de la dynamique de l'ODC dans deux composés de la famille $RE_5Ir_4Si_{10}$ (RE étant un atome de terre rare) : un à base de lutétium et un à base d'erbium. Il apparaît clairement dans les données présentées dans le chapitre 7 que les échantillons montrent un changement extrêmement faible du signal lors de l'apparition de l' ODC. C'est pourquoi notre activité s'est ensuite limité à leur étude à pression ambiante.

D'un point de vue expérimental la possibilité de mesurer l'évolution de l'ODC en fonction de la pression aurait été très intéressante car l'état d'onde de densité de charges et l'état supraconducteur semblent être en compétition à basse température.

En effet, ces deux échantillons, bien que essentiellement 3D, révèlent une physique typique des systèmes fortement couplés à une onde de densité de charge même à pression ambiante. La détermination de l'énergie du gap ouvert lors de l'apparition de l'OCD, a permis de vérifier en accord avec les prédictions faites par McMillan [6], que la physique de ces composés est dominée par un fort couplage électron-phonon. Une forte contribution vibrationnelle aux propriétés thermodynamiques de ces composés a précédemment été proposée à cause du comportement anormal observé par conductibilité thermique et mesure thermoélectrique à la température de transition de l'apparition de l'ODC [7, 8, 9].

L'analyse basée sur le formalisme d'Eliashberg du couplage électron-phonon, du temps de diffusion en fonction de la fréquence au travers de la température de transition a permis de vérifier l'existence d'un mode d'Einstein à basse fréquence qui identifie le mode de vibration du cristal impliqué dans la formation de l'état fondamental de l'ODC. La constante électronique de couplage extraite des mesures montre, au moins qualitativement, une augmentation substantielle à la température de transition. De plus la présence d'un fort couplage électron-phonon combiné à la quasi-absence de fluctuations pour les températures précédent la transition, suggèrent un scénario où courte distance de corrélation et fort couplage inter-chaînes jouent un rôle important dans la détermination de l'état fondamental où l'onde-de-densité-de-charge et la supraconductivité sont simultanément présents [10].

Chapter 2

Principles of Optical Spectroscopy

> *The light that burns twice as bright*
> *burns half as long,*
> *and you have burned so very, very*
> *brightly.*
>
> Blade Runner - *Energy Conservation*

The use of light as a probe to extract information about the properties of materials has always been fascinating. First of all because *light* is probably the most natural way to grab physical information on matter since it represents a fundamental component of our daily experience, secondly because the use of light as a probe does not require a solid contact with the sample under investigation reducing to a minimum any possible spurious contributions to the measurement results.

In this chapter we will introduce formal arguments in order to give to the reader an overview of the physical quantities that can be extracted through an optical measurement. This explanation will be based on a formalism which describes the interaction between light and matter from a microscopic point of view. We anticipate that the mathematical derivations of the formulas won't be always presented since that is not the main focus of this chapter. We invite the reader wanting to expand on the concepts described in this section to refer to specialized text books on the subject [11, 12, 13].

Together with the theoretical presentation of the basic concepts of optical spectroscopy, we will also introduce the principles of the experimental techniques commonly used in our laboratory. Since a large part of this work will be dedicated to a non-standard technique we believe that an introduction to classical techniques could give to the reader the opportunity to better appreciate the differences and the novelties that will be explained in the subsequent chapters.

2.1 Microscopic quantum theory of light-matter interaction

The main effect of an electromagnetic wave impinging on a sample's surface is to modify the charge density distribution and the current densities inside the solid. In a very general way we can represent this latter effect with a generalized Ohm's law

$$\mathbf{J}(\omega) = \hat{\sigma}\mathbf{E}(\omega) \tag{2.1}$$

where $\mathbf{J}(\omega)$ is the total frequency dependent current density in the solid and $\mathbf{E}(\omega)$ is the time-dependent electric field of the electromagnetic wave. The complex quantity $\hat{\sigma}$ completely describes the electromagnetic properties of the solid and its determination is the main objective of any optical experiment.

In a general picture, a system of N electrons can be represented by the following hamiltonian

$$\begin{aligned} \mathcal{H} &= \frac{1}{2m}\sum_{i=1}^{N}\left(\mathbf{p}_i + \frac{e}{c}\mathbf{A}(\mathbf{r}_i)\right)^2 + \sum_{i=1,j=1}^{N,M} V_j^0(\mathbf{r}_i - \mathbf{R}_j) \\ &+ \frac{1}{2}\sum_{i=1,i'=1}^{N,N}\frac{e^2}{|\mathbf{r}_i - \mathbf{r}_{i'}|} - \sum_{i=1}^{N} e\Phi(\mathbf{r}_i) \end{aligned} \tag{2.2}$$

where the first term represents the coupling between the electromagnetic wave, represented by a frequency dependent vector potential $\mathbf{A}$, and electrons with momentum $\mathbf{p}_i$. The second term represents the interaction between electrons and the positive ionic potential V^0 which, in the case of a crystalline system, is periodic. The third term describes the mutual repulsion between electrons while the last term represents the contribution of the presence of external charges described by a scalar potential $\Phi(\mathbf{r})$. The other quantities are the electron charge e, the speed of light c and the electron mass m.

The hamiltonian can be easily written as the sum of two terms: one representing the unperturbed system and one describing the influence of the external potentials on the solid so that $\mathcal{H} = \mathcal{H}_0 + \mathcal{H}'$ where

$$\mathcal{H}_0 = \frac{1}{2m}\sum_{i=1}^{N}\mathbf{p}_i^2 + \sum_{i=1,j=1}^{N,M} V_j^0(\mathbf{r}_i - \mathbf{R}_j) + \frac{1}{2}\sum_{i=1,i'=1}^{N,N}\frac{e^2}{|\mathbf{r}_i - \mathbf{r}_{i'}|} \tag{2.3}$$

and in the first order approximation

$$\mathcal{H}' = \frac{e}{2mc}\sum_{i=1}^{N}\left[\mathbf{p}_i \cdot \mathbf{A}(\mathbf{r}_i) + \mathbf{A}(\mathbf{r}_i) \cdot \mathbf{p}_i\right] + \frac{e^2}{2mc^2}\sum_{i=1}^{N}|\mathbf{A}(\mathbf{r}_i)|^2 - \sum_{i=1}^{N} e\Phi(\mathbf{r}_i) \tag{2.4}$$

Since we are interested only in the transverse response of the system which is associated only with the vector potential $\mathbf{A}$, we can neglect the last term in Eq.2.4 which on the contrary determines the longitudinal response.

The expression for the transverse component of the electrical current density operator can be written as

$$\mathbf{J}(\mathbf{r}) = -\frac{e}{2}\sum_{i=1}^{N}\left[\mathbf{v}_i\delta(\mathbf{r} - \mathbf{r}_i) + \delta(\mathbf{r} - \mathbf{r}_i)\mathbf{v}_i\right] \tag{2.5}$$

where $\mathbf{v}_i$ is the velocity of the ith particle at position $\mathbf{r}_i$. Considering the relation between velocity, momentum and vector potential $\mathbf{v} = \mathbf{p}/m + e\mathbf{A}/mc$ the current density is a sum of two contributions:

$$\begin{aligned}\mathbf{J}(\mathbf{r}) &= \mathbf{J}_p(\mathbf{r}) + \mathbf{J}_d(\mathbf{r}) = \\ &= -\frac{e}{2m}\sum_{i=1}^{N}[\mathbf{p}_i\delta(\mathbf{r}-\mathbf{r}_i) + \delta(\mathbf{r}-\mathbf{r}_i)\mathbf{p}_i] - \frac{e^2}{mc}\sum_{i=1}^{N}\mathbf{A}(\mathbf{r}_i)\delta(\mathbf{r}-\mathbf{r}_i)\end{aligned} \tag{2.6}$$

where the first term represents the paramagnetic current while the second one the diamagnetic current. The idea here is to use the definition of current density expressed by Eq. 2.5 together with the interacting term of the hamiltonian (2.4) in order to derive a formula that expresses the current density as a function of the external time dependent electric field. Once obtained, the expression will also automatically give us the value of the optical conductivity.

From this point on we prefer to use the second quantization formalism. Using this notation we use the quantum mechanical creation and annihilation operators, $\hat{c}^{\dagger}_{k,\sigma}$ and $\hat{c}_{k,\sigma}$ respectively, to express the local field operator

$$\psi^{\dagger}_{\sigma}(\mathbf{r}) = \sum_{k} e^{-i\mathbf{k}\cdot\mathbf{r}}\hat{c}^{\dagger}_{k,\sigma} \tag{2.7}$$

where k defines the momentum and σ the spin state of a particle. With this definition the local particle density can be expressed as

$$\hat{n}_{\sigma}(\mathbf{r}) = \psi^{\dagger}_{\sigma}(\mathbf{r})\psi_{\sigma}(\mathbf{r}). \tag{2.8}$$

Working within the second quantization formalism it is often very convenient to work in reciprocal space instead of direct space. For the local density operator the Fourier transform is

$$\hat{n}_{\sigma}(\mathbf{r}) = \frac{1}{V}\sum_{q} e^{-i\mathbf{q}\cdot\mathbf{r}}\rho_q. \tag{2.9}$$

According to this formalism this allow us to rewrite the expressions for the density operator and for the velocity operator which will be useful, as anticipated, in the solution of the interacting hamiltonian. The two terms are respectively

$$\rho_q = \sum_{k,\sigma}\hat{c}^{\dagger}_{k-q/2,\sigma}\hat{c}_{k+q/2,\sigma} \tag{2.10}$$

$$\hat{\mathbf{v}}_q = \frac{\hbar}{m}\sum_{k,\sigma}\mathbf{k}\hat{c}^{\dagger}_{k-q/2,\sigma}\hat{c}_{k+q/2,\sigma}. \tag{2.11}$$

We can now rederive the expression for the interacting hamiltonian

$$\mathcal{H}' = -\frac{e\hbar}{c}\sum_{q} e^{i(\mathbf{q}\cdot\mathbf{r}-\omega t)}\mathbf{A}_q\cdot\hat{\mathbf{v}}_{-q} \tag{2.12}$$

and rewrite the velocity operator which should reflect the two main current density contributions as in Eq. 2.6

$$\hat{\mathbf{v}}_q \rightarrow \hat{\mathbf{v}}_q - \frac{e\hbar}{mc}\mathbf{A}_q e^{i(\mathbf{q}\cdot\mathbf{r}-\omega t)}\hat{\rho}_q. \tag{2.13}$$

Given two eigenstates of the system $|\Psi_n\rangle$ and $|\Psi_m\rangle$ with energies E_n and E_m, the probability of the transition is simply proportional to $|\langle\Psi_m|\mathcal{H}'|\Psi_n\rangle|^2$. Substituting Eq. 2.13 in Eq. 2.12 we find that the matrix element for the transition reflects the presence of the two current densities. For the diamagnetic term, considering the relation between field and vector potential in the second quantization formalism, we obtain

$$\mathbf{J}_d(\mathbf{r}) = -\frac{ne^2}{mc}\mathbf{A}(\mathbf{r},t) = \frac{ine^2}{m\omega}\mathbf{E}(\mathbf{r}) \tag{2.14}$$

where we used the definition $\mathbf{E}(\mathbf{r},t) = (i\omega/c)\sum_q \mathbf{A}_q \exp[i(\mathbf{q}\cdot\mathbf{r}-\omega t)]$.

For the paramagnetic density the situation is more complicated and after some algebra the relation between current and external field reads as

$$\mathbf{J}_p = \mathbf{E}(\mathbf{r},t)\frac{ie^2}{\omega V}\sum_n \mathbf{v}_{-q}^{nm}\mathbf{v}_q^{mn}\left[\frac{1}{\omega - E_n + E_m + i0^+} - \frac{1}{\omega + E_n - E_m + i0^+}\right], \tag{2.15}$$

where the matrix element $\mathbf{v}_q^{mn} \equiv \langle\Psi_m|\hat{\mathbf{v}}_q|\Psi_n\rangle$ reflects the fact that any light absorption process is dominated by the current (velocity) operator.

Combining Eq. 2.14 and Eq. 2.15 with the generalized Ohm's law we can finally derive an expression for the optical conductivity

$$\sigma_{\alpha,\alpha}(\mathbf{q},\omega) = \frac{ie^2}{V}\sum_{n,m\neq n}\frac{e^{\beta(\Omega-E_n)}}{\omega_{mn}}\left[\frac{v_{\alpha,q}^{nm}v_{\alpha,-q}^{mn}}{\omega-\omega_{mn}+i\eta} + \frac{v_{\alpha,-q}^{nm}v_{\alpha,q}^{mn}}{\omega+\omega_{mn}+i\eta}\right], \tag{2.16}$$

which can be easily adapted to the case where $\mathbf{q}\sim 0$ which is more appropriate when describing light induced excitations since the photon momentum is negligible with respect the typical electron momentum in solids. Using this latter approximation we can write the final expression for the transverse optical conductivity as

$$\sigma_{\alpha,\alpha}(\omega) = \frac{i\omega}{4\pi}\sum_{n,m\neq n}\frac{\Omega_{mn}^2}{\omega(\omega+i\gamma_{mn})-\omega_{mn}^2}, \tag{2.17}$$

where ω_{mn} is the energy difference between the final and initial state $E_m - E_n$, γ_{mn} is the relaxation rate of the excited state which is inversely proportional to its lifetime. The term Ω_{mn} is often defined as "oscillator strength" and it is defined as

$$\Omega_{mn}^2 \equiv \frac{8\pi e^2 e^{\beta(\Omega-E_n)}|v_\alpha^{nm}|^2}{\omega_{mn}V}. \tag{2.18}$$

In the last two equations the basic physics behind any absorption process is finally emerging in all its beauty. As it can be seen once again the matrix element connecting any couple of energy states in a physical system, determines, to a first approximation, its optical behavior. Equation 2.17, in particular, is very general and describes equally well both intraband processes and interband processes guaranteeing in both cases the fundamental energy and momentum conservation.

2.1.1 Drude-Lorentz models

The expression 2.17 is very general and represents equally well all kind of absorption processes between two energy states. Commonly this general picture is separated in two main cases describing the two main electronic states of matter: the metallic state and the insulating state. The metallic state is described by the Drude model which is suitable for representing all the absorption processes that promote an electron in the conduction band into an empty energy state located in the same band as shown in Fig. 2.1. Since there is no forbidden energy band separating the two states, an absorption process can take place for $\omega \rightarrow 0$ thus promoting an electron sitting right below the Fermi energy E_F into an empty state right above it. According to these considerations the optical conductivity can be written as

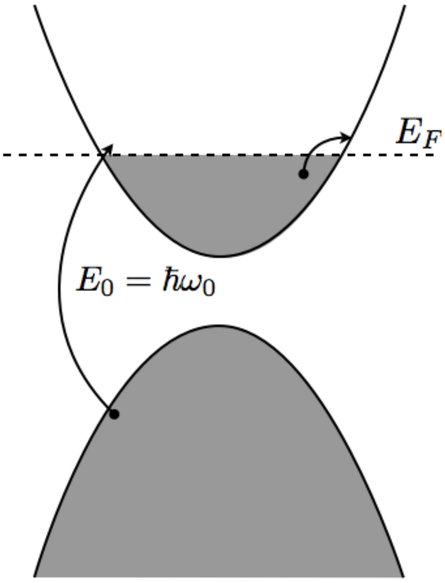

Figure 2.1: Intraband and Interband transitions - The Drude model is suitable for the description of the intraband transition, *i.e.* all the process where an electron is excited from its initial energy state below the Fermi energy to a final state above the Fermi energy. Both states belong to the conduction band. The Lorentz model describes processes where initial and final states are in two different bands separated by an energy distance $E_0 = \hbar\omega_0$.

$$\hat{\sigma}(\omega) = \frac{\omega_p^2}{4\pi}\frac{1}{\gamma - i\omega} \tag{2.19}$$

where $\omega_p = \sqrt{4\pi N e^2/m}$ is the plasma frequency.

In a similar way the Lorentz model describes the process where an electron is exited from its initial energy state into an empty state in a different band. This model is particularly suitable for insulators where indeed the initial and final states are separated by a forbidden energy band *i.e.* the gap. In this case the optical conductivity reads as

$$\hat{\sigma}(\omega) = \frac{\omega_p^2}{4\pi}\frac{\omega}{\omega\gamma - i(\omega^2 - \omega_0^2)} \tag{2.20}$$

where ω_0 is associated with the amplitude of the energy gap between the two states $E_0 = \hbar\omega_0$. As it can be seen comparing Eq. 2.19 and 2.20 the Drude model can be obtained from the Lorentz model by setting $\omega_0 = 0$.

Both in a real metallic and insulating case the situation is more complicated than the one just presented since the band structure cannot always be represented as a simple two bands model. In the real situation there will be more bands each of them with an associated transition energy $\hbar\omega_{0i}$, relaxation rate γ_i and oscillator strength Ω_i. The resulting total conductivity will thus be a combination of all the contributions coming from each band. In the spectroscopist's language each contribution is usually called an *oscillator*.

2.2 Macroscopic properties of solids

In the previous section we calculated, using a microscopic description of the solid, one of the most important and useful quantities characterizing a physical system: the frequency dependent optical conductivity. Equation 2.17 reveals that the conductivity is a complex function that we can express as

$$\hat{\sigma}(\omega) = \sigma_1(\omega) + i\sigma_2(\omega). \tag{2.21}$$

The frequency dependent conductivity itself gives a complete description of the system's response and can be used, following the standard macroscopic treatment of the problem in the linear response regime, to express all the other physical quantities like the dielectric function $\hat{\varepsilon}(\omega)$ and the complex index of refraction $\hat{N}$. For the dielectric function $\hat{\varepsilon}(\omega) = \varepsilon_1(\omega) + i\varepsilon_2(\omega)$ the relations are:

$$\varepsilon_1(\omega) = 1 - \frac{4\pi\sigma_2(\omega)}{\omega} \tag{2.22}$$

$$\varepsilon_2(\omega) = \frac{4\pi\sigma_1(\omega)}{\omega} \tag{2.23}$$

while for the complex index of refraction $\hat{N} = n + ik$ we can write

$$n = \sqrt{\frac{1}{2}\left[\left(1 - \frac{4\pi\sigma_2}{\omega}\right)^2 + \left(\frac{4\pi\sigma_1}{\omega}\right)^2\right]^{\frac{1}{2}} + \frac{1}{2} - \frac{2\pi\sigma_2}{\omega}} \tag{2.24}$$

$$k = \sqrt{\frac{1}{2}\left[\left(1 - \frac{4\pi\sigma_2}{\omega}\right)^2 + \left(\frac{4\pi\sigma_1}{\omega}\right)^2\right]^{\frac{1}{2}} - \frac{1}{2} + \frac{2\pi\sigma_2}{\omega}} \tag{2.25}$$

where we assumed the magnetic susceptibility of the medium $\mu_1 = 1$[1].

Combining the previous relations with the Drude-Lorentz expressions for the optical conductivity it is possible to determine the effect of each oscillator on the dielectric constant and in the general case we can write the total dielectric function as the sum of the contributions coming from intraband transitions and from interband transitions as $\hat{\varepsilon}_{\text{tot}}(\omega) = \hat{\varepsilon}_{\text{intra}}(\omega) + \hat{\varepsilon}_{\text{inter}}(\omega)$.

---

[1] This is generally valid for non-magnetic materials but considering that the magnetic susceptibility for paramagnetic and diamagnetic materials is usually much smaller than their dielectric susceptibility, the magnetic contribution to the optical properties of these kind of solids is usually negligible.

Even if the relations 2.23-2.25 do not add any additional information to the physics of the system compared to the simple knowledge of the conductivity function, in some situations it is more convenient to work with a particular representation and later on derive the remaining expressions. For example in optical experiments in reflection or transmission it is more convenient and natural to work with the expression of the refractive index which gives a direct image of the change of wavelength induced by the presence of the medium on the propagating beam. This is easily seen by writing the expression for the electric field of a plane wave propagating with a frequency ω along the z direction in a medium with a complex index of refraction $\hat{N}$

$$E(\omega,t) = E_0 \mathrm{e}^{-i(\omega t - \hat{N}\mathbf{q}\cdot\mathbf{z})}. \tag{2.26}$$

Writing the index of refraction in terms of its real and imaginary parts Eq. 2.26 becomes

$$E(\omega,t) = E_0 \mathrm{e}^{-i(\omega t - n\mathbf{q}\cdot\mathbf{z})} \mathrm{e}^{-k\mathbf{q}\cdot\mathbf{z}} \tag{2.27}$$

which reveals how the imaginary part of the index of refraction is associated with an exponential decay term while the real part is responsible for a phase term. The index of refraction of materials can be used to conveniently describe the reflection and transmission processes happening at the interface between two substances. The mathematical description of such a process expressed by the Fresnel's equations is the base for our experimental activity.

2.3 Kramers-Kronig Relations

From the relations introduced in the previous section, the reader can see that each function describing the properties of a material is complex. Without entering too much into the details of the theory [1, 14] it can be demonstrated using the causality principle, that the real and imaginary part of each function are correlated to each other. In particular, the complete knowledge of the real (imaginary) part of the conductivity or dielectric function over all frequencies, allows the calculation of the corresponding imaginary (real) part.

Given a complex function $\hat{F}(\omega) = F_1(\omega) + iF_2(\omega)$ which satisfies $\hat{F}(\omega) = \hat{F}^*(-\omega)$, the relations between its real and imaginary parts are

$$\begin{aligned} F_1(\omega) &= \frac{2}{\pi}\mathcal{P}\int_0^\infty \frac{\omega' F_2(\omega')}{\omega'^2-\omega^2}\,\mathrm{d}\omega' \qquad (2.28)\\ F_2(\omega) &= -\frac{2\omega}{\pi}\mathcal{P}\int_0^\infty \frac{F_1(\omega')}{\omega'^2-\omega^2}\,\mathrm{d}\omega'. \qquad (2.29)\end{aligned}$$

Kramers-Kronig relations are particularly useful in experiments where either F_1 of F_2 can be measureds. Using these relations in fact, it is possible to extract the missing part of information and thus to have a complete description of the properties of a sample. It is worth saying that since the KK relations rely on the causality principle the missing quantity that is extracted using Eq. 2.28 and 2.29 is unique.

While on the one hand the KK relations are a powerful tool, on the other hand there is a strong constraint that needs to be fulfilled: the known quantity that has to be used for the calculation of the missing part, has to be known over the full frequency range. Usually a single experimental technique cannot cover the entire spectral range and often a combination of measurements is used to fulfill the mentioned spectral range requirement.

As we will see below, among the different experimental techniques, ellipsometry represents an ideal tool since it allows one, in a limited spectral range, to directly extract real and imaginary parts of the dielectric constant $\hat{\varepsilon}(\omega)$.

2.4 “Classical” experimental techniques

In this section we will present the two main techniques used during the experimental activity presented in this work: the intensity reflection technique and ellipsometry. Although in many cases the proper use of those technique could be very complicated, we used the term “classical” just to distinguish them from the technique that will be discussed in the next chapters in combination with the pressure cell equipment. The main purpose of this section is to give the reader an idea of the basic principles of reflection and ellipsometry techniques in order to allow a better understanding of the main differences between a standard experiment and an experiment done in the presence of a pressure cell apparatus.

2.4.1 Reflection experiments

One of the most extensively used optical techniques is based on the determination of the reflection coefficient measured at the interface between two materials. In the simplest case the interface consists of air (or vacuum) and the sample of interest. Mathematically the problem can be described by considering the incoming beam as TEM radiation which impinges on the sample surface with a certain angle. The amplitude of the reflected signal can be found by writing the relations that connect the incident field with the reflected and refracted fields at the interface. Specifically, these relations are constrained by boundary conditions between electric and magnetic fields at the interface between the two materials [11]. Following this procedure it is possible to express the electric field of the reflected and refracted beams as a function of incident field, dielectric properties of the sample and angle of incidence of the incoming beam; these relations are commonly known as *Fresnel equations*.

Without entering into the details of the formulas, we expect the ratio between reflected and incident fields, called the *reflectivity*, to be a complex quantity defined as

$$\frac{E_r(\omega)}{E_i(\omega)} = \hat{r}(\omega) = r(\omega)\mathrm{e}^{i\phi(\omega)}, \tag{2.30}$$

where both r and ϕ are functions of the dielectric properties of the material. Usually the detector measures the intensity of the signal without giving any phase information. The resulting coefficient $R(\omega) = |\hat{r}(\omega)|^2$ is defined as the *reflection* coefficient of the material.

The reflection coefficient is also a function of the angle of incidence; in the optical setup that has been used for this experimental work, the relative position between source, sample and detector determines a quasi-normal incidence configuration. In particular the angle formed between the propagation vector of the incident light and the normal to the sample surface was approximatively 10°. In this situation it was demonstrated that $R(\omega, 10°) \simeq R(\omega, 0°)$. For the normal incidence case, and considering an interface between two materials having index of refraction $\hat{N}_1$ and $\hat{N}_2$, the reflection coefficient derived from Fresnel equation is

$$R(\omega) = \left| \frac{\hat{N}_1 - \hat{N}_2}{\hat{N}_1 + \hat{N}_2} \right|^2 . \tag{2.31}$$

In the simple case where the sample is exposed to vacuum $\hat{N}_1$ is real and equal to 1. It is important here to stress that in principle both indexes of refraction are complex quantities since they are coupled with the real and imaginary part of the conductivity function of the materials according to equations 2.24 and 2.25.

As we have seen in the previous section ε_1 and ε_2, σ_1 and σ_2 are all Kramers-Kronig related quantities. In the case of the optical reflectivity in Eq. 7.12 it is also possible to form a KK consistent pair defining a new quantity

$$\ln[\hat{r}(\omega)] = \ln r + i\phi. \tag{2.32}$$

Using this definition together with equations 2.28 and 2.29 it is then possible to calculate the missing phase information which was lost during the detection process and completely reconstruct the reflectivity function from the reflection function $R(\omega)$. The reflectivity is then used to calculate conductivity and dielectric functions.

We will now briefly explain how this kind of measurement is physically done. First the sample is carefully polished in order to obtain an optically flat surface, then it is mounted on a special semi-conical holder whose top surface has a dimension slightly smaller then the sample in order to avoid spurious reflections coming from the holder itself. Using a polychromatic source the reflected signal intensity is first measured for the bare sample surface as shown in the top part of Fig. 2.2. As a reference the same measurement is repeated once a thick gold layer has been deposited on the sample surface. The gold deposition is based on a simple evaporation procedure that can be

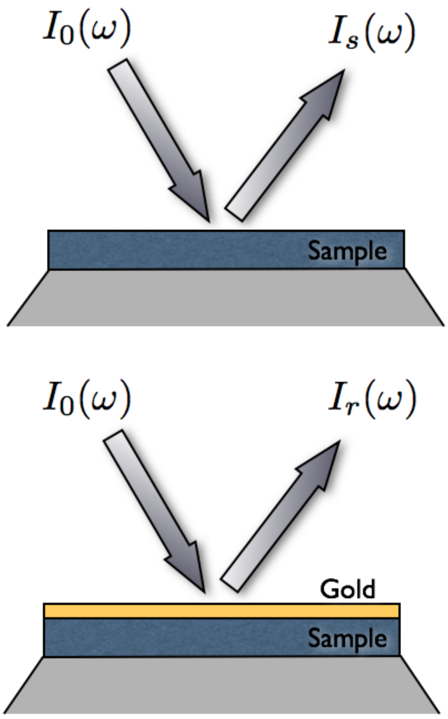

Figure 2.2: Reflection configuration - The intensity reflected from the sample is measured using a polychromatic source. The same measurement is repeated on a reference gold layer deposited *in situ* on the sample surface. The reflection coefficient is calculated dividing the two reflected signals.

done directly *in situ* without the need of moving the sample from its original position. The two measured signals are $I_s(\omega) = I_0(\omega)R_s(\omega)$ and $I_r(\omega) = I_0(\omega)R_r(\omega)$ respectively for the reflection on the sample and on the reference, where $I_0(\omega)$ is the intensity spectrum of the incident light. Taking now the ratio between the two spectra we obtain

$$\frac{I_s(\omega)}{I_r(\omega)} = \frac{R_s(\omega)}{R_r(\omega)}. \tag{2.33}$$

Since in the FIR and MIR spectral ranges, gold has $R_r(\omega) \geq 0.99$, the intensity ratio in Eq. 2.33 gives the absolute value of the reflection coefficient of the sample. Sometimes it is necessary to calibrate for the gold as well for which either the theoretical value is used, or an ellipsometry measurement of the gold film.

The main advantage of this referencing technique is the fact that the reference has a shape identical to the one of the sample allowing an extremely precise calibration of the reflection coefficient without introducing spurious contribution due to the mismatch between sample and reference shape. Another big advantage consists in the possibility to keep the sample alignment fixed during the reference deposition thus avoiding any change in the optical geometry of the system.

As last remark we would like to point out that even if in the practical case the incident beam is focused, thus having a certain distribution of angles of incidence, the quasi-normal incidence condition is fulfilled for every ray in the beam. Moreover, the use of focusing optics produces a spatial filtering effect due to the fact that only the light reflected at the sample position (the focal point) will be able to reach the detector. This is extremely convenient when the measurement is done in presence of an optical cryostat since the signal intensity reflected on the cryostat's windows won't be able to interfere with the sample's signal because of their large distance from the focal point.

2.4.2 Spectroscopic Ellipsometry

The second method that is commonly used in optical spectroscopy is ellipsometry [15]. The basic principle of ellipsometry is to measure both the intensity and the relative phase state of the light. As anticipated for the case of the intensity reflection technique the measurement of the absolute value of the phase is not possible since the detector only measures an integrated intensity. The interesting idea introduced with ellipsometry is that both intensity and phase are measured relative between the two states of polarization of the light.

In Fig. 2.3 the schematic shows the optical configuration for an ellipsometry measurement. A polarized incident field can be decomposed in two components E_s and E_p respectively parallel and perpendicular to the plane of incidence π. The reflection on the sample surface modifies the relative intensity and phase between the two polarization components accordingly to the sample properties represented by its dielectric function $\hat{\varepsilon}(\omega)$. Using a rotating polarizer placed right in front of the detector, the ratio between the reflection coefficients $r_{\|}$ and $r_{\perp}$ can be extracted and expressed as

$$\hat{\rho} = \frac{r_{\|}}{r_{\perp}} = \tan(\Psi)\mathrm{e}^{i\Delta} \tag{2.34}$$

where Ψ represents the relative reflection intensity while Δ describes the phase difference between the two reflection coefficients. Measuring these latter quantities as a function of frequency allow us to reconstruct directly the complex dielectric function using the formula

$$\hat{\varepsilon} = \sin^2\theta \left[1 + \tan^2\theta \left(\frac{1+\hat{\rho}}{1-\hat{\rho}}\right)^2\right], \tag{2.35}$$

where θ is the angle of incidence. Equation 2.35 is an exact solution in the case of a completely isotropic sample. In all the cases where the dielectric function depends on the crystal orientation, Eq. 2.35 is called the pseudo-dielectric function since the reflected parallel and perpendicular polarization components have a response which depends also on the material anisotropy and orientation. In this case a series of measurements, repeated for different sample orientations, allows to completely determine the problem and to extract the dielectric function for every optical axis.

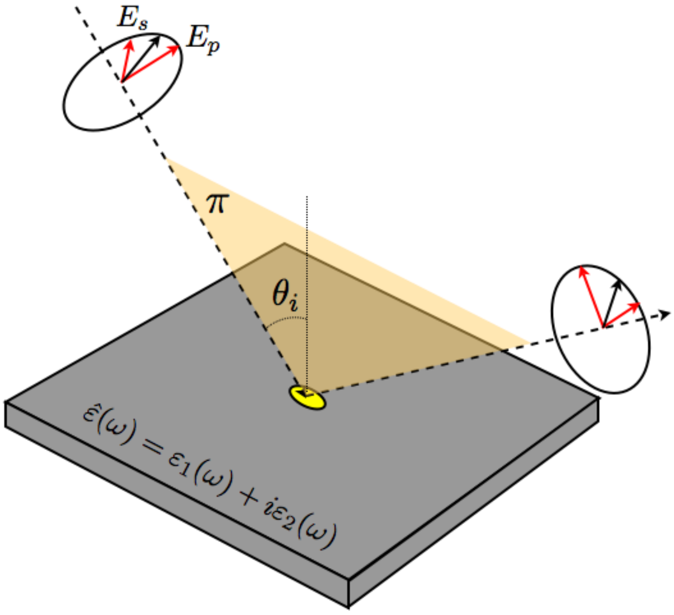

Figure 2.3: Schematic of an ellipsometric measurement - The incident light has polarization components parallel and perpendicular to the plane of incidence π. The polarization state of the reflected light is modified according to the dielectric properties of the sample represented by the complex and frequency dependent function $\hat{\varepsilon} = \varepsilon_1 + i\varepsilon_2$. The relative intensity and phase difference between the the two reflected states of polarization allows to completely reconstruct the dielectric function.

Comparing the two above methods the reader may immediately understand the enormous power of ellipsometry with respect to reflectivity since using the former method there is no need of Kramers-Kronig transformations in order to derive the real and imaginary part of the dielectric function. Another important advantage is also given by the fact that the measurement of absolute values of the optical quantities can be done without any reference measurement contrarily to the case of reflectivity.

As usual some of the most important limits to experimental techniques are related to the frequency dependent response function of some of the main components in the system; in the case of ellipsometry the major problems are encountered in the infrared spectral range where the quality of the polarizers available on the market is not sufficient to fulfill the precision requirements of the technique. In the case of reflectivity experiments the major limit is given by a non-ideal response of the reference material in the visible range[2].

What is usually done in order to circumvent those limiting factors, is simply to combine the two techniques in order to have experimental data over the largest possible spectral range.

2.5 Putting it all together

In this chapter we introduced the basic concepts related to optical spectroscopy and its experimental application, from the basic microscopic derivation of the optical conductivity using the Kubo formula to the working principles of two of the most important experimental techniques used in this field, reflectivity and ellipsometry. We conclude this chapter with a practical example on how all these concepts are combined together in order to extract the physics buried under a sample surface.

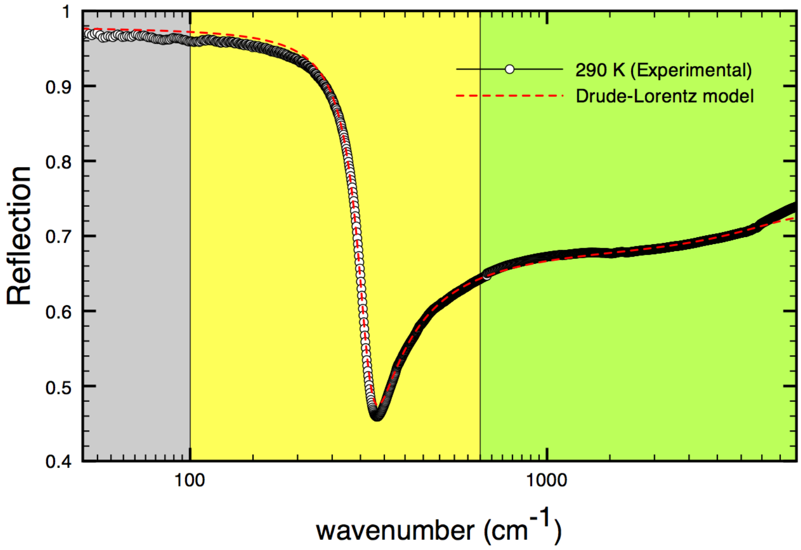

Figure 2.4: The experimental reflectivity - The measurement has been done using three different combinations of sources, detectors and beamsplitters in the spectrometer setup. The three covered spectral ranges are shown with different colors. The experimental data (black open circles) taken in different energy regions merge perfectly with each other at the boundaries, confirming the good quality of the measurements. The red dashed line represent the reflectivity obtained fitting the experimental data with a Drude-Lorentz model.

---

[2] In Eq. 2.33 the value of the gold reflection start to deviate considerably from the ideal case (1) already in the visible and drastically drops at the screened plasma frequency ($\sim$ 2.5 eV).

Since it will be the main subject of this work, we will consider the case of bismuth. We anticipate that here we will present only a didactic example without entering into the details of the physical interpretation. The reader is invited to refer to the following chapters explicitly dedicated to the study of bismuth.

As anticipated in the end of the last section the combination of different techniques is fundamental in order to have the sample properties measured over the widest spectral range. The techniques are usually complementary to each other in order to fill possible gaps in the spectra due to technical limitations imposed by other experimental approaches. For the IR spectral range the most reliable technique is based on intensity reflection; in particular using a combination of difference sources and detectors it is possible to cover the range between 50 and 6000 cm^{-1} corresponding to an energy range of 6.2-743.8 meV[3].

As shown in Fig. 2.4 the measurement has been done with different spectrometer configurations in order to cover the complete infrared range: a bolometer detector cooled with liquid He at 1.6 K has been used in combination with an Hg lamp in the range between 50 and 100 cm^{-1} while another bolometer has been used in the 100-650 cm^{-1} region. For the MIR spectral range an incandescence SiC source was used and the signal was detected using an MCT detector cooled with liquid nitrogen. The reflection coefficient of the material was calculated according to Eq. 2.33 and the different data sets are correctly matching at the boundaries of the different measurement regions.

In the visible spectral range we used a Woolam VASE ellipsometer in order to extract the real and imaginary part of the dielectric function as shown in Fig. 2.5.

Once all the data have been collected in the broadest possible spectral range, the analysis procedure consists in fitting the experimental data using a Drude-Lorentz model as a starting point. Using the user-friendly RefFIT program [16] it is possible to define a set of oscillators each one characterized by its own central frequency ω_{0i}, oscillator strength (or plasma frequency) ω_{pi} and inverse lifetime γ_i. The parameters can be varied in order to match in the best possible way the experimental data using, for example, a least-squares fitting method. This procedure can be done simultaneously on every data set independently by the physical quantity that a certain data set represents. In the case exemplified here we used two oscillators whose parameters are reported in Table 2.1. The resulting reflection and dielectric functions are shown respectively in Fig. 2.4 and 2.5 together with the experimental data.

Table 2.1: The basic Drude-Lorentz parameters used to model the bismuth's response at room temperature - ambient pressure.

ω_0	ω_p	γ_0
0	3300.5	37.31
5831.6	60875	9141.6

Even though the reflection function is not known over the entire frequency range, as required by Kramers-Kronig transformations, the use of the complex quantities ex-

---

[3] 1 eV = 8065.8 cm^{-1}.

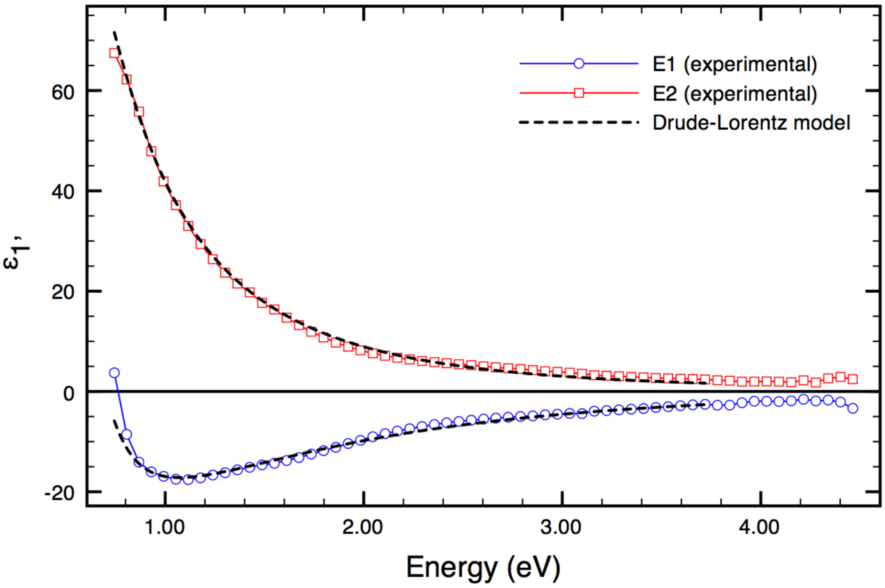

Figure 2.5: Ellipsometry data - The real and imaginary part of the dielectric function are shown respectively with red squares and blue circles for the room temperature case. The same functions for the Drude-Lorentz model are presented with black dashed lines.

tracted by the ellipsometry technique, constitutes a valid anchor point for the unknown complex part of the reflectivity in the fitting procedure. In other words, the incomplete knowledge of the real part of the reflection at high frequency can be compensated if a portion of the imaginary part is known in a certain spectral region.

The analysis can be further improved since using just the Drude-Lorentz model it is not possible to reproduce effects which are not intrinsically included in the derivation of the DL theory; that is why in the beginning of this section we defined the DL model as a good starting point for the analysis but certainly not the definitive solution. The last part of the analysis consists then in reproducing the fine structure (*i.e.* also the noise) of the experimental data using a variational dielectric function added on top of the original Drude-Lorentz model. The variational approach is done in a Kramers-Kronig consistent way so that the causality principle of the physical process is guaranteed. The result of this procedure is shown in Fig. 2.6 where the real part of the optical conductivity is plotted for the simple Drude-Lorenz model and for the cited variational approach. The difference is not enormous since the starting DL model was already a good approximation of the real physical situation, however as we will see in the dedicated chapter, the low temperature physics of bismuth requires clearly a more detailed model. In the conductivity spectrum are present small discontinuities: the one around 50 cm^{-1} is due to the fact that real experimental data are limited to that frequency value, while the little step around 6000 cm^{-1} is due to the small mismatch between the infrared and visible data sets. For clarity the graph only shows the real part of the conductivity function but the fitting procedure automatically produces both the

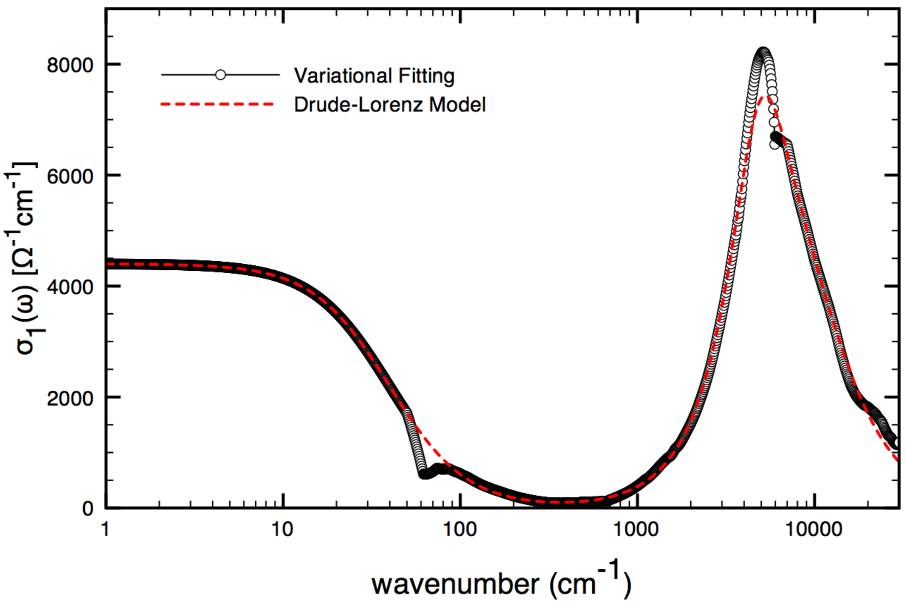

Figure 2.6: Optical Conductivity - The real and imaginary part of the dielectric function are shown respectively with red squares and blue circles for the room temperature case. The same functions for the Drude-Lorentz model are presented with black dashed lines.

real and imaginary parts as well as all the other relevant quantities like, for example, the complete dielectric function.

Chapter 3

Pressure Equipment

Pressure pushing down on me
Pressing down on you no man ask for
Under pressure - that burns a building down
Splits a family in two
Puts people on streets.

Queen - *Under Pressure*

This chapter is focused on the description of the pressure cell equipment used and developed during the thesis work. Before starting with the details on the apparatus, we wish to acknowledge Professor Forrò of the EPFL in Lausanne and his collaborator Dr. Richard Gaál who designed and constructed the pressure cell [17] that will be extensively described in this chapter. The fact of having a working pressure cell developed thanks to the long experience in the pressure cell technology of Dr. Gaál represented a big advantage for us and allowed to focus our attention on the optical and cryogenic adaptation of the cell to our commercial spectrometer and cryostat. It is worth saying that the constant technical support given by the EPFL group during our activity with the pressure equipment was a determinant for the scientific achievements discussed in this work.

It is useful to give a small introduction on pressure cell equipment in general in order to give to the reader an idea of the "joys and pitfalls" of this experimental activity. This introduction is not intended to be a complete review of all the possible aspects regarding the pressure experiments but would be more focused in the introduction of the concepts that can be useful in the later parts of the work. For a deeper and broader understanding of the pressure techniques the reader is invited to look for review articles [18, 19, 20, 21, 22] and books[23] written by the pioneers of this research activity.

Ever since the very early days of pressure experiments in the Fifties the number and type of pressure cells has grown tremendously. This was due to two principal aspects: the first one was mainly technological and related to the development of new and harder materials that could be used for the production of cells, the second one was strictly related to particular combinations between high pressure and well established experimental techniques which imposed design constraints on the geometry of the pressure cells. A common factor among various pressure cell designs is the use of *diamonds* as the main elements transmitting pressure to the sample in the cell. The use of diamonds represented a revolution for the high-pressure physics community since it introduced many advantages that allowed to shed even more light (not only from a metaphoric point of view) on this new field of research. In fact on the one hand diamond represents the hardest material known on earth, and on the other hand it is the broadest optical window available, since its transparency covers the infrared, visible, ultraviolet and X-ray spectral range. It is then immediately evident how, with the introduction of the diamonds, pressure techniques could be used in combination with "optical" techniques like optical spectroscopy, Raman scattering, Brillouin scattering and (soft and hard) x-ray techniques. In those fields a lot of progress has been made. Yet, there is still a lot to do in order to be able to extract experimental data with a quality comparable to standard techniques at ambient pressure.

3.1 Pressure Cells and Critical Aspects

Before starting with the description of the pressure cell used for the experiments, we will dedicate some space to the analysis of the most critical aspects deriving from the use of high-pressure equipment. We will mainly focus on the impact and consequences that those features have on the performances of the optical system interfaced to the cell.

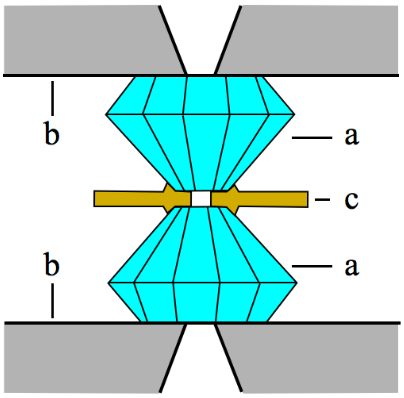

Figure 3.1: Diamond Anvil Cell (DAC) - The main parts of a DAC are the two diamond anvils (a) each one mounted on a metallic support plate (b). These plates have an aperture which serves as optical access for the radiation. The sample is placed in the tiny space created between the two anvils with the aid of a drilled metallic gasket (c).

Let us take as an example the typical working principle of a diamond anvil cell (DAC) shown in Fig. 3.1. Here the cell is constituted by two metallic supporting elements provided with a conical optical access, two diamond anvils resting on the two support plates and a drilled metallic gasket. The gasket-anvil system creates the tiny sample space shown in white that will host the sample, the pressure gauge and the pressure transmitting medium. The pressure is applied to the system via the supporting metal plates and be transmitted to the sample by the diamonds. In an optical experiment the light will enter into the system through the conical apertures, will then traverse a diamond and be transmitted (or reflected) on the sample; finally it will exit from the cell either by following the reverse path in the case of a reflection experiment, or by passing through the second diamond in the case of a transmission experiment[1]. From a spectroscopic point of view most part of

---

[1] The description is slightly simplified since the sample is surrounded at least on one side by the

the problems when doing experiments under pressure have their origin right at the definition of pressure! Considering in fact that pressure is defined as $P = F/S$, where F is the force and S is the surface over which the force is applied, we find that the main limiting aspect for pressure cells is the compressive strength σ_c of the materials constituting the cell itself. This constant has the dimensions of a pressure. In a pressure cell with diamond anvils, the weakest component is not the diamond itself whose compressive yield has never been measured [24], but the diamond's supporting plates. Just to give a rough idea we can consider for example a diamond anvil of 3 mm in diameter resting on a support plate with an aperture for optical access of 1 mm in diameter. With a force of 10 kN applied on the cell the pressure on the support plate would be 1.6 GPa. Taking materials that are commonly defined as "strong" we find that $\sigma_c \sim 1.2$ GPa for Cu-Be, ~ 1.5 GPa for hardened stainless steel and ~ 3 for tungsten carbide (WC). This already restricts a lot the range of possible materials which can be used to make the pressure cell. Assuming to be able to apply 10 kN on such a pressure cell the maximum pressure that could be applied to the sample (in a very unsafe situation!) with a diamond sizing 1.5 mm in diameter on the small culet, would be just ~ 5.6 GPa. This range of pressures is just enough to start to observe interesting phenomena like tunable charge density wave transitions [25, 26, 27, 28], metal-insulator transitions [29], superconductivity suppression [25, 30, 31, 32] and many more. This, together with the fact that it is always a good practice to work in a safe condition far from the failure limit, results in a much smaller diamond (therefore sample) size compared to the 1.5 mm case.

Certainly the sample's dimension represents a critical factor for an optical spectroscopist since the availability of an high brilliance[2] source (i. e. a synchrotron) is usually limited. In particular for the infrared spectral range if the sample size is reduced below the diffraction limit, all the classical Fresnel equations start to fail in their description of the optical transmission and reflection processes. In order to carry out experiments in the infrared, and in particular far-infrared spectral region, it is therefore necessary to increase the sample size thereby sacrificing the pressure range while gaining in signal to noise ratio.

3.2 Piston-cylinder cell for IR spectroscopy

In the previous section we underlined three main conclusions in order to plan an experiment under pressure using infrared spectroscopy:

1. Relatively large samples are needed in order to avoid the diffraction limit.
2. The increase of the sample surface will limit the maximum achievable pressure.
3. A diamond window is required for its optical and hardness properties.

With these points in mind, the goal of this thesis work is to develop a system able to measure the low energy physics of solid state systems either with a synchrotron source

---

pressure transmitting medium which guarantees hydrostatic pressure conditions onto the sample.

[2] the *brilliance* is defined as the brightness per unit of bandwidth. It describes the number of photons per second which hits a unitary surface per unit of solid angle and per unit of bandwidth, i. e. $W/(\mathrm{sr\,cm^2\,Hz})$.

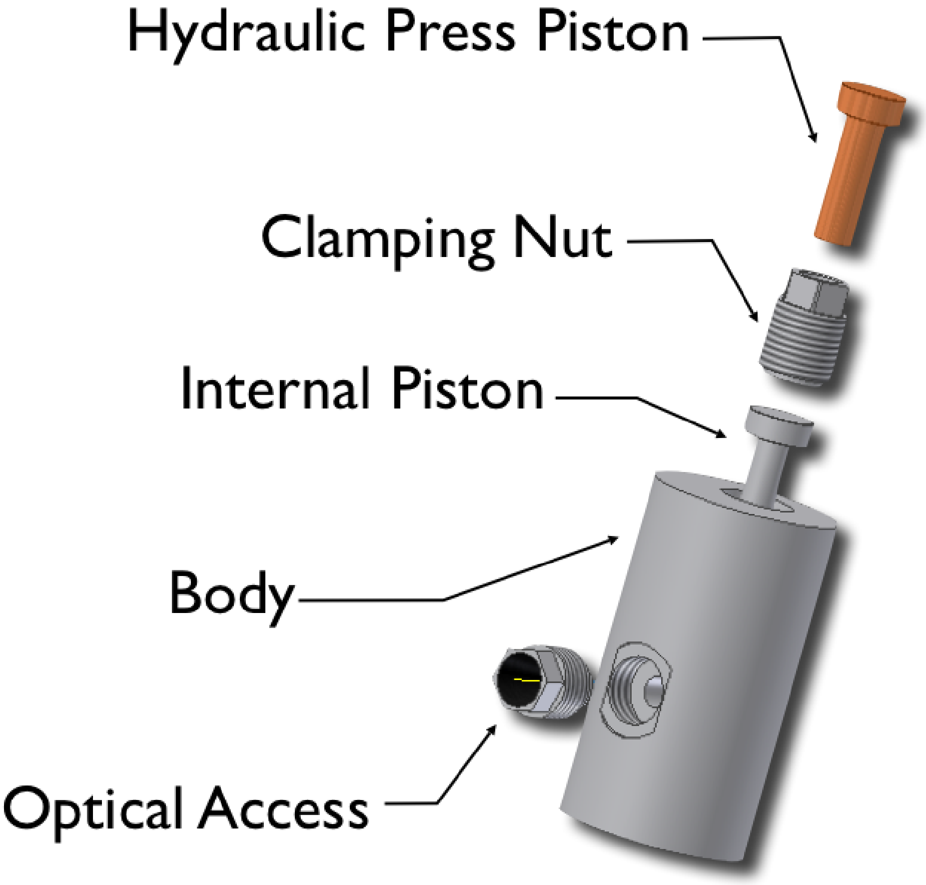

Figure 3.2: Pressure cell's parts - The figure shows the main pieces of the pressure cell: the body part has three apertures dedicated to host the pressure gauge (bottom aperture), the optical access with the diamond window (lateral aperture) and the pressurizing piston (top aperture). This latter one is held in place by a clamping nut which prevents it to move up once the pressure in the pressurizing hydraulic press is released.

or using instead a quasi-standard optical spectrometer with its standard light sources. Moreover, as it will be described in details in the following sections, the system should also be adapted in order to measure the sample properties at cryogenic temperatures via the use of an helium cooled cryostat.

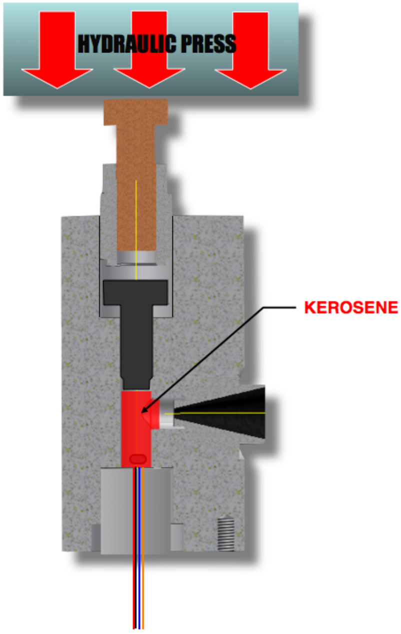

Figure 3.3: Section of the piston-cylinder cell - Once the sample has been mounted on the diamond window, the pressure cell is filled with kerosene which serves as pressure transmitting medium. The cell is the closed and pressure can be increased using an hydraulic press.

The pressure cell that was used is a piston-cylinder cell designed and developed at the *Ecole Polytechnique Fédérale de Lausanne* by Dr. Richard Gaál [17] whose main purpose was to measure the low temperature optical properties of materials under pressure using synchrotron radiation. Since the pressure cell matched the requirements previously exposed we decided to use it as a base for the entire optical and cryogenic system without spending time in the design and development process of a new cell.

As it can be seen in Fig. 3.2 the cell is rather different from the DAC concept illustrated in Fig. 3.1. The main body of cylindrical shape is made of hardened maraging steel (W720, Bohler) and has a diameter of 28.2 mm and it is 41 mm tall. On the body three apertures are present: two of them, located on the flat faces of the cylinder, serve as accesses for the pressure gauge electrical wires (the bottom one) and for the pressurizing piston (the top one). Finally along the side of the pressure cell's body there is a threaded hole used to mount the conical optical access provided with a diamond window. Since the cell has only one optical access, it can be used only for reflection experiments.

The way the pressure is applied to the sample is also completely different from the one used for DAC. The cell itself enters into the category of the "large volume" cells because the compressed space is large compared to the one of a DAC. For this reason and due to the diameter of the pistons, the pressure limit is fixed to about 25 kbar. On the other end, as we will see in detail in a while, this allows to use a larger diamond window and consequently a bigger sample thus increasing the optical performance.

In Fig. 3.3 a section of the pressure cell is presented together with the pressurization principle: the sample is placed on the inner face of the diamond window which is mounted at the extremity of the conical optical access. The bottom end is closed with a screw which serves also as a feedthrough for the electrical wires connecting the pressure gauge. Before the insertion of the inner piston the cell is filled with kerosene which is shown in red in the figure. Kerosene serves as a pressure transmitting medium

(PTM). In this case, more than in a DAC, the PTM is essential since the pressure on the sample has a direction perpendicular to the direction of the applied external force. In all the cases the PTM is used in order to guarantee hydrostatic pressure conditions around the sample and avoid shear stressed due to the direct contact between pressurizing elements, such as piston or diamonds, and the sample. The inner piston is kept in place using a clamping nut which is mounted directly above it. This latter one has an hole in the center in order to allow a second piston, shown in brown in the picture, to be inserted from the outside and used to push on the first piston using an hydraulic press present in the laboratory. The pressure can be checked in “real-time” during the entire pressurization process monitoring the resistance of a InSb gauge via a four-point measurement technique. Once the desired pressure has been reached, the clamping nut can be tightened on the inner piston and the hydraulic press gently released.

All the metals used for the construction of the pressure cell are maraging steels W720 from Bohler. Due to the process of slow cooling and age hardening these metals guarantee the necessary compressive stress required for this experiment.

The weak points in a pressure cell, no matter which design, are the apertures: gaskets and o-ring tend, fortunately, to break down much earlier than metal parts in the cell, preventing serious injuries to the operator in case of failure. Unfortunately since these joints are often close to the diamonds, when a failure in the sealing due to high pressure arrives, the shock generated by the expulsion of the pressure transmitting medium can bring the expensive diamond parts to a fatal end.

Any operator who has to deal with this kind of pressure cell for optical experiments will soon realize that the preparation of the sample and the assembling of the pressure cell constitutes itself half of the difficulty. For this reason and thanks to the experience gained during these years of pressure experiments, we decided to include a detailed description on the procedures required to correctly prepare the cell and mount the sample on the diamond window, underlining all the details which, even if apparently small, represent important key points for a correct pressurization.

3.2.1 The optical access and the diamond window

From the spectroscopic point of view the optical access and the diamond windows constitute the most important parts in the pressure cell. As said before, this kind of access represents the weakest point in any pressure system and require special care in the preparation. In Fig. 3.3 a section of the optical access is presented. It consists of a maraging steel screw machined in order to have a conical aperture of $\sim 28^\circ$. The inner part of the cone ends with a hole which gives direct access to the diamond window (not shown in the section). The inner optical aperture has a diameter of 1.5 mm and the metallic surface facing the inside of the cell has a dimension that allows the mounting of a diamond window sizing 3 mm in diameter. As briefly anticipated before, the support area for the diamond is large enough to allow to reach easily pressures around 20 kbar[3] and with special care (and some luck) also 26 kbar as reported by Kezsmarki *et al.* [17].

The preparation procedure, illustrated in Fig. 3.4a-i, starts by carefully polishing the metallic support for the diamond window. Using fine sand paper the part should

---

[3] 10 kbar $\simeq$ 1 GPa.

be treated in order to obtain a mirror-like surface which does not present significant scratches. Removing these imperfections is crucial since it will increase the final available pressure reducing the risk of a premature failure of the experiment. The next step consists in preparing the diamond window (Fig. 3.4b). The diamond itself is 3 mm tall and has a diameter of 3 mm. One important detail is that the flat faces of the diamond are not parallel to each other but they are tilted by 2°. This wedge angle, as will be extensively explained in the next chapter, serves to angularly separate the part of the light that is reflected on the first diamond interface by the one reflected on the second diamond interface where the sample is mounted. Because of this asymmetric geometry, the diamond window needs first to be aligned with respect the wedge angle: considering that the pressure cell's vertical axis will be perpendicular to the plane where the light is propagating in the spectrometer, the wedge should be oriented such

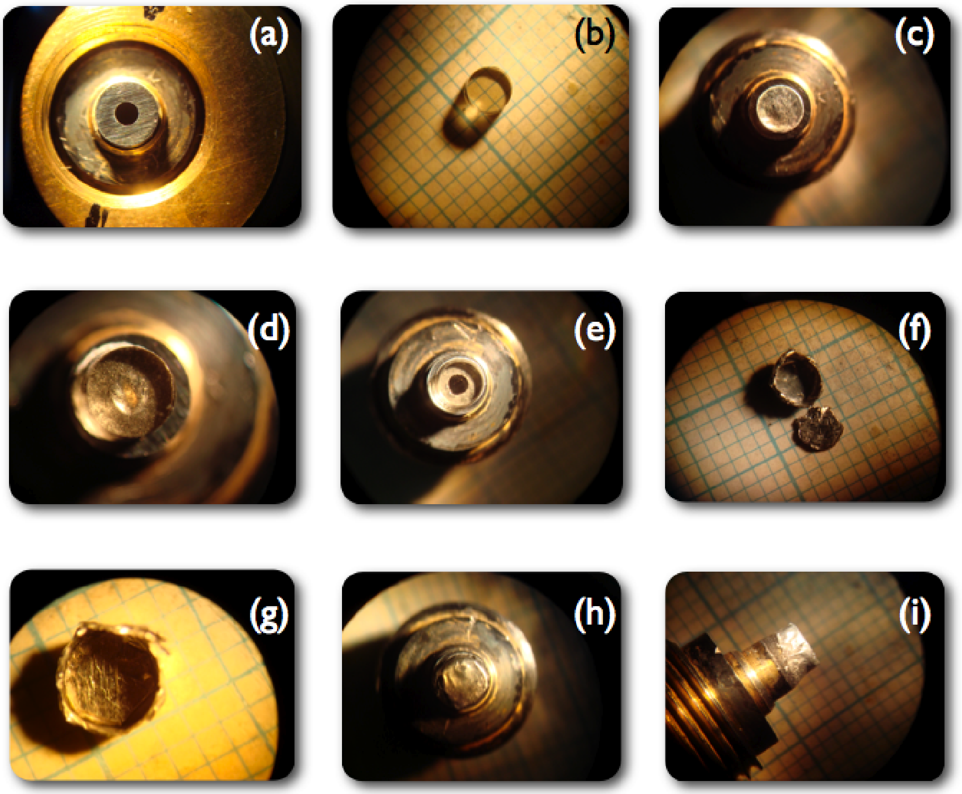

Figure 3.4: Preparation of the optical access - Various phases of the preparation of the optical access: (a) the metallic support for the diamond is polished to reduce imperfections, (b) the diamond window needs to be cleaned and oriented according to the wedge direction, (c) a small disk of indium foil is used as interface between the support plate and the diamond, (d) the window is positioned on the indium foil and centered with respect the hole, (e) once glue with epoxy resin the optical access can be cleaned from indium, (f) a small indium cap is prepared in order to host the sample, (g) once inserted in the indium cap the sample is ready to be mounted on the window, (h) the sample is sealed inside the indium protection using Araldite glue, (i) the sample is finally ready to be mounted inside the main body of the cell.

as to project both the reflected beams on the same optical plane perpendicular to the cell's axis. Since the thread on the body of the optical access allows this latter one to be mounted in a unique way on the main body, the operator should pay attention to correctly align the screw and the diamond window relative to each other.

Before mounting the window with glue it is necessary to insert between the diamond and its seat a small indium disk (Fig. 3.4c) with a diameter slightly bigger than the diamond window itself and a thickness between 150 and 200 μm. The presence of the In disk has two purposes: first it allows to fill, once squeezed by the pressure, small scratches which were not removed during the seat polishing process, second and most important advantage, it allows to distribute the stress uniformly over all the supported diamond surfaces, thus avoiding cracks in the diamond. With the In disk placed and centered on the metal seat the diamond can be carefully positioned, taking care of the right orientation of the wedge, on top of the In foil. A small pressure on the window as shown in Fig. 3.4d is enough to keep the diamond in place allowing also a better stability during the glueing process. For this latter step of the assembly procedure we used a two components Araldite® 2000 fast curing glue which is distributed in small quantities around the base of the diamond. It should be avoided to have glue extending beyond the seat's edges because this would cause mounting problems for the sealing o-rings which are very precise in diameter with respect the seat diameter. Once the glue is cured the window can be cleaned from the excess of indium using a long sharp knife from the conical access side of the piece. The final result is shown in Fig. 3.4e.

3.2.2 Preparation and mounting of the sample

The sample preparation is strongly dependent on both the measurement technique and the pressure apparatus. Optical measurements usually require a mirror-like surface quality. This result can be obtained by polishing the sample surface with diamond paper with submicrometer grain size. Although in the FIR spectral range such a fine polishing can be avoided since in this region the probing wavelength is larger than $\sim$ 15 μm, it is nonetheless useful to have a surface as flat as possible in order to improve the adherence between sample and window avoiding air interspace. This latter aspect is crucial for many reasons. From an optical point of view the presence of an air interspace will be the source of disturbing Fabri-Perot interference fringes in the spectrum. Such fringes could also turn out to be pressure dependent, since the interspace thickness may vary upon application of pressure, masking physically important changes in the sample reflectivity. Secondly a non-uniform interspace may cause strong mechanical stresses on the sample, ultimately provoking the cracking of this latter one, giving rise to a drastic change in the reflectivity response.

For the sake of completeness it needs to be said that in some cases it is not possible to polish the sample surface. In those cases the best result is obtained by cleaving the sample or to use it "as-grown" being careful to select the best quality surface compatible withe the mentioned prerequisites.

The prepared sample needs to be cut in order to completely cover the diamond window's surface and it has to be at most 1 mm thick. The thickness has to be limited in order to avoid the sample sticking out from the sample bore into the piston bore (see Fig. 3.3). In fact at high pressure the piston can reach the center of the cell thus possibly touching and displacing the sample from its initial position.

Due to the fact that this type of pressure cell works with a *liquid* pressure transmitting medium, i. e. kerosene, it is necessary to isolate the sample from the PTM in order to keep the liquid from filling the space between sample and diamond window. Together with interference fringes a tiny layer of kerosene would, in fact, also cause strong absorption lines in the spectrum, especially in the FIR. In order to avoid these issues, it is possible to use a small indium foil wrapped around the sample and the window as a protection. As shown in Fig. 3.4f, a small In foil has been carefully pre-folded and wrapped around the empty diamond window in order to obtain a small indium cup. Once prepared, the tiny cup can be loaded with the sample (Fig. 3.4g) paying attention to have the reflecting face of the sample well oriented with respect the diamond. It is worth pointing out that during all this mounting phase no glue is required. The glue needs to be used once the In cup is finally mounted on the diamond window. A fast curing epoxy glue serves both to fix the In cup to the base of the diamond window and to "seal" the sample into the cup itself. This phase is very delicate and presents many pitfalls. In fact since the In cup is molded out of a flat foil it may presents many tiny apertures which needs to be closed with the glue avoiding at the same time that the glue is sucked in by capillarity. The reason why a wrong glueing can be very annoying is that it will be possible to realize it only once the pressure cell is placed into the spectrometer, usually once the entire cell has been sealed, forcing the experimentalist to restart the preparation procedure from scratch. For these reasons the density and viscosity of the glue plays here a central role. The use of a low viscosity glue will certainly lead to an erroneous mounting. The best solution is to use a fast curing epoxy glue right before its solidification i. e. when its viscosity is higher. In Fig. 3.4h-i, the last mounting phases are shown together with the final result. The figures also show how the vertical edges of the diamond's seat are kept clean from any traces of glue.

3.2.3 Electrical feedthrough and InSb pressure gauge

The determination of the pressure into the cell is done using a heavily *n*-doped InSb gauge [33]. This material has a resistance which varies linearly with pressure with a rate of about $3.5\%/\text{kbar}$ in the range 2-12 kbar at room temperature. Before describing into details the calibration technique used to extract the value of the pressure, let's look how the InSb gauge is mounted into the pressure cell. As illustrated in Fig. 3.3, the bottom port in the main body of the pressure cell is equipped with an electrical feedthrough used for wiring the pressure gauge. As all the apertures present in the cell, this one also constitutes a potential source of failure and needs to be prepared with a certain care.

The feedthrough itself is based on a concept similar to the one used to design the optical access [34]: it consists of a special screw with a central bore of 0.8 mm in diameter at its smaller section that serves as access port for the wires. The wires are sealed into the bore using commercial cryogenic compatible epoxy glue[4] previously loaded with sapphire powder. There are two main reasons to use sapphire powder mixed with epoxy: first it decreases the thermal expansion difference between the pure epoxy and the metal parts surrounding the bore, thus reducing the possibility of

---

[4] we used Stycast 2850 FT, made by Emerson and Cuming with catalyst number 9 from the same brand.

cracks into the resin and second, it increases the compressive strength of the epoxy augmenting the maximum pressure that the cell can withstand.

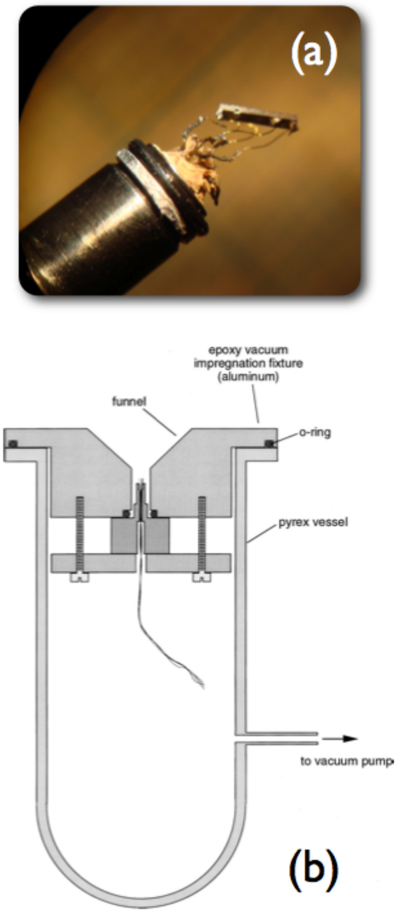

Figure 3.5: Electrical feedthrough and the vacuum impregnation fixture - (a) the assembled feedthrough: the InSb gauge is connected and suspended using gold wire and In soldering to the feedthrough wires. The white silicone paste support and reinforce the wires reducing the mechanical stresses. (b) The scheme of the vacuum impregnation fixture used to pour the degassed epoxy glue through the central bore of the feedthrough.

Before introducing the glue into the bore it is necessary to completely degrease the metal piece passing it in an ultrasonic bath with acetone. Also the wires need to be cleaned with solvents in order to remove any trace of oil and grease eventually present due manipulation or fabrication. Special care has to be taken in order to avoid the solvents removing the insulating coating around the wires thus provoking short circuits. If the wires are bundled and glued together it is a good practice to separate them; this will facilitate the epoxy glue to completely surround each wire avoiding empty spaces.

In order to use the epoxy glue into the feedthrough it is important to degas it. This is done by placing a small glass container with some glue in a vacuum chamber at around 10 mbar for 5-10 minutes. The end of the degassing process will be clear because the boiling activity of the glue will reduce drastically when all the air is expelled. This preparation step is fundamental since air bubbles in the glue are very dangerous during the pressurization procedure: in fact at high pressures, air bubbles can collapse around the wires causing them to break apart with the consequent loss of electrical contact with the pressure gauge.

The injection of the degassed glue into the bore needs to be done using a special vacuum impregnation technique which prevents the inclusion of air bubbles during the process. The principle used for this operation is illustrated in Fig. 3.5b. The feedthrough body needs to be connected to a metallic funnel which is mounted on a pyrex bell provided with a vacuum connection to a pump. The presence of rubber o-rings around the pyrex bell and at the connection between the feedthrough piece and the metallic funnel guarantees that the air is sucked in only by the bore of the feedthrough. Once the impregnation setup has been prepared the funnel can be filled with epoxy leaving the extremities of the wires to stick out from the bore of the feedthrough as shown in the figure. The vacuum pump can then be activated and the power regulated using a valve mounted at the entrance of the pyrex bell. The glue needs to be poured very gently to avoid the inclusion of air. Once the glue starts to pass in the vacuum chamber the wires need to be pulled down few millimeters to remove any interspace close to the entrance of the bore. At this point the pump can be disconnected and the feedthrough dismounted by its support. Before the epoxy is completely cured it is necessary to remove the excess glue via carefully using acetone. The curing process of the epoxy can then be accelerated moderately heating the metallic piece to 50-60 °C. The finishing touch of the feedthrough consists in covering both entrances of the bore with a small amount of silicone glue or with a soft epoxy glue. This detail is useful in order to reduce and distribute the stresses on the tiny electrical wires preventing them from breaking near the entrance of the bore where they result more fragile and hardly repairable.

It is important to note that the position of the feedthrough piece in the vacuum fixture is not casual: in fact leaving the high-pressure end totally covered by the degassed and sapphire-enriched epoxy in the funnel has the consequence of producing a higher sapphire density at the top part of the bore during the pouring process. This will give to the part of the bore directly exposed to high pressure a higher compressible strength. However for experiments conducted at relatively low pressures we verified that the use of pure degassed epoxy may be sufficient.

Once the feedthrough is ready the pressure gauge can be attached to it. The InSb chip needs to be cut in a dimension compatible with the pressure cell meaning that it should not exceed the diameter of the inner bore of the cell's body. Typical chip dimensions are $4 \times 1.5 \times 1$ mm^3 which allow to solder four contacts without many problems. The only inconvenient is that the gauge material's surface is not favorable for standard Sn-Pb solderings. A better result can be obtained using indium instead. The soldering can be done after surface activation using a mild solution of HCl and distilled water in a ratio of 1:10 for a couple of minutes. The InSb chip does not need to be soldered directly to the wires sticking out from the feedthrough bore but instead, the use of gold wires (with a diameter of 100-150 μm), bridging the chip and the feedthrough wires, will facilitate the operation. Figure 3.5a shows the final result of the procedure. In the illustration it possible to recognize the InSb gauge suspended over the feedthrough wires using gold wires. The whitish paste is silicone glue used to protect the wires from excessive mechanical stresses. Around the feedthrough neck are visible the two sealing o-ring, one made of rubber and the other one made of brass (a complete description of the sealing system will be presented in the next subsection).

3.2.3.1 Calibration of the InSb pressure gauge

As anticipated above the value of the pressure present in the pressure cell is extracted using a calibrated InSb pressure sensor. The measurement is made by monitoring the resistivity of the gauge as a function of temperature and pressure using a four-point measurement technique.

In Fig. 3.6 the resistivity curve of n-doped InSb is presented normalized by its value at liquid nitrogen temperature. The calibration procedure starts by measuring the resistance of a piece of InSb as a function of temperature in order to extract a normalized curve similar to the one illustrated in the figure. Since InSb can be found in standard wafer sizes the behavior of the normalized resistivity curve can be assumed to be identical for all pieces of InSb cut out from the same wafer. The experimental data can be fitted with a 4th order polynomial function of the form[5]

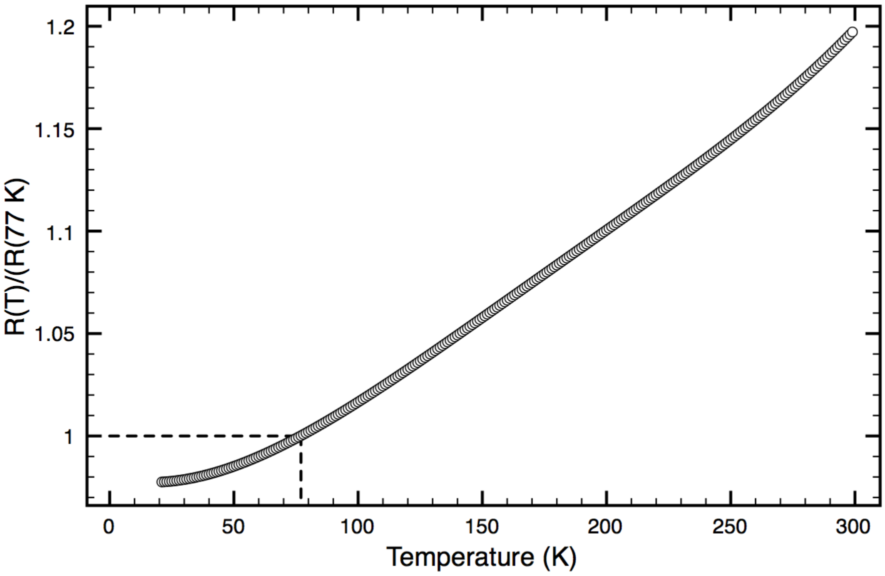

Figure 3.6: Normalized InSb resistivity - the temperature dependence of the electrical resistivity of heavily n-doped InSb. The values are normalized by the resistivity at liquid nitrogen temperature.

$$R_{77}(T) = A_0 + A_1 T + A_2 T^2 + A_3 T^3 + A_4 T^4. \tag{3.1}$$

As anticipated, this curve will be valid for all the chips coming from the same wafer, thus meaning that once known the resistance of a particular chip at a chosen reference temperature the entire resistance curve can be calculated very easily as

$$R_0(T) = R(T_0)\frac{R_{77}(T)}{R_{77}(T_0)} \tag{3.2}$$

where T_0 is the reference temperature. One of the reasons to use this formula is that the main interest here is just to know the resistance and not the resistivity. In this way it is possible to know the temperature dependence of the resistance neglecting the shape factor of the particular chip chosen. In the practical case we found the following values for the coefficients A_i: $A_0 = 0.97989$, $A_1 = -3.04136 \times 10^{-4}$, $A_2 = 9.9648 \times 10^{-6}$, $A_3 = -3.79394 \times 10^{-8}$ and $A_1 = 5.3992 \times 10^{-11}$.

---

[5] The choice of $T = 77$ K as reference temperature has been made for practical reasons since the value of the resistivity ratio $R(T = 294)$/R(T=77) can be easily verified by immersing the contacted gauge in liquid nitrogen.

Equation 3.2 is valid at ambient pressure, but as soon as the pressure increases, the corresponding resistance variation can be described by the equation

$$R_N(T,P) = aP^2 + bP + c \tag{3.3}$$

where R_N is a normalized resistance whose expression depends by the measurement's temperature and pressure. The coefficients of the polynomial function can be extracted calibrating the pressure curve with a standard ruby fluorescence technique [35, 36]. In our particular case we found $a = 1.0008$, $b = 0.3382 \times 10^{-1}$ and $c = 0.6435 \times 10^{-3}$. As just anticipated the expression for R_N is temperature dependent and in particular we report here the right formulas for $T \leq 77$ K and for $T > 77$ K:

$$R_N(T,P) \;=\; \frac{R(T,P)}{R_0(T)} \quad T \leq 77 \tag{3.4}$$

$$R_N(T,P) \;=\; \frac{(\xi+1) - \sqrt{(\xi+1)^2 - 4\xi R(T,P)/R_0(T)}}{2\xi} \quad T > 77 \tag{3.5}$$

where $\xi = \alpha(T-77)$ with $\alpha = 1.5576 \times 10^{-4}$, $R(T,P)$ is the measured resistance at temperature T and pressure P and $R_0(T)$ is the expected ambient pressure resistance at temperature T. The measurement of the pressure in the cell is straightforward since once calculated the normalized resistance using Eq. 3.5 and 3.5, the pressure value can be extracted solving Eq. 3.3.

The determination of the right value of the pressure inside the cell is fundamental during the experiments and in particular during the cool down processes: at low pressures, in fact, the drop of the temperature is associated with a consequent large pressure drop inside the cell with a possible complete depressurization of the cell at cryogenic temperatures. On the other hand a precise knowledge of the pressure allows to understand how close is the cell to its maximum sustainable pressure thus avoiding unrecoverable damages.

3.2.4 Sealing of the pressure cell and first pressurization

After the sample has been mounted and the pressure gauge calibrated and connected to the feedthrough, the cell is ready to be sealed and pressurized. This procedure involves the use of two types of o-rings which guarantee the sealing in two different pressure regimes. In Fig. 3.7 and 3.5(a) the sealing principle is presented: first an indium-coated brass o-ring is inserted around the cylindrical neck of all the closing components of the cell (*i. e.* the optical access, the electrical feedthrough and the inner piston) and later a greased rubber o-ring needs to be mounted on top of it as shown in the figures. The working principle of this double o-ring scheme is that the rubber o-ring will be effective at low pressure and prevent the pressure transmitting medium from squirt out during the pressurization process while the brass o-ring will be efficient at higher pressures. In fact while the pressure is increasing, the indium coating of the brass o-ring tends to fill all the empty spaces around the metallic neck followed by a plastic deformation of the brass itself onto its wedged support. Once deformed, the brass o-ring guarantees optimal sealing conditions at high pressure. It is worth underlining here that the high pressure sealing o-ring needs to be machined with high precision with respect the neck diameter. It is also fundamental that the brass o-ring is free from any scratches or defect since these latter ones could easily be the source of a failure at pressure rather far from the maximum one.

When all the components have been prepared with o-rings, the pressure gauge port and the optical aperture can be closed and their respective screws moderately tightened. As anticipated we used *kerosene* as a pressure transmitting medium. This PTM has been chosen for its low freezing point which is around 200 K at ambient pressure. Below this temperature the PTM becomes solid introducing small non-hydrostatic effects on the sample. When the pressure is increased the solidification temperature increases as well and at pressures around 13-15 kbar the PTM becomes solid already at room temperature.

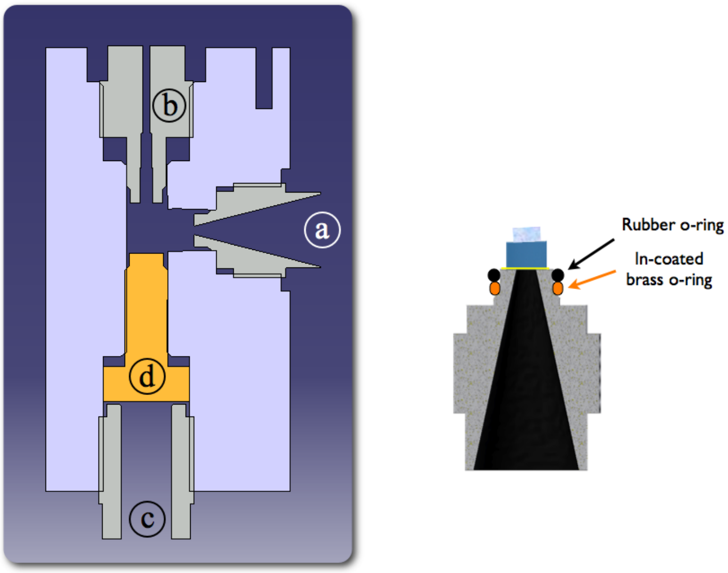

Figure 3.7: Sealing details - A section of the optical access with the sealing o-rings mounted. The rubber o-ring is efficient at low pressures while the In-coated brass o-ring becomes effective at high pressure when it starts to deform and fill the empty spaces around the cylindrical neck.

With the help of a small pipet the sample compartment can be filled with the PTM taking care to keep the kerosene level below the point where the central bore enlarges (close to the top of the inner piston shown in yellow in Fig. 3.7(d)). The inner piston can then be inserted and the clamping nut (Fig. 3.7(c)) tightened first by hand and then with the help of an hexagonal key. It is essential to not apply too much force because an excessive stress can damage the threads. Moreover it should be considered that just by hand it is possible to increase the pressure easily above 2 kbar. The main purpose of the first pressurization is just to seal the cell avoiding the loss of PTM.

Using the room temperature ambient pressure resistance $R_0(T = 294\,\mathrm{K})$ it is possible to monitor the pressure during the pressurization procedures using the method described in the previous section.

Normally the pressurization is done by subsequent steps intercalated by sets of measurements in the spectrometer. In order to increase the pressure, the cell is placed under a hydraulic press and an external piston is inserted in the bore present in the clamping nut as shown in Fig. 3.7(c). The press thus pushes on the external piston and then indirectly on the inner piston. Two quantities need to be controlled during this procedure: the displacement of the piston Δz and the resistance of the gauge. In Fig. 3.8 the piston displacement is presented as a function of the oil pressure in the hydraulic press, this latter one is expected to be a linear function of the applied force. The graph shows a series of eight pressurization from 1 bar to 17.2 kbar. The almost horizontally aligned points in the graphs are the consequence of the fact that when the cell is placed under the hydraulic press in order to increase the pressure, the piston position does not change until the applied force is identical to the maximum force applied in the previous pressurization process. Once the internal pressure is equalized, the piston starts to move quite quickly as a function of the applied force. As a final comment on Fig. 3.8, it should be noticed that by extrapolating the experimental data to 70 bar of oil pressure, the absolute variation of the piston position is ~ 5.2 mm. This value is very close to the maximum excursion allowed to the inner piston in the central bore of the pressure cell, confirming once more the importance of the proper filling of the sample space with the right amount of PTM.

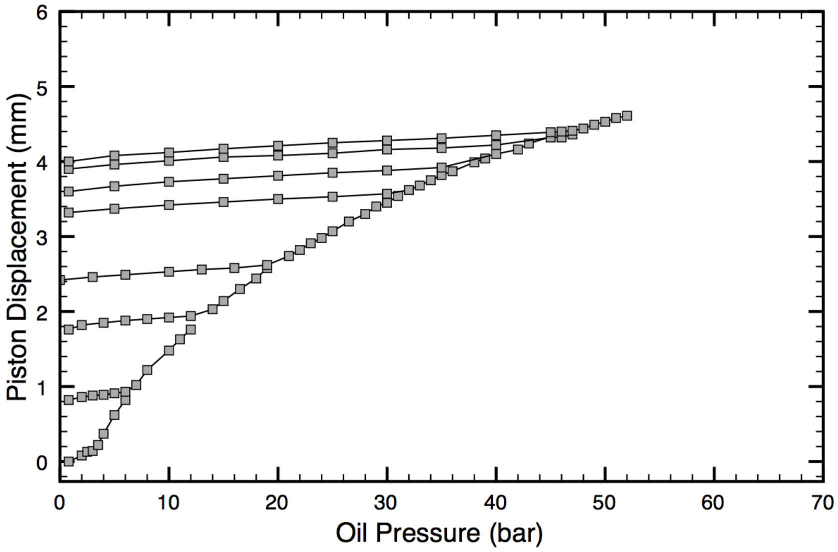

Figure 3.8: Piston displacement - The displacement of the inner piston is plotted as a function of the oil pressure in the circuit of the hydraulic press used to pressurize the cell. During successive pressurization phases the piston does not move until the external pressure does not equalize the internal one as demonstrated by the "straight" segments in the graph.

The plot presented in Fig. 3.9 has been constructed by monitoring the gauge resistance during subsequent pressurization and extracting the corresponding temperature using the formulas reported in the previous section. As it can be seen the internal pressure varies linearly with the force with a slope of 0.364 kbar per bar of oil pressure corresponding to roughly 4.1 kbar/Tons.

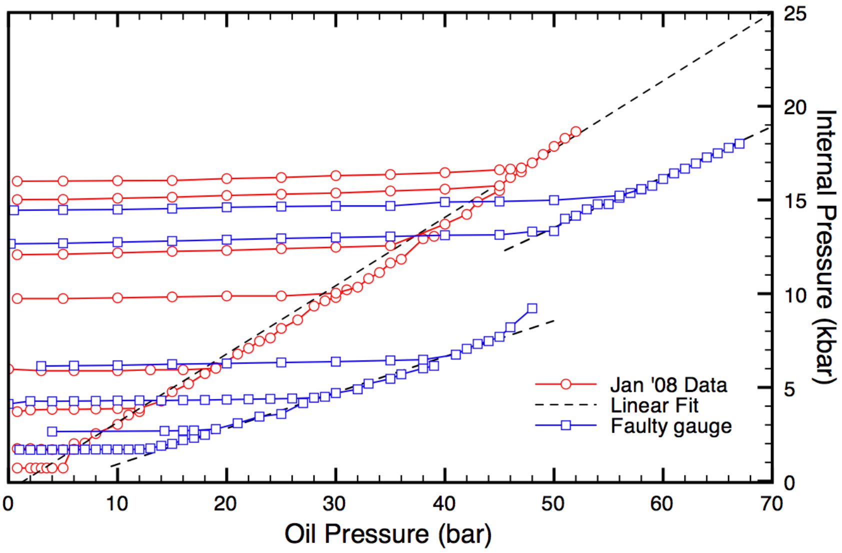

Figure 3.9: Internal Pressure - The value of the internal pressure has been measured using the technique explained in Sec. 3.2.3.1 and plotted versus the oil pressure in the hydraulic circuit of the external press. When the external pressure equalizes the internal one this latter one start to increase linearly with a slope of $\sim$ 4.1 kbar/ton in agreement with what reported by R. Gaal and coworkers[6]. In case of a faulty gauge, where for example the contacts onto the InSb chip are not properly fixed, the pressurization curve presents evident discontinuities (blue squares). Even though the curve shows a linear pressure dependence but its slope may deviate from the expected behavior (red circles).

At low pressure the pressurization procedure does not present particular difficulties but as soon as the pressure starts to be around the solidification pressure of the PTM everything needs to be manipulated very carefully. In fact, when kerosene becomes solid, the variations of pressure at the gauge position are transferred much more slowly with respect the situation where the PTM is still liquid. This means that an apparent small change in the resistance (pressure) of the gauge may very well transforms in a big pressure change just letting stabilize the entire system for few minutes. Being close to the pressure limit of the pressure cell this may cause the premature failure of some elements.

3.2.5 Accessory parts: goniometer and temperature sensor

One of the most important requirements while doing optical experiment is, as will result clear in the next section and in the following chapter, the mechanical stability of the system. Conducting optical experiments with a mechanically stable setup will not only improve the quality of a single measurement but will also positively affects the reproducibility of the measurement over time. Certainly one of the major problems connected to the use of a pressure cell of this type for optical experiments is that every time the cell needs to be pressurized it is necessary to move it from the optical system to the press thus modifying the optical alignment. In order to be able to compare the data taken at different pressures it is crucial after each pressurization to be able to reposition the cell in the spectrometer with extreme precision.

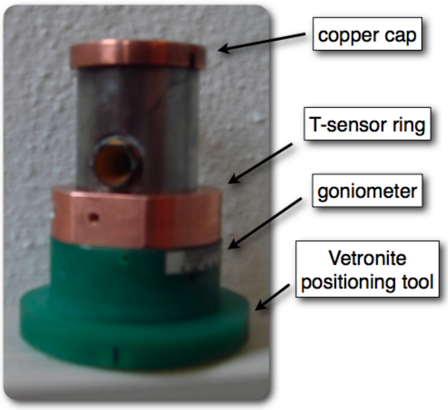

Figure 3.10: Alignment tools - The pressure cell is equipped with accessory parts useful for alignment purposes and for improving the mechanical stability of the cell in the cryostat. The green bottom part is a Vetronite piece which is equipped with a kinematic mounting that allows the correct positioning of the cell with respect to the cryostat. A linear scale is sticked on the outer wall of the Vetronite piece and it is used in order to precisely align the cell with respect to the geometry of the optical setup. A clamped copper ring is mounted right below the optical access and it carries a temperature sensor useful for monitoring the temperature at the sample position. The copper cap mounted on top of the cell has two purposes: it protects the wires of the feedthrough from being damaged once the cell is mounted on the cryostat and it improves the thermal contact between the cell and the cryostat's cold finger.

In Fig. 3.10 the pressurized cell is presented together with some additional accessories that are used for alignment purposes and for the determination of the temperature close to the diamond window. The green element in the figure is an hollow cylinder made of a glass fiber material commercially known as Vetronite®G-10. This material is characterized by excellent mechanical properties and guarantees an high degree of thermal insulation making it particularly suitable for the cryogenic applications. This tool is equipped with a kinematic mounting system on its bottom side. The cell's position can be blocked using lateral screws once the right alignment has been found.

In order to align the cell with respect to the optical elements of the spectrometer, a graduated high precision goniometer has been glued to the side of the Vetronite part, allowing an angular adjustment of the cell with a precision better then 1°. A precise angular alignment is very important since the use of a wedged diamond window will generate two reflected beams coming from the diamond-sample interface and from the vacuum-diamond interface. Since the two reflected contributions need to be disentangled, a precise and reproducible cell orientation is very important for this purpose.

Right below the optical access, as shown in Fig. 3.10 it is possible to recognize a copper ring clamped around the main cell's body. The ring serves both as alignment element, in combination with the Vetronite piece and the goniometer, and as a support for a Cernox temperature sensor mounted on the flat face opposite with respect the optical access (not visible in the figure). A temperature gauge in this position is very important because both the distance of the cell with respect the cold finger and the thermal mass of the cell itself have the combined effect of generating a large thermal lag between the cold finger parts and the cell itself during the thermal cycles. These solutions combined with the special cryostat design that will be described in the next section allows the cell to be dismounted from the optical system without the need of removing all the alignment components and temperature sensor, drastically reducing the time required for reassembling the experimental setup between successive cooling down processes.

The last element shown in the figure and mounted on top of the pressure cell is a copper cap which is used to protect the electrical wires coming from the pressure gauge from being damaged by the cold finger. Moreover it improves the thermal contact and heat transfer with the cold finger itself. This element is the only one that needs to be dismounted when pressurizing the cell and does not modify at all the alignment of the cell.

3.3 Kinematically Stable Optical Cryostat

The most important aspect in designing an optical system for spectroscopic experiments is certainly the degree of reproducibility of an experiment. Clearly if a measurement could be done tuning the sample environmental conditions without removing it from the optical system this would represent the best solution, but unfortunately sometimes this cannot be easily achieved. As anticipated in the previous section, this type of pressure cell requires a quite massive apparatus in order to change the pressure on the sample. Due to the clear impossibility to integrate such a huge press into the cryostat, the cell needs to be dismounted every time the pressure has to be varied. This phase of the experiment is crucial because, if not properly done, it will completely change the alignment of the cell with respect the optics of the spectrometer with the nefarious consequence of making it impossible to compare sets of data related to different pressures since they will present a strong difference only due to the relative cell's positioning changes.

In order to circumvent this extremely critical problem we designed and constructed a new cryostat and a new optical reflection unit which can be mounted in the standard sample compartment of a Bruker 66 spectrometer.

3.3.1 Aberration-free optical reflection unit (ORU)

The design of a new optical reflection unit for this particular experiment was necessary in order to avoid any optical aberration connected to the use of spherical focusing mirror used in the standard unit provided with the spectrometer. Such aberrations were producing a strongly elongated beam at sample position thus provoking strong signal losses due to the small size of the sample and to the narrow acceptance angle of the pressure cell's optical access.

The optical scheme of the newly designed unit is presented in Fig. 3.11 together with the path followed by the beam from the source compartment of the spectrometer to the detector's compartment. The sample is mounted at the center of the ORU and it is aligned in order to have the vector normal to the sample surface forming an angle of 11° with the direction of the optical beam which comes from the source compartment (from the right side in the figure). In the sketch it is possible to recognize the squared contour of the optical cryostat. The series of mirrors is arranged in order to allow the beam to propagate around the cryostat and to reach the detector compartment with the same optical properties of a beam that is transmitted through the sample compartment without the presence of any optical components. In order to avoid optical aberrations we adopted flat and parabolic aluminum coated mirrors. The unit is designed in a way that allows the insertion of extra optical elements, like polarizers for example, which can be placed in the section between the two parabolic mirrors (the two top ones) where the beam's rays propagate parallel to each other.

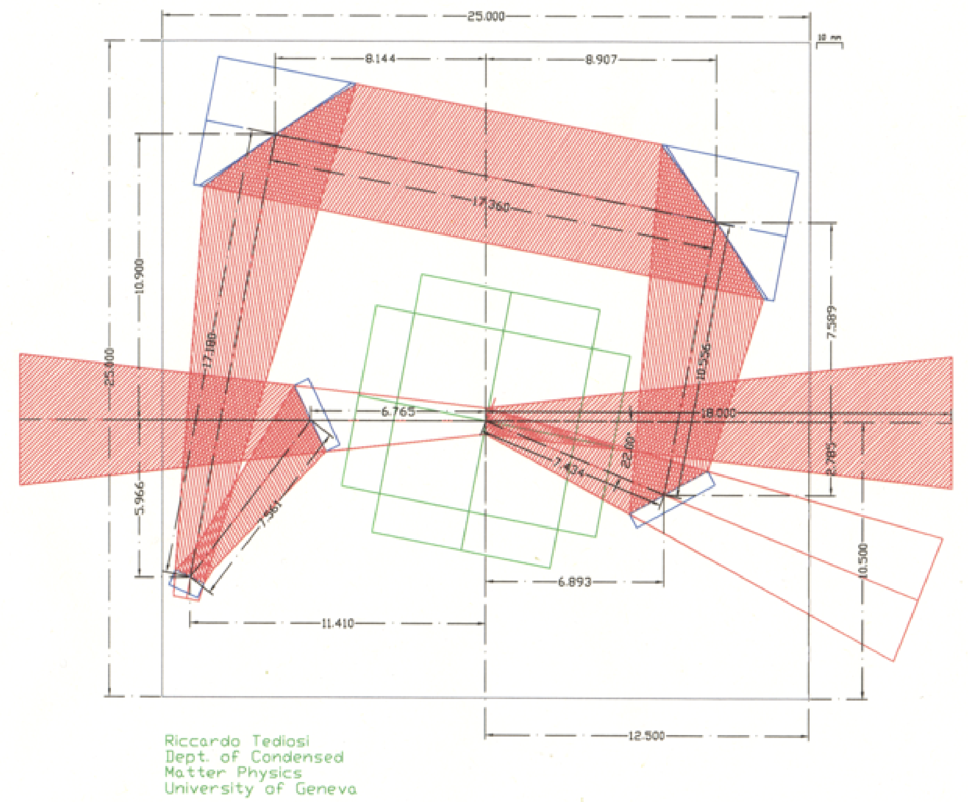

Figure 3.11: Optical reflection unit - The unit is realized using only flat and parabolic mirror thus preventing any optical aberration. The beam coming from the source compartment is impinging directly on the sample which is tilted by 11° with respect the beam direction. The outline of the cryostat body surrounding the sample is also shown.

The optical unit is equipped with an alignment tool placed right at sample position. This element consists of a small metallic disk provided with three metal balls sticking out from the surface and separated one from each other by 120°. These balls are coupled with a complementary element on the bottom of the cryostat guaranteeing a precise and reproducible kinematically stable mounting.

3.3.2 Cryostat design

Inspired by the need of precise reproducibility we redesigned an optical cryostat using as a base a commercial Janis® product, namely the model ST-100, which comes already equipped with optical accesses and windows. From the original cryostat design we just kept the cold finger design, and part of the outer case. We decided to drastically change the "classical" cryostat concept where the sample is attached and suspended to the cold finger without any anchor point to the outer case. Of course in many situations this classical solution should be preferred since the absence of contacts with the outer cryostat body improves the cryogenic performance of the system. In our design instead, we've chosen to anchor the sample, i.e. *the pressure cell*, to the bottom of the cryostat in order to have a stable reference during the cooling cycles. We knew from the very beginning that the improved stability should have been obtained sacrificing some other aspects, namely the minimum achievable temperature. The inspiring concept adopted in this particular cryostat design is already successfully implemented (though with some differences) in many cryostats used in our group for standard spectroscopic measurement at ambient pressure [37].

A detailed section of the cryostat design is shown in Fig. 3.12: the sample is not rigidly mounted on the cold finger but it is connected to the bottom of the outer case via alignment elements of the same kind used on the reflection unit plate. On the cold finger instead there is mounted a compressing system made of copper elements connected to each other via a spring. The bottom part of this compression system presents an element that couples to the copper top part of the pressure cell allowing a good mechanical and thermal contact with the cold finger parts. The spring itself has been designed in order to require the application of a moderate pressure on the cryostat cold finger at the moment of the sealing of the cryostat. According to the chosen spring dimensions about 35 kg are required to compress it by ~ 5 mm. In this way the pressure cell keeps its position on the kinematic mountings at room temperature and during the cool down process the shrinking of the cold finger is compensated by the elastic energy stored by the spring at room temperature.

The schematics shows also details on the alignment elements of the system. The same kinematic mountings are reproduced both outside and inside the cryostat so that the cryostat can be repositioned with respect the reflection unit and at the same time the pressure cell can be repositioned with respect the inner alignment system of the cryostat. We anticipated in the previous section the role of the green Vetronite element around the cell's body: it is positioned on top of a coupling disk which is provided with two sets of three glass balls and it rests on a complementary alignment unit fixed at the bottom of the cryostat. Glass has been chosen because, if on one side the use of spheres reduces drastically the contact surface between elements, on the other side glass provides an excellent thermal isolation avoiding excessive losses.

One very important feature of this design is that the bottom of the cryostat can be completely dismounted together with all the alignment elements always guaranteeing the correct relative orientations between all the pieces and the reflection unit. This is extremely convenient since the bottom part by itself can be used to take ambient temperature reference measurements on the cell being sure that once mounted back into the cryostat, the cell alignment will be identical to the one of the references.

The reader may ask if just the presence of a spring is enough for a good heat trans-

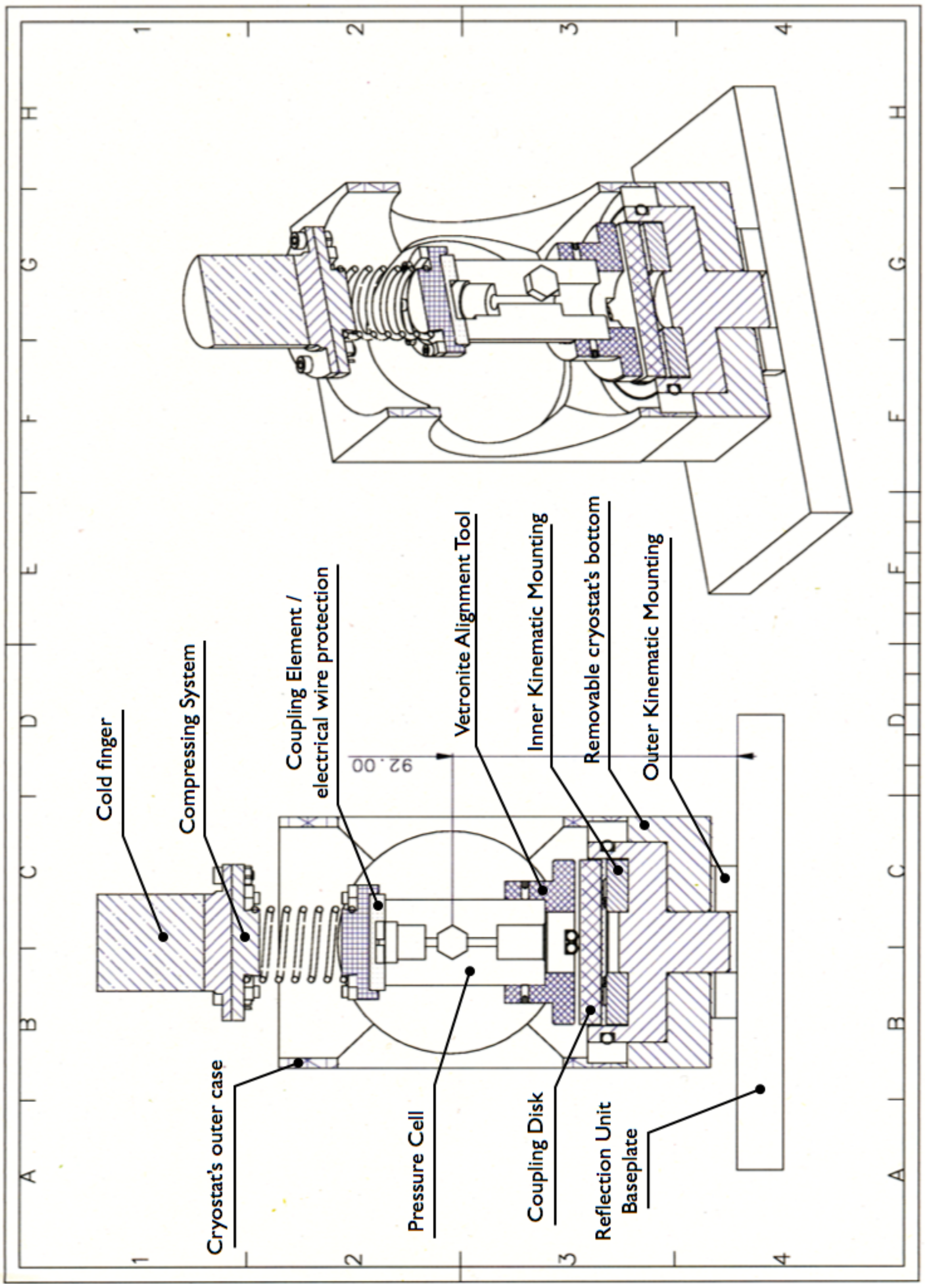

Figure 3.12: The new cryostat's design - The main novelty proposed by the new design is represented by the alignment system based on three-points kinematic stages and to the cryogenic compatible compressing system used to keep the pressure cell in place.

fer between cold finger and pressure cell. The answer is obviously negative, in fact for an efficient heat transfer we used bundles of tiny copper wires that were attached all around the compressing spring and glued using silver paste. Considering that for time limits we could not have a thermal shield installed around the cell and the cold finger, the cryogenic performances were acceptable and the system was able to reach 45 K at the pressure cell position and 7 K at the cold finger position. Certainly the thermal shield and an increased amount of copper wires around the spring could sensibly enhance the cooling performance.

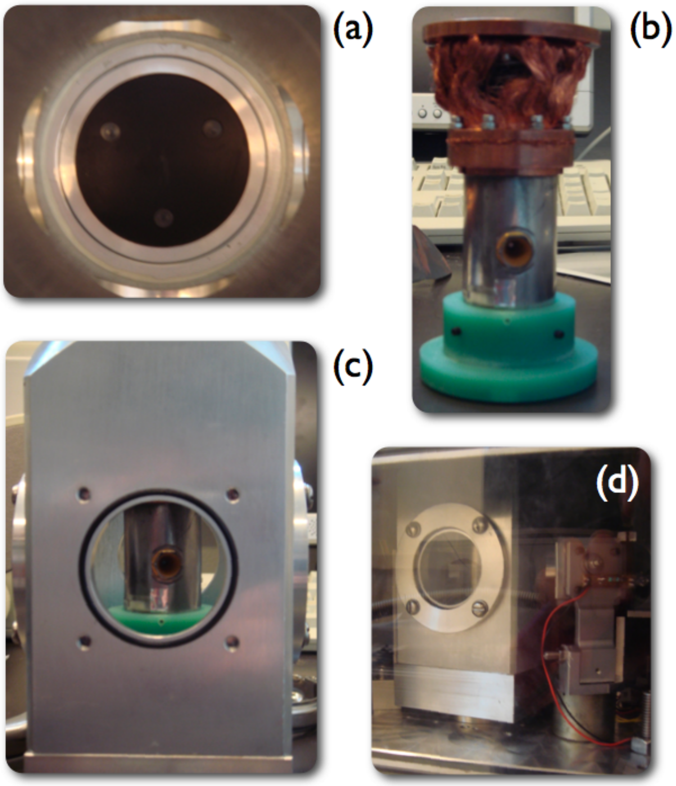

Figure 3.13: Details of the cryostat - (a) The coupling disk with one set of three glass spheres, (b) the dismounted compressing head is placed on top of the pressure cell as they would appear in the final assembly, (c) the pressure cell is posed on the alignment glass ball and the optical access results centered with the cryostat's window, (d) the cryostat is aligned into the spectrometer's sample compartment.

Some examples related to the described cryostat's elements can be seen in Fig. 3.13. In particular the working principle of the alignment system it is shown: the pressure cell with the clamped Vetronite base (Fig. 3.13-b) is mounted inside the cryostat where it rests on a three-points kinematic mounting based on glass balls embedded in a coupling disk (Fig. 3.13-a). As it can be seen in the inset (c), the system has been designed in order to have the optical aperture of the pressure cell precisely centered with respect the cryostat's optical access and this latter one aligned with respect the height of the beam propagating in the sample compartment of the spectrometer. Figure 3.13-d shows the cryostat correctly mounted into the system thanks also to the external kinematic stage which is barely visible between the base plate and the cryostat's bottom piece.

3.4 Conclusions and remarks

In this chapter we described in detail all the pieces and procedures that are required to prepare an optical experiment under pressure. Most of the effort was dedicated to the design of a system which was able to couple a clamped piston-cylinder pressure cell into a commercial Bruker spectrometer.

The details are necessary for the correct manipulation of the cell and for a deep understanding of the problems and issues connected with its use. Compared to a standard optical experiment many more precautions need to be taken, both from a purely experimental point of view and from the safety point of view. Due to the complexity of the system and of the experiment itself we documented the experimental procedure also to give the opportunity to future experimentalists to approach this activity with a (we hope good) guide which should prevent them from making beginner's mistakes.

Finally we stress the fact that, although this design process brought us to fully working system, there are some details that could be further improved especially regarding the cryogenic performance. We believe that the proposed setup serves as an excellent base for a fruitful experimental activity in the domain of infrared spectroscopy at high pressure.

Chapter 4

Data Analysis Procedure

Per varios usus artem experientia fecit.

Maniulius

The use of a pressure cell for optical experiments represents an unparalleled opportunity to extend the zero-frequency point physics, studied worldwide by many groups with transport techniques, to the region where electrodynamics starts to reveal other interesting phenomena. If on one side the combination of IR spectroscopy with pressure constitutes a novelty which gives to the experimental researchers an unexplored playground, on the other side the measurement technique deviates considerably from the standard optical procedures used for samples at ambient pressure. For this reason a complete redefinition of the analytical method is required to extract the physical information from the experimental setup. The reason why such a procedure is necessary is that, differently from the transport case, the pressure cell represents a "disturbing" element for the probe, i. e. *the light*.

4.1 The role of a pressure cell in an optical setup

A pressure transmitting apparatus used in optical experiments introduces a big change from the point of view of the beam propagating into the system [11, 38] and this is true for all the different types of pressure cell available nowadays. Although the diamond window mounted at the optical access of the pressure cell could be compared to any other window present in the optical setup (the cryostat's windows or the detector's window for example) the main and most important difference, as we will see, is determined by the distance between such a window and the sample. There is at least one reason for an optical spectroscopist working with pressure to feel lucky: the best material used to apply pressure, *the diamond*, it is also the best optical window over a broad spectral range from far infrared to visible[1]. In the development of a new pressure cell design a certain balance has to be made between the strength requirement of the

---

[1] On the other end the same spectroscopist could also feel unlucky because diamond is also one of the most expensive materials and high pressure research is known to be not so friendly with diamonds...

system, focused to obtain a certain maximum pressure, and the optical performance. Increasing the maximum reachable pressure would require a smaller diameter for the diamond while the improvement of the optical performance would require a larger diamond window making the two aspects contrasting with each other. Of course one can think to make a large and thick diamond but in this way the window will probably be too expensive. The main critical point from an optical point of view is represented by the fact that the diamond window is usually placed very close or in direct contact with the sample. In an optical system designed for reflection experiments where the the incident beam is not a parallel beam but on the contrary it is focused, the fact of having extra interfaces close to the sample (the vacuum-diamond or diamond-sample interface) produces some extra and unwanted light intensity which sums to the signal coming from the sample surface causing normalization problems.

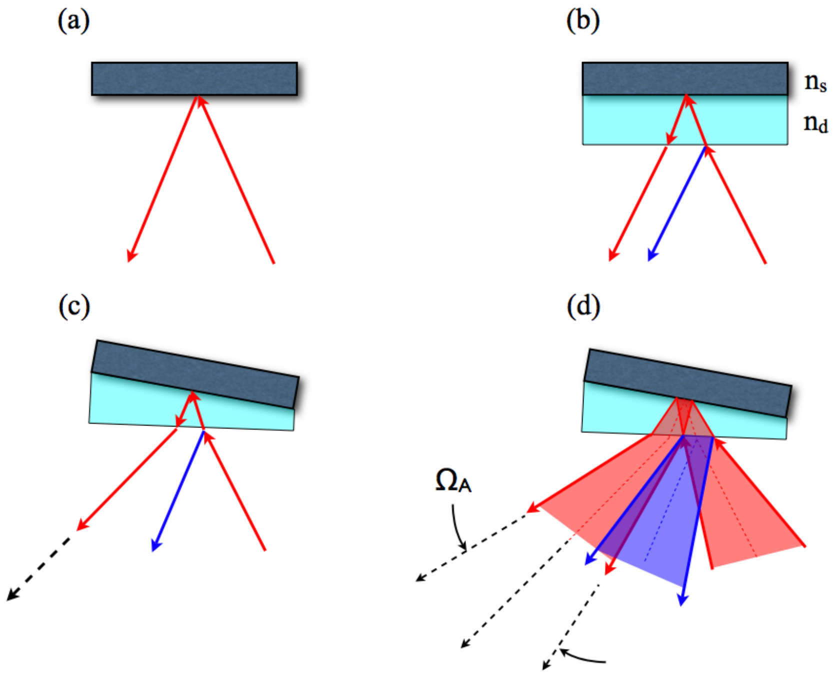

Figure 4.1: Different reflection configurations - (a) standard reflection configuration at ambient pressure, the probe (light) is reflected directly at the sample-vacuum interface, (b) the presence of a diamond window perturbs the measurement because the two reflections have the same outgoing angle, (c) the use of a wedged window allows to have different angles for the emerging beam in the ideal case where the acceptance angle of the detector is infinitely small. (d) The realistic working condition in the case of focusing optics and finite acceptance angle for the detector: the overlap between the two emerging beam introduces spurious signal.

In Fig. 4.1 a comparison between different experimental configurations is presented. The introduction of a window in close contact with the sample has the inconvenience of producing an extra reflection at the first vacuum-window interface. The consequence in the case of a window having flat parallel faces (case (b)) is that the emerging light, carrying the useful physical information from the sample, will have the same angle with respect to the light reflected at the first interface. This will cause the two beams to impinge both on the detector causing a strong interference on the main signal coming from the sample.

In order to avoid this problem one can use a wedged window as represented in Fig. 4.1(c). In this case a proper choice of the wedge angle α allows to make the two reflection angles different from each other so that just one of the two beams will be detected. We can imagine that in the ideal case (c) where the incident beam is infinitely narrow in diameter and in angular distribution Ω_{In} and in the case of an infinitely small acceptance angle for the detector Ω_{A} (black dashed line in the figure), a clockwise rotation of the sample-window system with respect to its vertical axis (perpendicular to the paper sheet) will produce on the detector a series of two δ functions corresponding respectively to the sample-diamond reflection signal and to the vacuum-diamond reflection signal. The experimental setup that better approaches the ideal situation is represented by a synchrotron radiation source where the characteristics of the beam are very similar to these described above.

One of the main objectives of this project was to develop a system able to measure optical reflectivity within a pressure cell without the need of a synchrotron radiation source. The system, adapted to a commercial spectrometer, would then allow one to use the standard Hg or SiC light sources present in the spectrometer. Unfortunately in this latter case the optical configuration is far from the previously described ideal situation: the main difference is represented by the fact that both Ω_{In} and Ω_{A} are finite as shown in the inset (d). This is a direct consequence of the use of Lambertian sources[2] in the system which requires the introduction of parabolic mirrors in order to maximize the light intensity impinging on the sample. The parabolic mirrors determine the values of both Ω_{in} and Ω_{A}. The drawback in using focusing optics is that even if the wedged windows helps in the separation of the two beams, there could still be some angular overlap between the beams reflected at the first and second interfaces causing unwanted extra intensity contribution in the detected signal.

4.1.1 The finite aperture-size effect

From the previous section it appears that a deep understanding of the geometrical arrangement of the optical elements in the system is crucial in order to extract meaningful physical quantities from the experiments. In our optical setup we used a configuration consisting of an incident beam with a central angle $\theta_{\mathrm{In0}} = 0°$ and with an angular distribution $\Omega_{\mathrm{In}} \simeq 26°$ symmetrically distributed with respect to θ_{In0}. The sample-window system was placed in the focal point of a parabolic mirror and could be rotated around its axis by an angle θ_{cell}. The wedge angle of the diamond window was $\alpha = 2°$. A collecting parabolic mirror with an angular acceptance $\Omega_{\mathrm{A}} = 26°$ (collecting the signal and redirecting it to the detector) was placed at an angle of 22° with respect to the incoming beam.

In Fig. 4.2 two distinct cases are presented: the first case (full lines and filled circles) represents the situation where the incident beam is centered around θ_{In0}, distributed with a gaussian profile over an angular range of 26° and the acceptance angle

---

[2] A Lambertian emitter is a light source which follows Lambert's law, which says that the surface brightness is independent of direction.

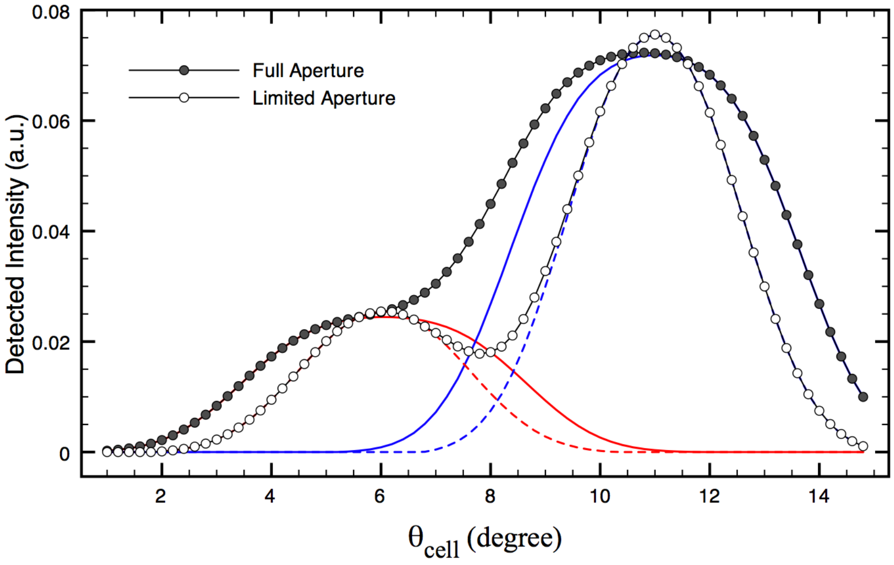

Figure 4.2: Aperture limitation effect - (colors online) Comparison between two optical configuration: in the first one (full circles) the signal is recorded as a function of the pressure cell angle using a full aperture configuration for both source and detector. In the second case (open circles) two diaphragms are introduced to limit the spread of angular distribution of the incoming and outgoing beam. The contributions to the total detected intensity generated from vacuum-diamond and sample-diamond interface are presented with blue and red lines respectively. The full lines refer to the full apertures case while the dashed ones to the case where aperture size was limited by the use of diaphragms.

for the detector is equal to the maximum allowed value i.e. 26° while the second case (dashed lines and open circles) describes the situation where both the incidence beam and detector acceptance angles are limited using for example adjustable diaphragms. First of all it is possible to observe the effect of the wedge angle on the emerging beam: the red and blue curves which represent respectively the sample-diamond reflection and the vacuum-diamond reflection appear to be separated by roughly 5°. Nonetheless the graph shows how the total detected intensity for different angular positions of the pressure cell θ_{cell} is affected in a certain angular range by both the reflected signals. In the case where diaphragms were used it is evident how the two contributions appear to be more defined and the overlap better confined in a small angular region around 8°. This proves that a better working condition can be obtained only by separating the two signal contributions for a given angle of the pressure cell. This can be achieved by reducing the default acceptance angles defined by the optical setup of the spectrometer by mean of adjustable diaphragms.

The comparison between calculated and measured angular dependence shows a very good agreement as demonstrated in Fig. 4.3.

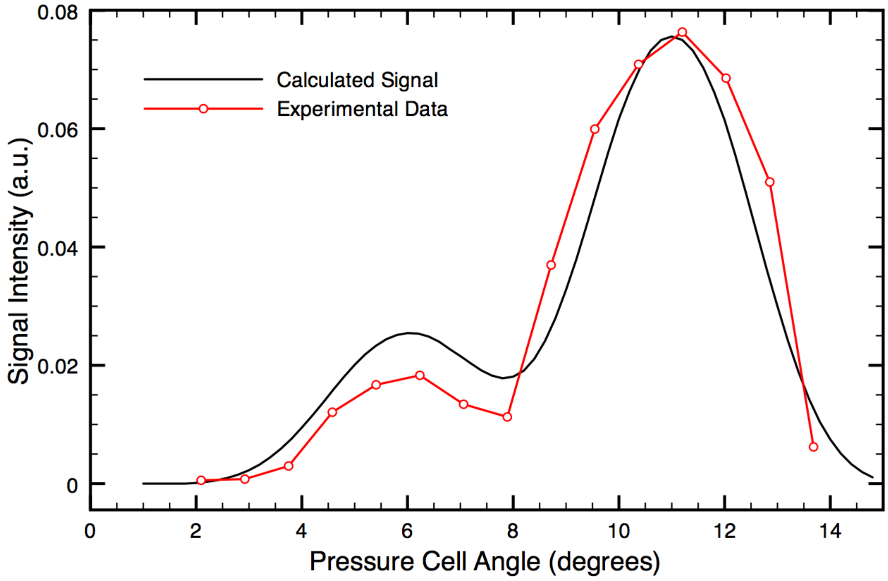

Figure 4.3: Comparison with experiments - Calculated total intensity as measured at the detector position (full black line) and the experimental result (red open circles) in the presence of diaphragms limiting the source aperture and detector acceptance angle.

4.2 Mathematical definition of the referencing procedure

Now that the effect of a wedged diamond window close to the sample has been analyzed considering the constraints imposed by the spectrometer design it is important to define a procedure that allows one to extract the absolute value of the reflectivity of the sample which will ultimately give us the opportunity to extract the physical properties of the system using standard Kramers-Kronig analysis.

Before starting with the mathematical description of the problem it is necessary to make some considerations on the stability of the system both as a function of time and pressure:

1. the detector has a sensitivity that is not infinitely constant with time. This is due to the fact that most detectors are cooled with nitrogen or/and helium and consequently the response decreases for decreasing amount of coolant. Moreover some detectors need to be physically moved in order to be filled causing a change in the geometry of the system and thus provoking a variation in the of absolute value of detected signal;

2. the pressure cell has to be removed from the system for pressurization, nevertheless due to the kinematic mounting described in Chapter 1 the position reproducibility is extremely good and uncertainties can be considered as marginal with respect the one described in the previous point;

3. the reflectivity of the vacuum-diamond interface does not change with pressure meaning that among the two reflected signals, one coming from the vacuum-diamond interface and the other one coming from the diamond-sample interface, it is just the latter one that is changing. This observation suggests that the signal reflected from the first interface could be used as a reference signal in order to correct for possible detector instabilities.

With the considerations made in the previous chapter we can imagine measuring the signal by choosing two orientations of the pressure cell: for one orientation we mainly detect the signal originating from the reflection at the *front* diamond interface I^F while for the other orientation the detected signal is mainly due to the reflection at the *rear* diamond interface (the diamond-sample interface) I^R. Looking for example at Fig. 4.3, we can imagine to measure I^F for $\theta_{\text{cell}} = 11°$ and I^R for $\theta_{\text{cell}} = 6°$. Now in order to have an idea of the effect of the cell position on the detected signal we should first measure the signal for the two orientations without any sample mounted. This would be the reference measurement and it could be taken one time at the beginning of the experiment. We can then write the two detected intensities as:

$$I^R_{\text{EC}} = I_{\text{IN}}(\alpha\tau^4_{vd}\rho^2_{vd} + \beta\rho^2_{vd}) \tag{4.1}$$

$$I^F_{\text{EC}} = I_{\text{IN}}(\delta\rho^2_{vd} + \gamma\tau^4_{ad}\rho^2_{vd}) \tag{4.2}$$

where the subscript EC is used to define the empty-cell case, τ_{vd} is the transmittivity of the vacuum-diamond interface defined by standard Fresnel's equations, ρ_{vd} is the corresponding reflectivity for the same interface and $\alpha, \beta, \gamma, \delta$ are just constant factors which defines the geometrical arrangement of the cell in the optical system. To clarify this latter point we can take for example Eq. 4.1 that represents the signal intensity mainly coming from the rear diamond window at the diamond-vacuum interface: the first term takes into account the fact that the incident intensity is first transmitted through a vacuum-diamond interface τ^2_{ad}, than reflected at the rear interface ρ^2_{vd} and finally again transmitted through the first interface (another τ^2_{vd} term). The coefficient

α takes into account the fact that the signal coming from the rear interface is changing with the cell angle and it should be considered as a constant since the measurement angles are chosen at the beginning of the experiment and than fixed until the end of the experiment. Coming back to the equation, the second term represents a spurious contribution due to the tail of the gaussian generated by the signal reflected from the first interface (see Fig. 4.3) and the constant β is just a way to quantify the amount of this spurious contribution. For Eq. 4.2 the meaning of the two terms is the same except the fact that now it is the γ constant which defines the amount of spurious signal coming from the rear diamond-vacuum interface adding to the main signal reflected at the first vacuum-diamond interface. A first approximation to this set of equations can be made considering that the tail of the rear diamond-vacuum interface reflection is much smaller than the intensity of the front reflection at the peak position (see Fig. 4.2 and 4.3) so we can assume that $\gamma \simeq 0$. The same consideration cannot be applied for the constant β since $I^R(\theta_{\text{cell}} = 6°)$ is small and the influence of the spurious contribution can be important for the total detected signal.

We can now define the ratio between the two equation as

$$\Gamma_{\text{EC}} = \frac{I^R_{\text{EC}}}{I^F_{\text{EC}}} = \frac{\alpha}{\delta}\tau^4_{vd} + \frac{\beta}{\delta}. \tag{4.3}$$

We can see that in the case where no spurious contribution is present, $\beta = 0$, and the ratio deviates from the ideal case τ^4_{vd} just by a constant which depends by the geometrical arrangement of the optical setup.

The same procedure needs to be repeated once the cell has been loaded (but not yet pressurized[3]) with a sample mounted on the window. The equations will then be

$$\begin{aligned} I^R_{\text{SC}} &= I_{\text{IN}}(\alpha\tau^4_{vd}\rho^2_{sd} + \beta\rho^2_{vd}) && (4.4)\\ I^F_{\text{SC}} &= I^F_{\text{EC}} && (4.5)\end{aligned}$$

where this time the subscript “SC” refers to the case where the Sample is in the Cell and ρ^2_{sd} is the reflection coefficient of the sample-diamond interface. The ratio of the two measured quantities this time will give

$$\Gamma_{\text{SC}} = \frac{I^R_{\text{SC}}}{I^F_{\text{SC}}} = \frac{\alpha}{\delta}\tau^4_{vd}\frac{\rho^2_{sd}}{\rho^2_{vd}} + \frac{\beta}{\delta}. \tag{4.6}$$

Given the relation between field and intensity transmission/reflection coefficients we can rewrite $\rho^2_i = R_i$ and $\tau^2_i = T_i$. Here as in the previous equations we assumed that the absorption coefficient of the diamond is negligible. This is true in the FIR spectral range and partially also in the MIR[39, 40]. In order to simplify the formulas we define $\alpha^* = \alpha/\delta$ and $\beta^* = \beta/\delta$ and we summarize here the results for the two cases:

$$\begin{aligned} \Gamma_{\text{EC}} &= \alpha^* T^2_{vd} + \beta^* && (4.7)\\ \Gamma_{\text{SC}} &= \alpha^* T^2_{vd}\frac{R_{sd}}{R_{vd}} + \beta^* && (4.8)\end{aligned}$$

---

[3] It is useful to apply a small pressure in order to allow the sample to be squeezed on the window. This will allow to have a reliable reference measurement since the sample will not move further during subsequent pressurizations thus guaranteeing the same geometrical configuration.

In order to remove the geometrical dependent part of the signal we divide out these two expressions obtaining

$$\frac{\Gamma_{\text{SC}}}{\Gamma_{\text{EC}}} = \frac{\alpha^* T_{vd}^2 \frac{R_{sd}}{R_{vd}} + \beta^*}{\alpha^* T_{vd}^2 + \beta^*}. \tag{4.9}$$

From the previous equation it can be readily seen that if the spatial overlap of the beam coming from the front and rear reflection could be reduced to zero so that $\beta \rightarrow 0$, than the experimentally determined ratio would directly give the physical quantity of interest R_{sd} since R_{vd} is a constant that can be calculated from the index of refraction of the diamond. In a more general case where this assumption cannot be verified the expression for R_{sd} assumes a much more complicated form

$$R_{sd} = R_{vd} \frac{\Gamma_{\text{SC}}}{\Gamma_{\text{EC}}} \left(1 + \frac{\beta^*}{\alpha^* T_{vd}^2}\right) - \frac{R_{vd}\beta^*}{\alpha^* T_{vd}^2}. \tag{4.10}$$

Looking carefully at Eq. 4.10 it can be seen that the R_{sd} is nothing then the experimentally measured ratio $\Gamma_{\text{SC}}/\Gamma_{\text{EC}}$ rescaled and shifted by some constant factors. The real unknown of the problem is the ratio β^*/α^*. As said before, those factors are not pressure dependent and once determined they can be used for all the rest of the experiment at any different pressures.

The final step of the normalization procedure consist in the determination of the scaling factor $R_{vd}\left(1 + \beta^* T_{vd}^2/\alpha^*\right)$ and the constant shift $R_{ad}\beta^*/\alpha^* T_{vd}^2$. In order to do that, it is necessary to know the real and imaginary parts of the dielectric function of the sample measured at room temperature and ambient pressure using standard techniques as described in Chapter 2. Using $\hat{\varepsilon}_s(\omega) = \varepsilon_{1s}(\omega) + \imath\varepsilon_{2s}(\omega)$, the expected value for R_{sd} can be easily calculated using Fresnel equations. Considering the geometry of our setup we used here the formula in the case of normal incidence, which gives

$$R_{sd} = \left(\frac{\sqrt{\hat{\varepsilon}_s(\omega)} - n_d}{\sqrt{\hat{\varepsilon}_s(\omega)} + n_d}\right)^2 \tag{4.11}$$

where n_d is the index of refraction of the diamond which in a very good approximation is constant in the FIR spectral range and equal to 2.418. Alternatively, if the measurements needs to be done in the MIR/VIS spectral range, the frequency dependent real and imaginary part of n_d should be specified since in this region diamond strongly suffers from multiphonons absorption processes.

Combining Eq. 4.11 and 4.10 we can finally determine the expression for the only unknown parameter as

$$\frac{\beta^*}{\alpha^*} = \frac{T_{vd}^2}{R_{vd}} \frac{R_{vd}\Gamma_{\text{SC}}/\Gamma_{\text{EC}} - R_{sd}}{1 - \Gamma_{\text{SC}}/\Gamma_{\text{EC}}} \tag{4.12}$$

which is a frequency independent quantity. Once again it worth to point out that if $\beta^* = 0$ than the problem is much simpler and the described procedure automatically corrects for the special position of the pressure cell in the system. On the other hand if the expression 4.12 is not zero then some contamination is present in the detected signal and the correction value can be used in Eq. 4.10 to extract R_{sd} for every considered pressure case.

4.2.1 Example

In order to check the validity of the previous discussion let's take, as an example, the case of bismuth. Let me anticipate that a more comprehensive treatment of the bismuth system is included in the next chapters since bismuth represent the main system explored by this thesis work. For the moment we ask the reader to focus on the normalization problem without entering too much in the details of the underlying physics.

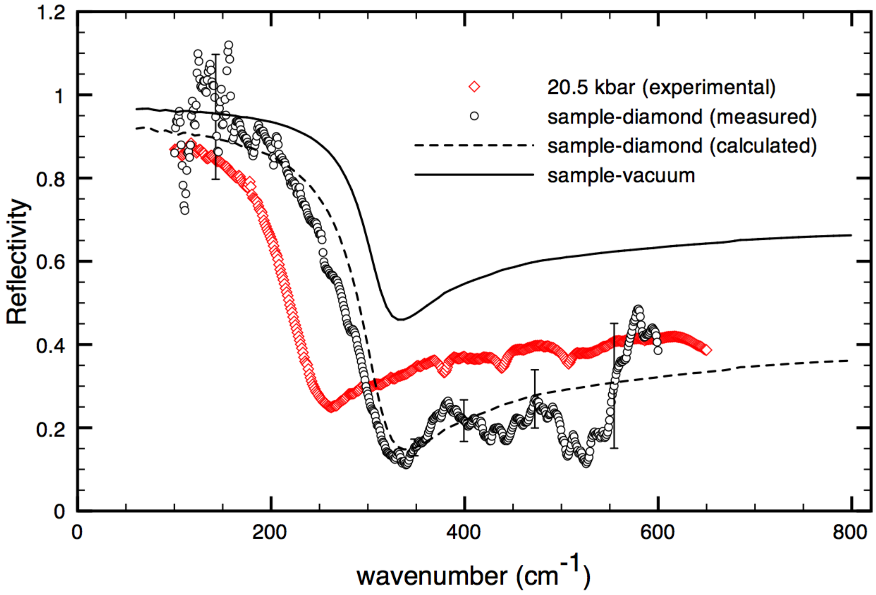

Figure 4.4: Absolute reflectivity calculation - Bismuth reflectivity measured using "classic" experimental techniques is shown with solid black line. Theoretical sample-diamond reflection is shown with dashed line while the experimental reflectivity measured within the pressure cell is presented with open circles. A value of $\beta^* = 2.3$ was used according to Eq. 4.12. The experimental reflectivity at 20.5 kbar has been also included (red diamonds).

The first thing that needs to be done is measuring the sample reflectivity using well established techniques which do not require any pressure equipment. In Fig. 4.4 the result of this preliminary measurement is shown with a solid black line. In the figure only the FIR part of the curve is shown but a much broader spectral range was actually covered combining different techniques. Using this data and the Kramers-Kronig relations we extracted the complex dielectric function $\hat{\varepsilon}_s$. We than inserted this latter result in Eq. 4.11 in order to calculate the expected reflectivity for a diamond-bismuth interface. The result of the calculation is shown in the graph with a black dashed line.

Finally we assembled the pressure cell with a properly aligned diamond window and we recorded the spectra for the two cases where the diamond window was left empty and when the sample was mounted on it following the procedure explained in the previous chapter. With those spectra we could calculate the ratio $\Gamma_{\mathrm{SC}}/\Gamma_{\mathrm{EC}}$ as defined in Eq. 4.1-4.9. The definition of this ratio was then used to determine the value of the factor β^*/α^* which takes into account and corrects for the geometrical position of the pressure cell in the system and for the possible contamination between the two reflected beams at the two diamond interfaces. As discussed before we expect this quantity to be a constant since none of the two correction factors should be frequency dependent. As a check we show in Fig. 4.5 the calculated correction factor according to Eq. 4.12. The plot confirms the supposition as the function is actually constant and equal to $\sim$ 2.3 over a broad spectral range. The cusp that is present is just due to the fact that for $\omega \simeq 270$ cm^{-1} the reflectivity of the diamond-vacuum interface equals the one of the bismuth-diamond interface. Substituting the calculated constant in Eq. 4.10 it was finally possible to extract the sample-diamond reflectivity which is shown with open circle in the Fig. 4.4. The agreement is definitely good considering the complexity of the experimental setup. The signal to noise ratio is certainly not as good as in a standard reflection experiment which is mainly due to the very low signal level coming out from the pressure cell. Another annoying effect is caused by the possible presence of a small air gap between the sample surface and the diamond window: this may well be the origin of the oscillations clearly observable above 300 cm^{-1}. This latter inconvenience can be avoided carefully polishing the sample surface before mounting the experiment[4].

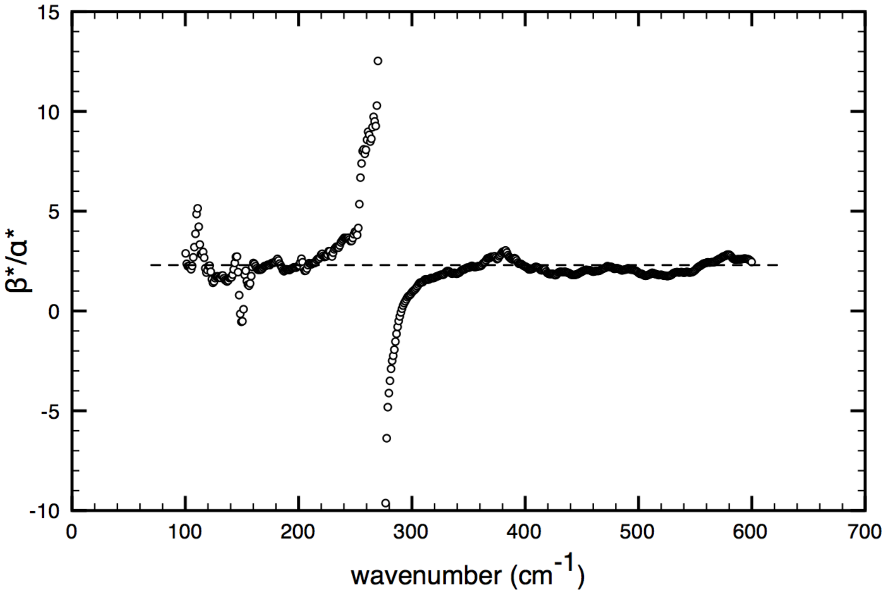

Figure 4.5: Correction factor calculation - β^*/α^* was calculated according to Eq. 4.12. The value appears to be almost constant for the entire considered spectral range except for a small region where $R_{vd} = R_{sd}$.

---

[4] Unfortunately on bismuth even a careful polishing destroys the order of the crystal surface and that's why we had to use a cleaved sample instead.

As a final comment to Fig. 4.4, 4.5, the reader can certainly notice that the reflectivity drop, corresponding to the screened plasma frequency ω_p^*, appears to be shifted toward lower frequencies with respect the calculated function. This effect is not an artifact of the procedure but rather a real physical effect originating from the small pressure present on the sample. The application of a small pressure was required in order to seal the cell. The consequence of this shift is also visible in the β^*/α^* function where the cusp seems to be broader on the low frequency side.

4.3 Low temperature reflectivity under pressure

The measurement of the absolute value of the reflectivity at low temperature using pressure cells has never been trivial due to the numerous technical difficulties. The combination of pressure cells and optical spectroscopy is giving its first results only in these days [41, 42, 43] thanks also to the progress that has been made in the individual experimental disciplines. Unfortunately in many of the most recent works the derivation of the low temperature reflectivity is never reported except in isolated cases [17]. One of the main reasons for this is that the use of a diamond-anvil cell (DAC) requires a mechanical stability of the cryostats which is orders of magnitude better than the one available in standard cryogenic systems thus requiring a special cryostat design or a special measurement technique which allows one to take a reference measurement directly at low temperature.

In most of the standard spectroscopic experiments the sample is mounted on a sample-holder which is attached at the extremity of the cryostat cold finger. During the cool down process the cold finger tends to shrink due to thermal contraction and, as a consequence, the sample will move in the direction of the cryostat's neck. In this process the critical quantities that should be carefully considered are the size of the sample, the beam's spot size and the absolute value of the displacement due to thermal contraction. It is clear that in optical systems like the ones used for microscopic spectrometry in DACs, where the sample has dimensions of about 100-200 μm and the beam diameter is of the order of 10-20 μm, a mechanical displacement of 0.5 mm will completely move the sample out of the beam causing the complete loss of the signal. The use of pressure cells with a large optical access allows one to circumvent many of these problems. The main advantages deriving from these kind of systems are related to the fact that in addition to a bigger signal and a better signal to noise ratio, a larger aperture guarantees that small mechanical displacements won't generate a large change in the signal impinging on the detector thus giving the opportunity to extract with a simple correction technique the absolute value of the reflectivity even at low temperatures. On the contrary, as you already realized, the use of a large optical accesses limits the maximum pressure that the cell can withstand.

4.3.1 Reflectivity extracted via percent signal change

The procedure described here is based on the assumption that given the reflectivity functions of a sample at two different temperatures T_1 and T_2 it is not difficult to demonstrate that the percent change in reflectivity between the two temperatures cases is exactly equal to the percent change of the respective signal intensities measured at the sample-diamond interface (or sample-vacuum interface). According to this statement and knowing the absolute value of the reflectivity at just one temperature it is then possible, in certain circumstances, to directly extract the absolute value of the reflectivity at all the other temperatures only knowing the relative change of signal intensity.

The derivation of the absolute value of the optical reflectivity at low temperature is done by measuring the intensity of the signal reflected from the sample-diamond interface during a slow cool down process. The signal which impinges of the detector can be decomposed in two different contributions: a signal coming from the sample surface and a small background signal coming from the first vacuum-diamond interface. As discussed in the previous section this latter contribution can be minimized by placing apertures along the beam path in order to block the rays impinging onto the cell with high angles of incidence. According to the description given above, the detected intensity can be written as

$$I_{\mathrm{Tot}} = aI_{\mathrm{s}} + (1-a)I_{\mathrm{bkg}} \tag{4.13}$$

where a is just a constant which defines the relative ratio between signal coming from the sample I_{s} and signal coming from the "background" I_{bkg}.

When the system is cooled the pressure cell moves slightly from its initial position causing a small variation of the detected signal. This change is mostly due to the movement of the beam with respect the detector's sensor and not due to a change in the relative weight of the two signal contributions a. This can be avoided using a spot size slightly bigger than the window 's dimensions[5]. The final effect of the mechanical shift of the pressure cell is to rigidly increase (or decrease) the detected signal intensity. More formally we can write this effect as

$$I_{\mathrm{Tot}}(T) = \Phi(T)\left[aI_{\mathrm{s}} + (1-a)I_{\mathrm{bkg}}\right] \tag{4.14}$$

where $\Phi(T)$ just represents the signal change as a function of temperature. We can now write the expression for the percent change in the signal intensity between a temperature T and a temperature T_0 that we will consider the reference temperature where the absolute value of the reflectivity $R(T_0)$ is also known. Using Eq. 4.13 for the signal at T_0 and Eq. 4.14 for the signal at T we can define

$$\begin{aligned} P(T,T_0) &= \frac{I(T)-I(T_0)}{I(T_0)} = \\ &= \frac{[\Phi I_{\mathrm{s}}(T) - I_{\mathrm{s}}(T_0)]a - (\Phi-1)[(1-a)I_{\mathrm{bkg}}]}{aI_{\mathrm{s}}(T_0) + (1-a)I_{\mathrm{bkg}}} \end{aligned} \tag{4.15}$$

With the previous expression we cannot succeed in calculating the real percent signal change because a strong background contribution is still present at the numerator and clearly visible in the $P(T,T_0)$ function. The only solution to this problem, assumed that what has been said before about the constant proportion between sample signal and background is verified, is to multiply the signal at temperature T by a constant factor

---

[5] Considering that the optical aperture on the pressure cell is 1.5 mm in diameter, using a spot size of 3 mm guarantees, in the practical case, to have the sample always illuminated by the beam at every temperature.

M so that $M\Phi = 1$. In this way all the background contributions to the numerator will be canceled. Once the correct value for M has been found the previous expression simplifies to

$$P(T,T_0) = \frac{I_s(T) - I_s(T_0)}{I_s(T_0) + \frac{(1-a)}{a} I_{\text{bkg}}}. \tag{4.16}$$

From the previous equation it is possible to see that in the situation where $a \to 1$, the ratio tends to be also equal to the percentage change of the signal coming purely from the sample which is identical to the percent change of the reflectivity. In order to check the validity of this procedure we compared the experimental intensity ratios as defined in Eq. 4.16 and measured on bismuth single crystal at 1.5 kbar, with the percent change calculated starting from the known ambient pressure reflectivity curves. In doing this we assumed that the response of the system at 1.5 kbar does not appreciably change with respect to the ambient pressure case. As it can be seen from Fig. 4.6 the agreement with the percent change curves calculated directly form the reflectivity spectra is very good meaning that the corrected experimental quantities can be used as a base to reconstruct the absolute reflectivity. In fact using a reference reflectivity $R(T_0)$ we can write

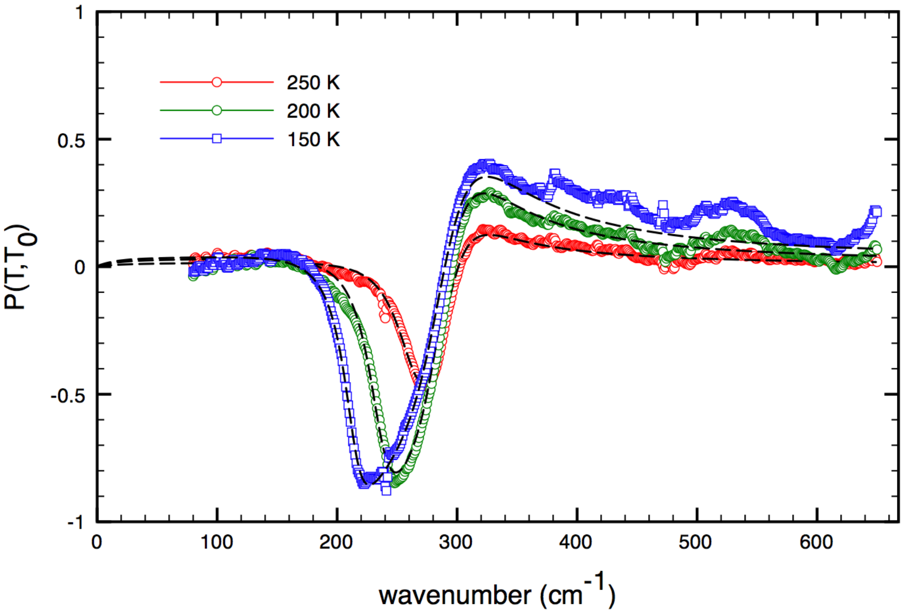

Figure 4.6: Experimental percent change - Using Eq. 4.15-4.16 the percent change of the signal of single crystal bismuth at 1.5 kbar was calculated for temperature $T = 250$, 200 and 150 K with respect room temperature. The dashed lines represents the theoretical curves calculated from reflectivity curves instead.

$$R(T) = R(T_0)\,[P(T,T_0) + 1]\,. \tag{4.17}$$

At this point there are two possibilities in order to continue in the analysis: the first one consists of using as a reference reflectivity $R(T_0)$ the experimental data extracted following the procedure described in the previous section (Fig. 4.4), otherwise the second possibility, consists in using a model reflectivity calculated by fitting the experimental result with a Drude-Lorentz model. Clearly the former solution is preferable but in the case where the experimental data are noisy or present strong artifacts due, for example, to beamsplitters or to Fabry-Perot interference fringes caused by a poor contact between sample and diamond window, it is better to adopt the second solution. In this case it is necessary to know exactly all the model's parameters required to fit the room temperature data in order to discard the artifacts and reproduce with the model only the changes to the system induced by the pressure. The knowledge of the Drude-Lorentz parameters extracted from standard ambient pressure spectroscopic measurement constitutes a solid base for the fitting process.

The advantage of this differential approach is that only the changing features in the spectra will be enhanced while the constant features like for example beam-splitter's artifacts or Fabry-Perot fringes will be self-compensated and not reproduced in the reconstructed reflectivity. We can say that in this way we can enhance the physics and dump the experimental details.

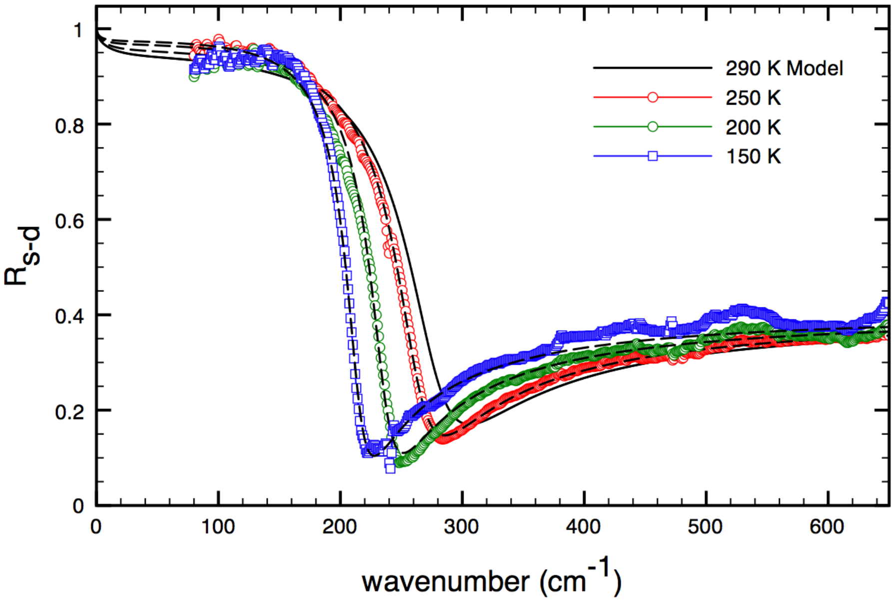

Figure 4.7: Reconstructed Reflectivity - Using Eq. 4.15-4.16 the percent change of the signal of single crystal bismuth at 1.5 kbar was calculated for temperature $T = 250$, 200 and 150 K with respect room temperature. The dashed lines represents the theoretical curves calculated from reflectivity curves instead.

Figure 4.7 gives a clear demonstration of this procedure for the same temperature cases reported in Fig. 4.6. The black solid line represents the reference reflectivity fit to the experimental data used in Eq. 4.17 while the reconstructed reflectivity curves are shown with empty symbols. We would like to stress here the fact that if the calculation of the temperature dependent percentage change of signal intensity was not correct, the reconstructed reflectivity would present clear features belonging to the reference reflectivity (like for example a dip around 310 cm^{-1}) or to the background signal. The fact that the reconstructed reflectivity curves appear so smooth derives on one side from the "self-compensating" approach and on the other size from the fact that both the procedure for the calculation of $P(T, T_0)$ and the fit to the real reference reflectivity are valid.

Once the reflectivity curves have been extracted they can be used to extract meaningful physical quantities like the dielectric functions and the optical conductivity curves by applying a standard Kramers-Kronig consistent Drude-Lorentz analysis. In the fitting process it is important to realize that the experimental reflectivities are relative to a sample-diamond interface requiring the substitution, in the calculation of the model reflectivity from the Drude-Lorentz parameters, of the index of refraction of vacuum with the one relative to diamond as pointed out in Eq. 4.11. In Fig. 4.7 the results of the fitting procedure are presented with black dashed lines together with experimental data. The parameters of the model will be discussed in the next chapter.

4.4 Conclusions

In this section we explained in great detail the technique used to extract the absolute value of the reflectivity from the experimental setup. We would like to point out that all the approximations that were used in the text are based on assumptions that were verified on the experimental setup. It is worth stressing the fact that in this kind of experiments the total mastering of the system and a complete knowledge of the details about the optics, the sources and the detectors are required in order to carry out successful experiments. What is generally considered a "small detail" in a standard spectroscopic measurement could be a determinant in an optical pressure experiment. Certainly the small volume of the literature about optical experiments under pressure is a good measure of the complexity of this experimental activity.

As a final remark to this section I would like to spend some words on the applicability of this method. For our particular experiments we have chosen single crystal bismuth. In this chapter we presented just some examples useful to illustrate the method without introducing any discussion relative to the physics of the system. In the following chapters a comprehensive description of the experimental activity will be presented together with the discussion on the physics of bismuth. Probably the reader is wondering up to which extent this method is applicable and which are the physical systems that are more favorable to be measured with this optical setup. The answer is somehow complex, because the problem embraces both the mechanical properties of samples and their physical properties in terms of temperature and pressure dependence. Considering the latter aspect, all the physical systems where the reflectivity is expected to have a small (few percents) pressure and temperature dependence should not be considered as the best choices. Clearly the differential method offers a "clean" and powerful approach able to detect tiny temperature dependent signal changes thus giving a qualitative idea about what is changing as a function of temperature. The problem arises when the reflectivity at low temperature has to be reconstructed from the reference reflectivity. As we said in fact, this latter quantity has to be determined with sufficient precision in order to allow a meaningful reconstruction of $R(P,T)$ for $T \neq T_0$. Taking bismuth as an example, we could define it as a “pressure-cell-friendly” material since the reflectivity has a strong pressure dependence at ambient temperature. This allows to extract (not without struggle) the absolute reflectivity for different pressure cases which would serve as a base to reconstruct the temperature dependent data. For these reasons good candidates for these kind of experiments are narrow bandgap semiconducting materials, low carrier density materials and systems with a clear pressure or temperature dependent phase transitions as for example, metal-insulator transitions or charge-density waves transitions.

Regarding the mechanical properties, it is necessary to have samples available in relatively large sizes in order to cover completely the optical window (3 mm in diameter) and that can be easily cleaved or polished in order guarantee a good adherence to the optical window therefore limiting the appearance of annoying interference fringes in the spectra. Brittle materials can be a problem since they could crack at high pressures but up to now we did not have the opportunity to verify this aspect.

Chapter 5

Bismuth: *“die weisse Masse”*

There are so many interesting things around! Unfortunately the time is limited and one has to choose what he really wants to do!

G. P. Banfi

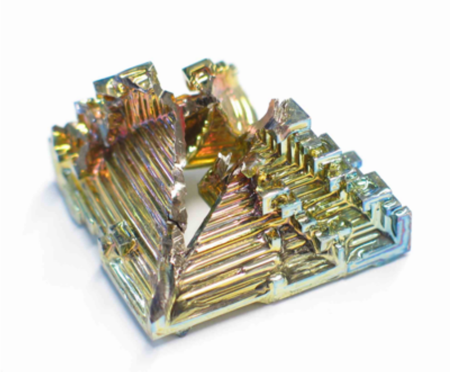

Figure 5.1: The multifaceted bismuth - An irregular bismuth single crystal sample. Though it has a whitish metallic aspect in its purest form, bismuth may present multicolor shadings due to interference effect caused by tiny oxide layers on its surface. The picture wants to symbolize the always fascinating and intriguing physics hidden in this material.

The history of bismuth is quite controversial and perfectly mirrors its physical properties. The first observation of bismuth is attributed to the Swiss physicist and alchemist Paracelsus[1], in the 16th century. The first curiosity regarding bismuth derives from its early discovery in some gold and lead mines in Germany; together with large quantities of precious metals like gold, used for economics, and lead, massively used for the many applications in metallurgy, it was discovered a weird whitish mass which was not resembling to any of the known metals though its properties were somehow comparable to those of the metallic materials commonly mined. Considering the mines as a system similar to trees where fruits need to mature before being eaten, the experts of that time used to consider bismuth as a sort of “imperfect” or “immature” form of metal. It was sort of *half* way from being a real metal which had not yet grown into a true one. Paracelsus himself explicitly defined it as a “bastard” or “half-metal” [44]. The name of bismuth originates from

---

[1] Also known as Phillip von Hohenheim (1493-1541)

the german words *"weisse Masse"*, namely "white material", that were initially used to identify the material in the mines.

It is rather surprising how, without any knowledge of band theories and electrical properties of materials, the pioneers of physics could correctly define bismuth as an *half metallic* system! Unfortunately due to its poor mechanical properties and to the superior importance of gold for the richness of kingdoms, bismuth was not very much considered and even if alchemy books report it among other useful substances, its role and use remained unclear for a long period of time.

Physical interest in bismuth started to grow with the first investigations of transport properties of materials, where it was found that bismuth could be classified neither in the list of metallic compounds nor in the one of insulating and semiconducting materials. Actually there are two other elements that show similar transport properties: arsenic (As) and antimony (Sb). This very limited class contains materials which are defined as semimetals. The main characteristic of this class is the extremely low carrier concentrations and the simultaneous presence of two types of carriers in the conduction band: hole and electrons. As we will see in detail later there is a hole band overlapping with the electron band which causes a certain amount of holes to be available for conduction. Semimetals are all self-compensated materials from the electronic point of view meaning that the total positive charge accounting for the holes is perfectly compensated by the free electrons in the conduction band. As said before the bad metallic properties of this class of materials is mainly due to the low charge density which is roughly five orders of magnitude smaller than a typical good metal like for example gold or aluminum.

But is the electron density all that matters in order to make this material so interesting? The answer is no, because together with the unusual low conductivity, it shows an extremely small and anisotropic mass tensor varying from $0.001m_0$ to $0.26m_0$ [45], low diamagnetic susceptibility ($\sim 10^{-5}$), high lattice dielectric constant $\varepsilon_\infty \sim 100$ and high values for the g-factor, up to ~ 200 [46]. The large electron wavelength and the long mean free path originating from the tiny Fermi surface make bismuth an ideal material for the study of quantum confinement effects which may manifests in unusual transport regimes [47, 48, 49, 50].

Because of these remarkable properties bismuth has been one of the best materials used to develop important experimental techniques and to observe for the first time many physical phenomena like the magnetoresistance effect, the de Haas-van Alphen effect, the Shubnikov-de Haas effect, the oscillatory magnetostriction, cyclotronic resonance in metals and magnetic surface levels. *A posteriori* the cited techniques and experiments constitute the milestones of experimental activities in condensed matter physics.

Even though at a glance bismuth may appear a simple system, the literature demonstrate how fascinating it is and how difficult is to get the real physics behind the scenes. Changes in the physical external conditions like temperature, pressure and also by doping give access to a vast variety of very rich phases which deviates considerably from standard models. Recently bismuth is again attracting a lot of attention because of its similarities with 2D graphite layers better known as graphene. In both cases field dependent crossovers, reminiscent of a metal-insulator transitions, have been observed [51, 52]. Isolated single layers of graphene have been shown to have novel transport properties and an anomalous quantization of the Hall effect resulting from their zero mass Dirac cone dispersion relation [53, 54]. On the technical side, advances in film growth [55], anomalously long spin diffusion lengths and very large magnetoresistive response make bismuth useful for possible incorporation in nanomagnetometers, magnetooptical devices and spintronics applications [56, 57].

It has been demonstrated [2, 3, 4] how the application of hydrostatic external pressure strongly affects the relative positions of the main bands responsible for the electronic properties of this material greatly reducing the carrier density. This effect could finally drive the system into a state much similar to the one found in graphene where the Fermi surface is ultimately reduced to a single point. The experimental interesting aspect is given by the fact that the pressure range where this semimetal to semiconductor transition (SMSC) is expected to happen is on the order of $\sim$ 20 kbar making the pressure cell apparatus, described in the previous chapter, the ideal equipment for the experimental investigation of this phenomena.

After an introduction dedicated to the description of the band structure of bismuth derived from its crystal structure, we will briefly describe the growth techniques used to produce single crystal samples. Then we will present a comprehensive study of the optical properties of single crystal bismuth at ambient pressure that has been used as a reference for the subsequent pressure dependent experiments. Here the reader will have the opportunity to appreciate one of the hidden facets of bismuth: in fact the temperature dependence of the ambient pressure bismuth phase revealed a strong signature of an electron-plasmon coupling process [5]. We believe that the observation of such an effect is the consequence of the low carrier density concentration which ultimately allows the energy scale for plasmonic effects to approach the energy region where transport phenomena starts to be relevant. We will then complete the analysis analyzing and interpreting the FIR optical data taken under pressure up to 21 kbar where the material exhibits a clear pressure induced decrease of optical conductivity which indicates the tendency of the material to loose its metallic character approaching the SMSC transition. At high pressure we observe a possible enhancement of the electron-plasmon coupling effect due to the strong reduction of the screened plasma frequency.

Although we observed a drastic change of the properties of bismuth, due to physical limits of the pressure apparatus we could not completely cross the phase transition which we estimated to be around 25 kbar. If on the purely scientific point of view this limitation constitutes an annoying factor preventing us to explore the most interesting part of the bismuth's phase diagram, on the other hand this pressure experiment proves the feasibility and reliability of the adopted technique which finally combines IR spectroscopy with high pressure techniques at cryogenic temperatures.

5.1 Crystal structure

Pure bismuth crystallizes with rhombohedral A7 symmetry (space group $R\bar{3}m$) and the resulting structure has two atoms per unit cell. In Fig. 5.2 the rhombohedral structure has been sketched using thick red sticks connecting the atoms of the rhombohedron. The two main atoms are found along the vertical diagonal $\mathbf{C}_3$ (dashed line in the figure) of the solid which defines the *c*-axis of the crystal and it is oriented along the 111 direction in the rhombohedral notation. One of the two atoms is placed on the corner of the unit cell while the second one is sitting along the diagonal slightly off-centered with respect to the middle point. The length ratio between the two sections of the diagonal defined by the central atom is $d_1/d_2 = 0.88$. In this regard the central atom is found to be closer to the three atoms lying right below it with respect the three above; this defines an alternation of bilayers along the c-axis which also explains why the crystal cleaves more easily along this crystal direction. Another interesting aspect

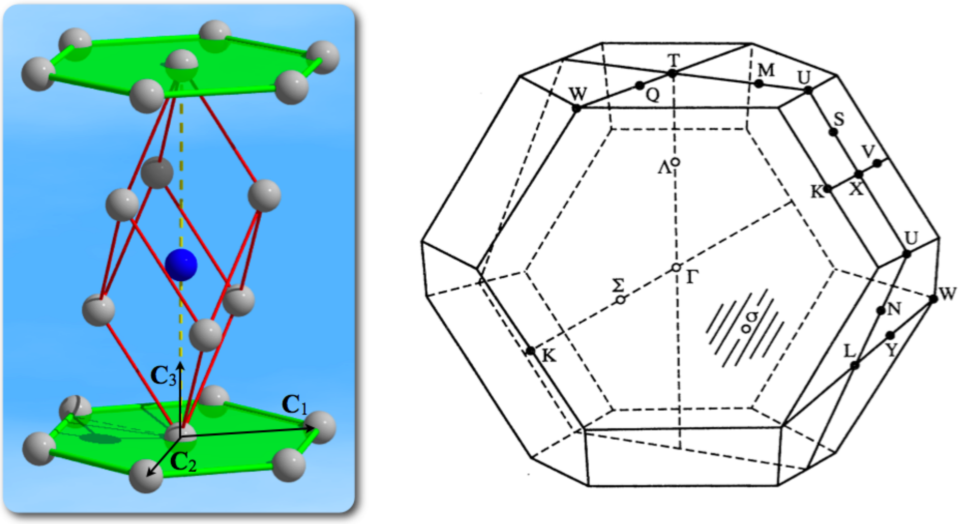

Figure 5.2: Crystal structure and Brillouin zone - Left: the rhombohedral unit cell (red sticks) is shown together with the main atoms that form the hexagonal unit cell. In the rhombohedral representation there are two atoms per unit cell which are found along the $\mathbf{C}_3$ axis (yellow dashed line). Right: the Briullouin zone [58] with the main symmetry points, notably the ΓT and the degenerate ΓL directions are determinant for the definition of the electronic properties of bulk bismuth.

of the crystal structure is the value of the angle between the three primitive translation vectors of the lattice which are connecting the atom at the center of the bottom hexagon with the three atoms right above it; this angle has been found to be $\alpha = 57.19°$ [59] and recognizing that for $d_1/d_2 = 1$ and $\alpha = 60°$ the structure would have been cubic, the actual structure can be seen as a deformed cubic cell. As we will see this small deformation is mainly responsible for the semimetallic character of this compound.

Even though the rhombohedral representation is the simplest one, in the literature the structure of bismuth is often found to be described by an hexagonal representation which, for the sake of completeness, is also sketched in Fig. 5.2. In particular the values of the a, b and c-axes, which are respectively oriented along $\mathbf{C}_1$, $\mathbf{C}_2$ and $\mathbf{C}_3$, are always referring to this latter representation. As it can be seen the a and b axis are equivalent and their experimentally determined value is $a = b = 4.5332$ Å while $c = 11.7967$ Å. By symmetry considerations $\mathbf{C}_1$, $\mathbf{C}_2$ and $\mathbf{C}_3$ are usually defined as bisectrix, binary and trigonal axis and since the structure repeats itself upon rotations of 120° around the trigonal axis, the bisectrix and binary axis exist three times.

The basis vectors for the rhombohedral representation may be written as a function of the hexagonal lattice parameters a and c as:

$$\begin{aligned}
\vec{a}_1 &= \left(-\frac{1}{2}a, -\frac{\sqrt{3}}{6}a, \frac{1}{3}c\right) \\
\vec{a}_2 &= \left(\frac{1}{2}a, -\frac{\sqrt{3}}{6}a, \frac{1}{3}c\right) \\
\vec{a}_3 &= \left(0, \frac{\sqrt{3}}{3}a, \frac{1}{3}c\right),
\end{aligned} \tag{5.1}$$

where for every $\vec{a}_i$, $|\vec{a}_i| = 4.7236$ Å.

From the electronic point of view Bi with its 83 electrons has 5 valence electrons in the 6*s* and 6*p* orbitals. Together with the previous considerations regarding its crystal as being a distorted cube, this suggests already the electronically ambiguous nature of bismuth. In fact if the structure would have been perfectly cubic there would have been only one atom per unit cell with an odd number of valence electrons which would have finally given a partially filled band giving a clear metallic character to the system. In the actual case, due to the *small* deviation from the purely cubic phase, there are instead two atoms per unit cell and ten valence electrons which should in principle form five spin-up spin-down couples and completely fill five bands, determining an insulating behavior. Since the distortion is very small, bismuth is actually lying in between these two very different states.

Band structure calculations [59, 58, 60, 61] confirmed this rough picture showing that among the two available *s*-bands and the six *p*-bands, the former are completely full but in the case of the *p*-bands there are just two which are completely full. In fact a third valence *p*-band, thought almost full, is slightly crossing the Fermi energy while a forth band also crosses E_F electrostatically compensating the former incomplete valence band. Fig. 5.3 reveals something even more interesting since this crossing takes place in two different points in the Brillouin zone, respectively at the L and the T points and with a completely different electronic nature. The crossing at the T point is in fact due to a "hole" band while the one at the L point is an "electron" band crossing forming respectively hole and electron pockets at the Fermi surface. As it can be seen in the expanded representation in Fig. 5.3 the energy scales are extremely small; at the L point the first full valence band is separated by the conduction band by a tiny energy gap of 13.7 meV and the bottom of the conduction band is lying 26.7 meV below the Fermi energy. Also at the T points the top of the hole band is only 13 meV apart from the Fermi energy. Due to the small energy scales close to the Fermi energy the carrier density is strongly reduced with respect to typical metals, determining many of the interesting properties of this material.

This kind of band structure is quite peculiar since it presents an overlap between the highest valence band and the lowest conduction band determining a negative energy gap; this overlap, which creates a small and equal numbers of free electrons at one point in the Brillouin and free holes at a different point, is the main distinctive peculiarity of semimetals.

According to symmetry considerations, the hole pocket at the T-point is non degenerate and has the form of an ellipsoid elongated along the trigonal direction. The

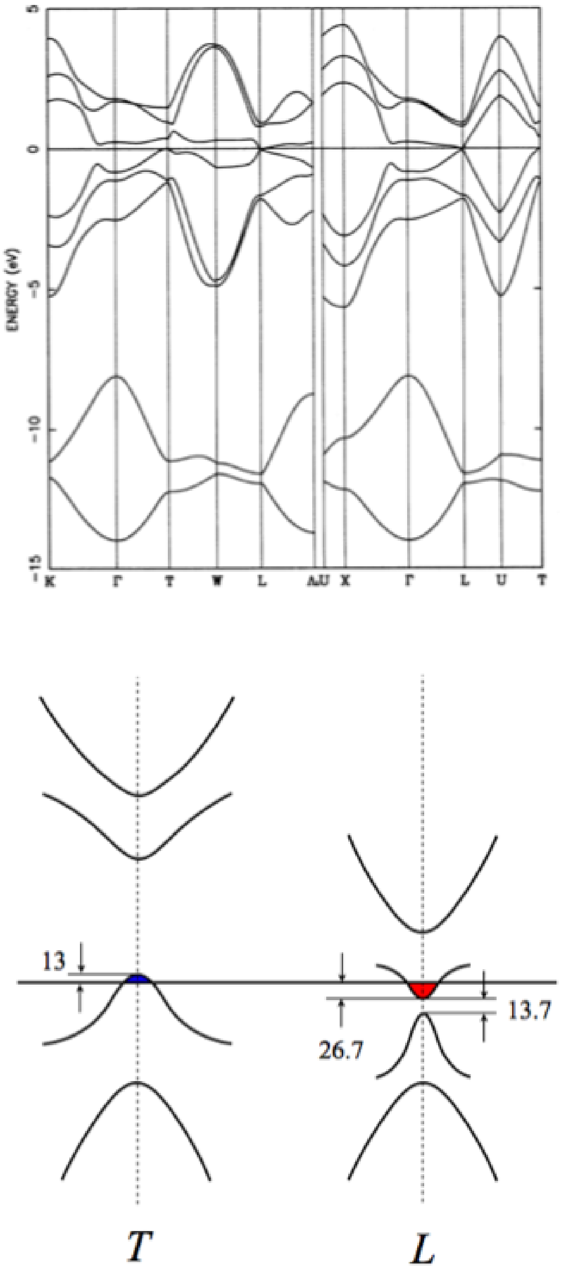

Figure 5.3: Bulk bismuth band structure - Top: the band diagram as calculated by Liu [58]. The graph shows clearly the two filled s-bands lying few electronvolts below the p-bands. Two valence p-bands are completely full while a third one crosses E_F at the T-point. The positive charge accumulated in this small hole pocket is compensated by free electrons in the first conduction band which also crosses E_F but at the L-point. Bottom: an expanded view of the band distribution at the relevant T and L-points. The energy scales that define the system are unusually tiny compared to simple metals giving rise to strong dependencies from external parameters like temperature, pressure, magnetic field or doping.

electron pocket at the L-points shows on the contrary a threefold degeneracy with respect the trigonal axis. The relative size and orientation of the two different carrier pockets is shown in Fig. 5.4. The three electron pockets are also elongated ellipsoids and are distributed symmetrically around the hole pocket which exhibits a circular Fermi surface on the $\mathbf{C}_1$-$\mathbf{C}_2$ plane. As it can be seen the principal axis of the electron pocket is not perfectly aligned along the $\mathbf{C}_1$ axis but it result tilted by $\sim 6°$. Due to the large anisotropy of the ellipsoids this small misalignment together with the relative orientation of all pockets needs to be taken into account for the calculation of the effective masses.

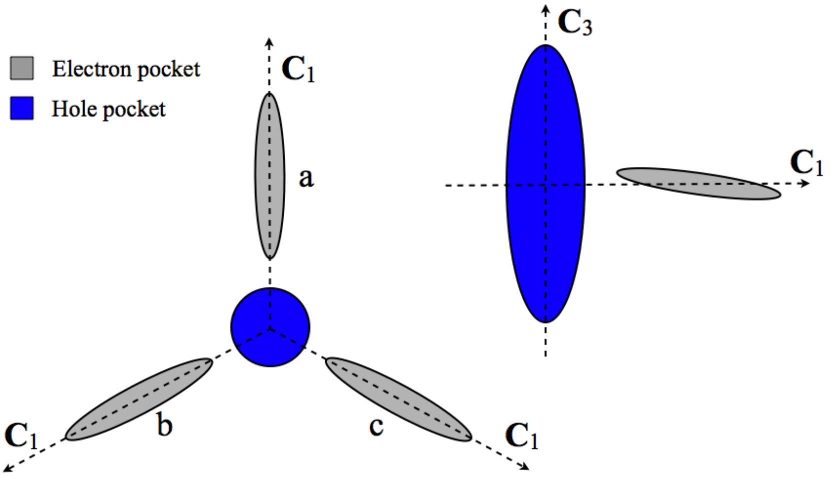

Figure 5.4: The electron and hole pocket orientations - The hole pocket is an ellipsoid with its principal axis oriented along the $\mathbf{C}_3$ direction. For sections taken on planes parallel to the $\mathbf{C}_1$-$\mathbf{C}_2$ plane the holes Fermi surface has a perfectly circular symmetry. On the contrary electrons are distributed in a threefold degenerate pocket around the $\mathbf{C}_3$ axis. The ellipsoids' principal axis are not perfectly aligned with respect the $\mathbf{C}_1$ axis but result tilted by $\sim 6°$. Due to the high anisotropy of both electron and hole pockets the resulting mass tensor is also strongly orientation dependent with masses that can vary from $0.001 m_0$ to $0.26 m_0$.

Bismuth displays a lot of interesting aspects mainly because its behavior can be strongly influenced by varying the temperature and by applying magnetic field and pressure. In particular, since its electronic properties are strongly affected by the small deviation of the crystal from a perfect cubic structure, pressure may play a determinant role in driving the system across an electronic semimetal to semiconductor transition (SMSC).

5.2 Crystal growth

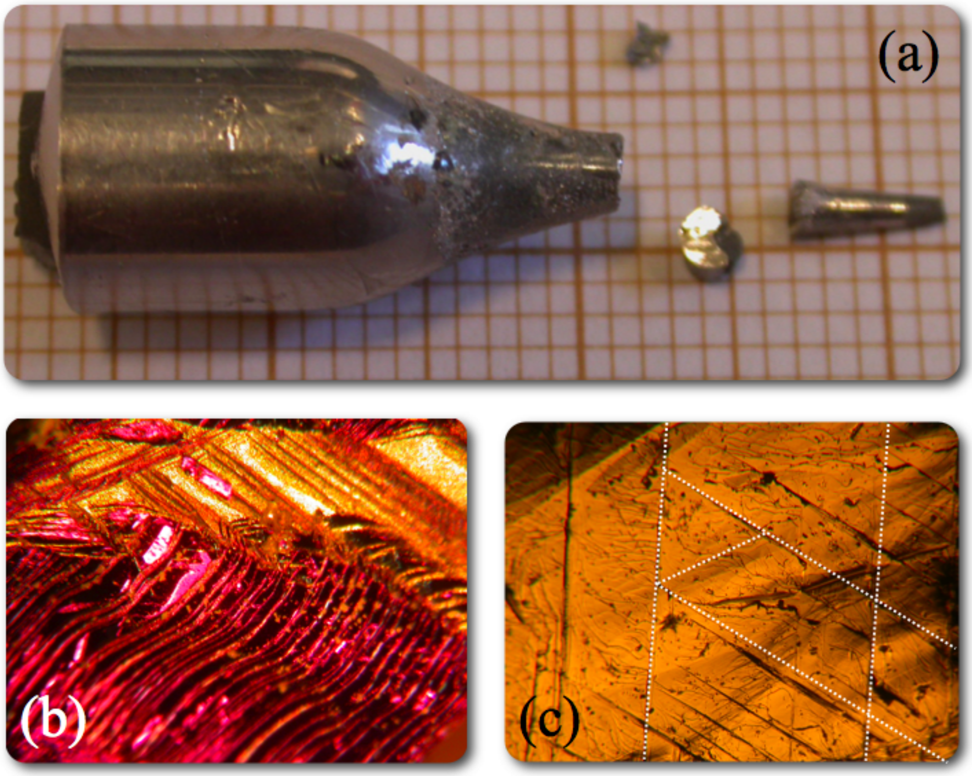

Figure 5.5: Crystal growth - (a) A typical as-grown sample. (b) The growth direction does not correspond to any main crystal axis and the crystal boule is made of platelet like crystallites stuck on top of each other with a stairs shaped structure. (c) The crystals for our measurements were transversally cleaved from these steps and exhibit rhombohedral features typical of the plane perpendicular to the trigonal axis (dotted white lines are shown to guide the eye).

The crystals used for the present study were grown by Dr. E. Giannini at the university of Geneva and their quality was carefully controlled. Bismuth crystals were grown by a modified Bridgman-Stockbarger technique in a vertical gradient furnace. A silica tube was filled with $\sim$5 g of 99.999% pure Bi powder (Cerac ®) and sealed under vacuum ($p < 10^{-5}$ torr). The growth process was performed in two different kinds of furnaces: 1) in an induction furnace and 2) in a three-zone resistive furnace, the latter proving to be more suitable for controlling the growth of Bismuth crystals. In the first kind of furnace, the rod-shaped starting sample (the silica tube filled with Bi powder) was inductively heated above the melting point of Bi (T_m =271.4 °C) in a RF-coil and then moved downwards away from the coil. The molten Bi was cooled down slowly, travelling through a strong temperature gradient that favors the oriented growth of crystalline Bi. It proved to be difficult to keep under control the T-gradient at the edge of the heating coil. Furthermore, the induced heating currents at the outer surface of the sample were likely to create strong radial gradient as well as very high temperature at the interface between Bi and the silica ampoule. As a consequence, the crystallization was not homogeneous and the outer layer showed oxide impurities. In the second growth technique, the ampoule was vertically held in a three-zone furnace and annealed above the melting point of Bi (T_m =271.4 °C) for 10 hours before decreasing the temperature. The controlled directional cooling of the melt was obtained by decreasing the temperature at a rate of 30 °C/h, while keeping a temperature gradient of 1015 °C/cm. Also in this case an oxide reaction layer formed at the bismuth-silica interface, however, the radial gradients were reduced and the cooling process was better controlled. Bi crystals were cleaved from the as-grown boule in liquid N2, in order to get round the softness of this material. We have observed that, due to the softness of the material, the quality of samples cleaved from the same bulk crystal could vary strongly, depending on the mechanical stresses experienced during cut and cleave. The samples were characterized by X-ray powder diffraction. Mirror-like cleavage surfaces were found to be [001] planes perpendicular to the trigonal axis, and used as reflecting planes for reflectivity experiments.

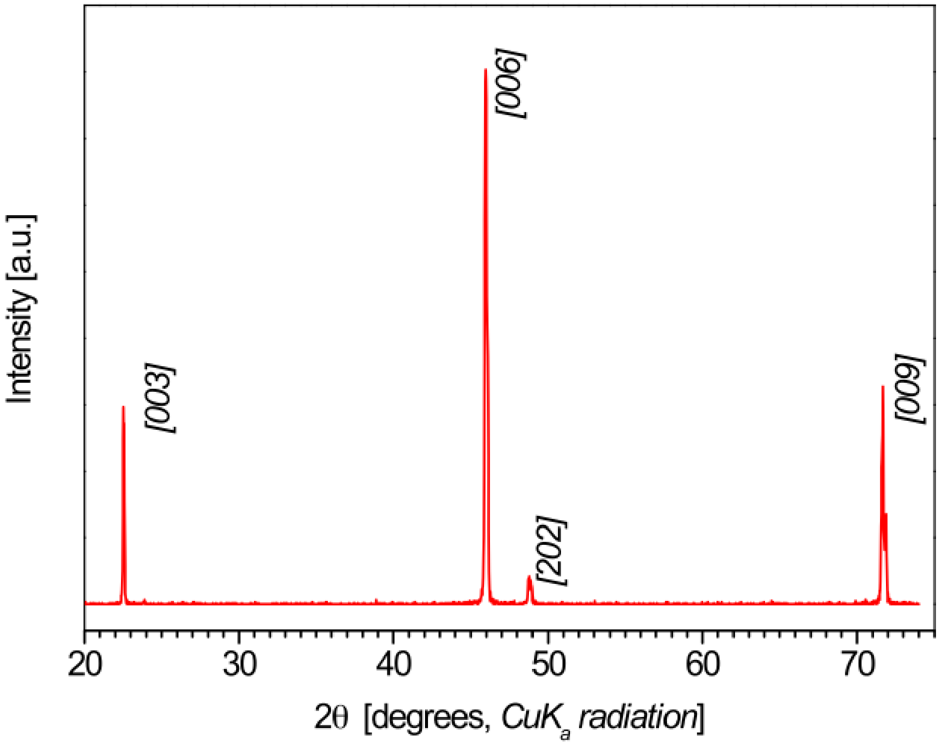

Figure 5.6: X-rays diffraction spectra - A typical XRD powder diffraction pattern acquired from the cleaved surface of such crystals is shown in Fig. 5.5. The three reflections due to the trigonal axis [001] (at angles of ∼ 22°, 46°, and ∼ 72°) show the crystalline nature of the sample. However, the crystal surface always cleaves spontaneously with steps that are difficult to remove and is rarely perfectly flat. This gives contributions from secondary planes in the diffraction patterns, as indicated by the peaks at ∼ 49° (reflection [202]).

5.3 Temperature dependent infrared spectroscopy

As mentioned in the chapter dedicated to the analysis of pressure data, before being able to proceed with the actual pressure experiments we need to carefully investigate the ambient pressure behavior of bismuth with standard spectroscopic techniques.

A large single crystal bismuth sample was prepared and carefully cleaved at liquid nitrogen temperature along the ab plane. This low temperature procedure is required in order to reduce the characteristic room temperature softness of the material and to avoid possible plastic deformations of the crystal surface. The obtained sample was not polished prior to measurement since it has been found that even a gentle polishing easily destroys the single crystal structure of the surface.

A complete spectroscopic measurement has been done in the FIR, MIR and VIS spectral range combining optical reflectivity and ellipsometry techniques as described in chapter 2. In order to measure the bismuth’s properties at low temperature we mounted the sample in custom made cryostats specially designed in order to guarantee the high stability level required by this kind of spectroscopic technique.

First the infrared reflectivity has been measured in the IR range in a standard Bruker 66 Fourier transform spectrometer using a different combinations of source and detectors in order to cover the complete spectral range from 50 cm^{-1} to 6000 cm^{-1} . The result of the reflectivity measurement is shown in Fig. 5.7 for five se-

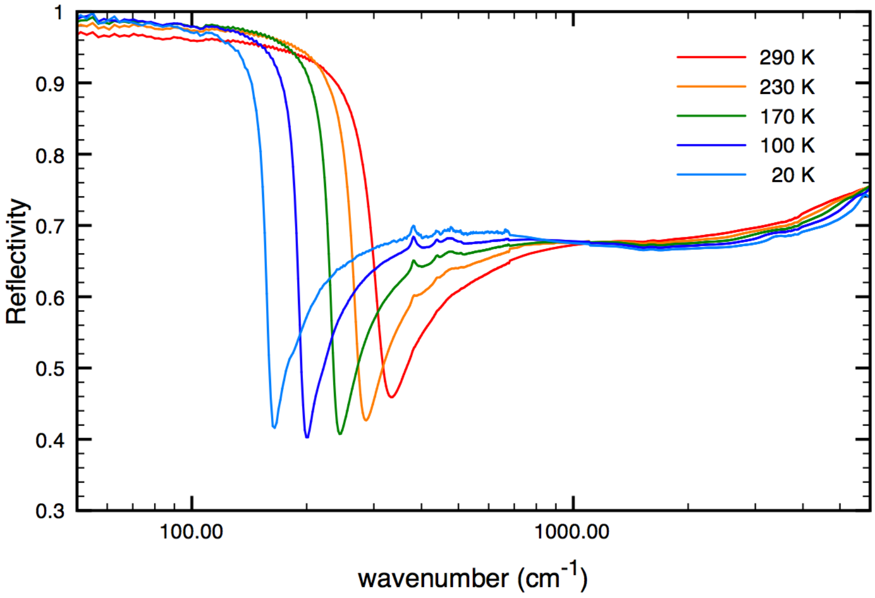

Figure 5.7: Ambient pressure reflectivity - (color online) $R(\omega)$ is shown for five selected temperatures in the FIR-MIR spectral range. The temperature dependence reveals a strong reduction of the screened plasma frequency indicating a drastic decrease of carrier density. The peak visible around 380 cm^{-1} is an artifact caused by a beam splitter and does not have any physical meaning.

lected temperatures. It is possible to observe a drastic reduction of the reflection edge corresponding to the screened plasma frequency ω_p^* upon cooling. The reflectivity below the plasma edge is increasing indicating an enhancement of the metallic properties of the sample and shows a clear tendency toward saturation at low temperature. The plasma edge itself sharpens at low temperature suggesting a considerable reduction of the scattering rate for the conduction electrons and holes. The small peak appearing around 380 cm^{-1} is an artifact due to a strong absorption of the beam splitter and does not reflect any intrinsic feature of the sample neither it affects the main conclusions of our study.

The FIR measurement was integrated with ellipsometric measurement of the real and imaginary part of the dielectric function, $\varepsilon_1(\omega)$ and $\varepsilon_2(\omega)$, in the visible range. As explained in chapter 2, this allows to use Kramers-Kronig relations without the need of a complete knowledge of $R(\omega)$ for $\omega \in [0, +\infty[$.

5.4 Drude-Lorentz analysis

Simultaneously fitting both the temperature dependent sets of data with using a variational KK consistent approach, we were able to extract the relevant parameters of the Drude-Lorentz model and to calculate the relevant physical functions $\hat{\sigma}(\omega)$ and $\hat{\varepsilon}(\omega)$.

In order to fit the data we used the the Drude-Lorentz definition of the dielectric function considering a limited set of N oscillators as

$$\hat{\varepsilon}(\omega) = \varepsilon_\infty + \sum_{j=1}^{N} \frac{\omega_{pj}^2}{\omega_{0j}^2 - \omega^2 - i\gamma_j\omega}, \tag{5.2}$$

where ε_∞ it is a constant which takes into account the contribution to the dielectric function of the oscillator which are outside the experimental measurement range. In the case of bismuth we found that in a first approximation a set of two oscillators describes fairly well the experimental data. The values for the two oscillators are reported in Table 5.1 for some selected temperatures. Using the DL analysis it was

Table 5.1: Parameters for the Drude-Lorentz model - A set of two oscillators (1 Drude and 1 Lorentz oscillator) gives, in first approximation, a good fitting to the experimental data. The reported temperature is in kelvin units while the oscillators' central frequency ω_{0j}, the plasma frequency ω_{pj}, and the scattering rate γ_j are in cm^{-1} units.

T	ω_{0D}	ω_{pD}	γ_D	ω_{0L1}	ω_{pL1}	γ_{L1}	ε_∞
290	0	3300.5	37.3	5831.6	60875	9141.6	1.64
250	0	3051.1	27.6	5807.0	61077	9214.2	1.65
200	0	2748.8	18.3	5765.8	61386	9327.2	1.66
150	0	2456.3	11.8	5712.7	61752	9477.9	1.66
100	0	2163.3	7.13	5658.7	62153	9681.7	1.61
50	0	1896.9	3.76	5604.0	62562	9934.4	1.53
20	0	1815.4	2.09	5581.3	62740	10071	1.47

possible to extract the value of the unscreened plasma frequency for the free electrons. The sharp drop in reflectivity in fact defines the screened plasma frequency which is connected to the unscreened one by the relation

$$\omega_p = \omega_p^* \cdot \sqrt{\hat{\varepsilon}_\infty}, \tag{5.3}$$

where $\hat{\varepsilon}_\infty = \varepsilon_\infty + \sum_j (\omega_{pLj}/\omega_{0Lj})^2$ is the total dielectric contribution of all interband transitions. With the knowledge of the plasma frequency it is possible to determine the carrier density since for free electrons $\omega_p^2 = 4\pi e^2 n/m_e$. However, as we observed before, electrons and holes pocket are strongly anisotropic and before being able to directly extract the electron's density n it is necessary to calculate the effective carrier mass with respect the crystal orientation used in the experiments. For this calculation we refer to the scheme presented in Fig. 5.4. The normalized mass tensor for the a electron pocket aligned along the vertical $\mathbf{C}_1$ bisectrix axis is

$$\frac{\mathbf{m_a}}{m_0} = \begin{pmatrix} m_1 & 0 & 0 \\ 0 & m_2 & m_4 \\ 0 & m_4 & m_3 \end{pmatrix} \tag{5.4}$$

where the indexes $i = 1, 2, 3$ are referring respectively to the values along the binary, bisectrix and trigonal axis. The off-diagonal component m_4 takes into account the small tilt angle of the electron ellipsoids with respect the bisectrix axis. The mass tensors for the other two electron pockets can be easily calculated considering the rotational symmetry of the system which gives $\mathbf{m_{b,c}} = \mathbf{S_{b,c}}^{-1}\mathbf{m_a}\mathbf{S_{b,c}}$ where $\mathbf{S_{b,c}}$ is a matrix of rotation defined as

$$\mathbf{S_{b,c}} = \frac{1}{2}\begin{pmatrix} -1 & \pm\sqrt{3} & 0 \\ \mp\sqrt{3} & -1 & 0 \\ 0 & 0 & 2 \end{pmatrix} \tag{5.5}$$

for a 120° rotation around the trigonal axis. Using these formulas and considering the negligible influence of the off-diagonal component of the mass in Eq. 5.4 we find

$$\mathbf{m_{b,c}} = \frac{1}{4}\begin{pmatrix} m_1 + 3m_2 & \mp\sqrt{3}m_1 \pm \sqrt{3}m_2 & 0 \\ \mp\sqrt{3}m_1 \pm \sqrt{3}m_2 & 3m_1 + m_2 & 0 \\ 0 & 0 & 4m_3 \end{pmatrix}. \tag{5.6}$$

Since we are interested in the total inverse mass tensor we can calculate it as $\mathbf{m}^{-1} = (\mathbf{m_a}^{-1} + \mathbf{m_b}^{-1} + \mathbf{m_c}^{-1}) + \mathbf{m^h}^{-1}$, considering also the important contribution given by the hole pocket. Given the diagonal mass tensor for hole pockets, the resulting total inverse mass tensor is also diagonal and its non-zero components are:

$$\begin{aligned} m_{11}^{-1} &= \frac{1}{2}\frac{m_1^e + m_2^e}{m_1^e m_2^e} + \frac{1}{m_1^h} \\ m_{22}^{-1} &= \frac{1}{2}\frac{m_1^e + m_2^e}{m_1^e m_2^e} + \frac{1}{m_2^h} \\ m_{33}^{-1} &= \frac{1}{m_3^e} + \frac{1}{m_3^h} \end{aligned} \tag{5.7}$$

From the previous expressions we can see that the effective mass is isotropic along the $\mathbf{C}_1$-$\mathbf{C}_2$ plane corresponding to the ab surface that we used for reflection experiments. Using the experimental values for the effective masses reported in Table 5.2 [46, 61] we can extract the carrier density taking also into account the non-parabolicity of bands in bismuth. This deviation from perfect parabolic dispersion is typically found in systems where the higher valence band and the conduction band are separated by a small energy gap [46]. In those cases the dispersion relation is

$$E\left(1+\frac{E}{E_g}\right)=\frac{\mathbf{p}\cdot\alpha\cdot\mathbf{p}}{2m_0}, \tag{5.8}$$

where $\alpha = \mathbf{m}^{*-1}$ and $\mathbf{p}$ is the momentum. As it can be seen, in standard metals this effect is negligible since E_g is usually large compared to the energy scales of conduction electrons. As anticipated, in bismuth, all energy scales are extremely small and $E_g = 26.7$ meV. According to this description the relation between the effective masses at the bottom of the conduction band and those at the Fermi surface is

$$m(E_F)=\left(1+\frac{2E_F}{E_g}\right)m_b, \tag{5.9}$$

which gives, considering that $E_F = 14$ meV, a remarkably large correction factor for the masses of about 4.8. Using then Eq. 5.9 together with the values in Table 5.2 and substituting in Eqs. 5.7 we find $m_{11} = m_{22} = 0.01437m_0$ and $m_{33} = 0.01164m_0$. Finally the electron density can be calculated for every temperature as shown in Fig. 5.8. For the lowest considered temperature, 20 K, we find $n = 5.27 \times 10^{17}$ cm^{-3} which is in good agreement with the value found in other experimental and theoretical works [61]. Moreover considering the volume of the unit cell and the number of atoms per cell, the number of free carriers per atom is $\sim 1.8 \times 10^{-5}$.

The temperature dependence of the carrier density $n(T)$ reveals a drastic reduction of the number of electrons and holes toward cooling. In order to better understand what is really happening from the electrodynamic point of view, we extracted from the experimental data the optical conductivity at different temperatures $\sigma_1(\omega, T)$. The room temperature frequency dependent conductivity in Fig. 5.9, presents a clear Drude peak at low frequencies and a strong interband absorption feature centered around 0.6 eV. The intraband and interband absorptions appear distinctly separated by a minimum around 60 meV.

Although the experimental curves may appear in good agreement with a typical metallic free electron model, there is a strong inconsistency with the expected behavior predicted by the calculated band structure. In the FIR range, as shown in the right panel of the figure, the Drude peak appears to shrink due to the reduction of scattering processes and the peak value tends to increase reflecting the reported decrease in DC resistivity with temperature [62]. The interesting aspect derives by the progressive increase of optical conductivity in the region around 80 meV which extends down to 20 meV for the lowest considered temperature. This situation is virtually incompatible with the band structure picture: in fact considering the zero temperature case (Figure 5.3) and the Pauli blocking principle, the first available vertical[2] interband transition

---

[2] Since in optical processes the photon's momentum is negligible with respect the typical electron's momentum in solids, a transition with zero-momentum transfer can be represented with a vertical line in an energy-momentum diagram.

Table 5.2: Experimental effective masses - The values of effective masses at the bottom (top) of the electron (hole) band for the bisectrix, binary and trigonal axes calculated by *Liu et al.* [58].

Type	m_1	m_2	m_3
Electrons	0.261	0.00194	0.00246
Holes	0.064	0.064	0.7

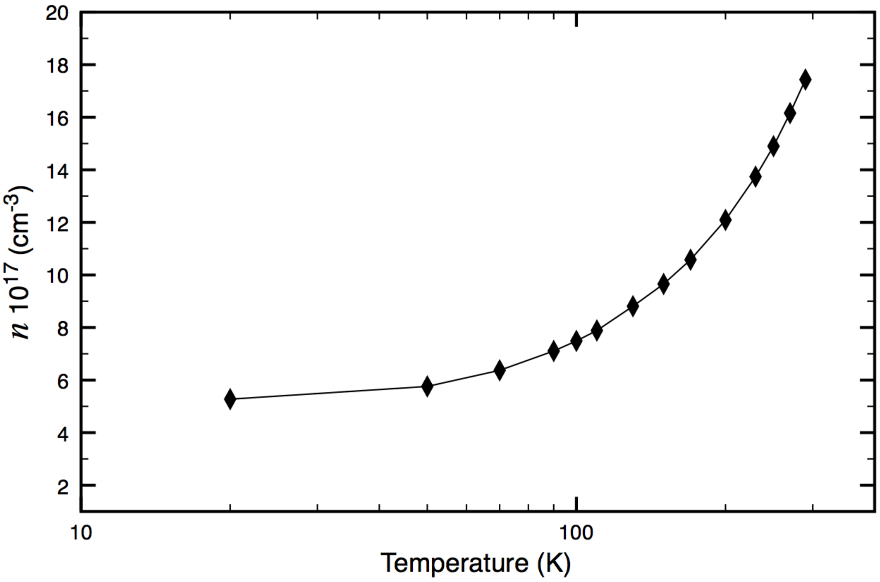

Figure 5.8: Carrier density - The temperature dependent $n(T)$ extracted from IR data considering the crystal orientation and the effective mass tensor for the ab-plane.

should be expected at energies $E_0 \simeq E_g + 2E_F = 67.1$ meV therefore much higher than the observed onset of interband absorption.

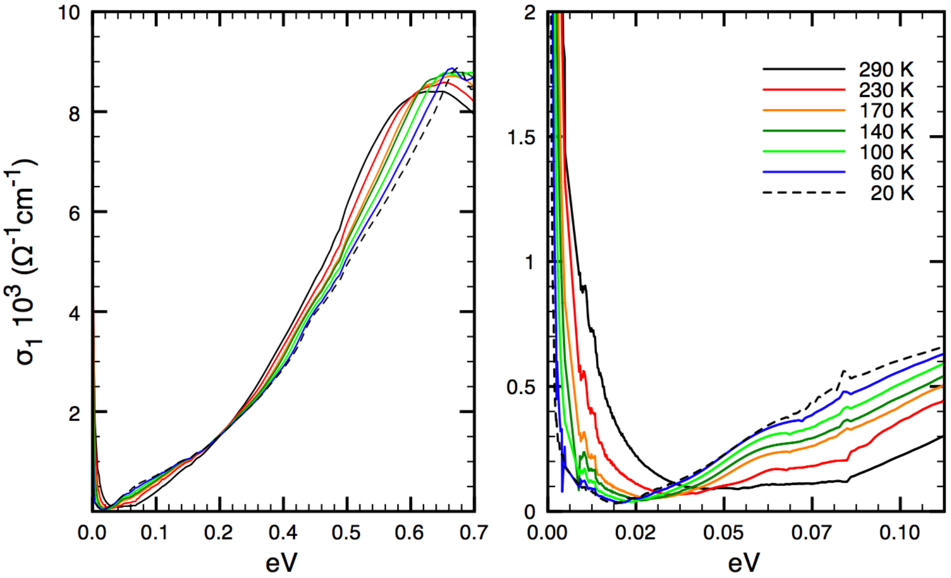

Figure 5.9: Optical conductivity - Left: the FIR-MIR optical conductivity is shown for selected temperature. A clear intraband Drude peak is clearly separated by a strong interband absorption peak centered around 0.6 eV. Right: for decreasing temperatures, the temperature dependence of the conductivity in the FIR reveals a peculiar increase of absorption processes well below the expected interband gap at 67.1 meV.

5.4.1 Spectral weight transfer and the f-sum rule

A further confirmation for the observed phenomenon comes from the application of the f-sum rule to the optical conductivity data. According to this formulation, for a single band model the integral of the real part of the optical conductivity with respect to frequency up to infinity is proportional to n/m^* and preserves charge conservation [63, 64]. In particular for the Drude term we obtain

$$\int_0^\infty \sigma_1(\omega)\,\mathrm{d}\omega = \frac{\omega_p^2}{8} = \frac{\pi n e^2}{2m^*}. \tag{5.10}$$

In the general case where the optical conductivity presents both the intraband and interband contributions the meaning of the free electron density n has to be changed and it represents instead the number of electrons per unit volume in the material structure. Ideally if it would be possible to exactly separate each contributions, integrating the optical conductivity in limited regions of the spectrum would allow the extraction of the number of electron per unit volume in each electronic band. In the present case we can apply this concept with a good precision since the intraband term is well separated by the interband one. We thus define the *spectral weight* (SW) function $W(\omega_c)$ as

$$W(\omega_c, T) = \int_0^{\omega_c} \sigma_1(\omega)\,\mathrm{d}\omega = \frac{\pi n(T) e^2}{2m^*}, \tag{5.11}$$

where ω_c is the cutoff frequency. In Fig. 5.10, $W(\omega_c)$ is presented for different temperatures in the FIR-MIR spectral range. The graph shows a progressive increase of SW in the FIR region followed by a plateau which extends up to the MIR range where SW starts to grow again due to the presence of the interband transition terms. Although the tail of the Drude peak only vanishes for $\omega \to \infty$, the plateau region gives testimony to the fact that already for small ω_c values most part of the Drude contributions have been taken into account. For this reason the width of this flat region is expected to be inversely proportional to the scattering rate and its absolute value, proportional to the carrier density. As anticipated, $W(\omega)$ is expected to grow as soon as the interband

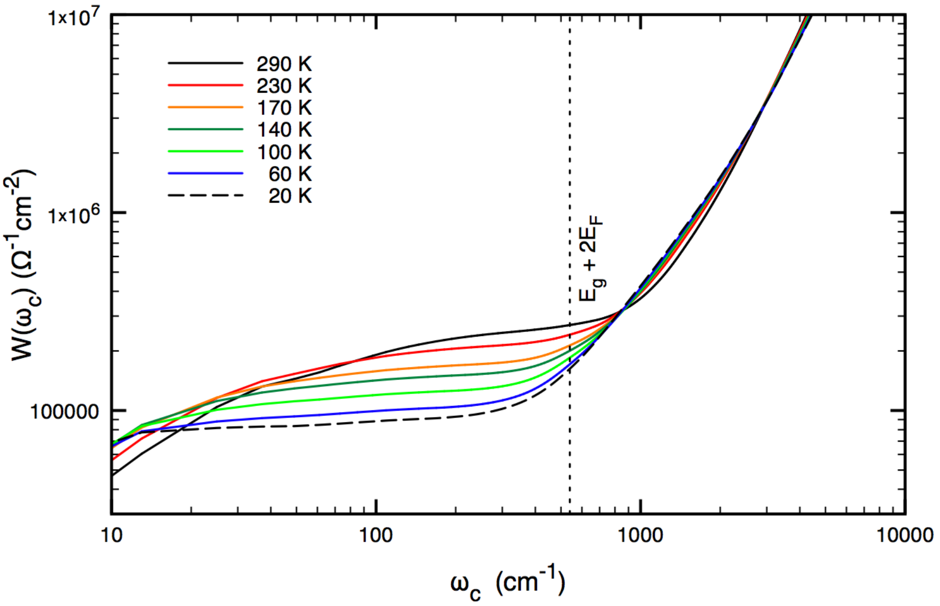

Figure 5.10: Frequency dependent spectral weight - The spectral weight W is presented as a function of the cutoff frequency ω_c according to Eq. 5.11 for selected temperatures. The dashed vertical line indicates the energy where the first interband transition are allowed at low temperature. The SW analysis demonstrates how interband-like processes start to be effective for energies well below the predicted $E_g + 2E_F$ cutoff. This is shown clearly by the lowest temperature curve.

absorption processes start to dominate the conductivity spectrum. Due to the direct gap and to the Pauli blocking principle, these contributions should appear and sharpen during the cooling process around $E_g + 2E_F$ as indicated by the vertical dashed line in Fig. 5.10. Surprisingly the experimental evidence shows a completely opposite behavior. In fact it appears that the onset of the interband absorptions is decreasing with temperature much below the expected cutoff value.

It is worth noticing here that since the f-sum rule guarantees the conservation of charge, the value of $W(\omega_c)$, for $\omega \rightarrow \infty$, should be independent of the temperature. In many practical cases, since the energy scales for infrared absorption and temperature activated processes is often rather low, the mentioned condition is often fulfilled at relative low frequencies. In the case of bismuth it can be seen that for $\omega_c > 3000$ cm^{-1} there is a complete recovery of the spectral weight. Actually the graph reveals that this condition is reached even before this energy value: in fact all the SW curves cross eachother for $\omega_c \simeq 900$ cm^{-1} .

The analysis of the temperature dependent SW leads us to two main conclusions:

1. there is a clear SW transfer from the Drude peak to higher frequencies upon cooling, indicating an effective charge transfer between the Drude peak and high frequency oscillators;

2. the transfered spectral weight is redistributed partly in an energy region above the direct gap and partly below it. This latter contribution seems to be more important for low temperature cases.

5.4.2 In-plane complex dielectric function

In order to clarify the behavior of the observed anomaly we analyzed directly the imaginary part of the dielectric function which is related to the optical conductivity by the simple formula $\sigma_1(\omega) = \omega\varepsilon_2(\omega)/4\pi$. Without the weighting factor ω, present in the expression of $\sigma_1(\omega)$, it is in fact easier to observe subtle details otherwise invisible in the raw conductivity spectrum. Figure 5.11 shows the FIR-MIR value of $\varepsilon_2(\omega)$ and in the inset, a closer view of the FIR region where the Drude peak vanishes and the aforementioned anomaly starts to appear. The low energy onset of this MIR absorption feature it is clearly preceded by a small, but distinct and temperature dependent *prepeak* absorption. This prepeak is a robust feature, which we have observed in even poly-crystalline samples. We note that this absorption is also readily visible in the raw reflectivity data itself. For instance, it is apparent in the 20 K curve where it appears as an inflection point slightly above the the sharp reflectivity minimum (Fig. 5.7). This observation directly proves that even if small, the prepeak cannot originate from any uncontrolled effect introduced by the analysis procedure.

In commenting on the observed features some colleagues wondered about the possibility of a small misalignment of the sample surface with respect the crystallographic *ab* plane. In this regarding we strongly exclude such possibility: in previous IR measurements [65] it was shown that the IR reflectivity curve is strongly dependent on the field orientation with respect to the *c*-axis . The main difference deriving from the crystal orientation is reflected in the position of the reflectivity minimum (which can be considered in first approximation as the value of the screened plasma frequency) for the two cases: for $E \parallel c$, $\omega_{\text{min}} \simeq 220$ cm^{-1} while for $E \perp c$, $\omega_{\text{min}} \simeq 310$ cm^{-1} . Assuming then a small crystal misalignment with respect to the *ab* plane, a second minimum would appear *below* the main reflectivity minimum at 310 cm^{-1} and not above it as observed in the present experiment. Moreover the temperature dependence of the shape of the prepeak shown in Fig. 5.11 is completely different from the one

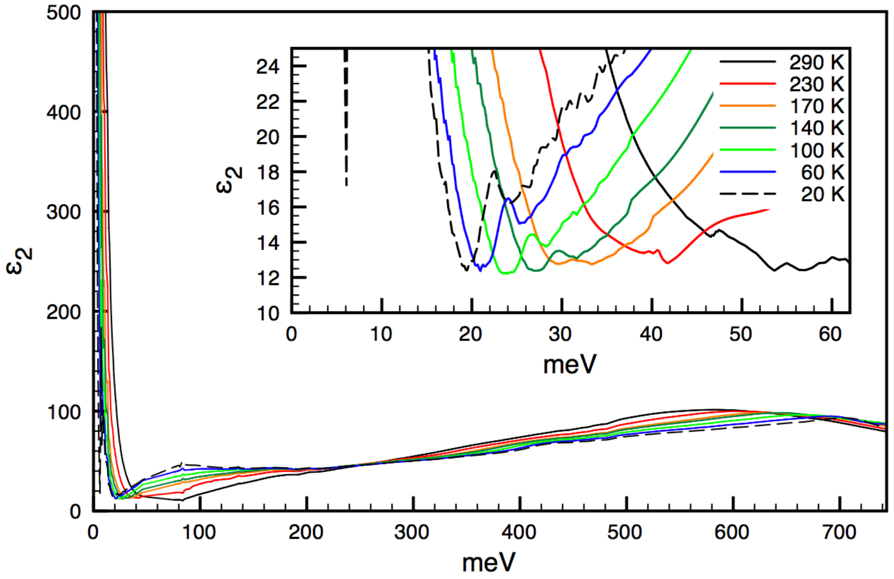

Figure 5.11: The imaginary dielectric constant ε_2 - Main plot: the imaginary part of the dielectric constant plotted versus frequency shows the general trend observed for the optical conductivity but it helps to better recognize subtle features. In the inset, ε_2 is shown in a limited energy range. A clear temperature dependent structure appears in the spectra between 20 and 35 meV.

expected in the case of a second underlying Drude peak representing the conduction electrons and holes along the *ac*-plane.

5.4.3 Extended Drude model

Using the data shown in Fig. 5.9 we analyzed the frequency dependent scattering rate and effective mass according to the extended Drude formalism [66]. This analytical tool is very effective in determining eventual scattering and mass renormalization in the case of important electron-electron or electron-phonon interactions. According to this formalism the frequency dependent quantities $\tau^{-1}(\omega)$ and $m^*(\omega)$ are related to the dielectric function by the formula:

$$\omega m^*(\omega) + i\frac{1}{\tau(\omega)} = \frac{\omega_p^2}{\omega}\frac{1}{\varepsilon_\infty - \varepsilon(\omega)} \tag{5.12}$$

where ω_p is the total *intraband* plasma frequency and ε_∞ is the total interband contribution to the zero frequency dielectric constant. These frequency dependent mass and scattering rate represents the complex self-energy of an optically excited electron-hole pair and reveals rather directly the effect of coupling of the conduction electron to the (typically bosonic) inelastic scattering channels. We emphasize that the extended Drude model is meaningful only below the onset of interband transitions. One can

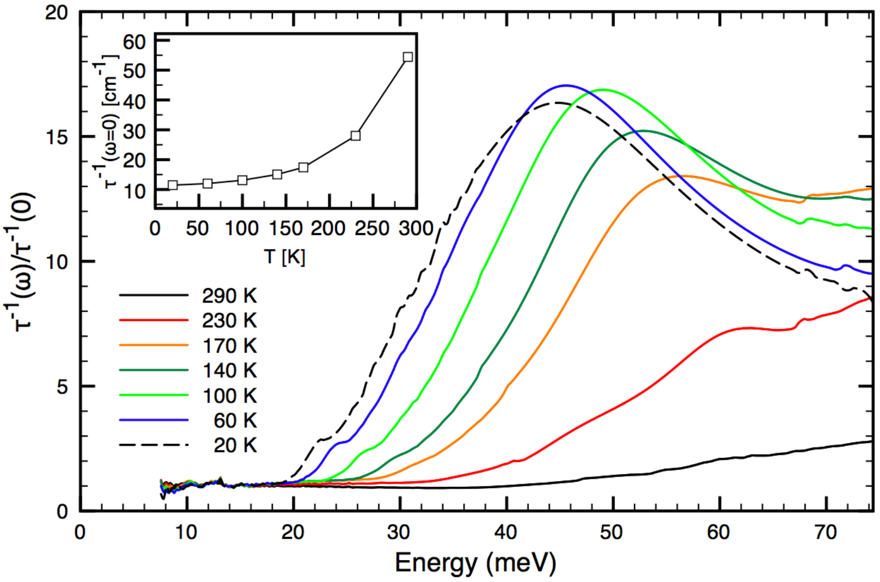

Figure 5.12: Anomalous scattering onset - The normalized frequency dependent scattering rate $\tau^{-1}(\omega)/\tau^{-1}(0)$ calculated according the extended Drude formalism. A clear deviation for the standard Drude model is observed: a strong temperature dependent scattering onset appears well below the expected interband contribution. In the inset the DC scattering $\tau^{-1}(w = 0)$ is presented for selected temperatures.

see in the normalized scattering rate $\tau^{-1}(\omega)/\tau^{-1}(0)$ in Fig. 5.12, that the data are relatively well described at lowest frequencies within the usual Drude framework where the scattering rates and masses are frequency independent. However we observe that together with the decrease of the DC scattering with temperature, shown in the inset of the figure, a sharp onset in the frequency dependent scattering rate clearly develops. This reflects the FIR absorption pointed out previously.

As noted earlier, according to band structure parameters [67], the position of the scattering onset $\omega_\mathcal{T}$ is too low to derive from a direct interband process. We observe that the temperature dependence of this absorption's onset and prepeak is reminiscent of the large temperature dependence of the screened plasma frequency itself. In fact, it almost exactly tracks the independently measured plasmon frequency as a function of temperature, as shown in the parametric plot in Fig. 5.13 where we plot the frequency of this onset in the $\varepsilon_2(\omega)$ function, $\omega_\mathcal{T}$, versus ω_p^* as defined by the zero crossing of the experimental $\epsilon_1(\omega)$, and the onset is defined by the energy position of the prepeak's half maximum on its low frequency side. Based on this parametric plot, we can conclusively identify the plasmon frequency (which changes a factor of 2 as a function of temperature) as setting the energy scale for the observed absorption process.

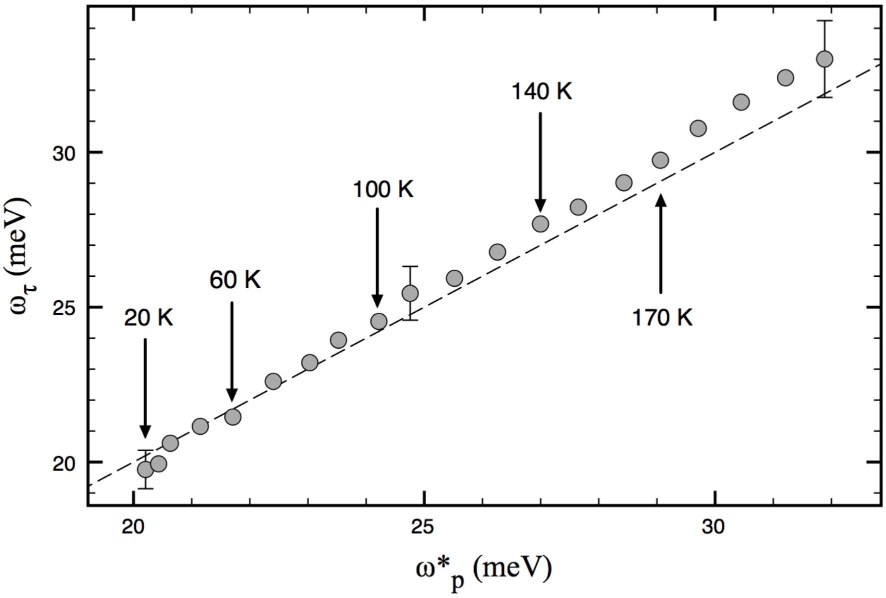

Figure 5.13: $\omega_\mathcal{T}$ **vs.** ω_p^* - A parametric plot $\omega_\mathcal{T}$ vs. ω_p^* shows a slope of 1, suggesting a strong interplay between the anomalous scattering process and the plasmon mode.

5.5 Evidence of Electron-Plasmon coupling

According to simple RPA calculations and in the limit of zero-momentum transfer processes (optical processes) where $\mathbf{q} \to 0$, the excitation of plasmon modes is only possible at the screened plasma frequency ω_p^*. Since IR optical spectroscopy, as described in this work, intrinsically probes only processes with transversal character, the direct excitation of longitudinal modes, different from the main plasmon, is forbidden.

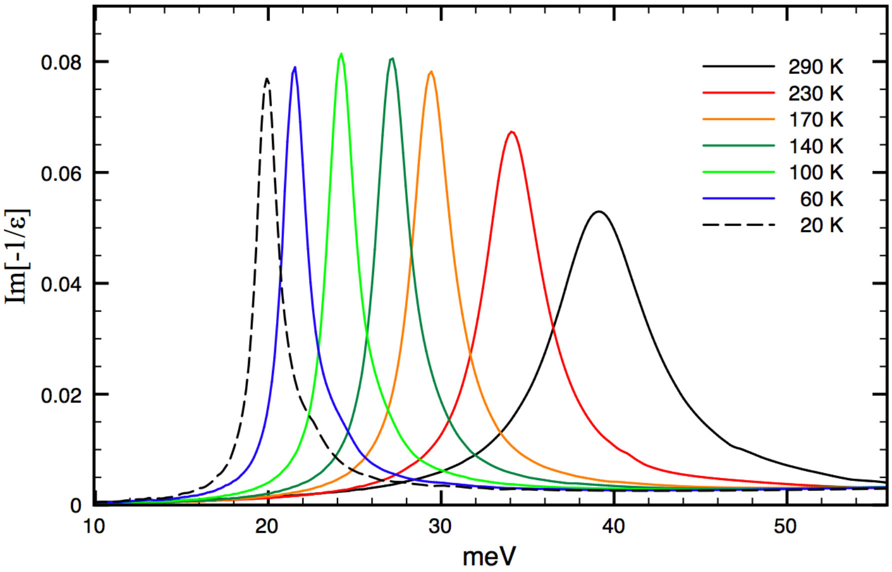

Figure 5.14: Loss spectra - Experimental $\mathrm{Im}[-1/\varepsilon(\omega)]$ at selected temperatures. The temperature dependence of the main peak shows both an energy shift due to the decrease of free carrier in the conduction band and a decrease of width originating from the reduction of scattering processes. The low temperature curves are asymmetric and present a clear shoulder on the high energy side of the main peak.

The longitudinal character of an absorption process can be seen very well using electron-energy-loss spectroscopy (EELS) which measures $\mathrm{Im}[-1/\varepsilon(\omega, q)]$. Though our measurements were essentially done in the $\mathbf{q} \to 0$ limit, the meaning of the EEL function remains unchanged. In Fig. 5.14 the loss function shows a clear plasmon peak with a strong temperature dependence reflecting the density change of free carriers in the system. Free carriers make contributions to collective excitations and e-h excitations simultaneously. The competition of these two kind of excitations determines whether the plasmon peak in enhanced or reduced by the temperature. The figure shows a progressive narrowing of the main plasmon peak for decreasing temperatures and a clear asymmetry present on the high frequency side for the lowest temperature cases.

A more detailed picture of this phenomenon is presented in Fig. 5.15 for $T = 20$ K. There the double peaked structure is clearly visible and the loss function was fitted with two Lorentzian functions. The main peak was found to be correctly centered at ω_p^* while the second one is centered in correspondence of the prepeak found in the conductivity curve. This suggests that this latter absorption feature has a strong longitudinal character and together with the strong interplay between plasmon and the

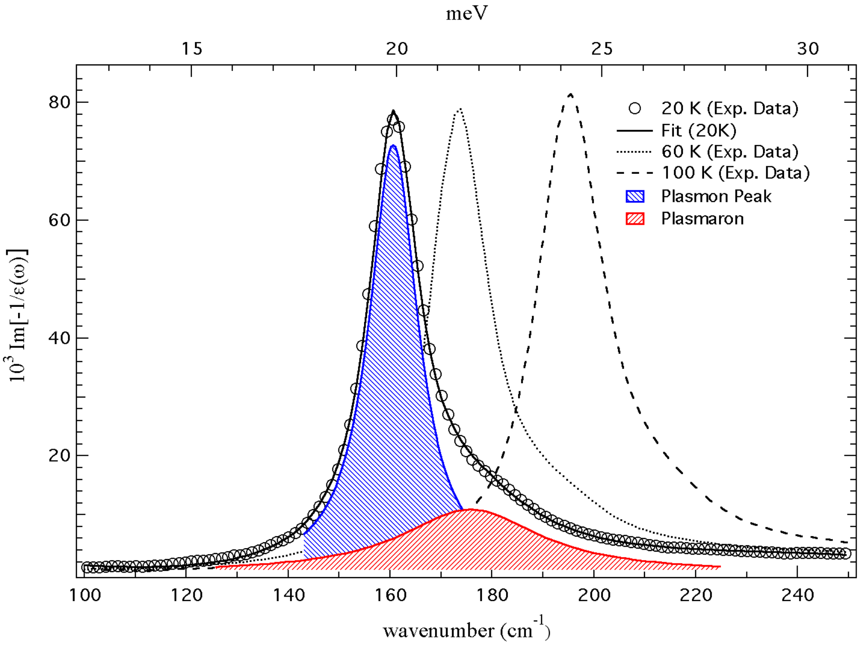

Figure 5.15: Low temperature EEL spectra - The comparison of the loss spectra for $T = 100$, 60 and 20 K shows the evolution of the prepeak with respect the plasmon peak. The loss function can be fit with two Lorentzian curves: the higher one centered at the screened plasma frequency ω_p^* while the lower one, fitting the high frequency shoulder, corresponds to the *prepeak* anomaly responsible of the increase of the scattering rate at ω_τ in Fig. 5.12.

prepeak's position, as clearly shown Fig. 5.13, it opens a certain number of scenarios that may indicate an electron-plasmon coupling effect.

Previously, an explanation for the appearance of the MIR absorption has been given in terms of an impurity-mediated electron-plasmon coupling [68, 69, 70, 71]. It was proposed that enhanced electron-charged impurity scattering is found near ω_p^* due to the divergence of $1/\varepsilon$. Although our data are in qualitative agreement with such scenario, the model used by Gerlach *et al.* [69] has a quantitative agreement only by considering an exceptionally large charged impurity concentration ($N = 1.5 \times 10^{19}$ cm^{-3}). This is approximatively two orders of magnitude greater than the carrier concentration itself and implies a *charged* impurity concentration of 1 part in 10^4, which we consider to be unrealistic considering the high purity of our samples.

We would like to emphasize here that simple RPA calculations which are often used for the description of the collective excitation spectra in electron gas may not be fully appropriate in this case. The reason rely on the fact that as the carrier density decreases the effect of electron-electron interactions, exchange and correlation start to become more and more important.

We thus propose that we are observing the excitation of plasmons via a decay channel of electron-hole pairs. The interaction should be similar to that considered in the context of electron-phonon [72] or electron-magnon scattering [73]. Such interaction has been theoretically anticipated. It may be captured within the same Holstein Hamiltonian that is used to treat the electron-longitudinal phonon coupling and describe polarons, and so this collective excitation has been called a *plasmaron* [74, 75]. Although the theoretical model is formally identical, a coupling process mediated by a longitudinal phonon mode has to be excluded since the temperature dependence of the secondary peak in way too large for a phonon. Such an excitation is only possible optically in a system where translational symmetry has been broken first. As anticipated the presence of charged impurities may satisfy such requirement but disorder and/or Umklapp scattering can equally well move oscillator strength to a frequency region near the plasmon energy. In normal metals, such an interaction is completely unobservable as the plasmon energy scales are many orders of magnitude higher than transport ones. In fact considering a simple RPA picture (Fig. 5.16), the excitation of a plasmon mode via an electron-hole decay channel happens for wavevector $\mathbf{q}$ satisfying

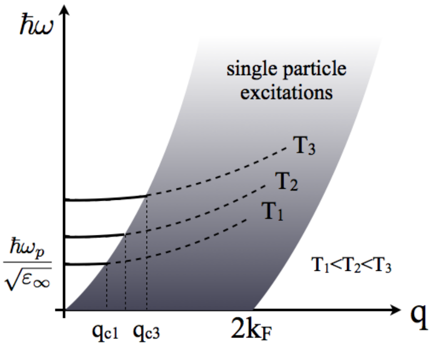

Figure 5.16: RPA model - Schematic diagram of the excitation of a 3D free electron gas.

$$\hbar\omega(q) = \frac{\hbar^2}{2m}(q^2 + 2qk_F), \tag{5.13}$$

while the plasmon dispersion relation is

$$\hbar\omega_p^*(q) \simeq \omega_p^* \left[1 + \frac{3}{10}\frac{v_F^2}{\omega_p^*}q^2\right]. \tag{5.14}$$

Equating the previous expressions and solving for q allows to find the value of the critical wavevector q_c which defines the limit between the region where plasma oscillations are well defined ($q < q_c$) from the region where plasma oscillations are damped due to single-particle excitations. It can be easily demonstrated that for $q \to 0$, $q_c \to \omega_p^*/v_F$, which means that in the case of a low density material like bismuth, the momentum transfer needed to couple electrons with plasmon is extremely small compared with the one needed in standard metals.

As a further confirmation for this latter statement we present in Fig. 5.17 the temperature dependence of the main plasmon peak and the one of the plasmaron peak. The graph shows that even though at high temperatures the estimation of the real width of the plasmaron peak is not trivial due to the broadening of the main plasmon peak, it is clear that the former is actually present at high temperatures. A quantitative estimation of the relative weight of the two peaks observed in the loss function can be extracted using a specific sum rule derived by applying KK relations to the longitudinal dielectric function of the material [76]. This sum rule gives

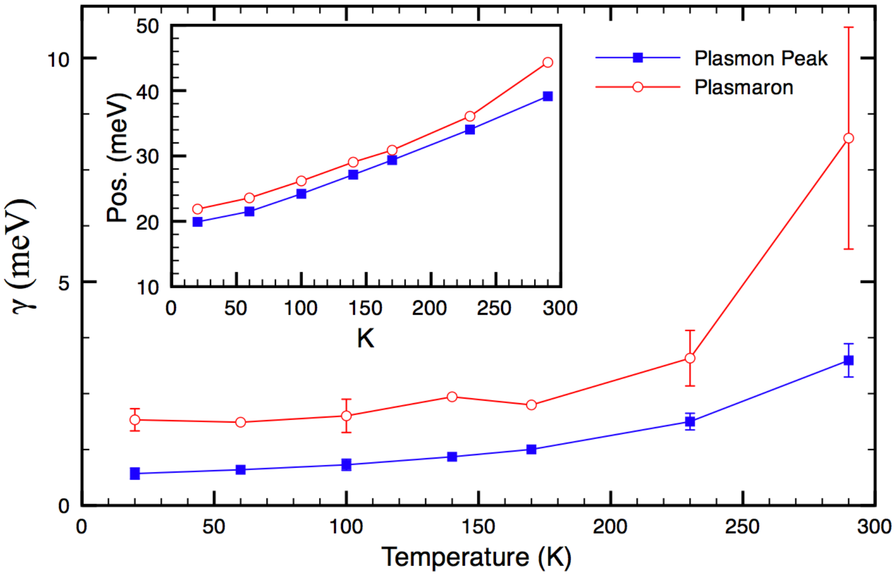

Figure 5.17: γ **vs.** T - Main figure: the temperature dependence of the plasmon and plasmaron width. Inset: the position of the two peaks is strongly correlated suggesting a strong interplay between the collective electron mode and the free carriers in the conduction band.

$$-\int_0^\infty \omega \mathrm{Im}\left[\frac{1}{\hat{\varepsilon}(\omega)}\right] \mathrm{d}\omega = \frac{\pi}{2}\omega_p^2 \propto \frac{N}{m^*}. \tag{5.15}$$

The temperature dependence of the individual spectral weight, shown in Fig. 5.18, demonstrates that on the high temperatures side the main contribution to the total weight is mostly due to the main plasmon peak while at low temperatures, where the thermal excitation processes from the valence band into the conduction band are drastically reduced, the weight of the two peaks becomes comparable and the effect more evident also in the bare reflectivity curves. This result integrates with the analysis previously done on the transfer of optical spectral weight: there we observed a massive SW transfer from the Drude peak to higher frequencies, while here we can observe that the transferred weight partially goes into valence band oscillators and partially remains coupled with the main plasmonic mode. The loss of carrier density leads to a weakening of the electron-plasmon coupling but thanks to the exceptionally low carrier density and to the very large ε_∞ of Bi this effect seems to be enhanced.

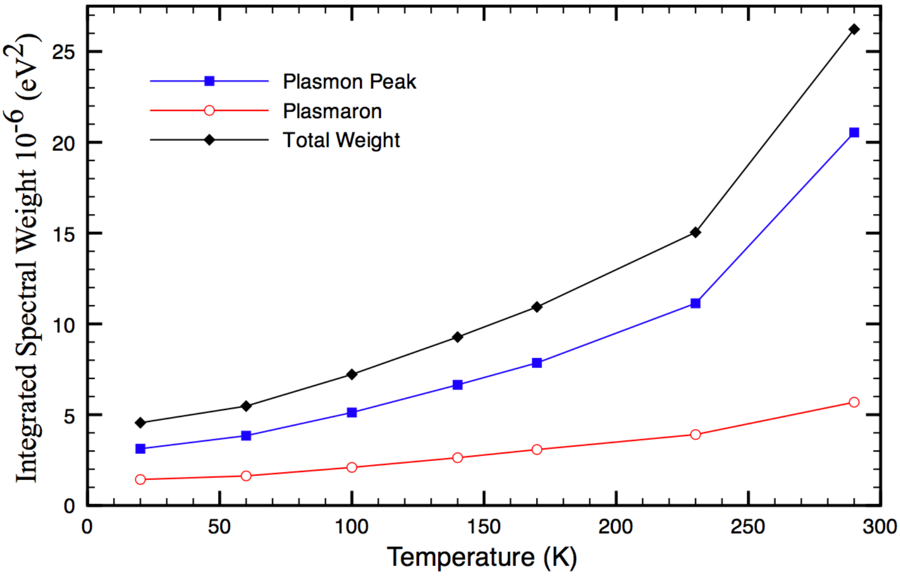

Figure 5.18: Plasmon and plasmaron spectral weight - The use of the sum rule in Eq. 5.15 allows to determine the relative spectral weight of the plasmon and plasmaron mode. Even thought at high temperature the total SW is dominated by the plasmon mode, at low temperature due to the unique properties of bismuth, the two contribution become comparable and the electron-plasmon absorption peak becomes more evident in the spectra.

Within the electron-hole plasmon decay channel scenario, one might try to model the scattering rate presented in Fig. 5.12 using an expression for the plasmon density of states $D(\omega)$ and a simple scheme for coupling of the spectrum to electronic excitations [72, 73]. Unfortunately, in the present case, such a calculation is hard to compare with the data exactly, due to the onset of interband contribution.

5.6 Discussion and Conclusions

Even though the optical study of the properties of pure bismuth was mainly intended to serve as an ambient pressure preliminary measurement for the subsequent pressure studies, we found a lot of exciting and yet new physics in this apparently simple system.

We have reported here a detailed analysis showing a clear optical signature of conduction electrons and holes coupled to plasmons, i.e. *plasmarons*. The anomaly observed in our optical investigations indicates a substantial departure from the conventional theory of metals. The possibility of this kind of purely electronic interaction has long been predicted [74, 75, 77] but it has never been experimentally observed in clean systems where the role of charged impurity is negligible. It has been demonstrated that the impact of electron-plasmon interaction on the transport properties of various low carrier density materials may be significative because it can influence the mobility of the free carriers [78]. The mathematical approach to the problem is substantially identical to the formalism based on the Holstein Hamiltonian which describes electronic polarons. The interaction term of the hamiltonian reads as

$$H_{\text{int}} = \sum_q \gamma_{\text{pl}}(q) a_k^\dagger a_{k-q} \left(b_{-q}^\dagger + b_q \right), \tag{5.16}$$

where $a_i^\dagger$ and a_i are the creation and annihilation operators for the electrons and $b_i^\dagger$ and b_i those for the plasmon. The coupling constant is represented by $\gamma_{\text{pl}}(q)$ which depends from the dielectric constant of the material.

The main difference in the present case is the fact that in the case of polaron the coupling term in the hamiltonian describe an electron-phonon interaction. Here the role of phonons is substituted with the one of plasmons and the resulting excitation is then constituted by an electron (or hole) dressed by a plasmon. However, the consequences of such a coupling can lead to the renormalization of the electron mass and its energy similar to the case of polarons in ionic crystals. In fact depending on the strength of the coupling and the electron density, the ground state of the system is characterized by a bound state constituted by an electron-plasmon excitation.

The key point for the detection of the electron-plasmon coupling effect seems to rely on the extremely low carrier density characterizing bismuth and probably similar semimetal systems. In these compounds in fact there is the unique opportunity to have a very small plasma frequency combined with small values of the scattering rate. In typical metals the effect is masked by the large value of ω_p and remains practically unobservable in the optical spectra. In this respect due to the fact that the study of low-dimenasional-low-density compounds like graphene [79], carbon nanotubes [80], semiconducting heterostructures and 2D layered materials [81] is becoming more and more popular also for possible applications in the field of quantum-electronics, this phenomena has to be taken into account.

It has been recently confirmed that electron-plasmon coupling plays an unusually strong role in renormalizing the bands in situations where the band structure is modified in order to approach a configuration similar to the one found in Dirac’s systems where the mass is renormalized in a way analogous to electron-boson coupling process commonly found in ordinary metals [82].

This conclusion increases even more the interest in pressure experiments since a further reduction of electron density by mean of the application of hydrostatic pressure may enhance the interactions and drive the system into an anomalous metallic state. Indeed the ambient pressure results show that electron-electron, electron-plasmon and electron-phonon coupling must be considered on an equal footing in attempts to understand the dynamics of quasiparticles in low-density electron systems.

Chapter 6

FIR spectroscopy on bismuth at low temperature and high pressure

> *This is Ground Control to Major Tom*
> *You've really made the grade*
> *And the papers want to know whose*
> *shirts you wear.*
>
> David Bowie - Space Oddity

As anticipated in the previous chapter bismuth shows a strong pressure dependence of its electronic properties due to the possibility of modifying the relative positions of conduction and valence bands close to the Fermi energy. In fact the semimetallic character of this compound which is ultimately determined by the small deviation of the unit cell from a perfectly cubic symmetry, can be strongly affected by pressure induced crystal deformations. It has been experimentally demonstrated that pressure reduces the deviation from the cubic symmetry making the L-point energy band more similar to those at the T-point [83]. In this way the band overlap which makes bismuth a perfectly compensated semimetal could be reduced gradually driving the system through a semimetal-semiconductor transition.

The possibility of this transition has been verified by combining pressure apparatuses and cryogenic setups with transport techniques [84]. It as been experimentally demonstrated that while at ambient pressure the temperature dependence of the resistivity shows a typical metallic behavior characterized by $\mathrm{d}\rho/\mathrm{d}T > 0$, at higher pressures the resistivity shows a metallic behavior at high temperatures followed by an insulating-like behavior with $\mathrm{d}\rho/\mathrm{d}T < 0$ below a certain characteristic temperature T_c. In Fig. 6.1 it can be seen that for increasing temperatures the position of T_c tends to move toward values close to room temperature eventually suppressing the characteristic metallic behavior. A complete metal-insulator transition was proposed for pressure around 25 kbar [4].

Despite of the large literature available on bismuth, the origin of the mentioned semimetal-semiconductor (SMSC) transition has been underinvestigated and the effect has been attributed to simple band structure modifications or thermal effects deriving

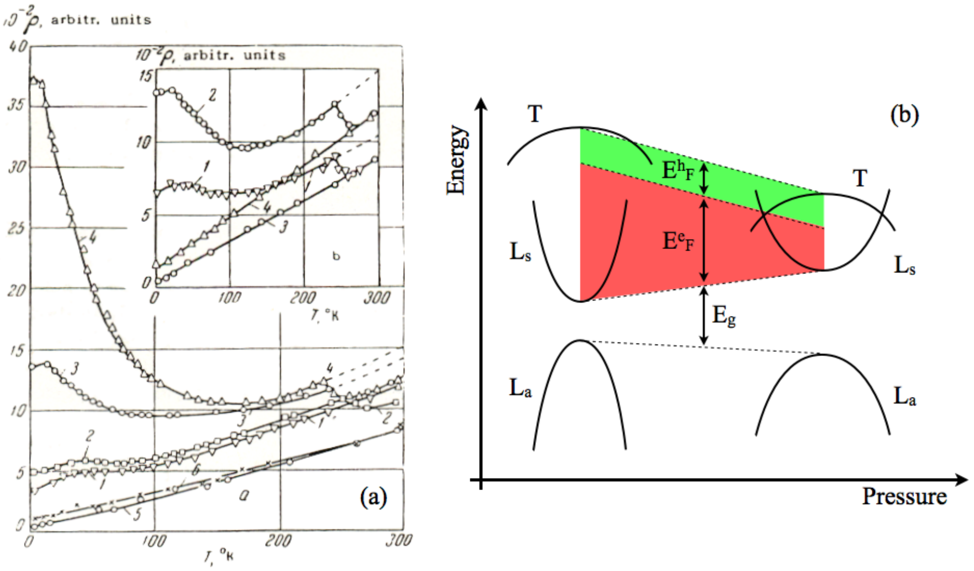

Figure 6.1: Pressure Effects - (a) The pressure and temperature dependence of dc resistivity $\rho(P, T)$ as reported by Balla *et al.* [84]. Curves 1 and 4 in the main graph correspond to the same sample measured at 8.6 and 20.6 kbar. Curves 2 refers to a second sample measured at 12.6 kbar and curve 3 to a third sample at 17.8 kbar. (b) The pressure dependence of the position of the main electron and hole bands and their corresponding Fermi energies.

from the small energy gap separating the electron's conduction and valence bands at the L-point.

One possibility that, we believe has not been taken in proper consideration, is the effect of strong correlations between electrons and hole. In fact by reducing the overlap between electron and hole bands by applying external pressure, it is possible to induce a strong reduction in the effective number of carriers. In particular for a 3D system it is well known that the electron's kinetic energy $E_K \propto n^{2/3}$ while the potential energy $E_P \propto n^{1/3}$ thus giving a ratio $E_P/E_K \propto n^{-1/3}$ which at low densities would lead to a strong localization effect due to the enhanced electron-electron interaction and possibly determining an insulating behavior. If the carrier density could be tuned to sufficiently low values the electron's system is expected to solidify in a Wigner crystal while for a wide range of concentrations, before the Wigner crystal phase, the electron system exists as a strongly interacting liquid [85]. In semimetallic systems like bismuth where electrons and holes are both simultaneously present at $T = 0$, it has been proposed that for sufficiently small concentrations, the Coulomb interaction between positive and negative charged carriers becomes less screened favoring the formation of bound states also known as *excitons* [86, 87, 88]. The spontaneous formation of excitons (nonconducting quasi-particles) would automatically lead to an insulating excitonic condensate. Even if the possibility of such excitonic insulating phase has been theoretically excluded for pure bismuth at ambient pressure, it has been proposed as a possible explanation for the magnetic field-induced SMSC transition observed in transport measurements on the same compound [89, 51]. However the exitonic insulator scenario is theoretically expected to occur in bismuth in absence of magnetic field but in a very limited pressure and temperature range (critical temperature $T_{EI} = 0.05^\circ$ K and $\Delta P \simeq 2 \times 10^{-3}$ kbar).

Recently a lot of attention has been given to the close similarities between the bismuth system and graphite. In particular bismuth has been shown to have tight connections with the low-dimensional graphite-based compound, *graphene*. The two materials in fact are both known to be narrow-gap Dirac electron systems. In this regard it has been experimentally [5] and theoretically [90, 91] demonstrated that in Dirac's systems when electron densities are very small and the relevant energy scales for interband transitions, collective modes and Fermi energy are similar to each other, a favorable conditions for strong interactions between quasi-particles and plasmons exists and a strongly coupled hybrid excitation known as a *plasmaron* can form.

In the present chapter we will describe our experimental activity based on the custom-made setup widely described in the first chapters of this thesis work. The proposed measurements will be mostly aimed to elucidate the behavior of the bismuth's system while approaching the SMSC transition. The possibility of tuning the pressure, changing consequently the electron and hole densities and contemporarily recording a frequency dependent spectrum will allow us to determine the origin of the SMSC transition beyond simple dc measurements. In particular every frequency dependent feature reminiscent of a strong coupling effect will be analyzed in terms of Drude-Lorentz parameter in a similar fashion with respect to the one presented in the previous chapter.

6.1 Experimental details

A single crystal bismuth sample was carefully cleaved at liquid nitrogen temperature from a ingot obtained using a modified Bridgman-Stockbarger technique as described in Chapter 5. The sample was then cut in an appropriate shape and size in order to be mounted on the inner face of a wedged diamond window which constituted the optical access of the pressure cell as described in great detail in Chapter 3. The self-clamping type pressure cell was closed and mounted in a custom made optical cryostat adapted to our Bruker 66 ifs spectrometer in such a way that a quasi-normal incidence geometry for the incident beam was guaranteed. The reflected signal from the sample-diamond interface was then recorded at different pressures while slowly cooling down the cryostat with liquid helium. In the temperature range from 300 K down to 25-50 K we recorded spectra in the FIR spectral region with a resolution of 5 K. In the FIR spectral region a LiHe cooled bolometer detector was used to record data from 50 cm^{-1} to 650 cm^{-1} with a resolution of 2 cm^{-1} . Because the absolute value of the reflectivity function for bismuth in this frequency range is quite small, a long signal integration period was chosen in order to increase the signal to noise ratio. With this combination of experimental parameters we managed to record the temperature dependence of the sample reflection with relative ease.

It is worth reminding here that our measurement technique is based on a differential method for the extraction of the absolute value of the reflectivity as extensively described in Chapter 4. According to this method, we took at every pressure step a reference spectra at room temperature T_0 which allowed us to calculate the absolute value of the reflectivity function $R(T_0, P_i)$ of the sample. This latter quantity was then combined with the temperature dependent data at pressure P_i in order to extract the absolute value of the pressure and temperature dependent reflectivity defined as

$$R(T, P_i) = R_0(T_0, P_i) \left[\Pi(T, T_0) + 1\right], \tag{6.1}$$

where $\Pi(T, T_0)$ is the percent change of the signal recorded within the cryostat with respect to the signal at the reference temperature T_0 (for more details on the method refer to Chapter 4).

As mentioned before there are two possible strategies for the choice of the reference spectra $R_0(T_0, P_i)$; in reference to Fig. 4.4 the first one consists in using the pure raw data while the second one consists in using a Drude-Lorentz (DL) fit to the raw data. Clearly the two methods present advantages and disadvantages; the main advantage in using raw data is due to the possibility of having a reference which could automatically deviate from a simple DL model; on the other end the disadvantage is connected to the features eventually present in the reference spectra which are not physical (mostly due to the small instability in the experimental setup) which will be propagated, according to Eq. 6.1 in all the spectra with the risk of masking small details which originate in important physical changes taking place in the sample. While keeping in mind the possible importance of subtle features like the plasmaron peak and considering the good agreement found for the ambient pressure and room temperature case with a DL model, we decided to adopt the second method for the analysis.

We measured the reflected IR signal at three different pressures: 6.5, 12 and 20.5 kbar. Unfortunately due to technical limitation of the pressure apparatus it was not possible to record spectra for pressure higher then 25 kbar which has been demonstrated to be the critical pressure for the SMSC transition.

In Fig. 6.2 a comprehensive summary of the raw reflectivity data measured at the sample-diamond interface is presented for selected temperatures and compared to ambient pressure data (Fig. 6.2(a)). This latter data set has been obtained using the data extracted using classical spectroscopic techniques and later using the calculated complex dielectric function to derive the reflection coefficient for a bismuth-diamond interface according to Eq. 4.11 and assuming $n_d = 2.418$.

From a first inspection of the reflectivity data the reader may appreciate the pressure induced shift of the screened plasma frequency ω_p^* roughly defined as the minimum of $R(\omega)$. Considering in fact curves at the same temperature, it can be seen that the position of the cited minimum tends to move toward lower frequencies indicating a possible pressure induced reduction of carrier density. The temperature dependence of the $R_{sd}(\omega)$ seems to follow a trend similar to the one observed at ambient pressure. However we noticed some important and surprising differences between the data at high pressure with respect to those taken at $P = 1$ bar: the big and unexpected surprise was determined by the appearance of a peak immediately above ω_p^*. In Fig. 6.2(a) it can be seen that such a feature is present, indeed barely visible, around 23 meV for the lowest temperature cases (25-50 K). In the high pressure regime, the peak clearly appears at higher temperatures compared to the ambient pressure case and its spectral importance seems to be strongly enhanced, determining a drastic change of the reflectivity curves in the region of ω_p^*. The possibility to observe such a subtle feature was honestly beyond our expectations considering the experimental complexity of the mea-

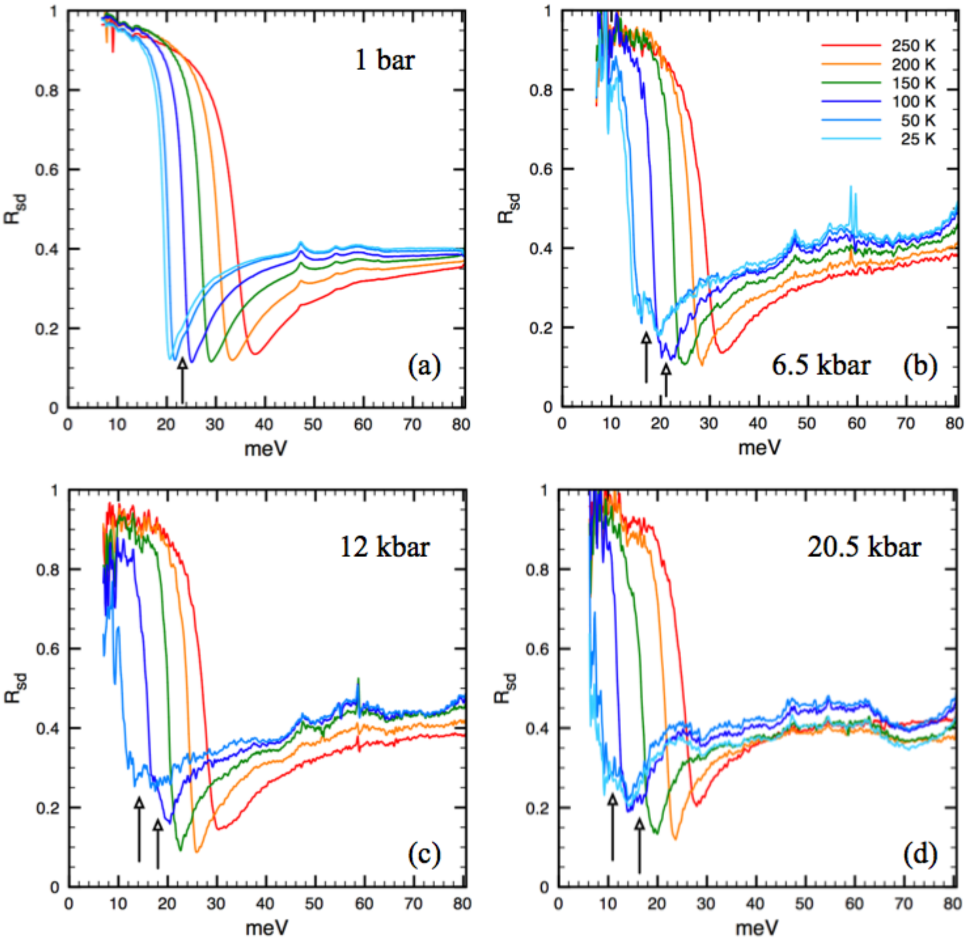

Figure 6.2: Reflectivity vs. (P,T) - From (a) to (c) the raw reflectivity data for pressure $P = 1 \times 10^{-3}$, 6.5, 12 and 20.5 kbar respectively. The data are presented for selected temperatures, namely 250, 200, 150, 100, 50 and 15 K (warmer colors refer to higher temperatures). The arrows in the graphs show the positions where a plasmaron peak appears. All the the data refer to a sample-diamond reflection coefficient. The small absorption feature present in all spectra at around 47 meV it is caused by a beam-splitter absorption. However its presence does not influence on the scientific conclusions of this work.

surement and the very low signal level emerging from the pressure cell. Another interesting feature that can be appreciated from Fig. 6.2 is the fact that the slope of the $R(\omega)$ curves at the screened plasma frequency does not seem to monotonically increase as the temperature is lowered; for the 6.5 kbar case for example, it can be seen that a clear reduction of the value of the slope occurs for temperature $T < 100$ K. This aspect will be discussed in detail later in this chapter but since $|\mathrm{d}R(\omega)/\mathrm{d}\omega|_{\omega\simeq\omega_p^*} \propto \tau(\omega \to 0)$, a reduction of the slope may indicate an increase of the scattering processes.

6.2 Pressure induced carrier density suppression

We analyzed the reconstructed absolute reflectivities using the well known RefFIT program [16]. Since the MIR and visible range were not measured for the considered pressures, we used the ambient pressure-room temperature ellipsometric data in the energy range between 0.8 and 4.4 eV in order to constrain the fit to physically consistent parameter. This choice is justified by the fact that the important physical parameters and energy scales like the Fermi energy E_F, the gap energy E_g, the screened plasma frequency ω_p^* and the scattering rate τ^{-1} determining the low energy physics of this material, all lie in the measured spectral range.

The fitting procedure of the experimental data was initially performed using a simple Drude-Lorentz model and subsequently refined using a Kramers-Kronig consistent variational procedure.

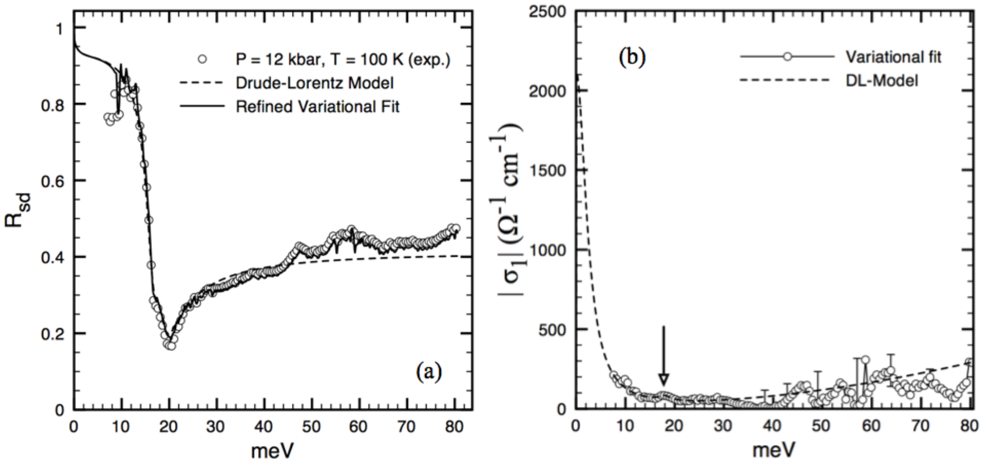

Figure 6.3: Variational data fitting - (a) the raw reflectivity spectrum of bismuth at 12 kbar of pressure and $T = 100$ K (open circles) is compared with a simple DL model (dashed line) and with the subsequent refined fit based on a KK consistent variational approach. (b) The optical conductivity extracted from the fitting procedure (open circles) and the starting DL model. The error bars in the region 35-65 meV account for the unphysical effect of beam splitter absorptions visible in the reflectivity curves. In both cases the density of the experimental points have been reduced to improve the readability of the graphs.

In Fig. 6.3 the main fitting steps together with the resulting reflectivity and conductivity are shown for data taken at $P = 12$ kbar and $T = 100$ K. The procedure allows one to reproduce, obeying causality requirements, every spectral detail present in the original reflectivity curve thus including the anomalous peak present around 18 meV. It is worth saying that the spectral features present around 48 and 58 meV are not physical but are just artifacts originating from uncompensated absorptions in the spectrometer's beam splitter. These very same features are also visible in the bare ambient pressure data shown in Fig. 6.2(a) and, as explained elsewhere [5], they don't influence in any way the analysis and the scientific conclusions of this work.

Using the complex dielectric function $\hat{\varepsilon}(\omega, P, T)$ extracted from the experimental data we were able to track the temperature and pressure behavior of the screened plasma frequency defined as $Re[\hat{\varepsilon}(\omega_p^*, P, T)] = 0$. The result of this analysis is shown in Fig. 6.4 together with the ambient pressure data. The temperature dependence of this quantity seems to follow the same trend observed for the ambient pressure case. The remarkable aspect is the vertical shift toward lower energies of the whole curves when the pressure is varied. Since ω_p^* is proportional to the bandwidth of the conduction band we deduce that pressure drastically changes the free electron's bandwidth via a reduction of the density n or an increase of effective mass m^*. On the other hand the DL analysis showed that ω_p^* is almost independent from the contribution of interband transitions; in fact the dielectric constant ε_∞ remains fairly unchanged over the considered pressure range at a value $\varepsilon_\infty \simeq 113 \pm 3$ at room temperature.

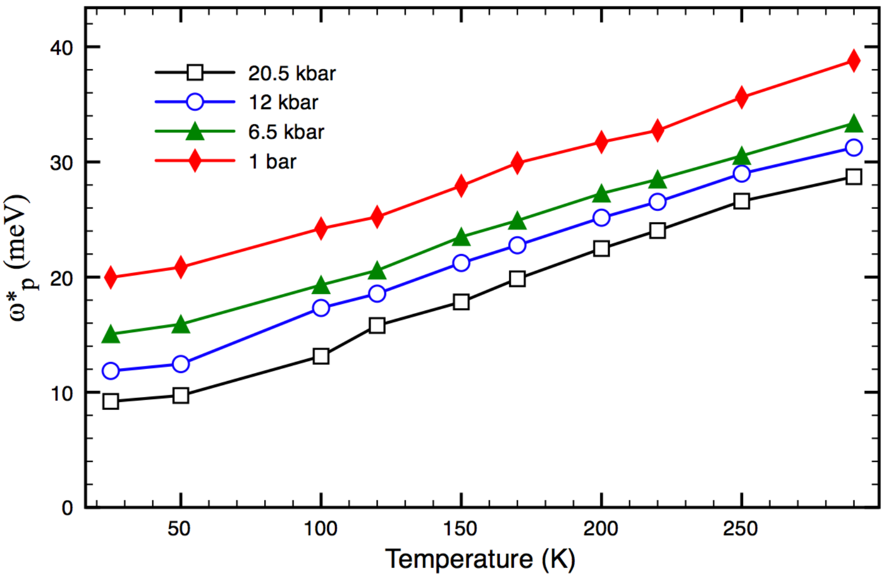

Figure 6.4: Screned plasma frequency - The temperature dependence of ω_p^* follows a common behavior at different pressures. The vertical shift induced by pressure changes, indicates a progressive reduction of the electron bandwidth. This suggests a pressure induced reduction of carrier density or/and a change in the carrier's effective mass

A better understanding of the effect of pressure on the carrier density can be extracted from the bare plasma frequency since $\omega_p^2 \propto n/m^*$. The phase diagram shown in Fig. 6.5 demonstrates how at every temperature the applied pressure can reduce the n/m^* ratio by more then a factor of 5. As reported by Balla [84], the pressure dependence of the bare carrier density at “zero”-temperature should follow a characteristic power low given by:

$$n(P) = n_0 \left(1 - \frac{P}{P_c}\right)^{\frac{3}{2}} \tag{6.2}$$

where n_0 is the carrier density at $P = 1$ bar and P_c is the critical pressure for the SMSC transition. A similar fit done on the low temperature data presented in Fig. 6.5 gives a value for the exponent $\alpha \sim 5/2$. This disagreement is probably due to the change of effective mass with pressure. Though it is not clear from Ref. [84] how the pressure dependence of the effective mass (in the cited paper they make a strong assumption considering the mobility as a constant over the entire temperature range) could be extracted from standard transport experiments, other experimental works confirm a mild reduction of this quantity in the considered pressure range [83]. The shaded blue region in Fig. 6.5 is proportional to the band overlap (bandwidth) between the electron and hole pockets and it should mirror the metallic ground state in bismuth.

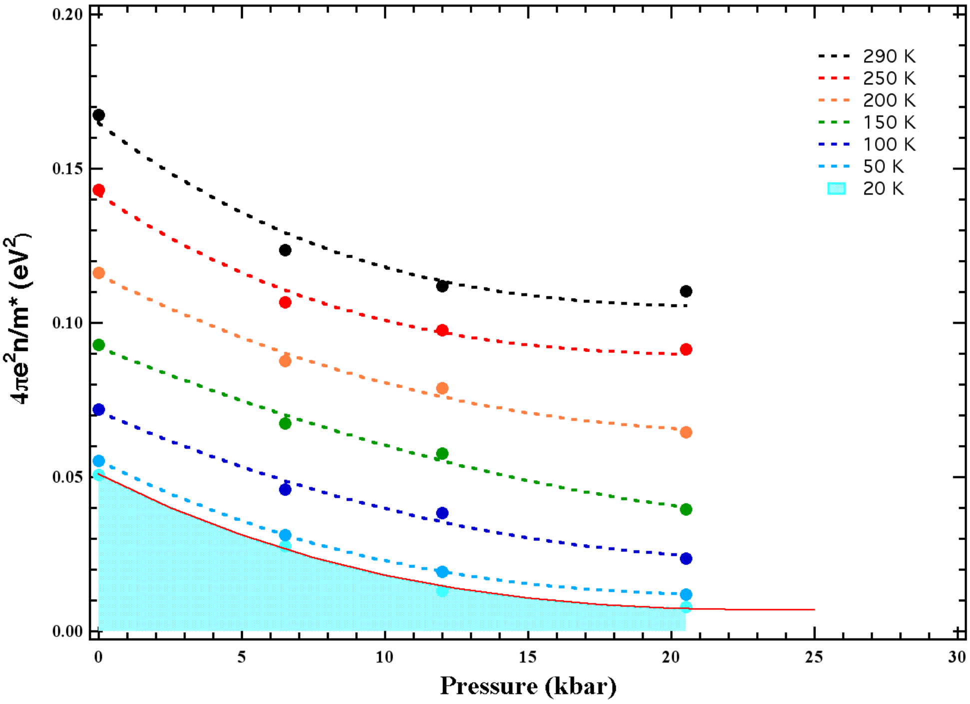

Figure 6.5: Pressure induced carrier density suppression - The pressure dependence of the n/m^* ratio at different temperatures. The effect of pressure on the electron system is mainly due to the reduction of the overlap between electron and hole pockets. At high temperature the pressure effect by itself is not enough to dramatically reduce the electron density while the combined effect of temperature and pressure can reduce n/m^* by more then one order of magnitude. The width of the shaded blue region is proportional to the cross-section of the electron and hole pockets and shows a clear tendency to disappear around $P_c \sim 25$ kbar.

Unfortunately since the experimental setup did not allow further investigations below $T = 20$ K and for pressure higher then 20.5 kbar we could not precisely describe the (P, T) region where the Fermi energies cross-sections approach zero.

6.3 DC resistivity and anomalous scattering processes

As we already did for the ambient pressure case, we tried to compare the DC resistivity data measured using transport techniques with the optical resistivity calculated extrapolating the frequency dependent optical conductivity for $\omega \rightarrow 0$. The dc value extracted from optics (Fig. 6.6) agrees very well with previously published data. Quite surprisingly the pressure and temperature dependence of $\rho_{\text{opt}}(P, T)$ reproduces most of the features presented in Fig. 6.1(a). In particular it reproduces the pressure effect on the characteristic temperature T_c which separates the metallic regime ($\mathrm{d}\rho/\mathrm{d}T > 0$) from the one indicating the tendency toward an insulating behavior. In fact T_c tends to move toward higher temperature values for increasing pressure.

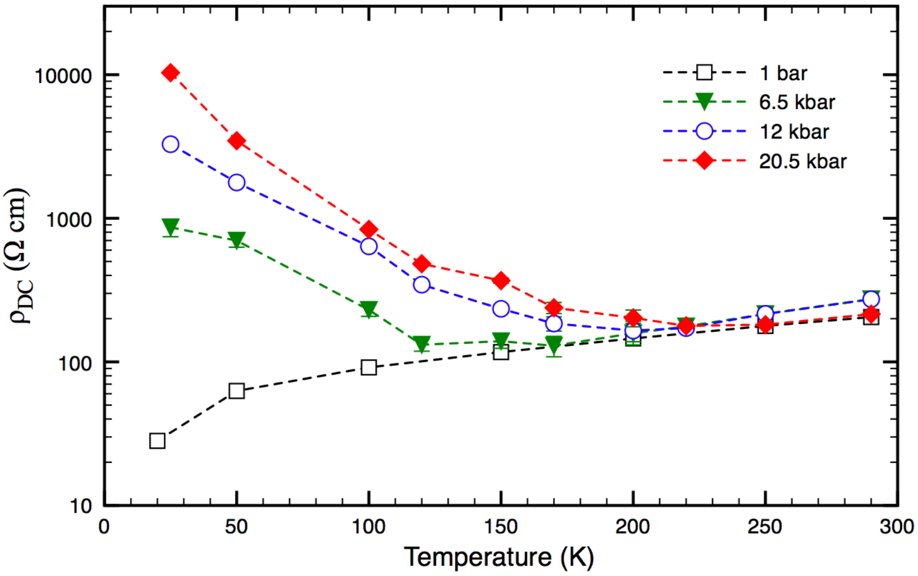

Figure 6.6: "Optical" resistivity - The extrapolated $\sigma_{\text{opt}}^{-1}(\omega \rightarrow 0)$ shows a very good qualitative agreement with transport data presented in Fig. 6.1(a). The optical data correctly reproduces the pressure dependent insulating behavior characterized by two temperature regimes: an high temperature metallic regime and an insulating-like regime below T_c. The critical temperature separating the two regimes tends to move toward higher values for increasing pressures. It should be noted that for the considered pressure the resistivity stays finite at low temperatures without actually diverging as expected in an insulating material. Our observations only show a clear tendency toward an insulating behavior.

Once verified the good agreement with transport data, we tried, thanks to optics, to go beyond this simple analysis and to decompose $\rho_{\text{opt}}(P,T)$ in terms of n/m^* ratio and scattering rate $1/\tau(P,T)$. It would be in fact very interesting to understand what is the origin of the saturation of the resistivity at low temperatures and the mechanism that determines the position of T_c. Moreover, as we demonstrated in Chapter 5, at low temperature the spectral contribution of the plasmaron mode becomes more and more important suggesting a possible further enhancement of this kind of interaction for reduced carrier densities.

A "dissected view" of the dc resistivity can be appreciated in Fig. 6.7 where it is decomposed into its density and mass dependent part (a) and into its scattering dependent part (b). Since the $\omega_p^*(\omega,P,T)$ presented in Fig. 6.4 was a decreasing monotonic function of temperature, the behavior of the carrier density contribution to resistivity presented in Fig. 6.7(a) is not surprising. What is quite remarkable instead, is the behavior of the scattering rate: at ambient pressure the scattering processes exhibit the expected metallic behavior that combined with a relatively weakly temperature dependent n/m^* gives the typical metallic resistivity of Bismuth. On the other hand, already at moderate pressure the scattering rate seems to deviate heavily from the behavior expected for a typical electron-phonon scattering mechanism for $T \gg \theta_D$ (Debye temperature). In fact, while at high temperatures there is always a clear reduction of scattering processes, very similar to the ambient pressure case, at low temperatures there is a sharp upturn at a temperature that we previously defined as T_c.

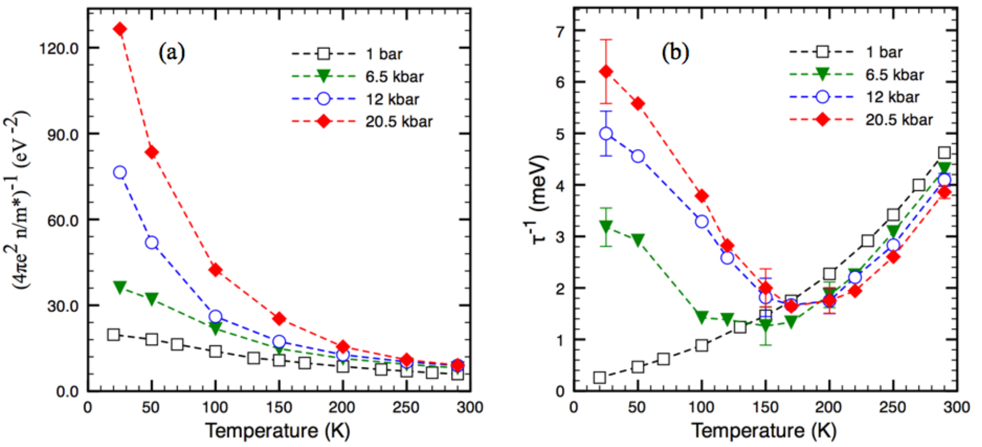

Figure 6.7: The dissected dc resistivity - The graphs show the two main contributions to the dc resistivity presented in Fig. 6.6. The left panel (a) shows the quantity $4\pi e^2 n/m^*$ which takes into account the change of carrier density and the electron's effective mass. The right panel (b) shows the contribution to ρ_{dc} due to the scattering rate τ^{-1}. This quantity shows the same saturating behavior at low temperature in agreement with the dc transport data.

This case is conceptually different from the one of typical semiconductors; there in fact the observed reduction of resistivity at low temperatures, followed by a regime where $\rho \propto T$ is originated by thermally excited carrier across the energy gap. This kind of mechanism would be then more effective in the density dependent part of the resistivity rather then in the scattering part. Here the effects of the two contributions are clearly reversed and the density part does not show any particular temperature dependent feature which could justify a semiconducting scenario.

It should also be noticed that since in bismuth both electrons and holes are simultaneously available for conduction, there could be a strong contribution to the scattering given by the interaction between the two types of carriers [92]. In the case of semimetals in fact, e-h scattering processes do conserve momentum but not necessarily the current. In particular in self-compensated systems like in bismuth, the role of e-h scattering is to reduce the relative velocities of electrons and holes to zero [93, 94]. Below the Debye temperature where the phonon contribution to the resistance can be neglected, e-h scattering give rise to a T^2 temperature dependence. In the extrapolated $\tau^{-1}(T)$ data, this behavior is reasonably reproduced for the ambient pressure case but a clear deviation is observed at higher pressure.

The analysis of the dc resistivity in terms of these two contributions allows one to derive two important, but partial conclusions: first it is evident that the characteristic upturn in the resistivity is the result of a delicate balance between scattering and density, in particular, in the temperature region where m^*/n is more or less similar at different pressures ($T > 200$ K) it is the effect of the scattering that dominates producing characteristic metallic behavior. On the other hand at low temperatures the rapid increase of resistivity due to a pressure induced decrease in carrier density is enhanced by an equally and unexpected enhancement of the scattering. This latter quantity tends to saturate at low temperature partially explaining the plateau previously reported by Balla *et al.* [84]. Due to the reduction of carrier density the anomaly in the scattering rate could be itself an indication of a localization process. In this case we expect also an increase of the effective mass m^* of the carriers. However, even if the pressure and temperature dependence of $m*/n$, presented in Fig. 6.7(a), is compatible with an enhancement of the mass, it is not easy to understand up to which extent the observed upturn is related to a carrier density change and how much it is influenced by a change of the mass. Considering that the anomalous scattering behavior is observed for pressures quite far from P_c, we tend exclude a large mass renormalization. The scattering anomaly can be thought as a precursor effect of the SMSC transition. Further confirmations of this hypothesis will be presented in the next sections where a detailed analysis of the optical data will be done considering also the presence of the electron-plasmon interaction peak.

6.4 Pressure dependence of the electron-plasmon interaction

Even if not strictly essential for the explanation of the upturn of the dc resistivity at low temperatures, the scattering rate certainly plays a determinant role. In particular one question that remains unanswered at this point of our experimental activity on bismuth is on the evolution of the scattering at lower temperature and in particular for pressure closer to P_c. It seems in fact that the insulating behavior develops along two apparently separate channels. It would be interesting to understand if the decreased electron density could determine an increase of scattering. In the previous chapter we introduced the possibility of an interaction between free electrons and plasmons and we observed that such an effect was clearly enhanced at low temperatures where the electron density (E_F) was much smaller with respect to room temperature. As we

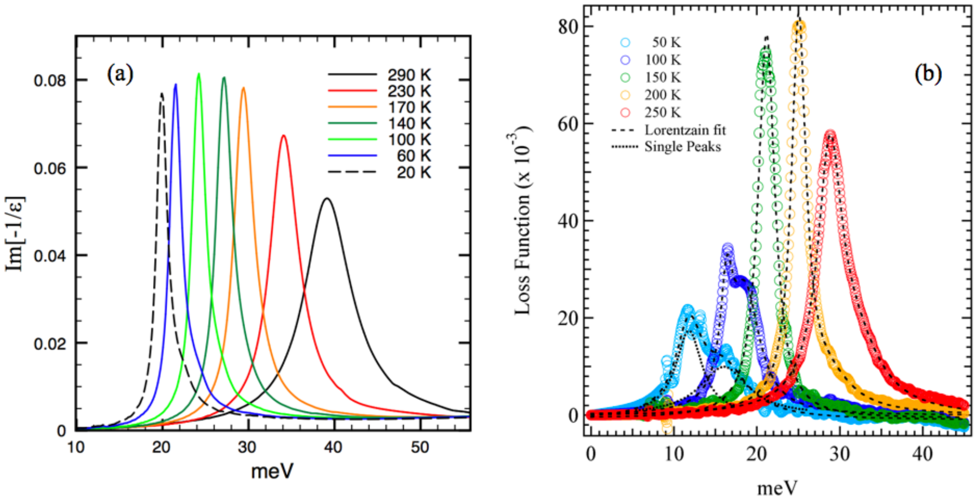

Figure 6.8: The effect of pressure on the plasmaron peak - (a) The ambient pressure loss function at different temperatures. The secondary peak appears only at low temperatures with a SW which is very small with respect to the one of the main plasmon peak. (b) The loss function at $P = 12$ kbar shows a much clearer plasmaron peak that is evident already at higher temperatures. At the lowest considered temperature the two peaks appear broadened and comparable in intensity.

previously pointed out bismuth represents a favorable system for the observation of this kind of phenomenon but clearly if the density could be tuned toward lower values the coupling effect between electron and plasmon could be drastically enhanced, eventually leading the system into a non-Drude regime.

Given the longitudinal character of the electron-plasmon coupling we analyzed the optical data in terms of the loss function $\mathrm{Im}[-1/\varepsilon(\hat{\omega}, q)]$ for $q = 0$. A comparison between the ambient pressure data and the data at $P = 12$ kbar is presented in Fig. 6.8. Even if qualitatively the temperature dependence of the main plasmon peak is comparable for the two pressure cases, it is clear that at low temperatures the presence of the secondary peak appearing on the high energy side of the main peak, is increasingly important. In the ambient pressure data in fact, the secondary peak appears more like a shoulder then a distinct peak; instead in the high pressure data, the two peaks appear clearly separated. Moreover the relative intensities seems to become increasingly similar for lower carrier densities.

The importance of density in this kind of interaction can be also appreciated noticing that the lowest temperature case for $P = 1$ bar (Fig. 6.8a) is quite similar to the loss spectrum at $T = 150$ K for $P = 12$ kbar, this means that at ambient pressure the temperature dynamic of the density is not large enough to bring the system in a strongly interacting electron-plasmon regime. On the contrary, since pressure reduces the ambient temperature carrier density, conditions similar to those found for $P = 1$ bar and $T = 20$ K can be obtained already at 150 K at 12 kbar thus allowing the observation of the dynamic of the two peaks in a density region where their interaction appears strongly enhanced.

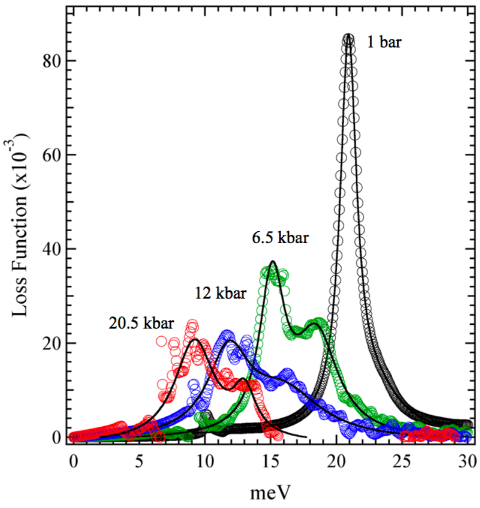

Figure 6.9: Loss function comparison - The pressure dependence of Im$[-1/\hat{\varepsilon}]$ for $T = 50$ K. The shift of the main peak toward lower frequencies is the clear manifestation of the reduction of carrier density. The secondary peak appears clearly separated from the plasmon peak at high pressure.

As a further proof we compared in Fig. 6.9 the low temperature energy loss spectra for selected pressures: at high pressure there is a strong reduction of the amplitude of the plasmon peak together with an increase of the scattering visible from the increase of the half-width-half-maximum of double peaked structure. The secondary peak, the *plasmaron*, appears distinctly separated from the main peak with respect to the ambient pressure case. On the other hand its amplitude does not seem to follow, as a function of pressure, the drastic reduction observed for the plasmon peak. At sufficiently high pressure the integrated peak intensity appears comparable for the two peaks and it is in this regime where the the strong increase of scattering is observed. This finding may indicate a strong interaction between the free electron-hole bath and the plasmonic collective mode in the low density regime.

In order to quantify this observation we decomposed the experimental loss function curves using a multi-oscillator fitting procedure based on lorentzian components. This analysis allowed to construct a parametric plot where the position of the two main peaks is plotted versus the screened plasma frequency ω_p^* defined as the zero-crossing frequency of the real part of the dielectric function. In Fig. 6.10 the temperature dependent positions are plotted for different pressures. It can be seen that the main peak, represented with open symbols, exactly tracks the temperature dependent ω_p^* (the dashed line describes the ideal case where just a pure Drude component is present in the loss function). On the contrary the secondary peak follows a different behavior; in the high temperature regime the secondary peak, visible in the loss spectra mostly as an asymmetry of the main peak, tends to approach the plasmon frequency while in the low temperature regime where it appears as a clear peak in the spectra, its distance tends to increase with respect to the main peak's position. It is worth to notice that for different pressures, the separation between the two peaks at low temperatures tends to saturate around $\sim$ 4-5 meV moreover, extrapolating the experimental data for higher pressures, it is possible to predict a situation where the energy of the plasmon mode is identical to the energy difference between the two peaks. This situation may lead to a possible resonance effect which could explain the observed increase of scattering.

Using the parameters extracted from the fit of the loss spectra, we calculated the

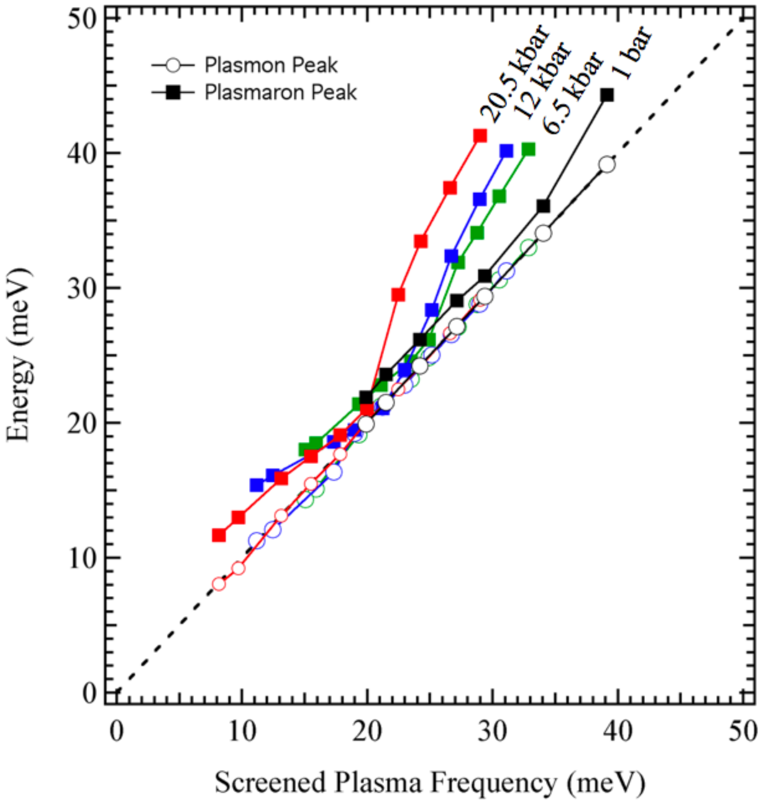

Figure 6.10: Peak splitting dynamics - The positions of the main plasmon peak and of the secondary peak are plotted versus the screened plasma frequency ω_p^* for $P = 1$bar, 6.5 kbar, 12 kbar and 20.5 kbar. The dynamics of the secondary peak is different in the high and low temperature regime. At low temperature the separation between the peaks tends to saturate to value around 4-5 meV.

spectral weight of each peak applying the following sum-rule:

$$-\int_0^\infty \omega \mathrm{Im}\left[\frac{1}{\hat{\varepsilon}(\omega)}\right] \mathrm{d}\omega = \frac{\pi}{2}\omega_p^2 \propto \frac{N}{m^*}. \tag{6.3}$$

We extracted the temperature and pressure evolution of the main plasmon peak and of the satellite, *plasmaron*, peak. The results of this analysis is presented in Fig. 6.11 together with the data relative to the ambient pressure case. As it can be seen, the data taken at high pressure deviate considerably from the ambient pressure results: in fact while in this latter case the plasmon peak dominates in terms of spectral weight in the entire temperature range except for the lowest temperature point where the two curves seem to approach each other, for increased pressures, the relative weight of the two peaks becomes comparable already for temperatures around 100-150 K. We notice that this temperature range corresponds to the region where the scattering rate tends to increase in a non-metallic fashion (Fig. 6.7). In the considered pressure range we did not observe a role exchange, in terms of total borne spectral weight, between the two peaks and within the experimental error it seems that the plasmon peak remains the dominant one in all the considered temperature and pressure range.

6.5 Discussion and conclusions

The experimental findings described in this chapter, in particular the strong increase of scattering associated with the strengthening of the plasmaron mode with pressure, are open to different interpretations. The strong pressure induced suppression of carrier density is an indication that suggests scenarios where strong interaction effects may dominate. Probably the most appealing scenario is related to the possibility of Wigner crystallization. In an electron gas this electronic crystalline phase can be achieved when the typical potential energy determined by Coulomb repulsion among free carriers becomes comparable with their kinetic energy. Up to now this crystalline phase has been predicted for low density 2D materials [85] like in semiconducting interfaces or in thin layers of liquid helium [95]. In the case of a 3D material the potential and kinetic energies of a free electron system are respectively

$$V(r_n) = \frac{1}{4\pi\epsilon_0\epsilon_\infty}\frac{e^2}{r_n} \tag{6.4}$$

$$K(n) = \frac{\hbar^2}{2m^*}(3\pi^2 n)^{2/3}, \tag{6.5}$$

where $r_n = (3/4\pi n)^{1/3}$ is the radius of the sphere that encloses one particle on the average, ϵ_∞ is the screening effect of the interband terms and m^* is the effective mass of the particle. The ratio between these two quantities, which finally sets the scale between the weak and strong localization regimes, gives

$$r_s = \frac{V(r_n)}{K(n)} = \frac{m^* e^2}{3\sqrt[3]{2}\pi^2\epsilon\epsilon_0\hbar^2} n^{-1/3}. \tag{6.6}$$

This equivalent distance, expressed in unit of Bohr radius r_0, is expected to give a Wigner crystal phase for values $r_s > 65$ [96, 97]. Clearly, the negative exponent characterizing the density, indicates the possibility of such crystalliation. Unfortunately,

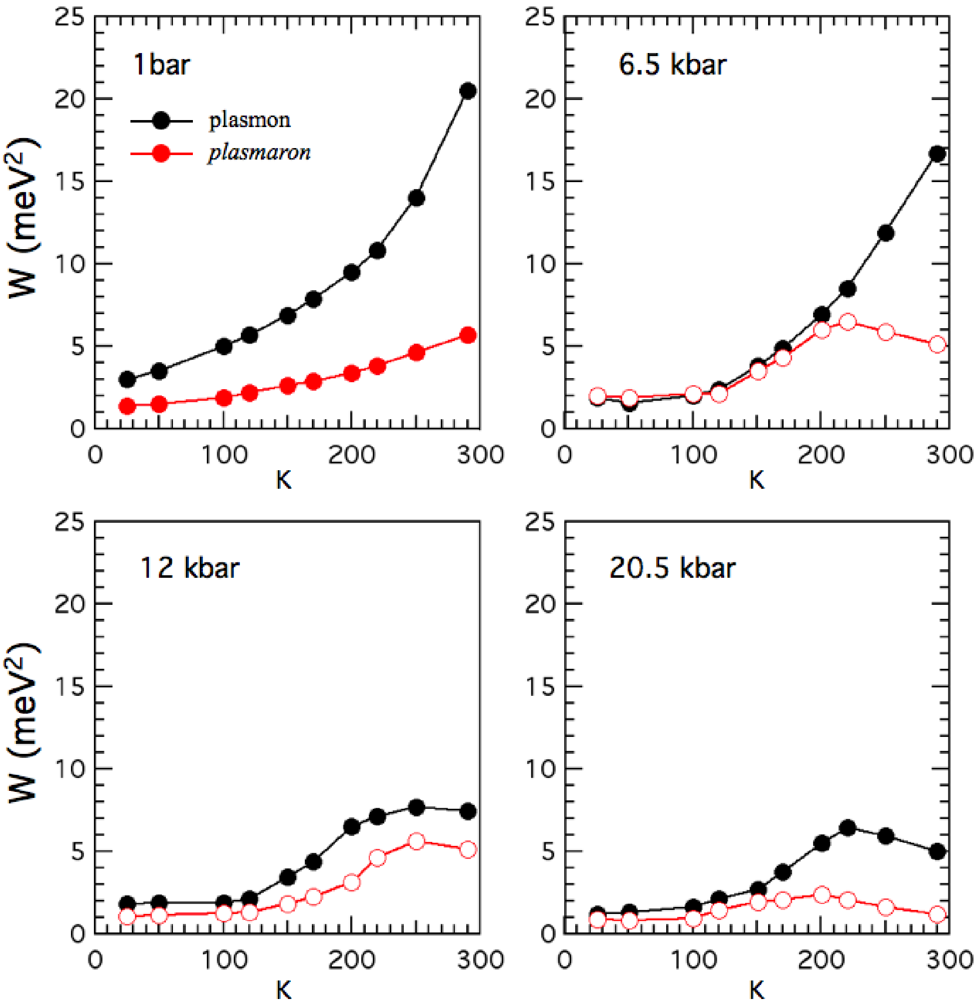

Figure 6.11: Spectral weight analysis of the double peaked structure - The temperature dependence of the integrated spectral weight of the main plasmon peak (black circles) and of the secondary peak (full and open red circles). The results for high pressure cases are clearly different from the data at 1 bar. At high pressure, the SW of both peaks becomes comparable around 100-150 K without revealing any SW transfer between the two modes.

using typical low temperature values for bismuth ($n \sim 10^{17}$ cm^{-3}, $m^* \sim 0.015$ and $\epsilon_\infty = 100$) we found that $r_s \simeq 0.02$ which is very far from the crystallization region. Even considering the expected decrease of the electron density as a function of pressure [84], r_s remains significatively smaller than 1 for pressures almost up to the critical pressure $P_c = 25$ kbar. The main arguments against Wigner crystallization are certainly the large effect of screening and the low value of the carrier's effective mass which does not drastically change as a function of applied pressure. According to these arguments, although we don't exclude the possibility of the Wigner crystal phase, we believe that this scenario should become realistic only in a very limited pressure region close to P_c while in the pressure region covered in this work, the kinetic energy of carriers is largely dominating over the Coulomb repulsion. Consequently, from this point of view, pressure values such as those considered in our experiments, leave the system practically unchanged with respect to the situation found at ambient pressure.

The insulating behavior observed in recent magneto-resistance measurements conducted on semimetal graphite and bismuth [51] was proposed to be the consequence of a field induced exitonic insulator (EI) transition of Dirac fermions. Since the physical properties of bismuth are drastically affected by the presence of magnetic field, an explanation of the optical data under pressure in terms of EI cannot be given using the same arguments as in the presence of a magnetic field. Despite this consideration, the possibility of an excitonic insulator at the semimetal-semiconductor transition has been proposed for semimetal systems where electrons and holes are both simultaneously available for conduction [87, 86, 88]. In an indirect gap semiconductor or semimetal it is predicted that pressure, acting as a tuning parameter on the carrier density, may favor together with the simultaneous presence of two types of carriers, the formation of nonconducting electron-hole pairs, *i.e. excitons*. Experimentally speaking, all the methods for spontaneous exciton creation based on the variation of hydrostatic pressure, should be in this sense preferred over, for example, optical pumping, since they guarantee thermal equilibrium in the system with a consequent more favorable condition for condensation.

According to the EI scenario [87, 88], the value and the sign of the indirect energy gap E_{ig} compared to the exciton binding energy E_b, determines the ground state of the system: in particular when E_{ig} becomes smaller than E_b, the system becomes unstable since the energy scales are favorable for the spontaneous formation of excitons. In the undoped ambient pressure bismuth case where E_{ig} is negative, the formation of bound states is forbidden at high temperature and it has been shown that an excitonic phase very similar to the Cooper pairs condensation, may suddenly appear at very low temperatures [88]. However the critical transition temperature is strongly reduced if the difference in electrons and holes band dispersion is large. In the case of bismuth this consideration results in a strong suppression of the EI phase from the semimetal side of the phase diagram with a transition temperature T_{EI} pushed down to the mK temperature region.

The impossibility to have excitons at high temperature on the semimetallic side of the phase diagram automaticaly excludes also any explanation in terms of electron-hole droplets defined as a noncondensed state characterized by an high density of excitons.

Jérome and coworkers [86], though indicated bismuth as a possible candidate for the observation of such phenomenon, estimated an exciton binding energy $E_b \simeq 1.3 \times 10^{-5}$ eV and a critical temperature for EI transition around 0.05°K. Moreover they estimated, starting from the pressure dependence of the electron and hole density, that the pressure range where the EI could be observed covers a pressure window of about 2 bar around P_c. These values, together with the extreme experimental requirements needed for the observation of this strongly interacting phase, are clearly inconsistent with our observation of an enhanced scattering over a large pressure range and at temperatures up to 100 K and thus making the e-h droplets scenario very remote.

Recently an optical study on the semimetal $1T$-TiSe$_2$ compound revealed a behavior similar to the one found in high pressure bismuth [98]. The infrared reflectivity of this material, shows in fact the same sharp plasma edge centered around 45 meV that characterizes our data on bismuth and in general indicates a very low carrier density. This material is known to have a CDW phase transition for temperatures around 150-200 K. The transition is accompanied by the opening of a CDW gap recognizable in the conductivity spectra at low temperatures, though some spectral weight remains present in the energy region between the Drude peak and the gap energy. The loss function shows also the appearance of a secondary peak in the region of the gap which does not have a particular temperature dependence compared to the situation described in this work for bismuth. Kohn analyzed theoretically the dynamics of low density semimetals and semiconductors with an indirect energy gap [99] and concluded that for small values of the energy gap, the eigenfunctions of the ground state are a linear combination of eigenstates in the original hole and electron bands. This combination results in a charge density modulation with a period which is inversely proportional to the distance, in k-space, between the electron and hole bands. The opening of the CDW gap, consequence of the so called Overhauser charge density fluctuation, can occur by acting on the distance between these bands both coming from the semiconducting and semimetal side of the phase diagram. Although this scenario appears quite appealing, there are still some open questions especially regarding the efficiency of the nesting condition in a 3D system and inevitably on the possibility to reach the appropriate carrier density which allows the formation of a stable excitonic phase in a system characterized by large interband screening effects and low carriers' effective mass.

What follows from the previous discussion is that all the scenarios based on excitonic condensation seem quite unrealistic although it has been suggested that the inclusion of phonon coupling terms in the hamiltonian describing the system could lead to important renormalization effects especially in multivalley band structures [88].

As already mentioned before and in a previous work [5] the fact of having a secondary peak in the loss function is an indication in favor of a coupling process with longitudinal modes (*i.e.* plasmons or phonons). A complete description of a free electron system coupled to phonons can be given by using the Holstein [100] or the Toyazawa [101] Hamiltonians which differ from each other only by the type of phonon modes included in the calculation (optical modes in the Holstein model and acoustic modes in the Toyazawa model). Formally the same description that is extensively used to describe polaronic effects can be used to describe the coupling of free carrier to plasmon modes. This analogy has been extensively covered in the work of Lundqvist [74]. In this regarding the term "plasmaron" was introduced to describe an excitation consisting of a plasmon coupled to a hole. In general the similarity between the polaron and electron-plasmon interactions led to a more general definition of plasmaron which identify an interaction between single-particle excitations and collective modes.

Formally the analogy can be seen by writing the general Holstein hamiltonian

$$H = -t \sum_{\langle i,j \rangle} c_i^\dagger c_j + g \sum_i n_i \left(b_i^\dagger + b_i \right) + \sum_{\mathbf{q}} \omega_{\mathbf{q}} b_{\mathbf{q}}^\dagger b_{\mathbf{q}}, \tag{6.7}$$

where the first term represents the nearest-neighbor electron hopping term, the second sum the interaction which couples the electronic density with phonons and the last term is the purely phononic contribution. In the above equation, we used the standard notation where $c_i^\dagger$ and c_i are the real space electron creation and annihilation operators, $n_i (= c_i^\dagger c_i)$ is the number operator, $b_i^\dagger$ and b_i are the phonons creation and annihilation operators. $b_{\mathbf{q}}^\dagger$ is the Fourier transform of $b_i^\dagger$ and $\omega_{\mathbf{q}}$ is the frequency of the phonon with vector momentum $\mathbf{q}$. The hopping term is governed by a parameter t which defines the nearest-neighbor hopping integral while the coupling between the electron system and the phonon modes is determined by the coupling constant g.

Starting from this model it can be demonstrated [74] that the role of phonons can be exchanged with plasmons by defining $b_i^\dagger$ and b_i as plasmons creation and annihilation operators and substituting the electron-phonon coupling constant g with the momentum-dependent function

$$g^2(q) = \frac{4\pi e^2 \hbar}{q^2} \left(\frac{1}{\partial \varepsilon(q,\omega)/\partial \omega} \right)_{\omega=\omega_p} = \frac{4\pi \omega_p^2}{q^2 \omega_p(q)}, \tag{6.8}$$

where ω_p is the long wavelength plasmon frequency[1]. The problem is then analogous to the polaron problem except that in this latter case the hamiltonian is governed only by two constant parameters i.e. the phonon frequency and a coupling parameter while in the case of electron-plasmon or hole-plasmon interaction, the problem becomes more complicated because the coupling strength is dependent on the momentum of the plasmons [102]. We note here that the formal solution of an electron-plasmon interaction is identical to the case of hole-plasmon interaction. In a semimetallic system this may lead to interesting consequences since both conducting electrons and holes are simultaneously able to interact with the plasmon modes.

It is well known that polaronic systems are characterized by localization effects which produce a strong renormalization of the carrier's effective mass. We wondered, considering the striking analogy between the hamiltonians, if the same localization scenario could be possible in a system where free carriers are coupled to plasmons. The problem has been theoretically addressed by Pinsook and coworkers using a Feynman variational path integral method [105] and comparing their results with earlier works by Lundqvist and Overhauser [74, 102]. The result of their work is extremely interesting and confirms that when the density of the free particle system is decreased, the "dressed" particle passes from a regime of high mobility with an $m^*/m \simeq 1$, to a regime where it starts to be localized and its effective mass tends to increase. Earlier works [105] demonstrated that a decrease of density with a corresponding decrease of plasmon frequency ω_p leads to a strongly coupled situation with the tendency toward charge localization despite the behavior expected by only looking at the unintegrated expression for the coupling constant $g(q)$ in Eq. 6.8. In this regarding both the band

---

[1] The result of Eq. 6.8 has been obtained for a plasmon spectrum of the form $\omega_p^2(q) = \omega_p^2 + \frac{4}{3} k_F^2 q^2 + q^4$ and a simplified dielectric function for the electron system.

structure near the Fermi energy and plasmon dispersion may play a determinant role in the definition of the effective coupling strength. The purely electronic self-trapping process is similar to the Wigner crystallization and even if the carrier density required for a total localization are much smaller than those obtained in our experiments, our finding may indicate a precursor of such localized phase.

Indeed a similar calculation which takes into account also the simultaneous presence of both electrons and holes, together with their interaction, is at the moment missing. In this regard, the strong e-h scattering observed in bismuth below the Debye temperature may result determinant for the enhancement of the localization process induced by a purely electronic interaction.

The study of bismuth is particularly complicated by the fact that there are a lot of temperature and pressure dependent variables that need to be taken into account in order to properly model the electron and hole system. We hope that these experimental findings may contribute and stimulate future theoretical works which could verify our observations and derive numerically the expected optical response for a system dominated by electron-plasmon coupling effects in presence of an interacting e-h system. Indeed we believe that in both the plasmaronic and the excitonic scenarios the inclusion of the phonon coupling terms in the calculations may result important for the correct estimation of the excitation spectra. From the experimental point of view, though we successfully demonstrated the possibility to extract meaningful and detailed data using IR spectroscopy under pressure, we believe that a finer pressure grid and an optical investigation extending in the MIR-VIS spectral range could clarify some aspects of the problem that we could have underestimated using exclusively FIR data.

Chapter 7

Charge ordering in three-dimensional $RE_5Ir_4Si_{10}$ compounds

> *Tarditas et procrastinatio odiosa est.*
>
> Cicero

The main motivation inspiring the study done on $RE_5Ir_4Si_{10}$ compounds derives from the extremely high sensitivity of charge-density-wave systems to hydrostatic pressure. Charge density waves are a type of coupled electronic-lattice instability found in quasi-low dimensional materials. The driving force behind the instability is the reduction in kinetic energy of electrons in the material as a consequence of establishing a spontaneous periodic modulation of the crystalline lattice with an appropriate (often incommensurate) wave vector. The symmetry of the CDW state is very sensitive to the electronic structure of the host material and this aspect mainly determines the high sensitivity of this kind of system to pressure.

Clearly the best candidates for these kind of studies are low-dimensional materials where the CDW nesting condition is extremely enhanced due to the peculiar shape of the Fermi surface. Although the compounds in the $RE_5Ir_4Si_{10}$ family are not strictly mono-dimensional, they show very peculiar properties in a pressure range compatible with the one accessible using our pressure cell. In particular $Lu_5Ir_4Si_{10}$ shows a clear competition between the CDW ordered state and the superconducting state at low temperature [106]. It has been experimentally demonstrated that by the application of a moderate pressure ($P_c = 21.4$ kbar) the charge modulation can be suppressed and at the same time the superconducting temperature T_{SC} enhanced from 3.8 to 9.1 K due to the increased carrier density available for the formation of the Cooper's pairs.

In another work the suppression of the CDW state has been demonstrated by applying chemical pressure via the progressive substitution of Si atoms with Ge atoms confirming the intimate relation between CDW and SC state at low temperature [107].

Clearly optical spectroscopy represents a valid tool to study the transition and the competition between the two states when pressure is applied to the system. Large single crystals of $RE_5Ir_4Si_{10}$ compounds are available and their mechanical properties perfectly match the requirements for our pressure cell equipment together with the pressure range necessary to observe the full dynamics of the CDW suppression.

As we will explain in the sequel of this chapter the main drawback for optical experiments under pressure is related to the extremely small signal change observed at the CDW transitions for both Lu$_5$Ir$_4$Si$_{10}$ and Er$_5$Ir$_4$Si$_{10}$ compounds. Already at the stage of the preliminary ambient pressure measurements done without the pressure equipment we soon realized that in the case of Er$_5$Ir$_4$Si$_{10}$, the experimental system sensitivity and stability required for a quantitative analysis of the optical spectra was beyond the limits of our equipment. The lutetium-based compound on the other hand represented an experimentally "easier" system but unfortunately, considering the present limits of the pressure apparatus, the measurements and the consequent analysis were limited to the ambient pressure case.

7.1 Introduction

Charge-density-wave (CDW) formation was demonstrated [108] to be the consequence of an interaction between phonons connecting nested sides of the Fermi surface (FS) and metallic electrons in the system. For a particular phonon mode with wavevector $Q = 2k_F$ a charge density modulation is induced leading to a rearrangement of the original atom positions which tend to open a gap at the FS. If the net energy balance between the reduced electron energy and the increased elastic energy due to the deformation of the crystal is favorable than the charge density modulation becomes the ground state of the system. This mechanism has its largest efficiency in low-dimensional systems where the density of states available for the perfect nesting condition is higher. In ideal 1D systems [109] the CDW state is unstable even at $T = 0$ but small deviations from the ideal case (coupling between pure monodimensional channels) allow the CDW transition to develop at finite temperature and long range order results in the crystal. At T_{CDW} a full gap can be ideally opened and the system can undergo a metal-insulator transition (MIT), also known as Peierls transition [108]. Experimentally the density wave formation was demonstrated in many quasi-monodimensional compounds like K$_{0.3}$MoO$_3$ [110, 111, 112], also known as "blue bronze", NbSe$_3$ [113, 114, 115], TaSe$_3$ [115] and in different families of engineered organic materials (TTF-TCNQ and Bechgaard salts [116, 117, 118]).

The theoretical description of the CDW instability can be derived in a very general way considering an external potential $\phi^{\text{ext}}(\text{r})$ which induces a spacial density modulation $\rho^{\text{ind}}(\text{r})$ in a simple monodimensional electron system. Consequently, the induced modulation creates itself an induced potential $\phi^{\text{ind}}(\text{r})$ in the system. The relation between induced modulation and induced potential can be written in the reciprocal space as

$$\phi^{\text{ind}}(\mathbf{q}) = -g\rho^{\text{ind}}(\mathbf{q}), \tag{7.1}$$

where g is a coupling constant. The spatial modulation is related to the total potential by mean of the susceptibility function which captures the specific properties of the band dispersion of the electron system. Formally, this relation reads as

$$\rho^{\text{ind}}(\mathbf{q}) = \chi(\mathbf{q})\phi(\mathbf{q}), \tag{7.2}$$

where $\chi(\mathbf{q})$ is the Lindhard response function defined, for a d-dimensional system, as

$$\chi(\mathbf{q}) = \int \frac{d\mathbf{k}}{(2\pi)^d} \frac{f_k - f_{k+q}}{\epsilon_k - \epsilon_{k+q}}. \tag{7.3}$$

In the previous equation, f_k and ϵ_k are respectively the Fermi function and the energy for a given wavevector k. Rewriting the expression for the density modulation as a function of the external potential we obtain

$$\rho^{\text{ind}}(\mathbf{q}, T) = \frac{\chi(\mathbf{q}, T)\phi^{\text{ext}}(\mathbf{q})}{1 + g\chi(\mathbf{q}, T)}. \tag{7.4}$$

This expression predicts the possibility of a diverging behavior in presence of a negative coupling constant g. This description is very general and it allows to represent all types of density fluctuations where electron-electron or electron-hole pairs are formed. The nature of the zero-temperature ground state will be established by the interaction potential that will determine the nature of the coupled e-e or e-h states. For example when the total momentum of the e-e couple is zero then a Cooper pair will be formed, on the contrary, when the total momentum is $q = 2k_F$, a charge or spin density wave ground state will be the solution [109]. From these arguments, the reader may observe that superconductivity and density waves have a common mathematical origin and as will be clear below, even if not identical, many of the properties of these two ground states can be described with the same set of equations. For example it can be seen that for both types of condensate the order parameter can be described as a complex quantity $\Delta = |\Delta| \exp i\phi$ which represents the supeconducting gap in the case of superconductivity and the CDW gap, proportional to the amplitude of the charge density modulation, for the CDW ground state.

The description of a CDW system can be made by including all the necessary ingredients in an Hamiltonian. This has to take into account the free electrons contributions, the lattice modes and the coupling between electrons and phonons which are the essential terms able to determine the observed instability, better known as Peierls transition. A complete Hamiltonian for the problem is the Frohlich Hamiltonian [119] given by

$$\mathcal{H} = \sum_k \epsilon_k a_k^\dagger a_k + \sum_q \hbar\omega_q b_q^\dagger b_q + \sum_{k,q} g_q a_{k+q}^\dagger a_k (b_{-q}^\dagger b_q) \tag{7.5}$$

where the first term describes the purely electronic contribution, the second term describes the lattice vibrations while the last term represents the electron-phonon coupling characterized by a coupling constant g_q. In a purely monodimensional system it can be easily demonstrated that considering the electrons close to the Fermi energy, where the energy dispersion can be approximated with a linear function, the entire electon-phonon coupled system is unstable against phonon modes with $q = 2k_F$ which are able to connect (nest) states situated at opposite sides of the Fermi surface. It is worth saying that the classical solution to the hamiltonian in Eq. 7.5 is determined in the *weak coupling* regime. With “weak coupling” we refer to the electron-phonon coupling process. This coupling condition is valid in the cases where the gap energy is much smaller than the Fermi energy $\Delta \ll E_F$, or alternatively when the displacement of the ions due to the CDW instability is small compared to the typical interatomic distances.

The main consequence of the CDW instability is to reduce or renormalize the frequency of the phonon mode which is involved in the coupling process. In the mean field approximation, the expression for the renormalized phonon frequency is

$$\omega^2_{\text{ren},q} = \omega_q \left(\omega_q + \frac{2g^2}{\hbar} \chi(q,T) \right). \tag{7.6}$$

At the phase transition the renormalized frequency will go to zero and the phonon mode will be completely “frozen-in” determining a static charge density wave modulation. We can observe that the second term in Eq. 7.6 has the same structure of the denominator of Eq. 7.4. Considering then $\omega^2_{\text{ren},q} = 0$ and looking for a non-trivial solution to the equation for $q = 2k_F$ we find

$$\omega_{2k_F} = -\frac{2g^2}{\hbar} \chi(q,T). \tag{7.7}$$

The correct expression for $\chi(q,T)$ can be found by solving the integral in Eq. 7.3 considering the proper topology of the Fermi surface and the appropriate dimensionality. For a purely monodimensional system in the linear dispersion approximation we get

$$\chi(2k_F,T) = -e^2 n(\epsilon_F) \ln \frac{1.14\epsilon_0}{k_B T}. \tag{7.8}$$

Substituting equation 7.8 in 7.9 we obtain

$$k_B T_{\text{CDW}} = 1.14\epsilon_F \exp\left[-\frac{\hbar\omega_{2k_F}}{2g^2 n(\epsilon_F)} \right] \tag{7.9}$$

where we can define the argument of the exponent as a dimensionless electron-phonon coupling constant $\lambda = 2g^2 n(\epsilon_F)/\hbar\omega_{2k_F}$.

The ground state of the weakly-coupled electron-phonon system can be evaluated in the mean field approximation also in terms of the complex order parameter Δ defined as $|\Delta| \exp i\phi = g(\langle b_{2k_F} \rangle + \langle b_{-2k_F} \rangle)$ where $\langle b_{2k_F} \rangle$ is the expectation value for the phonon mode involved in the coupling. The resulting hamiltonian can be used to calculate the contribution to the total energy of the electronic part and of the lattice part. This latter contribution represents the variation of the elastic energy in response to the lattice deformation induced by the CDW modulation. The minimization of the total energy in the case where $q = 2k_F$ allows one to demonstrate that the CDW ground state is more favorable with respect to the normal state and that the order parameter Δ satisfies the condition

$$\Delta = 2\epsilon_F \exp\left[-\frac{1}{\lambda} \right]. \tag{7.10}$$

The direct comparison between Eq. 7.10 and Eq. 7.9 allows to derive the following relation:

$$2\Delta = 3.52 k_B T_{\text{CDW}} \tag{7.11}$$

which is identical the expression that relates the gap energy and the transition temperature in BCS supeconductors.

As we have seen these results are valid in the "weak coupling" approximation. An important aspect that needs to be clarified before continuing, is the consequence of the electron-phonon coupling on the thermodynamical properties of monodimensional systems. Moreover we need to understand up to which extent a "weak" or "strong" coupling may drastically change the material's response. We know that at the transition temperature $T_{\mathrm{CDW}}^{\mathrm{MF}}$, long range order develops in the system; the ground state is characterized by a coherence length ξ_0 that represents the spatial dimension of the coupled e-e pair. The weak coupling limit defines a situation where $\Delta/\epsilon_F \ll 1$; for this reason, since the coherence length $\xi_0 = \hbar v_F/\pi|\Delta|$, its value is expected to be large with respect to the case where strong e-ph coupling is present. The main consequences of a long coherence length may be appreciated considering two electrons sitting at two opposite sides of the Fermi surface, as schematically shown in Fig. 7.1. Since the coherence length is approximately inversely proportional to the spread of momenta of the electron's states, a large ξ_0 will result in very localized states at ϵ_F as represented by the two small circles in the figure. On the contrary, for small ξ_0 the momentum spread increases as symbolically represented by the large circles. The dramatic consequence of this difference is that in the long coherence length regime, the number of phonon modes which participates in the CDW phase transition is limited by a cutoff imposed by ξ_0.

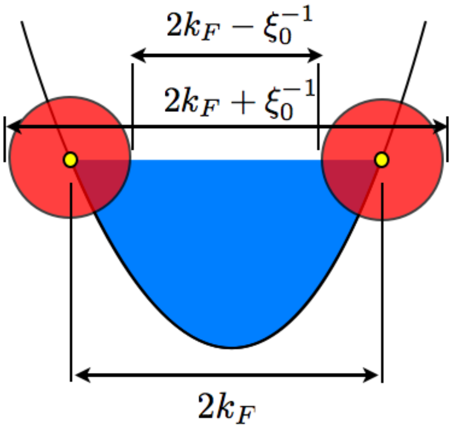

Figure 7.1: 1D Fermi surface - Long coherence length determines a condition where the momentum spread around $k(\epsilon_F)$ is negligible (yellow circles). For this reason the number of possible phonon modes that can contribute to the CDW instability is limited. On the contrary where the system is dominated by short coherence length the momentum spread is large (large red circles) and the number of phonons involved in the transition can be large determining important consequences in the thermodynamical properties of the sample at T_{CDW}.

McMillan [6] proposed a description beyond the weak-coupling limit. In his mathematical derivation he pointed out that since in the weak coupling regime the phonon frequencies are modified over a small region of the reciprocal space, the phonon entropy is unimportant with respect to the electrons' entropy.

On the contrary, in the case of short coherence length, the phonon contribution to entropy turns out to be dominant over the electron's contribution. In order for the strong coupling regime to apply and the phonon entropy to dominate, the order parameter should satisfy the relation $2\Delta \geq 7k_BT_{\mathrm{CDW}}$ which deviates from the one reported in Eq. 7.11.

This theory has been successfully applied to practical cases where a CDW transition was accompanied by anomalously large transitions observed by mean of specific heat, thermal conductivity as well as thermoelectric power measurements. For example it could at least qualitatively explain the anomalies observed in $2H$-TaSe$_2$ [120, 6].

In this regard Lu$_5$Ir$_4$Si$_{10}$ has many interesting properties that deviate from the standard weakly coupled CDW behavior and seems to show signatures of a strongly coupled system. In this compound the CDW and the superconducting transitions were found respectively at T$_{\text{CDW}}$ $= 83$ K and T$_{\text{SC}}$ $= 3.9$ K and the two states coexist below the superconducting transition as confirmed via x-ray-diffraction [7]. The first intriguing aspect is that the anisotropy of the material ($\rho_a/\rho_c \simeq 3.5$) is much lower than what expected for typical monodimensional systems. Furthermore the system does not go through a pure metal-insulator transition across T_{CDW}. It remains metallic down to the superconducting transition where eventually the resistivity drops to zero. The other interesting aspect concerns its thermodynamical properties, which show the same anomalies observed for strongly coupled systems. The specific heat, thermal conductivity and thermoelectric power measurements [7, 8, 9], indicate a large specific-heat jump ($\Delta C_p = 55$ J/mol K for a polycrystalline sample [9] and $\Delta C_p = 160$ J/mol K for a single-crystal sample [7]) developing in a very narrow temperature range ($\Delta T_{\text{CDW}} \sim 1\%$) accompanied by a significant entropy variation ($\Delta S = 0.12R$, Ref. [9], $\Delta S = 0.5R$ Ref. [7], where $R =$ gas constant). The relative size of the specific heat variation has been compared to the expected 1.43 value predicted assuming a weak coupling approximation and the result showed an important deviation from this latter value giving $\Delta C/C \simeq 8.4$ [9]. All these features were attributed to the possibility of a strong coupling regime which requires, as proposed by McMillan [6], a theoretical description beyond the standard theory based on weak electron-phonon coupling.

The isostructural compound Er$_5$Ir$_4$Si$_{10}$ on the other hand shows two CDW transitions: the first one at 155 K is a transition to an incommensurate CDW state while at 55 K another transition establishes the final commensurate CDW state. Also in this case the CDW instability is originated in an apparently 3D system since the resistivity ratio along the two main principal axis $\rho_a/\rho_c \sim 2.33$. The substitution of lutetium with erbium adds to the system a net magnetic moment which determines at low temperature (2.8 K) an anti-ferromagnetically ordered state without displaying any signature of superconductivity as observed for the Lu$_5$Ir$_4$Si$_{10}$ compound. Also in this case it has been shown that the charge-density-wave state and the antiferromagnetic ordering coexist below the Neel temperature.

In this chapter we report a study of the optical properties of Lu$_5$Ir$_4$Si$_{10}$ and Er$_5$Ir$_4$Si$_{10}$ single crystals in the temperature range between 20 K and room temperature and in the spectral region between 0.01 and 4 eV. For the Lu$_5$Ir$_4$Si$_{10}$ case the plasma frequency anisotropy along the main optical axes is rather small, around 1.13 considering the ratio $\omega^*_{Pc}/\omega^*_{Pa}$, the CDW gap is larger than expected for the standard BCS-like scenario applied to weakly coupled CDW systems in good agreement with McMillan's theory of strong el-ph coupling.

The temperature dependent optical constants show sharper changes around T_{CDW} than one would expect for a conventional second order phase transition predicted in the weak coupling approximation [109]. This latter aspect has been observed also in other experiments [9, 7] and seems to indicate the absence of fluctuations which usually characterize any real low-dimensional CDW system where the network of ideally independent monodimensional channels is transversally coupled. It is worth saying that the transversal coupling between 1D chains is essential in order to allow a 3D long range order to develop at $T_{3\mathrm{D}} \neq 0$. In the temperature region $T_{3\mathrm{D}} < T < T^{\mathrm{MF}}$[1], a system of weakly coupled chains is commonly dominated by strong fluctuations which can be experimentally observed and that contribute to the broadening of the transition. Moreover while for weak interchain coupling $T_{3\mathrm{D}}$ is significantly smaller than T^{MF}, we can expect that in the opposite regime $T_{3\mathrm{D}}$ would approach the mean filed transition temperature thus reducing the temperature region where fluctuations are dominant. According to this scenario, which is not embraced by McMillan's theory, the response of the system should present a strong 3D character with a clear signature of the underlying CDW instability due to the presence of nested portions of the Fermi surface.

The optical spectral weight is known to be related to the charge carriers kinetic energy [121, 122]; in the case of a BCS like electron-phonon interaction it has been shown that the low frequency spectral weight should decrease, implying an increase of the electronic kinetic energy [121]. We observe a decrease of the low frequency (0-0.31 eV) SW below the T_{CDW} and a corresponding increase at higher energies (0.31-3.7 eV) in agreement with what one would expect in a BCS scenario. Via an extended Drude analysis combined with the analysis of the temperature dependence of the optical spectral weight, we were able to estimate the size of the CDW pseudogap opening below T_{CDW}. The analysis of the frequency dependent scattering rate across the transition allowed us to observe, via the Eliashberg electron-phonon coupling model, the appearance of an intense low frequency Einstein mode which is identified as the phonon mode(s) involved in the formation of the CDW state. This observation and the important increase of the electron-phonon coupling constant at the transition is consistent with the strong electron-phonon coupling scenario dominated by a short coherence length which allows a large number of phonon modes to participate in the CDW phase transition.

Both the samples of the $\mathrm{RE_5Ir_4Si_{10}}$ family seem to follow a typical 3D behavior although the observed CDW transition clearly indicates that some portions of the Fermi surface are nested below T_{CDW} suggesting the presence a network of quasi-1D channels embedded in a 3D matrix.

7.2 Sample preparation

$\mathrm{RE_5Ir_4Si_{10}}$ single-crystal was grown using a modified Czochralski technique as described in Refs. [7, 123]. Its crystal structure belongs to the tetragonal $\mathrm{Sc_5Co_4Si_{10}}$ family (*P4/mbm*), thus the *a* and *b* axis are degenerate $a = b = 12.4936$, while the c-axis size is $c = 4.1852$. The atom positions are represented in Fig. 7.2; the blue lines are the Ir-Si-Ir bonds around the Re atoms placed in the corners and at the center of the main cell, while the red lines are the Re-Re bonds. The five Re atoms seated at the corners and in the center of the cell surrounded by four Ir atoms interleaved with Si atoms are kept apart from each other by a network of eight Re atoms in the *ab* plane. This description [7] was introduced to explain the two-fold nature of this class of compounds: on one side the CDW transition is a signature of monodimensionality while

---

[1] T^{MF} is the transition temperature derived using the mean field approximation.

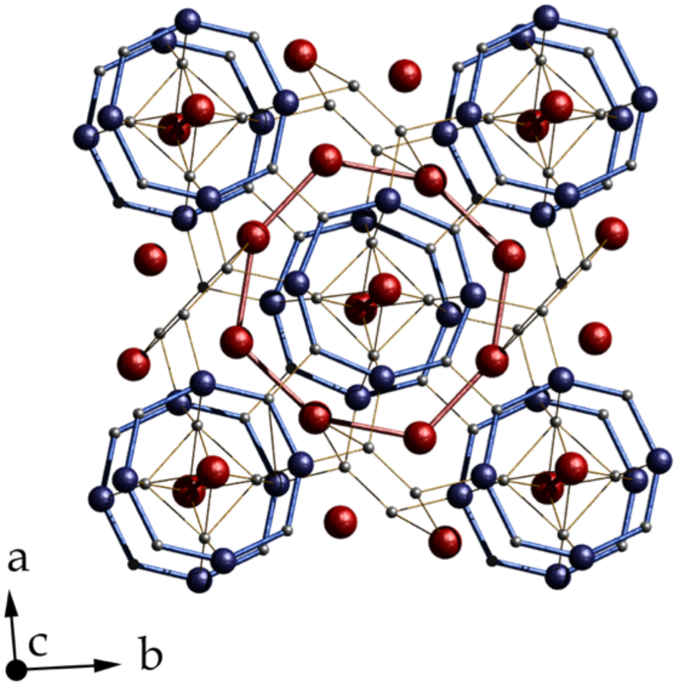

Figure 7.2: Crystal structure of $RE_5Ir_4Si_{10}$ - Rare earth atoms are represented with big red spheres, Ir atoms with medium blue spheres and Si atoms with light-grey spheres. With thick blue lines are represented schematically the five chains extending along the *c*-axis which seems to be responsible for the quasi-monodimensional behavior of the system and with thick red lines the Re-Re network separating the five chains.

a constant metallic behavior below T_{CDW} indicates that the transport perpendicular to the chains is not completely forbidden. By analyzing the distances between atoms in the main cell it was found that Re atoms in the corners and in the center of the unit cell have the shortest interatomic distance with respect to all the other bonds; this suggests that the monodimensional conducting channel is the Re-Re chain developing along the *c*-axis (perpendicular to the paper sheet). Accordingly, the Re network around the central site can be viewed as a conducting channel parallel to the 1D chains, preventing the system to have a complete MIT transition and allowing conduction perpendicular to the chains to take place.

The crystals (surface area $\sim$ 18 mm^2 and thickness $\sim$ 1 mm) were oriented with a Laue camera, and polished with a diamond sand paper of 0.1 μm grain size until a flat and mirror-like quality surface was obtained. The samples, whose optically treated surface contained the *ac* plane of the crystal, were mounted on a conical copper holder using silver paint to guarantee an optimal thermal contact and aligned with respect to the instruments using an He-Ne laser source.

7.3 Experimental details

The optical measurements on $\mathrm{Lu_5Ir_4Si_{10}}$ and $\mathrm{Er_5Ir_4Si_{10}}$ were done in the wavelength range from 50 cm^{-1} (6.2 meV) up to 30000 cm^{-1} (3.8 eV) using two different techniques: inverse Fourier-transform spectroscopy (IFTS) in the infrared range and ellipsometry for the visible and UV region. In the infrared ($6.2 \rightarrow 700$ meV) we used a custom-made optical cryostat, whose stability allowed reflected signal variations on the order of 0.1% to be measured, in combination with a Bruker 113 spectrometer. The sample was mounted in a quasi-normal incidence configuration and the absolute value of the reflectivity $R(\omega)$ was calculated by taking as a reference measurement a gold layer evaporated *in situ* as explained in Chapter 2. We acquired data continuously during slow temperature scans ranging from 295 K down to 20 K (1 K of resolution) and we used a rotating polarizer in order to measure the response of the *a*- and *c*-axis orientations. In the ellipsometry measurements we used an angle of incidence of 74° with respect to the normal to the sample surface. In this experiment a UHV cryostat able to guarantee a pressure lower than 10^{-9} mbar was used in order to avoid any problem due to atmospheric absorptions. The *a*- and *c*-axis responses were obtained rotating the sample in the cryostat. The alignment of the crystal axis with respect the incoming polarized light was carefully checked in order to reduce the alignment error to values smaller than 1°.

In the ellipsometry measurements, we measured the pseudodielectric functions for the two sample orientations, which are a mixture of the *a/b* and *c*-axis dielectric functions. We used a Kramers-Kronig (KK) constrained fitting routine [16], based on a Drude-Lorentz model, in order to fit simultaneously all the data taking into account the geometry of the optical setup and the sample orientation. A flexible function based on a large number of oscillators [16] allowed us to fit all the small details of the measured optical quantities. We extracted the pure dielectric constant $\epsilon_a(\omega, T)$, $\epsilon_c(\omega, T)$ and the optical conductivity $\sigma_{a,c}(\omega, T)$, for the two main crystal axes from this model. Figure 7.3 shows the experimental reflectivities for the two considered samples along the *a*- and *c*-axis . The comparison reveals large similarities in the infrared and visible

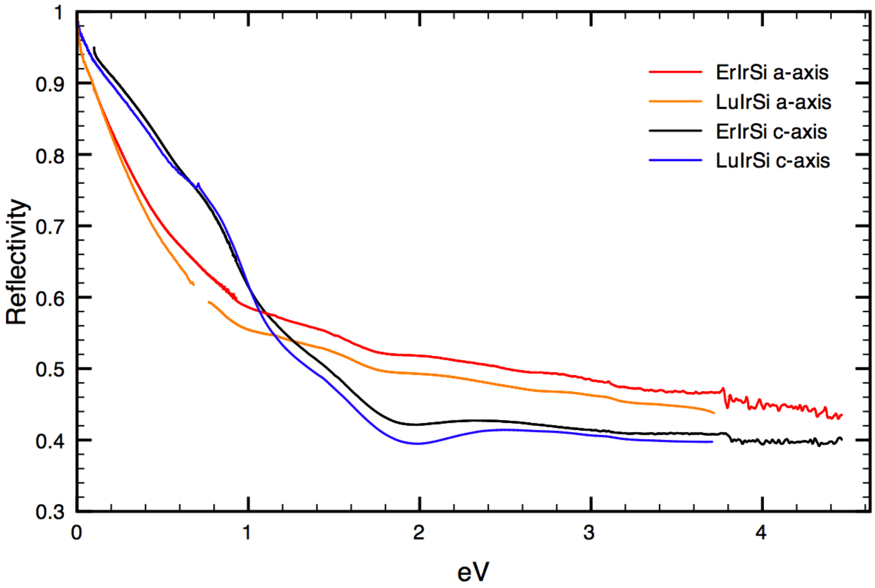

Figure 7.3: Reflectivity Comparison - The infrared and visible response of the two considered materials $Lu_5Ir_4Si_{10}$ and $Er_5Ir_4Si_{10}$ appear quite similar over the entire frequency range. In both cases the reflectivity measured along the *a*-axis results less metallic below 1 eV. In contrast although the reflectivity along the *c*-axis is higher in the FIR-MIR spectral region the plasma frequency position does not seem to be well defined indicating a certain overlap between intraband and interband spectral contributions.

response of the two materials. In both cases the c-axis has a more metallic response below 1.3 eV. For both the crystal orientations the reflectivity measurements do not indicate a clear plasma frequency edge suggesting a certain admixture between the intraband and interband contributions. The measured anisotropy confirms, at a first look, that the chains parallel to the c-axis constituted by the Re-Re bonds at the corners and at the center of the unit cell (Fig. 7.2) are actually the preferred conductivity channels in these kind of systems.

In Fig. 7.4 the measured optical reflectivity in the case of $\mathrm{Lu_5Ir_4Si_{10}}$ is shown in great detail (from 6.2 meV up to 743 meV) together with the reflectivity extracted from the ellipsometric data using the relation:

$$R_i(\omega) = \left| \frac{1-\sqrt{\epsilon_i(\omega)}}{1+\sqrt{\epsilon_i(\omega)}} \right|^2 \qquad , (i = a, c) \tag{7.12}$$

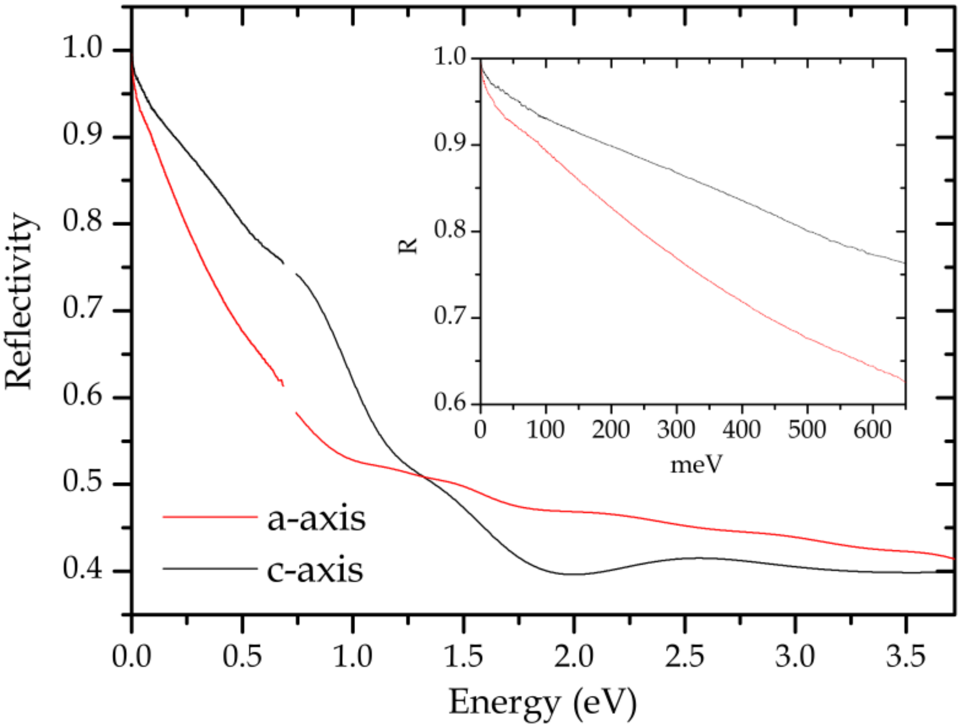

Figure 7.4: $\mathrm{Lu_5Ir_4Si_{10}}$ Room temperature reflectivity - The c- and a-axis response respectively represented with black and red lines. The reflectivity in the range 6.2-740 meV (shown in the inset) was directly measured using FT spectroscopy while the higher frequency part of $R(\omega)$ was calculated using a KK constrained multioscillator fit using ellipsometric data.

The agreement of the calculated reflectivity and the experimental data in the range 6.2 meV - 3.72 eV is excellent and the measured and calculated curves show an almost perfect matching in the energy region merging the two experimental ranges ($\sim$ 0.7 eV).

7.4 Temperature dependent optical spectra

In order to avoid confusion in the following sections, from this point on we will separate the discussion of the two considered materials. From the presented ambient temperature reflectivities the reader can correctly guess that the corresponding complex dielectric and conductivity functions are very similar in the two cases. As it will be demonstrated in the following subsections, the temperature dependence of the material responses on the contrary are rather different. Lu$_5$Ir$_4$Si$_{10}$ presents a unique and sharp transition at 83 K while Er$_5$Ir$_4$Si$_{10}$ shows two separate transitions respectively at 55 and 148 K.

7.4.1 Lu$_5$Ir$_4$Si$_{10}$

From the anisotropy visible in the reflectivity curves the sample appears to be more reflecting at low frequency for light polarized along the *c*-axis, Fig. 7.4. The small gap present in the data at around 740 meV is due to the mismatch between different experimental data sets obtained with different techniques in the low and high frequency range. As visible in the inset, in the far infrared $R(\omega)$ is around 97% along the *c*-axis and around 92% along the *a*-axis . The CDW transition is visible in the temperature dependent spectra, Fig. 7.5, as a depletion of the reflectivity below T_{CDW}. The drop in reflectivity while cooling the sample is present at all frequencies. We point out here that even though the changes in reflectivity at the transition are extremely clear in the data, the absolute reflectivity variation on of the order of less then 0.5% in the low frequency region.

The abrupt change in reflectivity that we observe is located at 78 K, very close to T_{CDW}= 83 K measured using transport techniques. This temperature has been defined as the maximum of $\partial R(\omega_i, T)/\partial T$. As expected from the room temperature data, the *c*-axis shows a more metallic behavior with respect to the *a*-axis. The screened plasma frequency ω_p^* is in fact very anisotropic, varying from 0.69 eV along *a* to 1.61 eV along *c*. This anisotropy is most likely due to a stronger screening by the interband transitions along the a axis, visible as two intense peaks at 990 meV and 1.86 eV respectively, and does not reflect the real anisotropy of the free carriers. The unscreened plasma frequency in fact ($\omega_p = \omega_p^* \cdot \sqrt{\epsilon_\infty}$) is found to be 7 eV along c and 6.17 eV along a, reducing even more the small anisotropy value found in transport measurements.

In the visible spectral region (0.7 - 4 eV) the ellipsometric data presented in Fig. 7.6 reveal the screening effect of the high frequency oscillators on the plasma frequency; there in fact a renormalization effect is visible in the values of ω_p^* defined as $\varepsilon_1(\omega_p^*) = 0$ for the two crystal orientations . The imaginary part of the dielectric function ε_2, not affected by the interband screening contributions, does not show the strong anisotropy present in $\varepsilon_1(\omega)$.

The temperature evolution of the real and imaginary part of the dielectric function (Fig. 7.7), shows a clear signature of the CDW transition up to frequencies as high as 3.1 eV. One very peculiar thing is that the temperature dependence close to T_{CDW} is not following the same trend for all the frequencies: for example along the *c*-axis (right column of Fig. 7.7) it can be seen that $\varepsilon_2(T)$, increases upon cooling at T_{CDW} for $\hbar\omega < 1.48$ eV and decreases at higher frequencies. The same thing seems to happen for $\varepsilon_1(T)$ along both axes but with different cutoff frequencies.

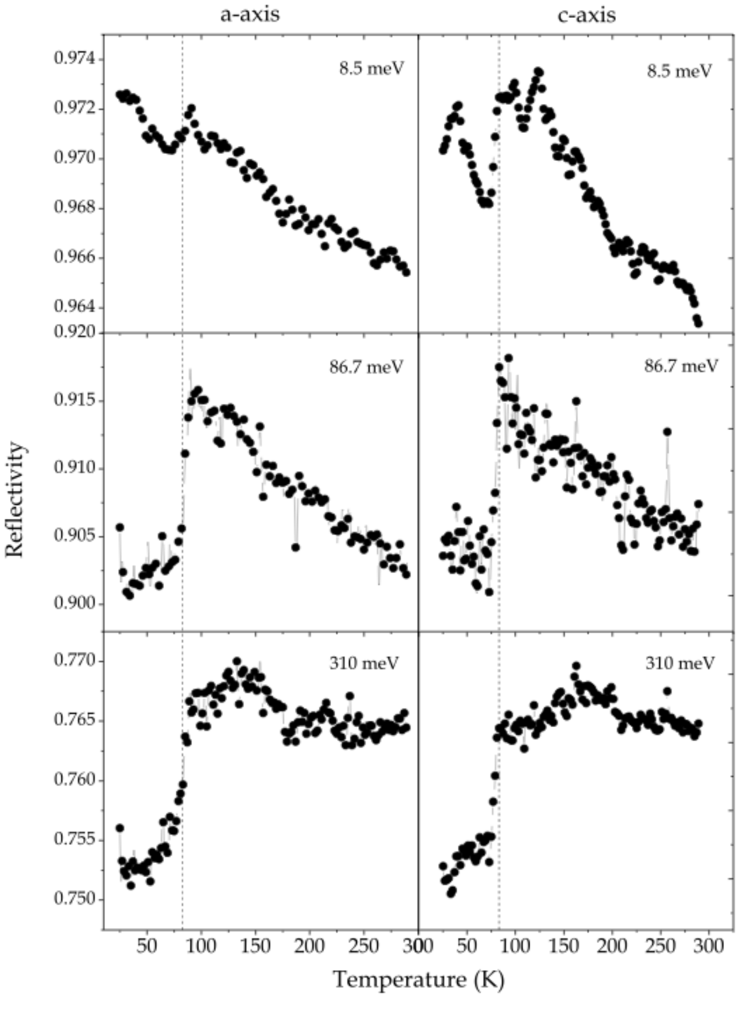

Figure 7.5: Reflectivity vs Temperature - The temperature dependence of the reflected intensity is presented for the cases $E \parallel a$ and $E \parallel c$ and for different frequencies. Both axes show a softened effect for $\hbar\omega < 12.4$ meV where the change in reflectivity between 60 and 120 K seems to follow a general increasing trend (cooling) instead of an abrupt drop.

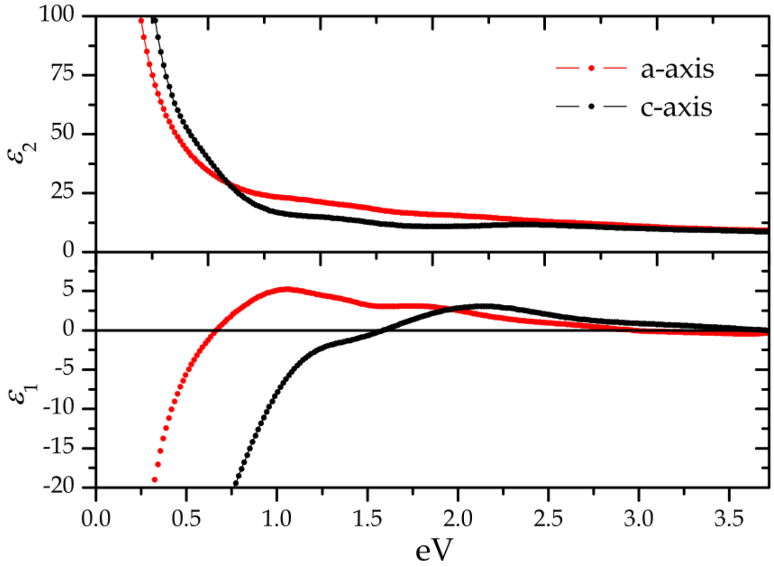

Figure 7.6: $\hat{\varepsilon}(\omega)$ **vs** T - The temperature dependence of the complex dielectric function is presented for the cases $E \parallel a$ and $E \parallel c$ and for different photon energies. The left and right column refer to the *a* and *c*-axis response respectively. ε_1 is shown with open circles while ε_2 is displayed with full black circles.

Combining the infrared reflectivity data and the VIS light ellipsometric data, we calculated the optical conductivity $\sigma_1(\omega)$ for each temperature. In figure 7.8 the comparison between the two crystal orientations is presented for temperature $T = 290$ and 60 K. As anticipated by the small absolute changes in the relevant spectroscopic functions at T_{CDW}, the difference in the optical conductivity for temperatures above and below the CDW transition is extremely small. A first look at the conductivity curves does not show any evident feature that could be related with the opening of a gap. The data only show the expected narrowing of the Drude peak at low temperature with a consequent increase of the zero-frequency conductivity. In both the log-log and linear plots it is evident a strong admixture between intraband and interband contributions in the region around 1 eV. There the tail of the Drude peak overlaps strongly with intense Lorentz oscillators centered around 1.5 and 3 eV.

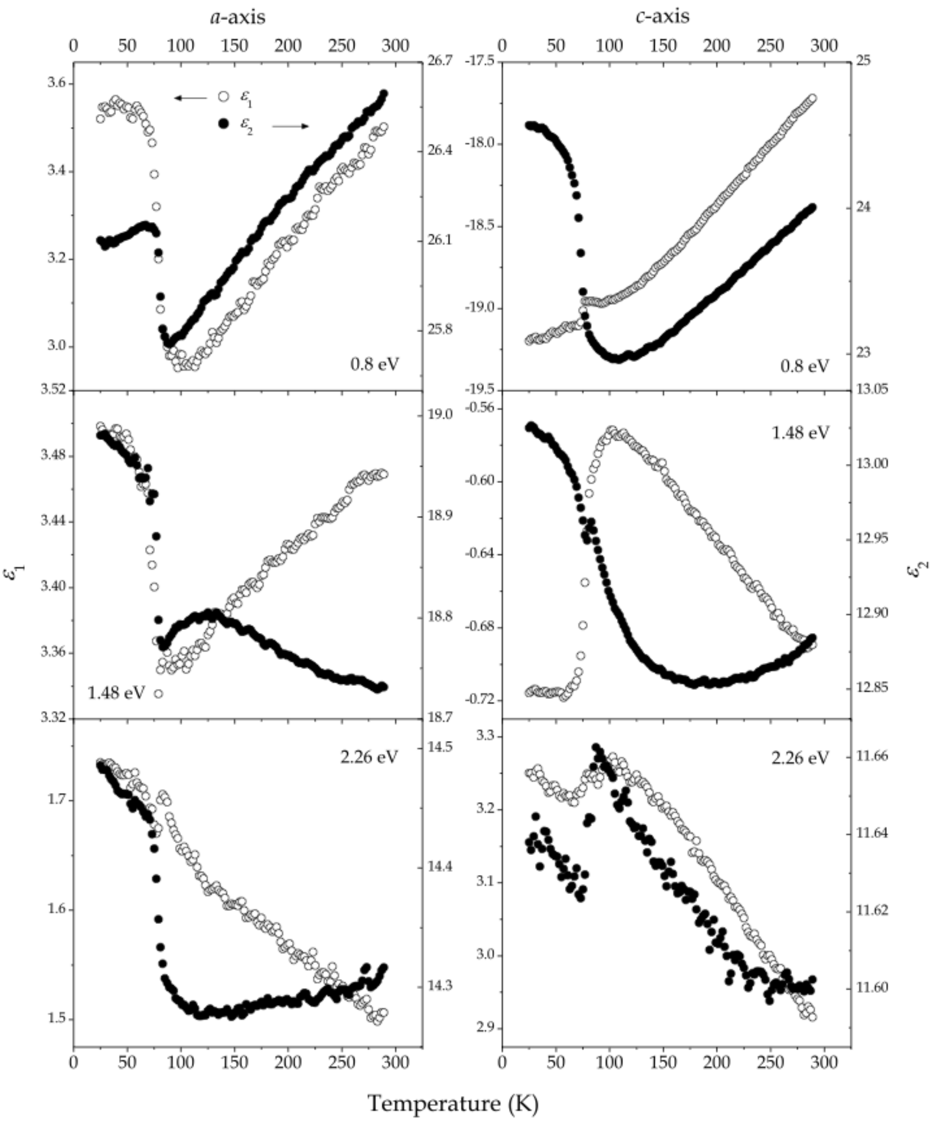

Figure 7.7: Temperature dependent dielectric constants - In the left column the temperature dependent variation of the real (full circles) and imaginary (open circles) part of the dielectric constant is presented for $E \parallel a$. The right columns shows the same quantities for $E \parallel c$. A strong signal change is recorded in the entire energy range for both crystal orientations. Here we show only the data relative to three selected energies: 0.8, 1.48 and 2.26 eV.

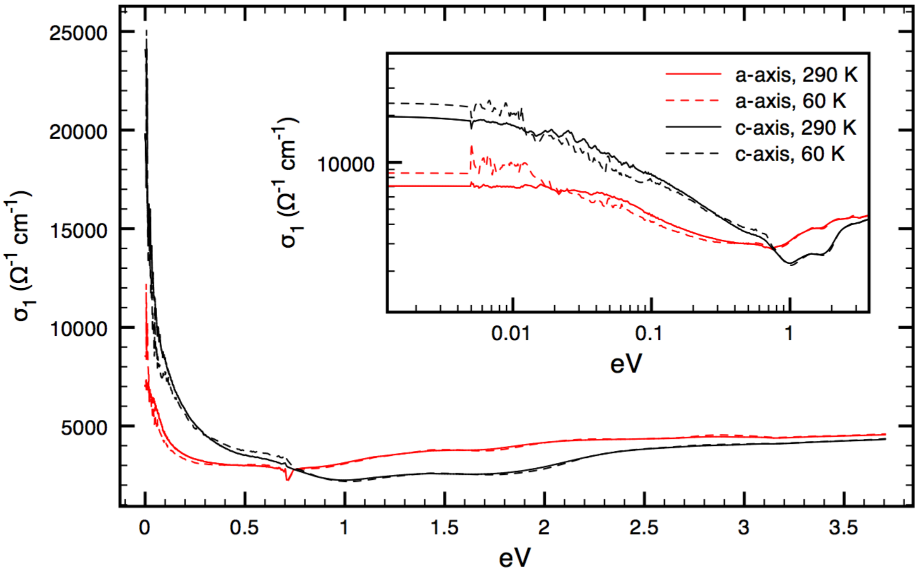

Figure 7.8: Optical conductivity across T_{CDW} - $\sigma_1(\omega)$ for the c-axis and a-axis is presented respectively with black and red lines. The full line refers to data taken at 100 K while data at 60 K are plotted with dashed lines. The inset shows a log-log plot of the same quantities in order to amplify the low frequency features of the spectra.

7.4.2 $Er_5Ir_4Si_{10}$

The spectroscopic measurement on $Er_5Ir_4Si_{10}$ has been made using the same procedures and techniques a in the case of $Lu_5Ir_4Si_{10}$. As anticipated in the introduction, the Er based compound should show two separate transitions at two different temperatures.

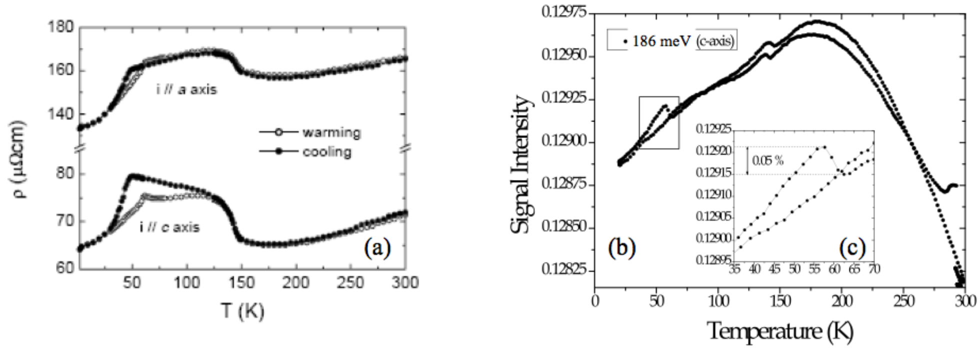

Figure 7.9: Reflectivity signal changes - (a) The temperature dependent dc resistivity as reported by Galli *et al.* [124]; (b) the temperature dependence of the reflected signal at 186 meV measured along the *c*-axis . The measurement shows clearly the two CDW transitions at 148 and 53 K. This latter one presents also a clear temperature hysteresis as expected from the dc data. (c) The low temperature CDW transition is characterized by a signal change of about 0.05%.

As visible in Fig. 7.9, the temperature dependence of the reflected signal (b) at 186 meV reveals the two transitions at 148 and 53 K as anticipated by previously published transport data [124, 8] shown in Fig. 7.9(a). As the reader may notice by comparing the temperature dependence of the spectral quantities for $Er_5Ir_4Si_{10}$ with the one of $Lu_5Ir_4Si_{10}$, the absolute change of the signal at both the transition temperatures, is rather small in the case of the Er-based compound. For example, considering the low temperature transition which correctly shows a clear temperature hysteresis, the percent change of the signal is only of the order of 0.05%. Moreover this value refers to the *c*-axis orientation where the dc conductivity signal shows a bigger percent change with respect to the *a*-axis . Along this latter crystal orientation in fact, the detection of the CDW transition in the optical spectra was impossible within the instrumental noise. For these reasons and considering the strong admixture of intraband and interband contributions which may mask the opening of the CDW gap, we decided to limit the analysis of the $Er_5Ir_4Si_{10}$ compound to just a qualitative description.

7.5 Pseudogap opening in $Lu_5Ir_4Si_{10}$

As we reported in section 7.4.1 it is not easy to recognize at a glance the opening of a gap or pseudogap directly by looking at the frequency dependent conductivity spectra. The most direct way to observe such a subtle feature consists in examining the relative change of the bare optical conductivity $\sigma_1(\omega)$ across the transition temperature. The evolution of σ_1 across T_{CDW} is summarized in the upper panel of Fig. 7.10. The low

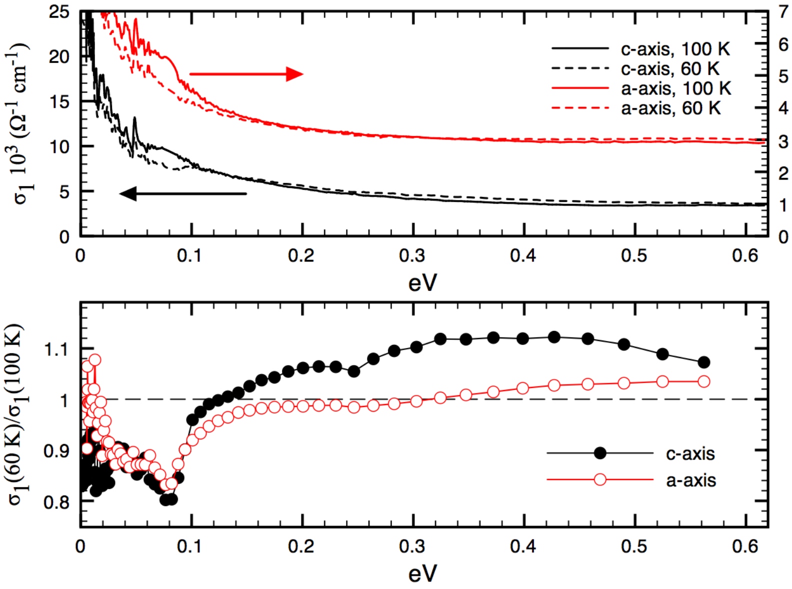

Figure 7.10: Optical conductivity and the opening of a pseudogap - In the upper panel the optical conductivity is shown for the a-axis (red curves) and for the c-axis (black curves) for $T = 60$ K (dashed lines) and $T = 100$ K (full line). In the lower panel the ratio $\sigma_1(T = 60K)/\sigma_1(T = 100K)$ reveals a clear reduction of the conductivity below 90 meV for both crystal orientations indicating the opening of a pseudogap.

frequency spectra of the optical conductivity are plotted for 60 K (dotted lines) and 100 K (full lines). At the transition temperature there is a decrease of the conductivity below 0.33 eV along the a-axis while at higher energies the conductivity increases. The same behavior has been observed for the c-axis except for the crossover energy that is in this case 0.095 eV. In order to clarify this observation in the lower panel of Fig. 7.10 the ratio $\sigma_1(T = 60K)/\sigma_1(T = 100K)$ is shown. Apart from the different crossover frequencies where the ratio is equal to one, in both cases there is a clear decay right at 90 meV preceded by a slow increase for $\hbar\omega < 90$ meV. This behavior is in qualitative agreement with a simple CDW transition model with a strong metallic background. In fact a pure monodimensional system is metallic above $T_{3\mathrm{D}}$ and enters into a CDW state for $T < T_{3\mathrm{D}}$ where long range 3D ordering is stable. In this ordered state the Fermi surface gets gapped and all the free electrons are transfered above the gap energy region causing a semiconductor-like behavior. In the present situation since the material shows low anisotropy and a clear three-dimensional character, the gap opens over a limited portion of the Fermi surface. For this reason the general behavior observed below T_{CDW} remains typical of a metal showing signatures of the opening of a pseudogap. This effect leads to a decrease of conductivity for frequencies below the single-particle gap ω_{SP} and a consequent increase of the conductivity for $\omega > \omega_{\mathrm{SP}}$ due to the redistribution of the electronic spectral weight in the new band structure.

The value of the optical gap is actually renormalized by lattice modes present in the phonon spectrum determining an onset for the optical transition across the gap at energy $\hbar\omega_g = \omega_0 + 2\Delta$, where ω_0 is the frequency of a particular phonon mode. Taking the Debye frequency $\omega_D = k_B\theta_D/\hbar$ as the cutoff frequency for the phonon spectrum and considering that $\theta_D = 366$ K, we estimate that $58 \leq 2\Delta \leq 90$ meV. These gap values give ratios $2\Delta/k_B T_{\mathrm{CDW}}$ between 8.1 and 12.6 respectively which are clearly larger than the 3.52 value expected for weakly coupled systems in the mean-field approximation.

According to Gruner [109] and Kim [125], the CDW has an associated low frequency mode that represents the collective mode of the ordered state. In our experiments the lowest measured energy was 6.2 meV, for this reason the collective mode contribution, which lays at even lower energies, was not directly measured; in our Drude-Lorentz model this contribution is included and hidden in the the low frequency Drude response.

7.6 $\mathrm{Lu_5Ir_4Si_{10}}$: spectral weight analysis

A deeper understanding of the dynamics at the CDW transition temperature can be obtained by analyzing the optical data in terms of the optical spectral weight (SW). This quantity is defined as the integrated optical conductivity as a function of a certain cutoff frequency ω_c

$$W(\omega_c, T) = \int_0^{\omega_c} \sigma_1(\omega)\,\mathrm{d}\omega. \tag{7.13}$$

In general, the optical conductivity is composed of an intra-band free carriers contribution $\sigma_1^{\mathrm{intra}}$ and a series of inter-band contributions $\sigma_1^{\mathrm{inter}}$. The integration of the intra-band part with $\omega_c \to \infty$ gives $W = \omega_p^2/8$, where ω_p is the plasma frequency of the Drude term. Of course in practice it can be difficult to separate $\sigma_1^{\mathrm{intra}}$ and $\sigma_1^{\mathrm{inter}}$ and usually the value of ω_c is chosen to be somewhere between the intra- and inter-band spectral region in order to monitor just the change due to the free carrier contributions; thus the integrated conductivity can be regarded as the effective number of carriers $N_{\mathrm{eff}} \cdot \pi e^2/2mV$ whose energies are smaller than $\hbar\omega_c$. In the limit where $\omega_c \to \infty$ the effective number of charges should equal the total number of electrons in the system. The dynamics of $W(\omega_c, T)$ crossing a transition temperature quantifies the redistribution of the carriers in the energy spectrum of the system. Looking at the optical conductivity of $\mathrm{Lu_5Ir_4Si_{10}}$, it is not clear how to define ω_c because of the overlap between inter-band contributions and the Drude term; however it is possible to analyze the temperature behavior of the SW as a function of cutoff frequency. In Fig. 7.11 N_{eff} is plotted versus ω_c for three different temperatures and for the two polarization directions for $0 \leq \omega_c \leq 0.6$ eV; the inset (a) shows the same quantity over the full measurement range for $T = 290$ K. From the temperature dependence of N_{eff}, a sudden drop in the SW function is clearly visible for both axis cooling the sample across T_{CDW} indicating a reduction of effective number of carriers. The cutoff frequency at which the low and high temperature N_{eff} merge, suggesting a full recovery of the SW, is around 0.6 eV for the c-axis and around 3.6 eV for a-axis (this point is not shown in the figure but it will be discussed later).

If one considers only the nearest neighbor hopping term in the Hamiltonian, an intimate relation exists between the free carrier spectral weight and the electronic kinetic

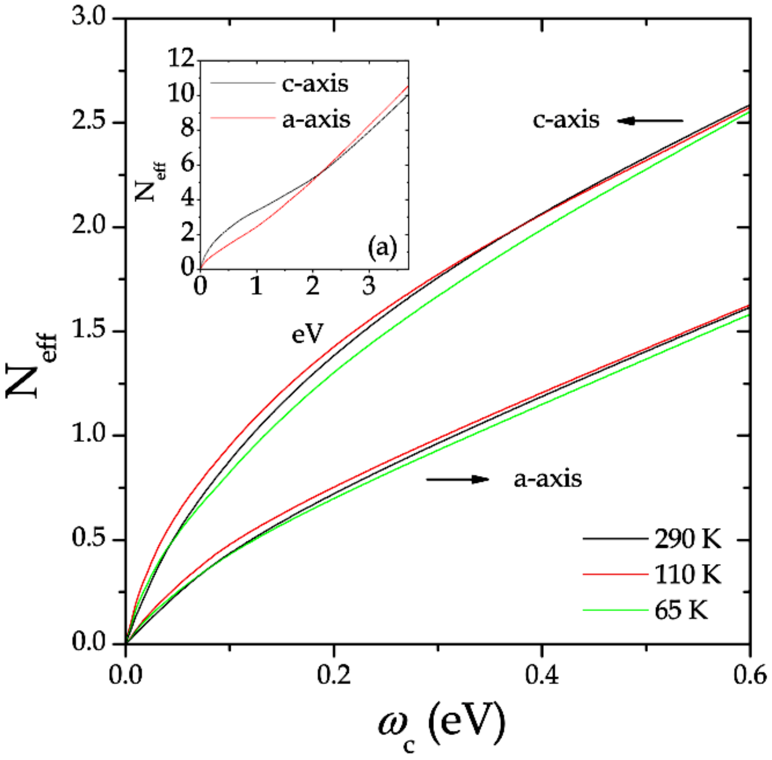

Figure 7.11: N_{eff} **(electrons/atom)** - Effective number of carriers as function of the cutoff frequency ω_c for both crystal orientations for $T = 290$ K, $T = 110$ K and $T = 65$ K. In the inset N_{eff} is presented over the complete measurement range for the room temperature case and for both crystal orientations.

energy (KE) via a linear relation of the kind $W \sim -\mathrm{KE}$. It is thus possible to measure experimentally the changes in KE of the system across the phase transition. In order to do that, one has to extrapolate the optical conductivity down to zero frequency, i.e. below the range where experimental data are available, with a Drude-Lorentz model [11]. We can check the reliability of our extrapolations comparing the value of the dc resistivity calculated from the DL model parameters with the one directly measured on the very same sample using standard transport techniques. The extrapolation was carried out by fitting with our Drude-Lorentz model the experimental data available down to 6 meV and than using the analytical model to calculate $\sigma_{1\mathrm{DC}} = \sigma_1(\omega \to 0)$. The DC resistivity was than calculated as $\rho_{\mathrm{DC}} = \sigma_{1\mathrm{DC}}^{-1}$. In Figure 7.12(a) the resistivity

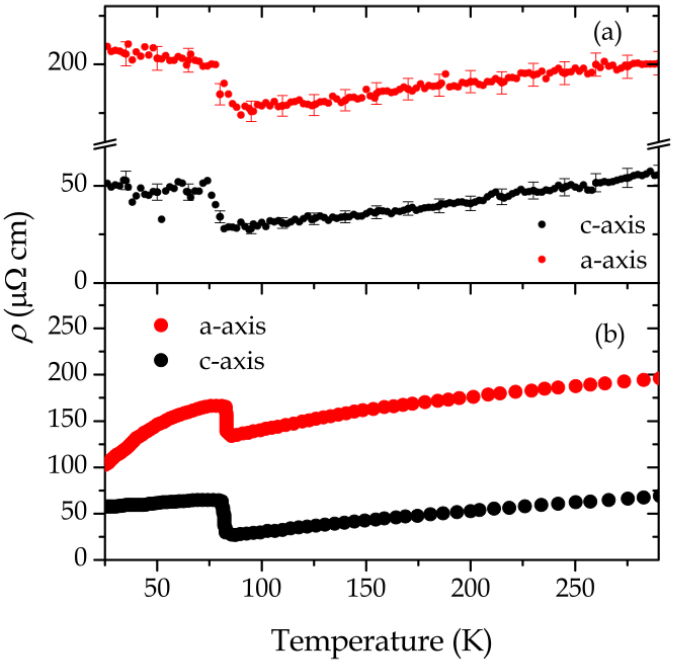

Figure 7.12: Resistivity comparison - (a) DC resistivity extracted from optical data as a function of temperature for *a*- (red circles) and *c*-axis (black circles). The error bars are calculated considering an error in the absolute value of reflectivity of ± 0.5 %. (b) data from Ref. [7]

data extracted from the optical measurements are compared with those obtained via a standard four-point measurement [7] (Fig. 7.12(b)). It is evident that the agreement is almost perfect at room temperature where the resistivity values are very close to each other both for the *a* and *c*-axis (the error bars on the optical results are obtained shifting up and down the reflectivity spectra by 1%, which is a very pessimistic estimation of the precision of our calibration method). The temperature dependence $\rho(T)$ is also in good agreement especially for the *c*-axis. The *a*-axis behavior deviates slightly from data in Fig. 7.12(b). This discrepancy is evident especially below the transition temperature where the typical metallic decreasing resistivity is not reproduced by the optical data. We believe that the reason for this small difference can be due to some system instabilities during the temperature dependent measurements; however considering that the variation of the reflectivity as a function of temperature in the overall spectral range is of the order of 1.5% (see Fig. 7.5) from room temperature down to 25 K and just 0.5% at T_{CDW}, the extracted DC resistivity can be considered astonishingly good.

We now analyze the temperature dependence of $W(\omega_c, T)$. The SW for different temperatures is plotted in figure 7.13 for an $\hbar\omega_c = 0.31$ eV for both crystal orientations. The graph shows that the low energy SW (represented with open markers) is decreasing abruptly below T_{CDW}. The SW above ω_c (i. e. $\int_{\omega_c}^{+\infty} \sigma_1(\omega)\, \mathrm{d}\omega$) has the opposite behavior which suggests that the loss of SW at low frequencies is compensated by an increase of SW at higher energies. This behavior is consistent with the CDW model where the opening of a gap at the Fermi surface causes a spectral weight transfer from the region within the gap to the region were the low-frequency CDW mode appears and above the created single-particle gap. This observation agrees also with the scenario predicted for systems where the electron-phonon mechanism is responsible for CDW formation. In these cases in fact the CDW transition is accompanied with an increase of the electronic KE below T_{CDW}, i.e. a decrease of the low frequency SW [121].

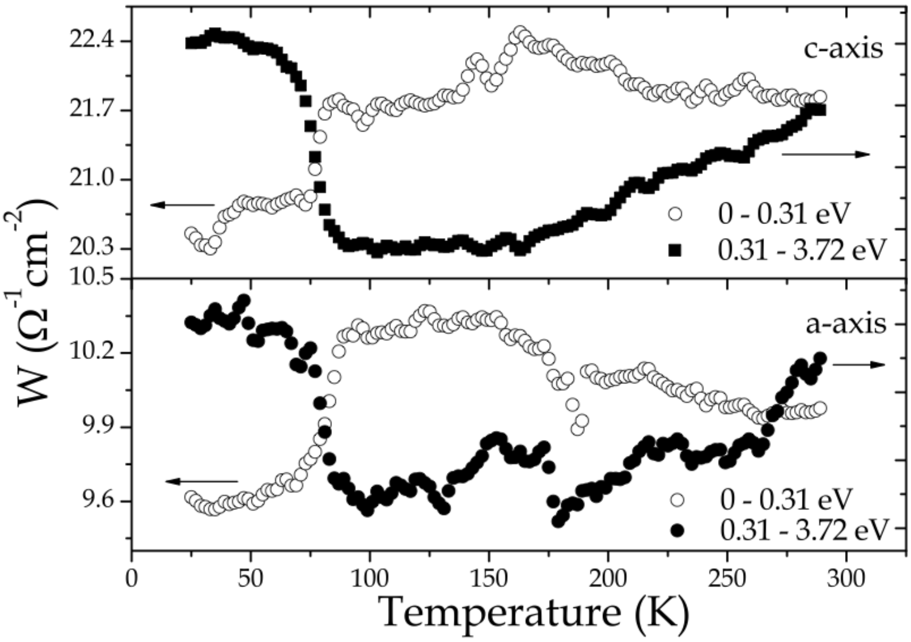

Figure 7.13: Temperature dependent SW - Spectral weight $W(T)$ for a (lower panel) and c-axis (upper panel) calculated using a cutoff frequency $\omega_c = 0.31$ eV. The spectral weight behavior for $\omega > \omega_c$ is shown with full markers while the SW for $\omega < \omega_c$ is shown with empty circles.

From the increase of the superconducting temperature at the critical pressure of 21 kbar [106] the opening of the gap was estimated to extend over 36% of the Fermi surface. The fact that in our optical data the change in the spectral weight appears in both polarization directions can be interpreted as the effect of diagonal nesting instead of one developing purely along the c-axis orientation.

Using the information given by the SW, we can estimate the extension of the CDW gap and try to quantify the percentage of Fermi surface that gets gapped at the transition. Some useful informations in this direction can be extracted calculating the percent change of spectral weight across the transition defined as

$$\Delta W(\omega_c) = \frac{W(\omega_c, T = 100\,K) - W(\omega_c, T = 65\,K)}{W(\omega_c, T = 65\,K)}. \tag{7.14}$$

This quantity gives an estimation of the number of free carriers removed from the Fermi surface and transferred to the energy region above the CDW gap. From the theory of CDWs [109] it is demonstrated that the CDW ground state is characterized, in an ideal 1D case, by a density of states which is zero for $\hbar\omega < 2\Delta$, divergent when approaching the gap energy and finally finite for $\hbar\omega > 2\Delta$. In the present situation where a strong metallic component is always present together with the CDW modulation for $T < T_{\text{CDW}}$, the choice of two temperatures relatively close to the transition would allow to disentangle the effect of the CDW transition from the natural narrowing of the Drude peak due to the reduction of the thermal scattering. For values of the cutoff frequency ω_c well within the gap (low frequencies) the percent change should be maximum and gradually decrease in the region of the gap edge where the thermal broadening starts to be effective. Finally ΔW is expected to go to zero well above the gap where the electrons' system remains unperturbed by the CDW.

The temperature dependence of SW is shown in Fig. 7.14(a) in the case of $\hbar\omega_c =$ 124 meV: a clear drop in SW is visible at T_{CDW} meaning that a certain amount of carriers is removed from the frequency region below ω_c and transferred at higher frequencies. The same behavior has been observed along the a-axis. The experimentally determined ΔW versus cutoff frequency is presented in the main panel of Fig. 7.14. For the c-axis the percent change is constant and equal to 17.5% up to 45 meV ($\sim$ 360 cm^{-1}) and starts to decrease above this frequency value. As already pointed out the SW is fully recovered for $\hbar\omega_c \simeq 0.68$ eV even if above this value an unexpected inversion seems to occur in the SW transfer. This feature disappears at higher frequencies and our data indicates the tendency toward a complete SW recovery for energies larger than 3.7 eV. In a similar fashion the a-axis presents a constant plateau extending up to the same energy but with a value of 15% followed by a slow recovery of SW that converges to zero around 3.7 eV. In this latter case for energies larger than 3.7 eV we cannot exclude a negative overshoot similar to the c-axis case. This analysis shows clearly that the CDW strength remains constant over a broad frequency range indicating that the reduction of charge density in this energy region is poorly affected by thermal broadening. However the determination of the position of the energy gap is not as simple as in the case where the ratio of conductivity spectra was considered (Fig. 7.10). Intuitively since the gap may not be well defined for the two temperature values used for the calculation of ΔW (Eq. 7.14), its position can be roughly estimated as the middle point of the decreasing section of the ΔW curves at about 1100 cm^{-1} . This value, corresponding to 130 meV, though higher than the result obtained in the previous section, confirms the deviation from the gap value expected for a typical weakly coupled system. Considering the relation between spectral weight and the effective number of free carriers together with both the contributions from the a and

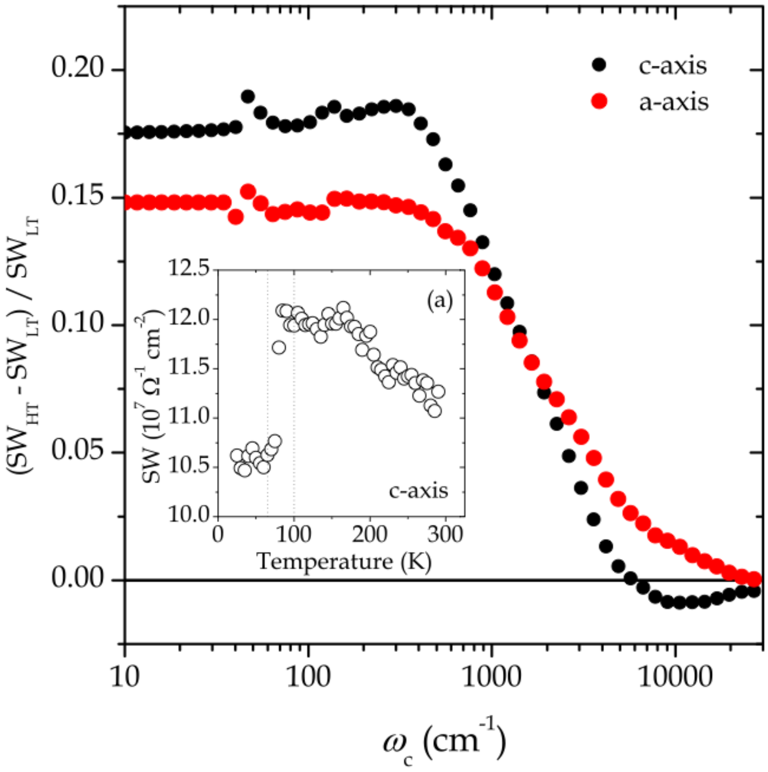

Figure 7.14: Percent change of SW across $T_{\mathbf{CDW}}$ - The percentage increase of SW as defined in Eq. 7.14 plotted versus cutoff frequency. The comparison between c-axis (black-dotted line) and a-axis (red-dotted line) reveals a saturation region below 45 meV. The recovery of SW extends up to 3.7 eV for both axis with a negative overshoot around 1.24 eV in the c-axis case.

c-axis , we calculated a total 32.5% SW reduction. This value is consistent with the 34% reported by Shelton *et al.* [106] on polycrystalline $\mathrm{Lu_5Ir_4Si_{10}}$ sample.

Another interesting aspect that can be noticed is related to the energy scale where there is a full recovery of SW; apparently the charge transfer does not appear to influence just the frequency region close to the gap position but it extends at very high frequencies as already observed in our visible-light ellipsometry measurements where a strong transition at T_{CDW} has been recorded basically at all frequencies in the considered spectral range.

7.7 Analysis beyond the standard Drude-Lorentz model

In this section we will carry out a detailed analysis of the measured optical properties where the optical response of the quasiparticles is explained in terms of frequency-dependent scattering rate $1/\tau(\omega)$ and effective mass enhancement $m^*(\omega)/m$.

A more general expression for the optical conductivity is obtained introducing a damping term that is complex and frequency-dependent (often called “memory function”) defined as $M(\omega) = 1/\tau(\omega, T) - i\omega\lambda(\omega, T)$. Substituting this expression in the standard Drude formula [126], one obtains

$$\sigma(\omega, T) = \frac{\omega_{\mathrm{P}}^2}{4\pi}\frac{1}{1/\tau(\omega, T) - i\omega[1 + \lambda(\omega, T)]}. \tag{7.15}$$

Here the quantities $1/\tau(\omega, T)$ and $\lambda(\omega, T)$ represent respectively the frequency dependent scattering rate and the mass enhancement of electronic excitations due to many-body interactions. Their values can be obtained once the complex conductivity is known via simple inversion formulas:

$$\frac{1}{\tau(\omega)} = \frac{\omega_p^2}{4\pi}\mathrm{Re}\left(\frac{1}{\sigma(\omega)}\right) \tag{7.16}$$

$$1 + \lambda(\omega) = -\frac{\omega_p^2}{4\pi}\frac{1}{\omega}\mathrm{Im}\left(\frac{1}{\sigma(\omega)}\right). \tag{7.17}$$

In the above equations the presence of the plasma frequency $\omega_p = \sqrt{4\pi ne^2/m^*}$ (n is the carrier density and m^* is the effective mass) requires the definition of a cutoff frequency ω_c so that ω_p can be determined directly by integrating the optical conductivity

$$\omega_p^2 = 8\int_0^{\omega_c} \sigma_1(\omega)\,\mathrm{d}\omega. \tag{7.18}$$

Usually ω_c is fixed in a frequency region that allows us to exclude from the integral (7.18) the interband transition contributions. In our particular case, choosing $\hbar\omega_c$ = 745 meV for both polarizations the values of the plasma frequencies are 35000 cm^{-1} and 28440 cm^{-1} respectively for the *c* and *a-b* axes. An important aspect to consider for the discussion to come is that the temperature dependence of the plasma frequencies is negligible ($\sim$ 0.5 %) in the considered temperature range. This observation is important for the determination of the causes of the transition observed in resistivity at 83 K. In particular since the DC resistivity is a combination of carrier density, scattering rate and effective mass through the relation $\rho_{\mathrm{DC}}(T) = 1/\sigma_{\mathrm{op}}(T, \omega \rightarrow$

$0) \propto n^{-1}m^*(T,0)\tau^{-1}(T,0)$, the CDW transition may effect all the relevant quantities which determines the dc transport value. We note for example that even though the analysis of the spectral weight revealed a decrease of this quantity in the region of the gap, the reported percent change cannot explain on its own the large increase of resistivity shown in Fig. 7.12.

In the following discussion the reader should keep in mind that the graphs presenting the frequency dependent scattering rate and effective mass have a consistent physical meaning only in the frequency region where the contributions from interband transition are negligible. The energy regions where the extended Drude model starts to loose its validity will be presented as shaded areas. We will nonetheless report some similarities that characterize the frequency dependent response of materials similar to Lu$_5$Ir$_4$Si$_{10}$.

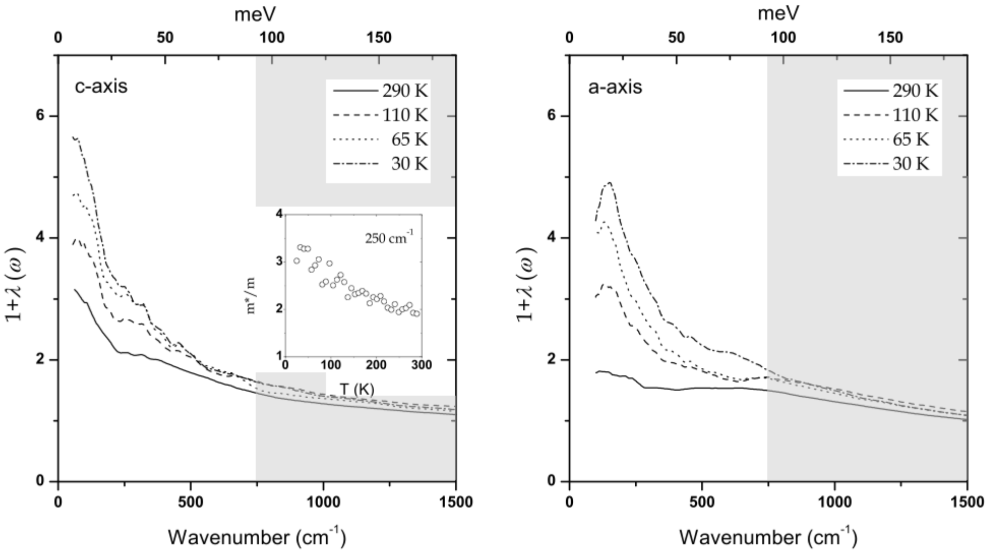

Figure 7.15: Frequency dependent effective mass - $1 + \lambda(\omega)$ for $E \parallel c$ (left panel) and $E \parallel ab$ (right panel). Data are shown for the case of 290 K (full line), 110 K (dashed line), 65 K (dotted line) and 30 K (dash-dot line). The inset in the left panel shows how the effective-mass enhancement is monotonic with temperature and does not present any clear signature of the transition at T_{CDW}.

In Fig. 7.15 the effective-mass $m^*(\omega)/m_\infty = 1 + \lambda(\omega)$ is shown for different temperatures above and below the transition. The mass enhancement is similar for the two axis orientations and does not present any abrupt change crossing the transition as demonstrated by the inset for the case where $\omega = 250$ cm^{-1} (31 meV). Above 700 cm^{-1} the effective-mass enhancement is less pronounced and tends to saturate. For the a-axis case the drop in effective mass visible below 200 cm^{-1} is most likely an experimental artifact due to the finite precision of the calibration procedure when the absolute value of the reflectivity is close to 100%.

The frequency-dependent scattering rate along the c-axis presented in Fig. 7.16 reveals a negative curvature with a tendency to become linear above $\omega > 700$ cm^{-1} , while for the a-axis the curvature is negative everywhere in the considered frequency region. This deviates from the typical electron-electron scattering, $1/\tau \sim \omega^2$, pre-

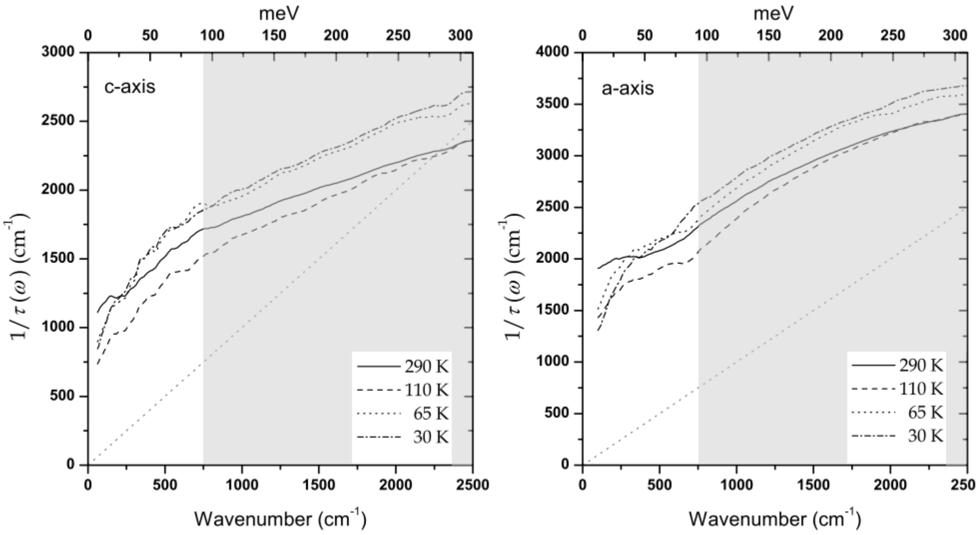

Figure 7.16: Frequency dependent scattering rate - $1/\tau(\omega)$ for $E \parallel c$ (left panel) and $E \parallel ab$ (right panel). Data are shown for the case of 290 K (full line), 110 K (dashed line), 65 K (dotted line) and 30 K (dash-dot line). The data shows for both crystal orientation a rigid increase of scattering rate when temperature is lowered below T_{CDW}.

dicted for a standard Fermi liquid as experimentally observed in typical 3D metals [127, 128]. This peculiarity has been found in several other 2D layered compounds like for example 2H-TaSe$_2$ and 2H-NbSe$_2$ [129, 130, 131] and in all the high-temperature cuprate superconductors (HTSC) [132, 126] where $1/\tau(\omega)$ shows a linear frequency dependence. Another analogy with the cited materials is an abrupt change in the slope of $\tau^{-1}(\omega)$ at low frequencies; in our data this kink-like feature is visible at around $\Omega_c = 700$ cm^{-1} for both crystal orientations. Even if the static temperature picture of $1/\tau(\omega)$ in Lu$_5$Ir$_4$Si$_{10}$ seems to be fairly similar to the one observed in HTSC and other quasi-2D layered compounds, its temperature dependence appears quite different from these cases. There in fact for $T < T^*$ (in the under-doped HTS) a progressive suppression of the scattering rate was found to occur below a certain cutoff frequency Ω_c. The behavior observed in the present case does not show a clear scattering suppression below Ω_c but rather it appears more similar to the behavior found along the *ab* plane in 2H-NbSe$_2$ [130] where the progressive change of temperature, introduces a constant contribution to the scattering rate which is added to the whole $1/\tau$ curve without showing any particular frequency dependent feature. Contrary to the tendency observed in the case of the effective mass, here it is possible to observe a strong change of scattering at the transition temperature. While for $T \gg T_{\mathrm{CDW}}$ we observe a progressive reduction of the scattering rate as expected for a typical metallic system, at T_{CDW} we register a sudden increase of $1/\tau$ over the entire frequency region. The change is of the order of 15% for the *c*-axis and of 10% for the *a*-axis when comparing the curves relative to $T = 110$ K and $T = 65$ K.

However, a careful look at the *c*-axis scattering rate, reveals that together with a rigid increase of the scattering value below T_{CDW}, we register a change of slope below Ω_c which, by subtracting the constant shift introduced at the transition, would result in a frequency dependent decrease of scattering similar to the one observed in HTC and 2D-layered compounds. This picture seems to suggest that the scattering rate is actually dominated by two main contributions; a mild reduction of electron-electron scattering due to the reduction of the available scattering phase space as a consequence of the opening of the CDW gap and the simultaneous activation of an important scattering channel probably associated with a strong lattice mode as suggested by thermal-expansion measurements [133].

The high-frequency behavior of $1/\tau$ for the *a*- and the *c*-axis is quite different: in the former case the curves don't show any tendency toward saturation while for the latter case all the curves show a plateau approaching 300 meV. This disparity, as pointed out by Dordevic [130] and Shulga [134], can be interpreted as a signature of inelastic scattering channels most probably due to the presence of a mid infrared absorption bands.

We believe that the previous observations are consistent with a scenario where electron-phonon scattering dominates. The modification to the electronic properties of metals due to e-ph interactions can be described using the formalism introduced by Eliashberg [135, 136]. Starting from the single-electron Greens function and introducing the electron-phonon dependent self-energy, it is possible to derive the expression for the frequency dependent scattering rate

$$\begin{aligned}\frac{1}{\tau(\omega)} &= \frac{\pi}{\omega}\int \mathrm{d}\,\Omega\alpha^2F(\Omega)\cdot\left[2\omega\coth\left(\frac{\Omega}{2T}\right)-\right.\\ &\quad -(\omega+\Omega)\coth\left(\frac{\omega+\Omega}{2T}\right)+\\ &\quad \left.+\,(\omega-\Omega)\coth\left(\frac{\omega-\Omega}{2T}\right)\right]+\\ &\quad +\frac{1}{\tau_{\text{imp}}}\end{aligned} \tag{7.19}$$

where $\alpha^2F(\omega)$ represents the weighted phonon density spectrum, τ_{imp}^{-1} the constant impurity scattering and T is the temperature expressed in units of frequency. Using this model and our experimental data we tried to derive an expression for the spectral function $\alpha^2F(\omega)$ using a least-squared fitting routine starting from a phonon density spectrum decomposed into a basis of Einstein modes centered at frequencies ω_i:

$$\alpha^2F(\omega)=\sum_i \alpha_i F_i\delta(\omega-\omega_i) \tag{7.20}$$

The result of the fitting procedure is presented in Fig. 7.17 where the experimental data at $T = 110$ K and $T = 65$ K are compared with those extracted from the fit. The resulting spectral densities, shown in the lower panels, guarantee an excellent agreement on the entire frequency range for both the polarization directions. Here we want to emphasize some recognizable features predicted by the theory: the change in the slope at Ω_c for both polarization directions is often considered as the cutoff frequency of the phonon spectrum [134, 126]. From the comparison between the low and high temperature spectra, it is evident that below T_{CDW} there is an increase of $\alpha^2F(\omega)$ at low frequencies which is in the end responsible for the whole rigid increase of the scattering rate curves. This result may confirm that as the CDW sets in, a strong scattering channel is activated. Such behavior is opposite to the one seen in layered dichalcogenides and in HTSC where, below the transition temperature where the pseudogap opens, there is only a characteristic suppression of the scattering rate below the critical phonon cutoff frequency Ω_c due to the reduction of the density of carriers as a consequence of the partial gapping of the Fermi surface. As we already pointed out, the optical conductivity spectra does not present a clear signature of the opening of a gap with a large spectral weight transfer from the frequency region within the gap to higher frequencies. Thought not immediately evident through a simple comparison of the conductivity spectra across the transition temperature, we demonstrated, by analyzing the spectral weight temperature dependence, that for temperature T $<T_{\text{CDW}}$ part of the Fermi surface is actually removed and spectral weight transferred above the CDW gap. Here we demonstrate that the reduction of carrier density is accompanied by a simultaneous increase of the scattering processes. In order to prove quantitatively this statement it is possible to calculate the electron-phonon coupling constant as

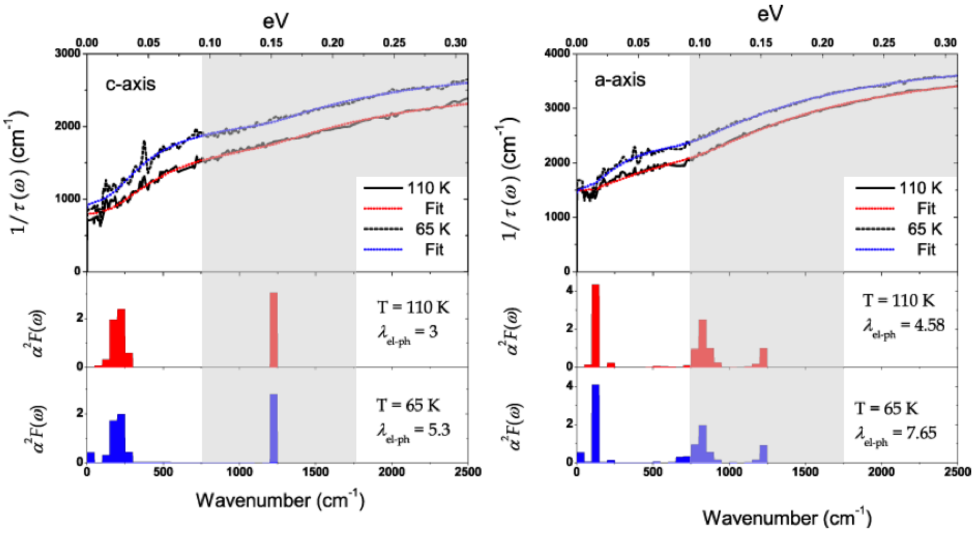

Figure 7.17: Electron-phonon scattering - The top left and right panels present a comparison between the experimental scattering rate measured at 110 K and 65 K and the results of the fitting routine implemented starting from Eq. 7.19 for c- and a-axis respectively. In the lower panels the resulting phonon spectral densities decomposed on a basis of Dirac δ functions are compared. For both the cases it is evident a low frequency mode appears below the transition temperature.

$$\lambda_{\text{el-ph}} = 2\int_0^\infty \frac{\alpha^2 F(\omega)}{\omega}\,\mathrm{d}\omega \tag{7.21}$$

where in our case we substituted the integral with a summation for the discrete ω_i set. A summary of this calculation is presented in Table 7.1. Even if the values for the coupling constants appear unrealistically large, their ratio reveal that a strong electron-phonon enhancement dominates the phase transition.

The results of the analysis presented in Fig. 7.17 shows that the frequency dependent scattering rate above T_{CDW} can be originated by two main groups of Einstein

Table 7.1: Summary of the electron-phonon coupling constant calculated from spectral densities presented in Fig. 7.17 using Eq. 7.21.

	λ (110 K)	λ (65 K)	λ(65 K)/λ(110 K)
a-axis	4.58	7.65	1.67
c-axis	3.8	5.29	1.39

modes, one centered around 30 meV and another one centered in the MIR spectral range around 150 meV. This latter group seems to be broader for the a-axis . Most likely, part of the scattering contributions present in this frequency region are due to interband transitions overlapping with the tail of the Drude peak.

The temperature dependence of the Einstein modes' spectrum gives an important indication about the mechanism which sets in at T_{CDW}: in fact as the graph demonstrate, the high frequency part of the spectrum remains substantially unchanged. The main difference which shows up comparing the low and high temperature phonon spectra for both crystal orientations, is a low frequency mode which determines an important increase of scattering. By expressing this increase in terms of electron-phonon coupling contribution we found that its value is about $+67\%$ for the a-axis and $+39\%$ for the c-axis with respect the values found in the normal state.

The group of phonon modes present around 200 cm^{-1} remains substantially unchanged in the CDW state. In principle the opening of a gap should determine a shift of the phonon spectrum toward higher frequencies. In this regard we wish to stress the fact that $Lu_5Ir_4Si_{10}$ has a strong three-dimensional character even below T_{CDW} meaning that the phonon modes which are not involved in the CDW instability will remain practically unchanged despite the opening of a gap.

Although the position of the lowest frequency mode, responsible for the increase of scattering, is below the minimum experimental frequency that we actually measured, we believe that this analysis gives a clear indication of the enhancement of a phonon mode which couples with the charge density modulation in the crystal contributing to the stabilization of the CDW state. In this regarding it has been demonstrated [137] that the interaction between the CDW ground state and the optical phonons has important consequences on the optical conductivity. In particular each phonon mode coupled to the spatially modulated electron system via a coupling constant λ_i should result in a conductivity peak in $\sigma_1(\omega_i)$, where ω_i is the phonon frequency. These vibrational modes, according to general spectral weight conservation laws, should subtract SW to the single particle excitations and consequently the optical signature of the opening of a gap will appear less clearly evident in the bare conductivity curves.

7.8 Conclusions and outlooks

In this chapter we studied the optical response of two members of the $RE_5Ir_4Si_{10}$ family: $Lu_5Ir_4Si_{10}$ and $Er_5Ir_4Si_{10}$. The original motivation of this study was the possibility to characterize the electrodynamics of these compounds when hydrostatic pressure changes were applied. In materials with low dimensionality where CDW states are favorable, the effect of pressure gives dramatic changes due to the high sensitivity of these materials to changes in the lattice parameters. Although the compounds in the $RE_5Ir_4Si_{10}$ family cannot be seen as typical examples of low dimensional systems, they exhibit CDW transitions revealing some typical features of low-D materials. Moreover in the case of $Lu_5Ir_4Si_{10}$ it has been demonstrated that at low temperature the CDW state coexists with the superconducting state indicating a system where strong on-chain coupling is combined with strong interchain coupling [10]. These peculiarities make this compound an ideal candidate both from the experimental and the scientific point of view.

Unfortunately due to technical limitations of our pressure apparatus the original project had to be revised after the preliminary measurements. As has been shown the variation of the signal at T_{CDW} was, in both the lutetium and erbium cases, extremely tiny and the measurement of the reflectivity within the pressure cell wouldn't have revealed such a small variation. Perhaps the use of a brighter source which would improve the signal to noise ratio would allow a pressure dependent spectroscopic measurement as the one conducted in the case of bismuth.

In conclusion we studied the optical conductivity of single crystal $Lu_5Ir_4Si_{10}$ and $Er_5Ir_4Si_{10}$ along the two main crystal orientations. In the case of the lutetium based sample we were able to fully resolve the optical anisotropy which appears to be weaker than expected for a typical monodimensional system. From a careful analysis based on the spectral weight function we were able to estimate the position of the CDW gap for the two crystal orientations. For both crystal orientations the gap 2Δ was estimated to be around 58 and 90 meV. These gap values give ratios $2\Delta/k_B T_{\text{CDW}}$ between 8.1 and 12.6 respectively. As anticipated in the introduction, these values are much larger than expected for a standard weakly coupled CDW system and they agre well with McMillan's predictions for strong coupling. In this respect, another important confirmation of the presence of a strongly coupled electron-phonon system came from the analysis of the scattering rate in terms of the Eliashberg electron-phonon coupling theory. A decomposition of the phonon spectrum in terms of independent Einstein modes allowed us to determine an important increase in the coupling constant at T_{CDW}. The position of the phonon mode, mainly responsible for the large increase of scattering below the transition temperature, is found at very low energies in a region which falls outside the available experimental data. Indeed this observation is compatible with the results obtained using other techniques where it was repeatedly suggested that the CDW transition in $Lu_5Ir_4Si_{10}$ is dominated by strong phonon contributions in accordance with a short coherence length scenario.

Moreover the temperature dependent optical data confirmed a sharp first-order-like transition at T_{CDW} which indicates a reduced, or almost absent, effect of fluctuations which is typically expected for strongly coupled mono-dimensional systems in the temperature region between T_{3D}, where three-dimensional range order is established, and the mean-field transition temperature $T_{\text{CDW}}^{\text{MF}}$. The difference between these two temperatures is reduced in presence of transverse coupling between independent monodimensional conducting channels, which makes the problem more three-dimensional. We believe that in this respect $Lu_5Ir_4Si_{10}$ and $Er_5Ir_4Si_{10}$ have to be considered more like three-dimensional systems, where some portions of the Fermi surface satisfy the nesting condition necessary for the formation of the CDW ground state, than systems with barely independent monodimensional conducting channels.

We argue that the effect of transversal coupling may be determinant for the interpretation of the experimental data. In fact, according to previous investigations by Imada and Scalapino [10] the effect of short correlations combined with transverse interchain coupling can produce the coexistence of the CDW ground state with a superconducting ground state, as indeed experimentally verified in the case of Lu$_5$Ir$_4$Si$_{10}$ [106].

A detailed study of the band structure of this material is missing at the moment and would be very useful to investigate *ab initio* the electronic structure responsible for the effects observed in our optical experiments.

Acknowledgements

In my personal time scale five years is probably the right amount of time for drawing an horizontal line on the imaginary piece of paper, which is our life, and make a balance of the things that have been done, on the experiences and mistakes that we encountered, on the people met along the way... Somehow these five years coincide with the duration of my PhD work in Geneva and balances add to each other in a nonlinear way, also because the life and work experiences in Geneva have always been extremely tightly connected and mutually influenced.

The first day that I entered in the department of physics I honestly found it a little grayish, a little hard with its sharp edges, the massive stones and the artificial lights. After five years I discovered what makes that institute so special and, in a still figurative sense, colorful: *the passion*. Every single person that I met in this long period of time had, each one in a very special and personal way, its own inspiration and passion. It would be too easy to say that everybody was just inspired by the passion for science and knowledge but it is amazing to discover how different and peculiar can be the interpretation of the same common feeling.

It is by using the idea of the personal interpretation of passion that I would like to start my acknowledgments. The first person that I wish to thank is you Dirk. Among the multitude of people that I met, you are certainly the most clear example of devotion and passion for physics. I would like then to thank you not only for the unpaired opportunity for my scientific and professional growth, but also for the practical example that you gave me regarding the importance of following our own passions and inspirations. In this regard I really appreciated your ability to let us interpret the PhD following our own way without imposing decisions which would have been orthogonal to our own attitudes. I need to express you my gratitude and admiration for your ability for always finding a connecting point between your experienced view of physics and our, sometimes oversimplified, representations.

From the point of view of technical experience and scientific knowledge I really think that the opportunity that you gave me constitutes an invaluable treasure which will certainly serve me in my future job and career. I would spend a last written "thank you" for the sustain that you gave me while I was looking for a job outside the university even if that was in a way opposite to your interest.

I wish to thank Fabrizio which has always been a friend for me, more and before than being a colleague. Fabbri, you're the person that somehow has the responsibility for all this or at least you were the one that prospected me the opportunity of a PhD in

Geneva... Of course then I have chosen this way but in the end it seems to be clearly the winning choice (how much did you bet?!). Me, you, Ana and Milena, we shared together a big piece of life outside the department and even if now and in the future the distances will be large, I'm sure that we will always stay in touch, if not for science, at least for a good dinner and for a match at Richard. I'm really glad that you found, as I did, your way and I really wish that you can calm down your scientific thirst with your preferred drink! Milena thank you for many things but first of all for being my best fan whenever I had one of my not-so-funny jokes ready!

A large "grazie" goes to Prof. Armitage, Peter. Together we formed the "pressure developers" team and I really think we had the perfect skills' balance in order to conduct a successful experimental activity. I will never forget the long days and nights that we spent together in the lab, mounting and dismounting cryostats, pressure cells and thinking to possible solutions on how to possibly improve the setup. I still have the bonus card for the "kebab-place" next to the university so whenever you wish we can go there and remember the old good times in Geneva with a little less *pressure*. I really appreciate your positive attitude in starting very difficult projects and I'm sure this will bring you a lot of success in the field of physics. I'm also very grateful to you for the remote support that you constantly gave me despite your new project in Baltimore, also Skype should feel proud to be an important piece of our scientific successes!

A special dedication goes to Prof. Mydosh who kindly provided me with beautiful samples. I would like to thank you on one side and to apologize for the delay on the other but unfortunately the pressure project has been really demanding for me in these last years.

I wish to thank Alexey and its sharp scientific mind and because with his precious advices and experience he has been a constant reference point for many aspects in our experimental activity. You are certainly one of the best expressions of pure talent that I found in the world of physics. What else can I say...? You really FIT in the field of science!

I need to spend some words for Enrico who represented another piece of Italy in the department. I remember that the first day when I started at the department you gave me the first course in Geneva: a crash course on swiss bureaucracy! That was really a brilliant introduction. I would say that that day I really had a complete overview on your personality: friendly, prepared and always available! Thank you so much for the time that you spent in cooking bismuth samples for me, I can assure you that the scientific taste was incredibly good and sweet! I won't cite here any of the tough discussions that we had from time to time on monday... But I know that passion plays a central role in the typical italian Monday!

I wish to say thank you to Mehdi for his patience and for the technical support during the design process of the experimental setup. I appreciated a lot the technical discussions that we had together and the useful "tips and tricks" that you taught me about all these complicated technical drawing softwares.

A special acknowledgment goes to my office mates Erik and Violeta: I think we have been a real singularity in the infinite universe of the possible sets of office mates. Even if our projects have been really orthogonal to each other I learned a lot of positive things from you. I wish you all the best for the continuation of your scientific career wherever it will be on this planet. And do not drink too much coffee, ok?!

I could not forget about the largest french-speaking community in our group:

Jeremie and Romain. Jeremie, I'm still wondering why you abandoned us in order to join the crystal growth team of Enrico. We had the Nespresso machine, wasn't it enough!? Ok, I understand that you also needed to bake a lot of cakes but... I really think we had a great time together and I appreciated your attitude strongly renormalized by your beautiful little daughters. Thank you Romain for your enthusiasm and for the curiosity that you always demonstrated for my project.

I would like to really thank Dook and Joachim for many things... We had so much fun together that I would need an extra page just for you two. I will never forget the dish of "pizzoccheri" that we had together after our biking adventure over the Bernina pass. I'm sure that even if scattered around the world we will stay in touch. Dook, I'll be always available to hear from you your latest technological fancy improvements and to give you good advices on the Mac's business. Ah, and if you're going to organize another big event with such a fantastic dinner, keep me in your mind and let me sneak in somehow!

Joachim I really hope to meet you one day at the seaside for an intense windsurf session. Honestly, Geneva is a very nice city but the wind is not really great!

I'm really grateful to Natalia and Florence who joined the group in these last months and demonstrated to be really valid partners in the pressure activity. I'm sure you won't get discouraged by the many technical issues that you'll encounter in this activity. I appreciated the high quality standards of your work and the conviction that you demonstrated in starting these new pressure project. Florence, you deserve a special thank since you "saved" me in this last months from the TP activity. Let me have a picture of your high pressure creation when it will be ready! And you Natalia, you (together with your german) saved me from being an homeless scientist in Zurich! Thank you indeed for the invaluable psychological support in these tough period, it was really really nice. Though you're good in the real estate business I really hope for you a successful career in science.

I wish to thank Hajo, Cor, Alexander and Francesco, former members of the group, who have been always very kind with me. Even if not directly on the same project I'm sure we spent sometime together trying to solve some technical issue.

Even if the temporal overlap was not very big I wish to thank also Yuxing, Rolf and Iman.

Patrick Magnin deserves a special acknowledgment for his technical support on all that was binary and for his extreme kindness. I hope I did not mess up too much the server, but you can always send me emails and complain!

For the experience at the synchrotron and for the strong collaboration during the beamtime and later for the analysis of some x-ray data, I really have to thank Sakura and Olivier. The time that I spent with you at ESRF though not very long, was certainly very dense and exciting. I really learned a lot of things from you, both from the scientific point of view and from the human one. You certainly have the right spirit which is needed to make a good idea a successful experiment, I really appreciated it.

Many thanks for the long and fruitful discussion to Prof. Frank Marsiglio, Thomas Jalborg and Didier Jaccard. This latter one, with his incredible experience, has always been ready to give me precious advices about technical aspects related to the experimental activity with pressure equipment and I really felt honored for this. Thank you so much.

I wish to thank Prof. Bowtell who introduced me to the world of MRI (Magnetic

Resonance Imaging) with very clear and very stimulating lessons.

Carmine, I'll really miss your funny jokes in the corridors! That should be a good excuse for you to move in the northern part of Switzerland... soon!

Thank you Fabienne and Christine for being so efficient and for your kindness, I'm sure I'll miss your gentle smiles in my future activities.

I would like to wish good luck to Iris for her future in Geneva. I hope that you'll progress in physics and in cooking fantastic italian risotto.

I cannot forget to thank all Genève Natation and in particular the Master team for the determinant role that they had in my life. My nerves wouldn't have survived to the stress without the weekly 7 Km that we swam together. Special thanks go to Alain "Secco", Preben, Fatima and Craig. Leaving Geneva is very painful also because of all of you guys!

For the extremely intense moments spent together in many restaurants, bar, apartments and parties I want to thank my italian friends in Geneva, Giovanni, Cyril, Fra and Francy. We have been very busy all together and I always find myself smiling when ever I think to how messy are our lives! It was amazingly funny to fix appointments two-three months in advance because of the too many things that we had to do.

Finally I wish to thank my old italian friends who helped me along this adventure being always there whenever I came back to Italy. Really every time we go out, like in the old good times, I have the impression that nothing is really changed... that gives a very nice sensation. So thank you Mike, Vale, Chiara, Chicca, Cecio, Andre, Michela, Marta, Giorgio and Gianni.

Really endless thanks to Zia Gio, Nonna Angela e Nonna Alice, I know that the fact that I leaved Italy has been hard for all of you but you've been always in my mind in the good and bad times of these five years being a constant support. Really thank you for your love and comprehension.

I still want to apologize in advance with those that were not included in these pages, I'll feel really guilty as soon I'll realize all the persons that I forgot. I hope we could compensate this in front of a chilly glass of beer.

References

[1] Kramers, H. A. *Nature* **117**, 775 (1926).

[2] Brandt, N. B., Gaidukov, Y. P., Itskevich, E. S., and Minina, N. Y. *Sov. Phys. JETP* **20**, 301 (1965).

[3] Brandt, N. B., Moshchalkov, V. V., and Chudinov, S. M. *Sov. Phys. JETP* **47**, 953 (1978).

[4] Itskevich, E. S. and Fisher, L. M. *Sov. Phys. JETP* **26**, 66 (1968).

[5] Tediosi, R., Armitage, N. P., Giannini, E., and van der Marel, D. *Physical Review Letters* **99**(1), 016406 (2007).

[6] McMillan, W. L. *Phys. Rev. B* **16**, 643 (1977).

[7] Becker, B., Patil, N. G., Ramakrishnan, S., Menovsky, A. A., Nieuwenhuys, G. J., and Mydosh, J. A. *Phys. Rev. B* **59**, 7266 (1999).

[8] Jung, M. H., Kim, H. C., Migliori, A., Galli, F., and Mydosh, J. A. *Phys. Rev. B* **68**, 132102 (2003).

[9] Kuo, Y. K., Lue, C. S., Hsu, F. H., Li, H. H., and Yang, H. D. *Phys. Rev. B* **64**, 125124 (2001).

[10] Imada, M. and Scalapino, D. J. *Phys. Rev. B* **34**(5), 3480 (1986).

[11] Dressel, M. and Gruner, G. *Electrodynamics of solids*. Cambridge University Press, (2002).

[12] Wooten, F. *Optical Properties of Solids*. Academic Press, (1972).

[13] van Heumen, E. and van der Marel, D. In *LECTURES ON THE PHYSICS OF STRONGLY CORRELATED SYSTEMS XI: Eleventh Training Course in the Physics of Strongly Correlated Systems,* Mancini and Avella, editors, volume 918, 203. AIP, (2007).

[14] de L. Kronig, R. *J. Opt. Soc. Am.* **12**, 547 (1926).

[15] Tompkins, H. G. and Irene, E. A. *Handbook of Ellipsometry*. Springer, (2005).

[16] Kuzmenko, A. B. *Rev. Sci. Instrum.* **76**, 083108 (2005).

[17] Kezsmarki, I., Gaal, R., Homes, C. C., Sipos, B., Berger, H., Bordacs, S., Mihaly, G., and Forro, L. *Physical Review B (Condensed Matter and Materials Physics)* **76**(20), 205114 (2007).

[18] Block, S. and Piermarini, G. J. *Physics Today* **29**, 44–52 (1976).

[19] Dunstan, D. J. and Spain, I. L. *J. of Physics E: Scientific Instruments* **22**, 913–23 (1989).

[20] Spain, I. L. and Dunstan, D. J. *J. of Physics E: Scientific Instruments* **22**, 923–33 (1989).

[21] Jayaraman, A. *Rev. of Modern Physics* **55**, 65–107 (1983).

[22] Jayaraman, A. *Rev. Sci. Instrum.* **57**, 1013–31 (1986).

[23] Eremets, M. I. *High pressure experimental methods*. Oxford University Press, (1996).

[24] Weidner, D. J., Wang, Y., and Vaughan, M. T. *Science* **266**(5184), 419 (1994).

[25] Jung, M. H., Kim, H. C., Migliori, A., Galli, F., and Mydosh, J. A. *Phys. Rev. B* **68**(13), 132102 Oct (2003).

[26] Torikachvili, M. S., Bud'ko, S. L., Law, S. A., Tillman, M. E., Mun, E. D., and Canfield, P. C. *Physical Review B (Condensed Matter and Materials Physics)* **76**(23), 235110 (2007).

[27] Suderow, H., Tissen, V. G., Brison, J. P., Martinez, J. L., and Vieira, S. *Physical Review Letters* **95**(11), 117006 (2005).

[28] Yomo, R., Yamaya, K., Abliz, M., Hedo, M., and Uwatoko, Y. *Physical Review B (Condensed Matter and Materials Physics)* **71**(13), 132508 (2005).

[29] Imada, M., Fujimori, A., and Tokura, Y. *Rev. Mod. Phys.* **70**(4), 1039–1263 Oct (1998).

[30] Terashima, T., Takahide, Y., Matsumoto, T., Uji, S., Kimura, N., Aoki, H., and Harima, H. *Physical Review B (Condensed Matter and Materials Physics)* **76**(5), 054506 (2007).

[31] Hamlin, J. J., Deemyad, S., Schilling, J. S., Jacobsen, M. K., Kumar, R. S., Cornelius, A. L., Cao, G., and Neumeier, J. J. *Physical Review B (Condensed Matter and Materials Physics)* **76**(1), 014432 (2007).

[32] Holmes, A. T., Jaccard, D., and Miyake, K. *Physical Review B (Condensed Matter and Materials Physics)* **69**(2), 024508 (2004).

[33] Kraak, W., Schaller, U., and Herrmann, R. *Phys. Stat. Solidi (a)* **85**(2), K183–K187 (1984).

[34] Walker, I. R. *Rev. Sci. Instrum.* **70**(8), 3402–3412 (1999).

[35] Mao, H. K., Bell, P. M., Shaner, J. W., and Steinberg, D. J. *Journal of Applied Physics* **49**(6), 3276–3283 (1978).

[36] *et al.*, H. K. M. *J. Geophysical Research* **91**, 4673–4676 (1986).

[37] Molegraaf, H. J. A. *Signposts to the mechanism of superconductivity in the cuprates*. PhD thesis, University of Gronigen, (2005).

[38] Ravel, B., Raphael, M. P., and Harris, V. G. *Phys. Rev. B* **65**, 184431 (2002).

[39] Eremets, M. I. and Timofeev, Y. A. *Rev. Sci. Instrum.* **63**, 3123 (1992).

[40] Ruoff, A. L., Ghandehari, K., Schmidt, S. C., Shaner, J. W., Samara, G. A., and Ross, M. volume 309, 1523–1525, (1994).

[41] Kuntscher, C. A., Frank, S., Pashkin, A., Hoinkis, M., Klemm, M., Sing, M., Horn, S., and Claessen, R. *Physical Review B (Condensed Matter and Materials Physics)* **74**(18), 184402 (2006).

[42] Frank, S., Kuntscher, C. A., Gregora, I., Petzelt, J., Yamauchi, T., and Ueda, Y. *Physical Review B (Condensed Matter and Materials Physics)* **76**(7), 075128 (2007).

[43] Drichko, N., Dressel, M., Kuntscher, C. A., Pashkin, A., Greco, A., Merino, J., and Schlueter, J. *Physical Review B (Condensed Matter and Materials Physics)* **74**(23), 235121 (2006).

[44] *The Enciclopaedia Britannica*. 11th edition, (1911).

[45] Isaacson, R. T. and Williams, G. A. *Phys. Rev.* **185**, 682 (1969).

[46] Smith, G. E., Baraff, G. A., and Rowell, J. M. *Phys. Rev.* **135**(4A), A1118–A1124 Aug (1964).

[47] Lin, Y.-M., Sun, X., and Dresselhaus1, 2, M. S. *Phys. Rev. B* **62**(7), 4610–4623 Aug (2000).

[48] Lu, M., Zieve, R. J., van Hulst, A., Jaeger, H. M., Rosenbaum, T. F., and Radelaar, S. *Phys. Rev. B* **53**(3), 1609–1615 Jan (1996).

[49] Hoffman, C. A., Meyer, J. R., Bartoli, F. J., Di Venere, A., Yi, X. J., Hou, C. L., Wang, H. C., Ketterson, J. B., and Wong, G. K. *Phys. Rev. B* **48**(15), 11431–11434 Oct (1993).

[50] Black, M. R., Lin, Y.-M., Cronin, S. B., Rabin, O., and Dresselhaus, M. S. *Phys. Rev. B* **65**(19), 195417 May (2002).

[51] Du, X., Tsai, S.-W., Maslov, D. L., and Hebard, A. F. *Physical Review Letters* **94**(16), 166601 (2005).

[52] Kopelevich, Y., Pantoja, J. C. M., da Silva, R. R., and Moehlecke, S. *Physical Review B (Condensed Matter and Materials Physics)* **73**(16), 165128 (2006).

[53] Zhang, Y., Tan, Y. W., Stormer, H. L., and Kim, P. *Nature* **438**, 201–204 (2005).

[54] Novoselov, K. S., Geim, A. K., Morozov, S. V., Jiang, D., Katsnelson, M. I., Grigorieva, I. V., Dubonos, S. V., and Firsov, A. A. *Nature* **438**, 197–200 (2005).

[55] Yang, F. Y., Liu, K., Hong, K., Reich, D. H., Searson, P. C., and Chien, C. L. *Science* **284**(5418), 1335 – 1337 (1999).

[56] Chong, B. K., Zhou, H., Mills, G., Donaldson, L., and Weaver, J. M. R. volume 19, 1769–1772. AVS, (2001).

[57] Lee, K. I., Jeun, M. H., Chang, J. Y., Han, S. H., Ha, J. G., and Lee, W. Y. *Phys. Stat. Solidi (b)* **241**(7), 1510–1513 (2004).

[58] Liu, Y. and Allen, R. E. *Phys. Rev. B* **52**(3), 1566–1577 Jul (1995).

[59] Golin, S. *Phys. Rev.* **166**(3), 643–651 Feb (1968).

[60] Ferreira, L. G. *J. Phys. Chem. Solids* **28**, 1891 (1967).

[61] Edel'man, V. S. *Advances in Physics* **25**(6), 555–613 (1976).

[62] Anagnostopulos, K. and Aubrey, J. E. *J. Phys. F: Metal Phys.* **6**(6), L181–L184 (1976).

[63] Kubo, R. *J. Phys. Soc. Japan* **12**, 570 (1957).

[64] Maldague, P. F. *Phys. Rev. B* **16**, 2437 (1977).

[65] Stepanov, N. P. *Russian Physics Journal* **47**(3), 262–272 (2004).

[66] Allen, J. W. and Mikkelsen, J. C. *Phys. Rev. B* **15**(6), 2952–2960 Mar (1977).

[67] Vecchi, M. P. and Dresselhaus, M. S. *Phys. Rev. B* **10**, 771 (1974).

[68] Gerlach, E. and Rautenberg, M. *Phys. Stat. Solidi (b)* **65**, K13 (1974).

[69] Gerlach, E., Grosse, P., Rautenberg, M., and Senske, W. *Phys. Stat. Solidi (b)* **75**, 553–558 (1976).

[70] Claessen, L. M., Jansen, A. G. M., and Wyder, P. *Phys. Rev. B* **33**, 7947 (1986).

[71] Mycielski, J. and Mycielski, A. *Phys. Rev. B* **18**, 1859 (1978).

[72] Marsiglio, F., Carbotte, J. P., and Schachinger, E. *Phys. Rev. B* **65**, 014515 (2001).

[73] Carbotte, J. P., Schachinger, E., and Basov, D. N. *Nature* **401**, 354 (1999).

[74] Lundqvist, B. *Phys. Kondens. Mater.* **6**, 193 (1967).

[75] Lundqvist, B. *Phys. Stat. Solidi* **32**, 273 (1969).

[76] Mahan, G. D. *Many-Particle Physics*. Plenum Press, New York, (1990).

[77] Sa-yakanit, V., Lakhno, V. D., and Hass, K. *Phys. Rev. B* **57**(10), 5772 (1998).

[78] Fischietti, M. V. *Phys. Rev. B* **44**(11), 5527 (1991).

[79] Bostwick, A., Ohta, T., MaChensney, J. L., Seyller, T., Horn, K., and Rotenberg, E. *Solid State Comm.* **143**(1-2), 63–71 (2007).

[80] Zhao, G. M. *Cond. Mat.* , 0307770 (2003).

[81] Xu, S., Cao, J., Miller, C. C., Mantell, D. A., Miller, R. J., and Gao, Y. *Phys. Rev. Lett.* **76**(3), 483–486 (1996).

[82] Bostwick, A., Ohta, T., Seyller, T., Horn, K., and Rotenberg, E. *Nature Physics* **3**(1), 36–40 (2007).

[83] Mendez, E. E., Misu, A., and Dresselhaus, M. S. *Phys. Rev. B* **24**(2), 639–648 (1981).

[84] Balla, D. and Brandt, B. *Sov. Phys. JETP* **20**(5), 1111–1117 (1965).

[85] Tanatar, B. and Ceperely, D. M. *Phys. Rev. B* **39**, 5005 (1989).

[86] Jerome, D., Rice, T. M., and Kohn, W. *Phys. Rev.* **158**(2), 462–475 (1967).

[87] Halperin, B. I. and Rice, T. M. *Rev. Mod. Phys.* **40**(4), 755–766 (1968).

[88] Bronold, F. X. and Hehske, H. *Phys. Rev. B* **74**, 165107 (2006).

[89] Kopelevich, Y., Lemanov, V. V., Moehlecke, S., and Torres, J. H. S. *Phys. Solid State* **41**, 1959 (1999).

[90] Polini, M., Asgari, R., Borghi, G., Barlas, Y., Pereg-Barnea, T., and MacDonald, A. H. *Physical Review B (Condensed Matter and Materials Physics)* **77**(8), 081411 (2008).

[91] Fuseya, Y., Ogata, M., and Fukuyama, H. *Cond. Mat.* , 0804.0076 (2008).

[92] Maldague, P. F. *Phys. Rev. B* **19**(12), 6172 (1979).

[93] Kukkonen, C. A. *Phys. Rev. Lett.* **37**(12), 782–785 (1976).

[94] Kukkonen, C. A. and Maldague, P. F. *J. Phys. F: Metal Phys.* **6**(11), L301 (1976).

[95] Peeters, F. M. *Phys. Rev. B* **30**, 159–165 (1984).

[96] Ceperley, D. M. and Alden, B. J. *Phys. Rev. Lett.* **45**, 566 (1980).

[97] Drummond, N. D., Radnai, Z., Trail, J. R., Towler, M. D., and Needs, R. J. *Phys. Rev. B* **69**, 085116 (2004).

[98] Li, G., Hus, W. Z., Qian, D., Hsieh, D., Hasan, M. Z., Morosan, E., Cava, R. J., and Wang, N. L. . *Phys. Rev. Lett.* (99), 027404 (2007).

[99] Kohn, W. *Phys. Rev. Lett.* **19**, 439 (1967).

[100] Holstein, T. *Ann. Phys.* **8**, 325 (1959).

[101] Toyozawa, Y. *Prog. Theor. Phys.* **26**, 29 (1961).

[102] Overhauser, A. W. *Phys. Rev. B* **3**(6), 1888–1898 Mar (1971).

[103] Emin, D. *Phys. Rev. B* **48**(18), 13691 (1993).

[104] Austin, I. G. and Mott, N. F. *Science* **168**(3927), 71–77 (1970).

[105] Pinsook, U. and Sa-yakanit, V. *Phys. Stat. Solidi (b)* **237**(1), 82–89 (2003).

[106] Shelton, R. N., Hausermann-Berg, L. S., Klavins, P., Yang, H. D., Anderson, M. S., and Swenson, C. A. *Phys. Rev. B* **34**(7), 4590–4594 (1986).

[107] Singh, Y., Nirmala, R., Ramakrishnan, S., and Malik, S. K. *Phys. Rev. B* **72**, 045106 (2005).

[108] Peierls, R. E. *Quantum Theory of Solids*. Oxford University Press, (1955).

[109] Gruner, G. *Density waves in solids*. Perseus Publishing, (1994).

[110] Travaglini, G. and Wachter, P. *Phys. Rev. B* **30**, 1971 (1984).

[111] Travaglini, G. and Wachter, P. *Solid State Comm.* **37**, 559 (1981).

[112] Degiorgi, L., Alavi, B., Mihali, G., and Gruner, G. *Phys. Rev. B* **44**, 7808 (1991).

[113] Perucchi, A., Degiorgi, L., and Thorne, R. E. *Phys. Rev. B* **69**, 195114 (2004).

[114] Fournel, A. and Sorbier, J. P. *Phys. Rev. Lett.* **57**, 2199 (1986).

[115] Sridhar, S., Reagor, D., and Gruner, G. *Phys. Rev. Lett.* **55**, 1196 (1985).

[116] Schwartz, A., Dressel, M., Gruner, G., Vescoli, V., Degiorgi, L., and Giamarchi, T. *Phys. Rev. B* **58**, 1261 (1998).

[117] Henderson, W., Vescoli, V., Tran, P., Degiorgi, L., and Gruner, G. *Eur. Phys. J. B* **11**, 365 (1999).

[118] Giamarchi, T., Biermann, S., Georges, A., and Lichtenstein, A. *J. de Physique IV* **114**, 23 (2004).

[119] Frohlich, H. *Proc. R. Soc. A* **223**, 296 (1954).

[120] Vescoli, V., Degiorgi, L., Berger, H., and Forro, L. *Phys. Rev. Lett.* **81**, 453 (1998).

[121] van der Marel, D., Molegraaf, H. J. A., Presura, C., and Santoso, I. In *Concepts in electron correlations,* Hewson, A. and Zlatic, V., editors, (2003).

[122] Molegraaf, H. J. A., Presura, C., van der Marel, D., Kes, P. H., and Li, M. *Science* **295**, 2239 (2002).

[123] Menovsky, A. A. and Franse, J. J. M. *J. Cryst. Grouth* **65**, 286 (1983).

[124] Galli, F., Ramakrishnan, S., Taniguchi, T., Nieuwenhuys, G. J., Mydosh, J. A., Geupel, S., Ludecke, J., and van Smaalen, S. *Phys. Rev. Lett.* **85**(1), 158–161 (2000).

[125] Kim, T. W., Donovan, S., Gruner, G., and Philipp, A. *Phys. Rev. B* **43**, 6315 (1991).

[126] Puchkov, A. V., Basov, D. N., and Timusk, T. *J. Phys.: Condens. Matter* **8**, 10049 (1996).

[127] van der Eb, J. W., Kuzmenko, A. B., and van der Marel, D. *Phys. Rev. Lett.* **86**, 3407 (2001).

[128] Valla, T., Fedorov, A. V., Johnson, P. D., and Hulbert, S. L. *Phys. Rev. Lett.* **83**, 2085 (1999).

[129] Dordevic, S. V., Basov, D., and Dynes, R. C. *Phys. Rev. B* **64**, 161103 (2001).

[130] Dordevic, S. V., Basov, D., Dynes, R. C., Ruzicka, B., Vescoli, V., Degiorgi, L., Berger, H., Gaal, R., and Forro, L. *Eur. Phys. J. B* **33**, 15 (2003).

[131] Valla, T., Fedorov, A. V., Johnson, P. D., Xue, J., Smith, K. E., and DiSalvo, F. J. *Phys. Rev. Lett.* **85**, 4759 (2000).

[132] Basov, D., Singley, E. J., and Dordevic, S. V. *Phys. Rev. B* **65**, 054516 (2002).

[133] Swenson, C. A., Shelton, R. N., Klavins, P., and Yang, H. D. *Phys. Rev. B* **43**, 7668–7675 (1991).

[134] Shulga, S. V., Dolgov, O. V., and Maksimov, E. G. *Physica C* **178**, 266 (1991).

[135] Eliashberg, G. M. *Sov. Phys. JETP* **11**, 696 (1960).

[136] Eliashberg, G. M. *Sov. Phys. JETP* **16**, 780 (1963).

[137] Rice, M. J. *Phys. Rev. Lett.* **37**, 36 (1976).